Acoustic reflectometry for airway measurement

Ian Marshall MA(Oxon) CEng MIEE MIPSM

PhD

University of Edinburgh

1992

Abstract

Measurements of upper airway dimensions would be useful in a number of medical specialities, but no suitable measurement technique is currently available.

Acoustic reflectometry is a method that may prove suitable. Pulses of sound are directed down the subject's airway, and the resulting reflections ("echoes") are analysed to yield the cross sectional area as a function of distance. However, the few existing reflectometers have limited performance and are not suited to routine clinical use.

Research and innovation are therefore necessary to develop a reflectometer that is simple to use in a clinical environment and produces reliable, "real-time" airway measurements.

After covering the theory of reflectometry, methods of acoustic pulse production are investigated, and a theoretical and experimental survey of area reconstruction algorithms is carried out.

A reflectometer suitable for clinical use is developed, being made compact by using short-duration pulses and a flexible source tube. Subject breathing during measurement sessions is made possible by means of a respiratory valve.

Measurement accuracy with simplified models of the upper airway is 10%, and *in vitro* reproducibility is 2%. Day-to-day reproducibility with human volunteers is a clinically acceptable 10%-20%. In the first reported comparison with Magnetic Resonance Imaging (MRI), acoustic estimates of airway areas are within 20% to 30% of MRI estimates, whilst pharyngeal volume estimates agree within 6%.

Preliminary trials demonstrate the effects of breathing mode, posture and respiratory phase. The reflectometer is used successfully with sleep apnoea patients and anaesthetized subjects.

A further innovation is a reflectometer having an arbitrarily short source tube.

Contents

Chapter 1

Introduction and outline of research programme

Measurements of airway dimensions would be of clinical benefit in the investigation of obstructive sleep apnoea and in the general anaesthetic management of patients.

Sleep apnoea is caused by occlusion of the upper airway, and results in unsatisfying sleep leading to daytime drowsiness, impaired work performance and increased frequency of road traffic accidents [Douglas 1988, Findley et al 1988]. It affects between 1% and 10% of the adult population [Lavie 1983]. Airway measurement might be useful in predicting sleep apnoea and in guiding corrective surgery.

A large percentage of anaesthetic accidents involves some aspect of airway mismanagement [Davis et al 1979]. An objective measure of airway patency during anaesthesia might help reduce the number of incidents.

At present there is no technique for measuring airways that meets the requirements of being noninvasive, portable, inexpensive and simple to operate [Douglas 1990]. X-ray computed tomography (CT) and Magnetic Resonance Imaging (MRI) can produce limited data under certain specialized conditions, but are not suitable for routine measurement or monitoring.

For some twenty-five years, speech researchers have experimented with acoustic methods for estimating the dimensions of the vocal tract. In the earlier work, the resonant frequencies were determined, from which airway dimensions were then inferred [Schroeder 1967, Mermelstein 1967]. Later, Sondhi and colleagues [Sondhi and Gopinath 1971] introduced a time domain reflection technique, in which a pulse of sound is directed into the subject's mouth and the resulting reflections are recorded. Suitable analysis can then directly determine the cross sectional area of the airway as a function of distance from the lips. It is this technique, known as acoustic reflectometry, which forms the subject of the present work.

Acoustic reflection measurements of airways have been reported by only two other research groups. Fredberg [Fredberg et al 1980, Brooks et al 1984] developed a complex He/O_2 reflectometer that was bulky, non-portable and difficult to operate. Identical equipment and analysis software has been used by Hoffstein and colleagues in the study of tracheal and pharyngeal dimensions [Rivlin et al 1984, Bradley et al 1986, Brown et al 1987], but there remains no independent assessment of the technique.

Research and innovation are necessary to see whether a reflectometer can be designed to produce reliable scientific measurements under routine clinical conditions. The specific objectives of the present work are;–

1. To develop a reflectometer that is portable and simple to operate:

2. To allow subject breathing during measurement sessions:

3. To display airway measurements in "real-time".

We begin in Chapter 2 with a survey of the literature pertaining to acoustical methods of airway measurement. Chapter 3 describes how reflections are formed within the airway, and Chapter 4 describes the reconstruction techniques available for calculating the airway cross sectional area from the reflected signals. This comprehensive comparison of reconstruction algorithms [Marshall 1992a] shows that approximate methods are much more rapid than the complete methods, and yet yield useful information.

To take full advantage of the speed offered by approximate reconstruction algorithms, the airway should be excited by short duration acoustic pulses to avoid the need for deconvolving the reflected pressure waves. The production of acoustic impulses using loudspeakers [Marshall 1990] is discussed in Chapter 5. By driving the loudspeaker to produce an approximate impulse, it is also possible to reduce the length of the reflectometer, hence making it more compact.

In Chapter 6, experimentally determined pulse shapes are combined with theoretical reflection functions to simulate the pressure waveforms expected in an actual reflectometer. The synthetic waveforms are then analysed with and without deconvolution, and the area profiles reconstructed.

A simple reflectometer is implemented in Chapter 7, using the ideas developed so far, and based on a standard microcomputer. Another innovation is the use of a flexible source tube to keep the apparatus compact and to assist with patient connection. The reflectometer is validated against test objects in Chapter 8, and its performance characterized.

To make the reflectometer more suitable for clinical use, several novel improvements are discussed in Chapter 9. These include a respiratory valve to enable free breathing during measurement sessions, special hardware to speed up data analysis, and the synchronization of measurements with the respiratory cycle. The improved reflectometer is used in a series of pre-clinical trials with volunteers, described in Chapter 10. The trials investigate reproducibility, the effects of breathing mode, posture and respiration. In a study of 11 volunteers, the first reported comparison of acoustic and MRI airway measurements is made. This study also represents the first validation of acoustic reflectometry for pharyngeal area estimation. The reflectometer is used with sleep apnoea patients, for nasal measurements, and with anaesthetized subjects.

Chapter 11 investigates the need for a source tube. A new analysis of reflectometry [Marshall 1992b] shows that, in principle, an arbitrarily short source tube will suffice. A short reflectometer is implemented, and used to measure various test objects.

Finally, the work is summarized in Chapter 12 and the important findings are restated.

Appendix A describes the units of pressure measurement, and Appendix B covers the mathematical theory of convolution and deconvolution. Software listings, circuit diagrams and mechanical drawings of acoustic test objects comprise Appendices C, D and E respectively. Appendix F is a glossary of symbols and abbreviations used in the text.

Chapter 2

Acoustic measurement of airway dimensions

The methods available for acoustic measurement of airway dimensions fall conveniently into two classes; those made in the frequency domain, and those made in the time domain. All the methods assume one-dimensional wave propagation along the airway, and estimate the cross sectional area as a function of distance. No information can be obtained about the shape of the areas, nor can curvature of the airway be detected.

2.1 Frequency domain methods

Most of the early work on airway dimensions was carried out at Bell Telephone Laboratories by speech researchers. Their interest was in the shape of the vocal tract (that part of the airway between the lips and the vocal cords) for different vowel sounds. According to the theory of speech production, the vocal cords are excited by a train of impulses, and the resulting pressure disturbances are filtered by the vocal tract to produce the characteristic vowel sounds. The resonances of the vocal tract determine the dominant frequencies (formants) of the particular vowels.

The vocal tract is regarded as being closed by the vocal cords (at the glottis) and open at the lips during normal speech. For a uniform vocal tract, the higher resonant frequencies would be odd multiples of the fundamental. When the tract departs from uniformity, the resonant frequencies are shifted. [Mermelstein 1967] and [Schroeder 1967] showed that each resonant frequency is determined by one coefficient in a Fourier expansion of the area function. That is, one writes the area function as–

$$A(x) = A_0 + A_0 \sum_{m=1}^{\infty} a_m \cos(\pi m x / L) \tag{2.1}$$

where A_0 is the cross sectional area from which the actual tract deviates, a_m are the coefficients to be determined, and L is the (assumed) length of the tract. Values of L in the range 16-20cm were used. The shifts in resonant frequencies from those for a uniform tract were given by [Schroeder 1967] as–

$$\frac{\delta f_n}{f_n} = -\frac{1}{2} a_{2n-1} \tag{2.2}$$

One extracts the formant frequencies from vowel sounds, compares them with the resonant frequencies f_n expected for a uniform tract, and hence determines the coefficients a_m. The subscript $(2n-1)$ in Equation 2.2 indicates that only the *odd* coefficients (corresponding to antisymmetric deviations) can be determined from the vowel formants. The even terms correspond to resonances with the lips closed, and cannot be determined from normal speech. Instead, [Schroeder 1967] showed how they can be estimated from impedance measurements made at the lips. The zeroes of the input impedance correspond to the resonant frequencies with the lips open, whilst the impedance poles correspond to the resonant frequencies with the lips closed. In practice, only the first few resonances can be determined, and a bandlimited area function is thus constructed. Losses due to viscosity, thermal conduction and airway wall non-rigidity are not taken into account. Despite having to assume some length L and using only six Fourier coefficients, Schroeder found good agreement with the actual area profiles of several test objects. It is unclear whether Schroeder and Mermelstein actually used the technique *in vivo*.

Researchers at Imperial College, London used a method based on the transfer impedance of the vocal tract [Stansfield and Bogner 1973]. By assuming some input volume velocity function at the glottis and measuring the pressure function produced at the lips, Stansfield and Bogner were able to estimate vocal tract areas. Their method was actually an indirect way of measuring the input impedance, from which the input impulse response was then calculated. Finally, a recursive time domain algorithm was used to reconstruct the cross sectional area.

2.2 Time domain methods

Sondhi and colleagues, also working at Bell Telephone Laboratories, published a largely theoretical paper [Sondhi and Gopinath 1971] in which they showed how measurement of the pressure waveform developed at the lips in response to an applied volume velocity pulse can be used to calculate the area profile of the vocal tract. The method of calculation was based on an integral form of the acoustic pressure and velocity relationships, and although mathematically complex, did not need Schroeder's prior assumption of vocal tract length. Again, no account was taken of losses in the airway. Only one preliminary measurement of a test object is presented in this 1971 paper. In a later paper [Sondhi 1974], it was shown how losses can be included in the analysis if they are assumed to have certain simple forms. The magnitudes of the losses can be estimated from the bandwidths of the vocal tract resonances. A full report of Sondhi's experimental work did not appear for many years [Sondhi and Resnick 1983]. In this paper, a custom built electrostatic transducer produces pressure pulses which are directed into the subject's mouth. Analysis of the reflections allows a reconstruction of the area profile during phonation. When run on a powerful minicomputer, up to 18 measurements could be made every second. A wide range of mouth and pharyngeal sizes was reported. For the vowel "ah", for example, the cross sectional areas of the mouth and pharynx were 15cm^2 and 4cm^2 respectively. For the vowel "ee", the corresponding values were $1cm^2$ and $2cm^2$.

Meanwhile, respiratory physiologists at Harvard University developed their own reflectometer. [Jackson et al 1977] reported a reflectometer that was used with excised canine lungs. In this implementation, a spark discharge produced the pressure pulses. Estimates of absolute areas and of area changes induced by bronchoconstricting agents agreed fairly well with X-ray measurements.

A substantially more complex form of this apparatus was reported by Fredberg three years later [Fredberg et al 1980]. To maintain measurement accuracy as far down the trachea and bronchial tree as possible[1], he argued that He/O_2 gas should be used to increase the working bandwidth without exciting cross modes. With more information from the frequency range in which airway wall non-rigidity can be neglected (above 500-1kHz), accuracy should be enhanced. Consequently, the apparatus and the subject's lungs were filled with He/O_2, and subjects had to rebreathe from a He/O_2-filled spirometer during measurement sessions. However, the acoustic pulse waveform used would seem incapable of exploiting the extended frequency range offered, and the need for He/O_2 has not been proved. To suppress cross mode propagation in the mouth, subjects used custom moulded mouthpieces to fill the front of the oral cavity. [Brooks et al 1984] reported on the accuracy and reproducibilty obtainable with this equipment. The coefficient of variation of measurements was typically 10%, and tracheal areas were overestimated by 6% compared with X-ray measurements. The cross sectional areas of glass models were overestimated by as much as 25%.

Fredberg's equipment and analysis software was duplicated for clinical trials with sleep apnoeic patients in Toronto. The He/O_2-filled reflectometer has there been used to investigate the size, compliance and lung volume dependence of the pharynx in small groups of normal controls, snorers, and sleep apnoeics [Hoffstein et al 1984, Brown et al 1985, Brown et al 1986, Bradley et al 1986].

[1] The area reconstruction algorithms begin at the lips and proceed downwards, with the errors progressively accumulating.

Pharyngeal areas in the range $3cm^2$ to $7cm^2$ are reported, with pharyngeal compliances of $4\%/cmH_2O$ [2] for controls and $9\%/cmH_2O$ for sleep apnoea patients [Brown et al 1985]. However, no validation of pharyngeal measurements is presented, and the definition of "pharynx" in all this literature is incorrect, in that it includes the rear of the oral cavity (see Section 10.2.1). Little reliance can therefore be placed on the discussions of "pharyngeal" properties. In a study of 6 patients with tracheal stenosis [Hoffstein and Zamel 1984], the acoustic method gave a mean (± standard deviation) tracheal area of $1.7 \pm 0.3cm^2$ compared with $1.2 \pm 0.3cm^2$ from X-ray measurements. In a later study of 11 patients [D'Urzo et al 1988], acoustic estimates of glottal areas were closer to the areas determined by X-ray CT, at $1.8 \pm 0.8cm^2$ compared with $1.7 \pm 0.9cm^2$. [Rubinstein et al 1987] showed that the bulky custom mouthpieces were not necessary.

The Harvard and Toronto studies are summarized in a useful paper which questions the need for He/O_2 gas [Hoffstein and Fredberg 1991]. This is probably unnecessary for upper airway measurements. Our present interest extends only as far as the glottis, and we expect to obtain clinically useful results with air as the working medium. This will allow a much simpler, more compact piece of equipment.

[2]See Appendix A for an explanantion of units of pressure.

Chapter 3

The theory of multiple reflections

In this chapter, the basic theory of acoustic reflectometry will be outlined. After a brief introduction, we will see how reflection coefficients arise, and how multiple reflections within the object being studied lead to the concept of the reflectance function. Methods for calculating the reflectance of a given object will be described. Energy relationships and the effect of branching will be discussed.

3.1 Introduction

The principle of acoustic reflectometry is appealingly simple, and is illustrated in Figure 3.1. An acoustic impulse is launched from a source transducer, and passes down a tube into the object being measured. The impulse and the reflection from the object are recorded by a pressure-sensitive microphone and computer system. Appropriate analysis of the reflected waveform leads to a reconstruction of the impedance (and hence the area) profile of the object. Much of the theory was originally developed by geophysicists for processing seismological survey data. Related fields are electrical transmission line theory, multi-layer optical filters, and optical time domain reflectometry (OTDR). The latter technique is employed

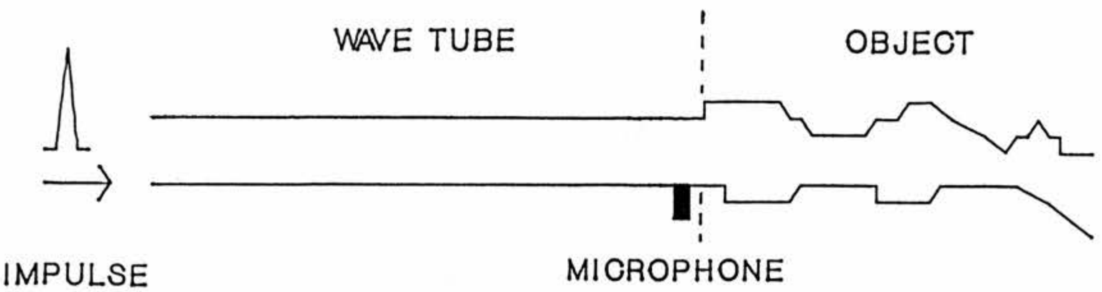

Figure 3.1: *The principle of acoustic reflectometry.*

for fault-finding in fibre-optic cables [Barnoski and Jensen 1976].

3.2 Acoustic reflection coefficients

Acoustic textbooks [Morse 1948, Beranek 1986, Kinsler and Frey 1982] invariably give a derivation of the fundamental wave equation for acoustic phenomena. For one-dimensional propagation in the x-direction, the wave equation in terms of the *acoustic pressure* p is–

$$\frac{\partial^2 p}{\partial x^2} = \frac{1}{c^2}\frac{\partial^2 p}{\partial t^2} \tag{3.1}$$

where c is the wave velocity, given by–

$$c^2 = \left(\frac{\rho_0}{\gamma p_0}\right)^{-1}$$

and ρ_0 and p_0 are respectively the equilibrium density and pressure of the gas, and γ is the ratio of the adiabatic and isothermal specific heats.

It can be shown that Equation 3.1 has solutions of the form–

$$p(x,t) = f(t - x/c) + g(t + x/c)$$

where f and g are generalized functions describing waves propagating forwards and backwards respectively. In particular, we can consider periodic solutions, because any function can (in principle) be represented by a suitable sum of periodic components. Thus we may write–

$$p(x,t) = C_1 e^{i\omega(t-x/c)} + C_2 e^{i\omega(t+x/c)} \tag{3.2}$$

where C_1 and C_2 are constants determined by the boundary conditions.

The equation of motion for the gas relates the particle velocity u to the acoustic pressure by the expression–

$$\frac{\partial u}{\partial t} = -\frac{1}{\rho_0}\frac{\partial p}{\partial x}$$

which gives us–

$$u(x,t) = \frac{1}{\rho_0 c}\left[C_1 e^{i\omega(t-x/c)} - C_2 e^{i\omega(t+x/c)}\right] \tag{3.3}$$

The product $\rho_0 c$ occurs often in acoustic theory, and is termed the *specific acoustic impedance* Z_s [Morse 1948]. It is the ratio of pressure to particle velocity in a medium.

Let us now consider the two semi-infinite media shown in Figure 3.2, separated by an interface at $x = 0$. Let the media have specific impedances Z_{s1} and Z_{s2}, and let a pressure wave with unit amplitude be incident from the left. This wave can be represented by $e^{i\omega(t-x/c)}$. At the boundary, the wave is partially reflected to form a backward-travelling wave $r_{1,2}e^{i\omega(t+x/c)}$ and partially transmitted into the second medium as $t_{1,2}e^{i\omega(t-x/c)}$, where $r_{1,2}$ and $t_{1,2}$ are respectively the reflection and transmission coefficients, the order of the subscripts indicating the direction of incidence at the boundary. The pressures and velocities must be continuous across the boundary, and by using Equations 3.2 and 3.3 we obtain–

$$1 + r_{1,2} = t_{1,2} \tag{3.4}$$

$$\frac{1}{Z_{s1}}(1 - r_{1,2}) = \frac{1}{Z_{s2}}t_{1,2} \tag{3.5}$$

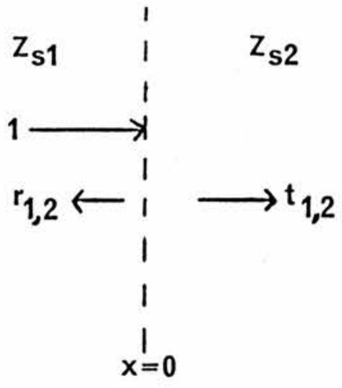

Figure 3.2: *Reflection and transmission at a boundary between two media.*

leading to–

$$r_{1,2} = \frac{Z_{s2} - Z_{s1}}{Z_{s1} + Z_{s2}} \tag{3.6}$$

$$t_{1,2} = \frac{2Z_{s2}}{Z_{s1} + Z_{s2}} \tag{3.7}$$

For a wave incident on the boundary from medium 2, we have $r_{2,1} = -r_{1,2}$, and $t_{2,1} = 2Z_{s1}(Z_{s1} + Z_{s2})^{-1}$. Notice that the combined transmission loss in travelling forwards and backwards across a boundary is $t_{1,2}t_{2,1} = 1 - r_{1,2}r_{2,1}$.

So far, we have considered media with different *specific* acoustic impedances, which is the case in seismological applications. In the present work we are concerned with one medium only—air—but because the extent of the wavefronts is restricted by the diameter of the object, the specific impedance is replaced by the *acoustic impedance* Z, which is the ratio of pressure to volume flow. It takes account of the cross-sectional area of propagation, and is given by–

$$Z = \frac{\rho c}{A}$$

where A is the cross-sectional area, and we have now dropped the subscript from ρ_0. Thus the acoustic impedance is inversely related to the area A.

3.3 Multiple reflections and the reflectance

The acoustic object being measured is represented as a series of discrete cylinders, each having the same length L with corresponding two-way travel-time $\Delta t = 2L/c$ (Figure 3.3). Lossless, one-dimensional wave propagation is ensured

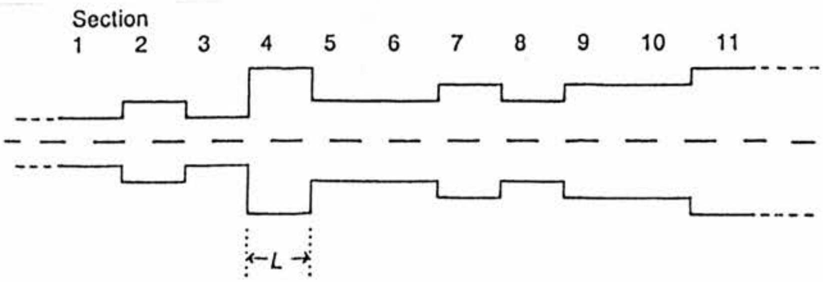

Figure 3.3: *Discrete representation of an acoustic object.*

by restricting incident waves so that the highest frequency has a wavelength greater than twice the greatest object diameter. Cross-modes cannot then form. Although normal incidence is assumed, for clarity it is customary to offset the rays in schematic diagrams such as Figure 3.4. The object is terminated at both ends by semi-infinite uniform tubes from which there are no returning reflections, the proximal tube being referred to as the *source tube*[1]. An impulse I incident on the object will be partially reflected and partially transmitted at each interface between sections. Energy undergoing a single reflection before emerging from the object (eg ray R_0) constitutes a "primary" reflection, whilst energy that has undergone multiple reflections before emerging (eg most components of ray R_3) constitutes "secondary" and higher order reflections. After an odd number of reflections, waves return in the incident direction, whilst after an even number of reflections, they are transmitted away from the source. The number of multiply reflected components increases very rapidly as the number

[1] We will show later how the need for semi-infinite terminations can be relaxed in practice.

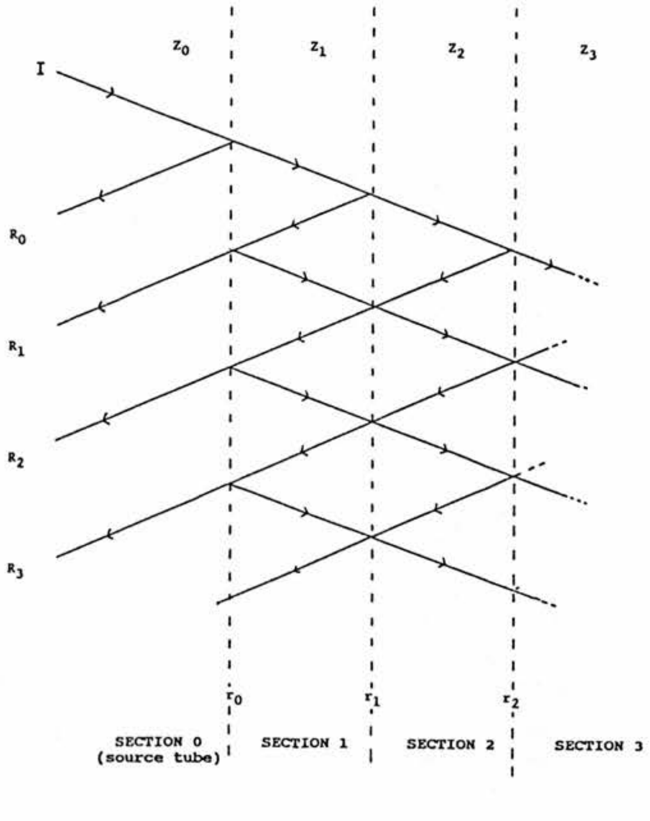

Figure 3.4: *Multiple reflections within a series of layers or sections. I is the incident impulse, with R_0, R_1, etc being the reflected pressure terms.*

of sections is increased. The pressure waveform observed at the mouth of the object consists of a series of returning impulses spaced apart by the time interval Δt, as shown in Figure 3.5. Expressions for this waveform in terms of the individual reflection coefficients at the interfaces are available in the literature [Ware and Aki 1969, Stansfield and Bogner 1973, Robinson et al 1986], and are developed using recursive formulae. [Stansfield and Bogner 1973] present a method which describes clearly the propagation of the incident impulse and its reflections, but the mathematics is a little cumbersome. Their method is not particularly suitable for inversion (ie reconstruction of unknown objects from the observed reflections), but we will use it later in calculating the reflectances of known objects. The equivalent exposition in [Ware and Aki 1969] is well suited

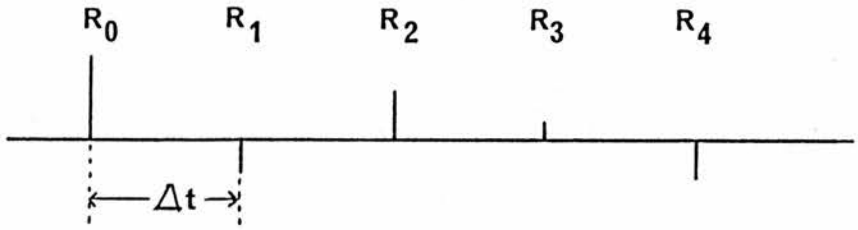

Figure 3.5: *The reflected pressure waveform observed at the mouth of the object.* $\Delta t = 2\,L/c$.

to the reconstruction problem, and so is the method summarized here. Their interest was in the seismological problem, and they referred to the forward and backward travelling waves as downward (D) and upward (U) waves respectively. They began by defining a "layer matrix" which relates the forward and backward travelling waves in two adjacent layers k and $k+1$ (Figure 3.6). The layer

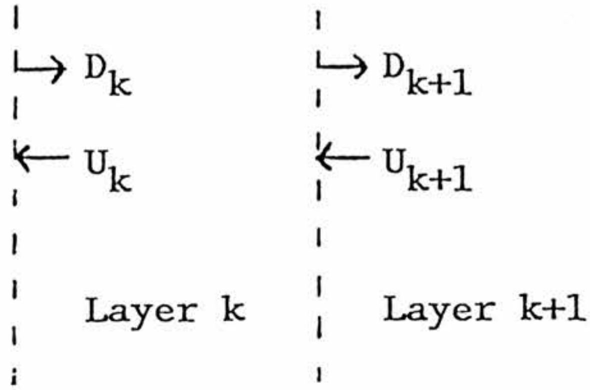

Figure 3.6: *Forward and backward travelling waves in adjacent layers or sections.*

matrix takes account of the reflection and transmission at the interface, and the travel time through the layer. To simplify the notation, they worked in terms not of pressure, but of pressure times the square root of the layer impedance, ie $p\sqrt{Z}$. For this variable, the reflection coefficient $r_{k,k+1}$ (which we now write simply as r_k) is given in the usual way as $r_k = (Z_{k+1} - Z_k)(Z_k + Z_{k+1})^{-1}$, where Z_k and Z_{k+1} are the impedances of the layers. The corresponding transmission coefficient t_k is given by $t_k^2 = (1 - r_k^2)$, and is independent of the direction of travel across the interface.. It is convenient to work in the z-domain, in which the two-way travel time Δt is transformed to $z = e^{i\omega\Delta t}$. Letting W represent the *one*-way travel time (ie $W^2 = z$), we obtain–

$$\begin{bmatrix} U(k,z) \\ D(k,z) \end{bmatrix} = \frac{1}{Wt_k} \begin{bmatrix} z & r_k z \\ r_k & 1 \end{bmatrix} \begin{bmatrix} U(k+1,z) \\ D(k+1,z) \end{bmatrix}$$

By multiplying together successive layer matrices, it is possible to relate section 0 (the source tube) to any section k in the general expression–

$$\begin{bmatrix} U(0,z) \\ D(0,z) \end{bmatrix} = \frac{1}{W^{k+1}\prod_0^k t_i} \begin{bmatrix} z^{k+1}F(k,1/z) & z^{k+1}G(k,1/z) \\ G(k,z) & F(k,z) \end{bmatrix} \begin{bmatrix} U(k+1,z) \\ D(k+1,z) \end{bmatrix} \tag{3.8}$$

The notation is kept to manageable proportions by introducing the recursive polynomials F and G which are functions of the individual reflection coefficients r_i and the travel time. They are given by–

$$F(k+1,z) = F(k,z) + r_{k+1}zG(k,z) \tag{3.9}$$

$$G(k+1,z) = r_{k+1}F(k,z) + zG(k,z) \tag{3.10}$$

with

$$F(0,z) = 1$$

and

$$G(0,z) = r_0$$

The particular case of interest in pulse reflectometry is that with the forward-travelling (D) wave in the first section being an incident impulse, with a z-transform of unity. The backward-travelling (U) wave in the first section is the observed reflection, and under these conditions it is called the "reflectance" $R(z)$ [Sondhi and Resnick 1983] or the "input impulse response" [Watson 1989]. The forward-travelling wave in the last (nth) section is some (unknown) transmission function, and there is no backward-travelling wave returning from the (semi-infinite) last section. Inserting these conditions in Equation 3.8 and re-arranging, we obtain an expression for the reflectance function of an object of n sections–

$$R(n,z) = \frac{z^{n+1}G(n,1/z)}{F(n,z)} \tag{3.11}$$

The reflectance function is thus seen to be a polynomial in z, representing a series of discrete returning impulses with time interval Δt. It is akin to the impulse response of any linear system —say an electrical circuit—but differs in that we are here concerned with the *reflected* response, rather than the more familiar *transfer* response.

Using Equation 3.11 to calculate the reflectance produced by a given object is possible in only a few very simple cases, because of the complexity of the polynomials.

The simplest non-trivial example of a reflectance function results from one intermediate section, ie 2 interfaces or n=1 (Figure 3.7). Evaluating the polynomials F and G, and inserting them in Equation 3.11 gives–

$$R(1,z) = \frac{z^2(r_1 + r_0/z)}{1 + r_0 r_1 z}$$

Expanding this expression using a binomial series, and collecting terms in ascending powers of z gives–

$$R(1,z) = \begin{array}{lllll} r_0 z & +r_1(1-r_0^2)z^2 & -r_0 r_1^2(1-r_0^2)z^3 & +r_0^2 r_1^3(1-r_0^2)z^4 & -\cdots \\ R_0 z & +R_1 z^2 & +R_2 z^3 & +R_3 z^4 & -\cdots \end{array} \tag{3.12}$$

The first two terms R_0 and R_1 are the "primary" reflections, resulting from single reflections from the two interfaces, whilst the remaining terms R_2, R_3, etc, are

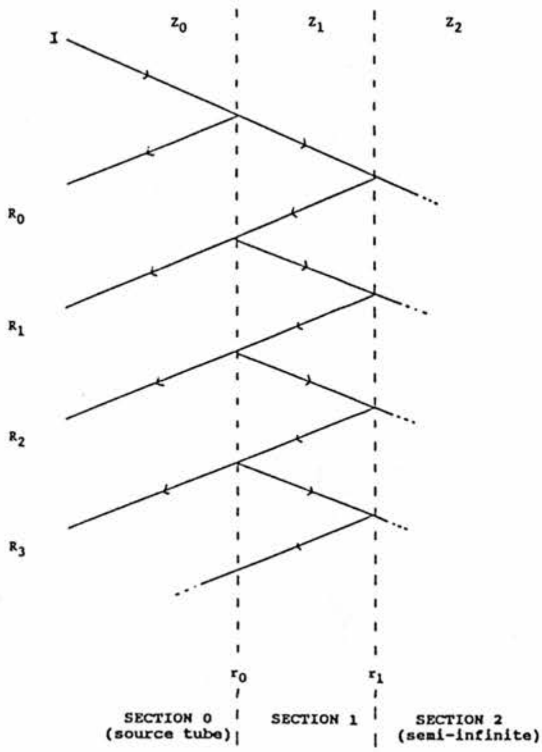

Figure 3.7: *Multiple reflections within one intermediate section.*

multiple reflections. Notice how the multiple reflection terms die away as $-r_0r_1$, and so quickly become negligible in many cases[2]

In the next section, a numerical method for calculating the reflectance of an arbitrary object is described.

3.4 The reflectance of an arbitrary object.

In their work on vocal tracts, [Stansfield and Bogner 1973] formulated the multiple reflection problem in a way that clearly shows the propagation of the impulses in the sections. In particular, successive backwards-travelling impulses in the first

[2]An important exception to this is the marine seismological case, where $Z_{air} \ll Z_{sea} \ll Z_{seabed}$ so that $-r_0r_1$ approaches unity, and slowly-decaying reverberations occur between the seabed and the surface. See Section 11.2.2.

section are the required terms in the reflectance function. It is quite straightforward to implement this method numerically, and hence determine the reflectance of an arbitrary object. The notation is shown in Figure 3.8, which depicts the forward (f) and backward (b) impulses in three successive sections $k-1$, k and $k+1$ at a given moment in time. If sections k and $k+1$ have areas A_k and A_{k+1}

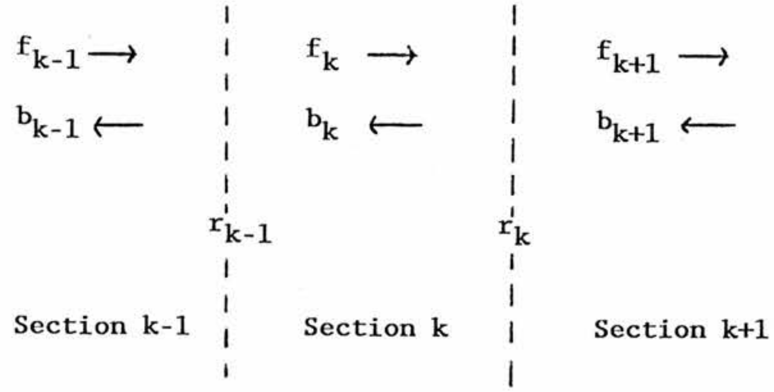

Figure 3.8: *The notation used to determine numerically the reflectance of an arbitrary object.*

respectively, then the forward reflection coefficient at their interface is given by $r_k = (A_k - A_{k+1})(A_k + A_{k+1})^{-1}$, and the forward transmission coefficient by $(1 + r_k)$. The reverse reflection coefficient is, as usual, $-r_k$. The impulses are therefore related by–

$$f'_k = (1 + r_{k-1})f_{k-1} - r_{k-1}b_k \tag{3.13}$$

$$b'_k = r_k f_k + (1 - r_k)b_{k+1} \tag{3.14}$$

where the primes denote new values one single way travel time later. The reflectance corresponding to N sections is determined by setting all f_k and all b_k to zero, and then "injecting" a unit impulse $f_1 = 1$ at time zero. At successive time intervals $t_i : i = 1, 2, 3, \cdots, 2N$ the recursive relations of Equations 3.13 and 3.14 are evaluated for $k = 1, 2, 3, \cdots, i$. At even-numbered time intervals, it will be found that all the multiply reflected impulses are travelling backwards, and b'_1 then gives the next term in the reflectance function.

3.5 Energy considerations

Let us now consider how the incident acoustic *energy* splits at a boundary between two sections. If the second section has N times the cross-sectional area of the first (ie $A_2 = NA_1$ or $Z_2 = Z_1/N$) (Figure 3.9) then the coefficients of reflection and transmission for pressure p are found from Equations 3.6 and 3.4 respectively–

$$r_{1,2} = \frac{1-N}{1+N} \tag{3.15}$$

$$t_{1,2} = 1 + r_{1,2} = \frac{2}{1+N} \tag{3.16}$$

The energy E in an acoustic wave is proportional to the square of the pressure,

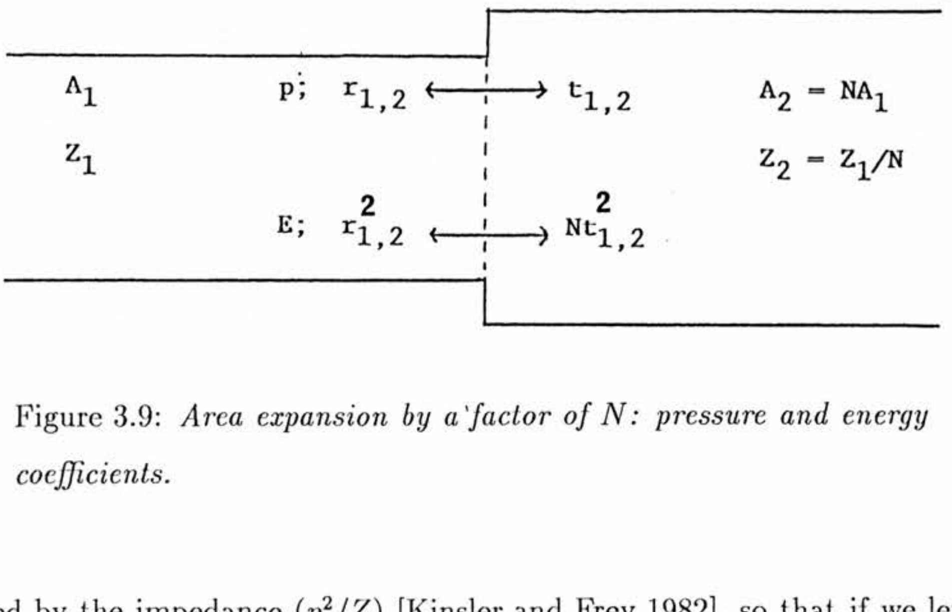

Figure 3.9: *Area expansion by a factor of N: pressure and energy coefficients.*

divided by the impedance (p^2/Z) [Kinsler and Frey 1982], so that if we let the first section have unity impedance, the reflected energy is proportional to $r_{1,2}^2$. The transmitted energy is given by $t_{1,2}^2/Z_2 = Nt_{1,2}^2 = N(1+r_{1,2})^2$. For example, if $N = 2$ (a doubling of the area) then $r_{1,2} = -1/3$; 1/9 of the energy is reflected and 8/9 is transmitted into the second section. For a wave incident *from* the second section, we have $r_{2,1} = -r_{1,2}$ and $t_{2,1} = 1 + r_{2,1}$. Again, 1/9 of the energy is reflected and 8/9 is transmitted. Thus we see that the reflection and transmission coefficients for energy are independent of the direction of travel.

3.6 Branching

We have so far been concerned with propagation along a single tube of varying cross section, and we have determined the pressure reflection coefficient when the area changes by a factor of N between two sections. Consider now the situation of Figure 3.10 where the single tube splits into $(M-1)$ tubes, each with its own impedance Z_i.

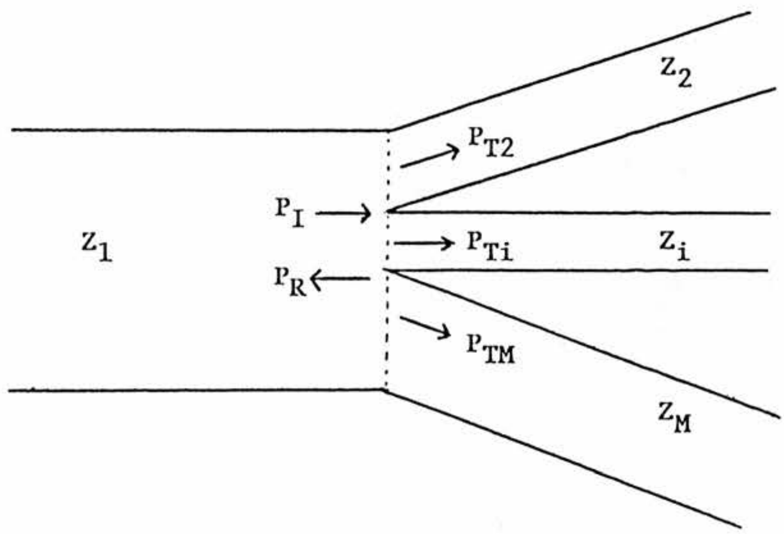

Figure 3.10: *Generalized branching of a tube.*

We will assume that these tubes are semi-infinite, or at least so long that reflections from their far ends are not observed. As always, we must have continuity of pressure and volume flow at the junction, and so we have–

$$p_I + p_R = p_{Ti} \tag{3.17}$$

$$\frac{p_I}{Z_1} - \frac{p_R}{Z_1} = \sum_{i=2}^{M} \frac{p_{Ti}}{Z_i} \tag{3.18}$$

where p_I and p_R are the incident and reflected pressure amplitudes respectively, and p_{Ti} is the pressure at the mouth of each of the $M-1$ branching tubes. Since

p_{Ti} is the same for all the branches, we can define reflection and transmission coefficients R and T in the normal way, and obtain–

$$1 + R = T$$

$$1 - R = Z_1 T \sum_{i=2}^{M} \frac{1}{Z_i}$$

which can be rearranged to give the reflection coefficient as–

$$R = \frac{1 - Z_1 \sum_{i=2}^{M} \frac{1}{Z_i}}{1 + Z_1 \sum_{i=2}^{M} \frac{1}{Z_i}} \tag{3.19}$$

With no branching, $M = 2$, and Equation 3.19 reverts to the usual expression $R = (Z_2 - Z_1)(Z_1 + Z_2)^{-1}$. Suppose now that the tube splits into two tubes ($i = 2, 3$), each having a cross sectional area (and hence impedance) equal to that of the initial tube, as shown in Figure 3.11. Applying Equation 3.19 with

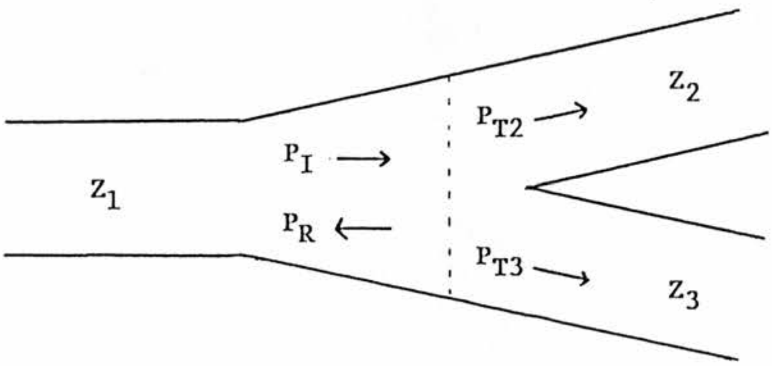

Figure 3.11: *Symmetrical bifurcation of a tube.*

$M = 3$ and $Z_2 = Z_3 = Z_1$, we obtain $R = -1/3$. This is identical to the case in which the area doubles without branching, and in fact we cannot distinguish between the two situations by observing the reflections. It does not matter how an area change occurs; whether by expansion, symmetrical or asymmetrical branching, the most we can deduce from reflectometry measurements is an *equivalent cross-sectional area.* In the symmetrical bifurcation example just given, the corresponding transmission coefficient is $T = 1 + R = 2/3$ for each of the branches, so that 4/9 of the incident energy enters each branch.

Chapter 4

The inverse problem : reconstruction

Having introduced the reflectance of an acoustic object, and described methods to calculate it for a given area profile, we now turn our attention to the *inverse* problem. Complete and approximate algorithms for reconstructing an unknown area profile from an observed reflectance function are presented, and are compared using a variety of examples [Marshall 1992a]. Confidence levels for reconstructed areas are derived.

4.1 Reconstruction algorithms

4.1.1 The Ware-Aki method

[Ware and Aki 1969] developed a reconstruction algorithm for the "inverse" problem encountered in estimating sectional impedances from a recorded reflectance function. Suitable rearrangement of Equation 3.11 and expansion of the polynomials leads to the following expressions, allowing the individual reflection coefficients to be evaluated in succession–

$$r_0 = R_0$$

$$\begin{aligned} r_1 &= \frac{R_1}{(1-r_0^2)} \\ r_2 &= \frac{(R_2 + r_0 r_1 R_1)}{(1-r_0^2)(1-r_1^2)} \\ r_3 &= \cdots \end{aligned}$$

By induction, they showed that the general result is–

$$r_{k+1} = \frac{\sum_{j=0}^{k} F_j R_{k+1-j}}{\prod_{j=0}^{k}(1-r_j^2)} \tag{4.1}$$

where F_j is the coefficient of z^j in the polynomial $F(k, z)$. Having evaluated a reflection coefficient r_i from Equation 4.1, the impedance of section $(i+1)$ can be found from–

$$\frac{Z_{i+1}}{Z_i} = \frac{1+r_i}{1-r_i} \tag{4.2}$$

and the Ware-Aki polynomials F and G are updated.

The Ware-Aki algorithm of Equation 4.1 has several interesting features;

1. To reconstruct N sections, it is necessary and sufficient to record the reflectance function up to the time that the primary reflection from the interface betweeen layers N and $N+1$ arrives back at the detector. It is not necessary to wait for all the reverberations to decay to an insignificant level, and the algorithm is not affected by later reflections. Consequently, it does not matter that the final section is of finite length.

2. It is a "marching" algorithm, in that the determination of distant reflection coefficients (and hence section impedances) depends on all the intervening coefficients already determined. Hence the accuracy obtainable must deteriorate with distance.

3. Inspection of the steps involved in the algorithm itself and in the polynomial updating (Equations 3.9 and 3.10) reveals that the number of multiplications required is of the order of $3N^2$ to determine N reflection coefficients. Hence the algorithm is computationally intensive and quite slow to perform.

4. The numerator is the *convolution*[1] of the observed reflectance with the Ware-Aki polynomial F. The new term R_{k+1}, appearing for the first time, is multiplied by $F_0 = 1$, and is readily identified as the primary reflection from the latest interface reached. All the other terms relate to the diminishing effect of multiple reflections. Implicit in a convolution sum is an integrating action, and this has an important bearing on the type of measurement inaccuracies ("noise") that can be tolerated.

5. The denominator is the correction for the combined transmission losses through all the preceding layers.

6. The algorithm completely and correctly deals with multiple reflections, and is to be regarded as the "Gold Standard" reconstruction method.

We now present some approximate reconstruction algorithms for comparison with the Ware-Aki method.

4.1.2 The Primaries method

We saw earlier how the multiple reflections die away as $-r_0 r_1$. If we are investigating an object with a modest change of impedance between sections, then the individual reflection coefficients will be small ($r_i \ll 1$), and multiple reflections diminish very quickly. Suppose we ignore completely all these multiple reflection terms, and consider only the primary reflection from each interface. Reconstruction involves only the leading term $F_0 R_{k+1} = R_{k+1}$ of the numerator of Equation 4.1, suitably weighted by the transmission attenuation correction of the denominator–

$$r_i = \frac{R_i}{\prod_{j=0}^{i-1}(1 - r_j^2)} \tag{4.3}$$

[1]Convolution and the inverse operation of deconvolution are discussed in Appendix B.

Thus each term in the reflectance function R_i corresponds directly to one reflection coefficient r_i. The section impedances are found by use of Equation 4.2. No convolution is necessary, and we do not need to use and update the Ware-Aki polynomials. The remaining computation involves only $3N$ multiplications, and consequently this algorithm runs much more quickly than the full Ware-Aki method. We will refer to it as the "Primaries" method. Watson [Watson and Bowsher 1988, Watson 1989] used this method for the reconstruction of musical instrument bores, and found it adequate for the modest flares encountered.

4.1.3 The Uncorrected Primaries method

If the individual reflection coefficients are small, then the transmission correction terms $(1 - r_i^2)$ will tend to unity, and we can simplify the Primaries method even further, by not correcting for the transmission losses. We simply equate the reflectance terms R_i with the corresponding reflection coefficients r_i, with no computation involved–

$$r_i = R_i \tag{4.4}$$

We will refer to this as the Uncorrected Primaries method.

4.1.4 The Integral method

The "Primaries" and "Uncorrected Primaries" methods are both fairly straightforward simplifications of the full Ware-Aki analysis. We look now at a rather different formulation of the reconstruction problem.

[Wright 1973] considered the impulse response of a region of continuous impedance change. He showed how the time integral of the reflectance function is equal to an effective cumulative reflection coefficient $r_{m,0}$ relating the impedance of the final section m to the impedance of the zeroth section–

$$\int_0^\infty R(T)\,dT \;= \tfrac{Z_m - Z_0}{Z_m + Z_0} \;= r_{m,0} \tag{4.5}$$

Although this holds strictly only for small reflection coefficients ($r_i \ll 1$), we can always break down an object into sufficiently small steps that this condition holds. The integral has an upper time limit of infinity to include the effects of all the multiple reflections within the sections. The integral up to some time t_i (being the time at which the primary reflection from the i^{th} interface arrives back) is in general not equal to the complete integral, because of the multiple reflections which may continue after time t_i. For example, if $R(T)$ is positive for $T > t_i$–

$$\int_0^{t_i} R(T)\,dT \leq \int_0^\infty R(T)\,dT \tag{4.6}$$

For regions of slowly-varying impedance change, where multiple reflections have a small effect, the equality approximately holds, and we may write–

$$\textstyle\int_0^{t_i} R(T)\,dT \;= S(t_i) \;\simeq \tfrac{Z_i - Z_0}{Z_i + Z_0} \;= r_{i,0} \tag{4.7}$$

We will refer to this as the "Integral" method, with the impedance reconstruction algorithm being given by–

$$\frac{Z_i}{Z_0} = \frac{1 + S(t_i)}{1 - S(t_i)} \tag{4.8}$$

where $S(t_i)$ is the integral appearing in Equation 4.7. Notice that, unlike the other methods, we do not explicitly evaluate the individual reflection coefficients r_i. In a practical implementation, the integral would be replaced by a discrete summation. The computation involved is again of the order of N for the determination of N impedance steps. [Jones 1975] has used the Integral method for determining the impedance of human tissue by an ultrasound technique. There is an obvious pitfall with Equation 4.8 in that under certain circumstances, $S(t_i)$ may approach unity, causing the algorithm to explode. The notation of Equation 4.7 explicitly brings out the fact that the time integral of the impulse response (reflectance) is equal to the *Step* response $S(t)$, which is true for any linear system. This relation suggests an alternative way of measuring impedance sections; namely by recording their response to a step function. In fact, as early as 1964, step excitation was used in determining electrical transmission line parameters [Oliver 1964]. More recently, [Harpham 1990] used the technique for the measurement of electrical component values. A step excitation is not really practical in acoustics, however, and we will continue to work with impulsive excitation.

4.1.5 Comparison of reconstruction algorithms

The various algorithms and their computational complexities (expressed in terms of the number of multiply or divide operations required) are summarized in Table 4.1.

Method	Algorithm	Equation	Complexity
Ware-Aki	$r_{k+1} = \frac{\sum_{j=0}^{k} F_j R_{k+1-j}}{\prod_{j=0}^{k}(1-r_j^2)}$	4.1	$3N^2$
Primaries	$r_i = \frac{R_i}{\prod_{j=0}^{i-1}(1-r_j^2)}$	4.3	$3N$
Uncorrected Primaries	$r_i = R_i$	4.4	—
Integral	$\frac{Z_i}{Z_0} = \frac{1+S(t_i)}{1-S(t_i)}$	4.8	N

Table 4.1: *Comparison of reconstruction algorithms.*

4.2 Performance of reconstruction algorithms

We will now compare the performance of the Ware-Aki and approximate reconstruction algorithms when applied to calculated reflectance functions. The algorithms were implemented in "Turbo Pascal", and run on a 10MHz 80286-based computer. Algebraic, numerical and graphical results are presented, together with representative processing times.

Three impedance distributions are investigated–

1. an impedance that decreases as the reciprocal of the square of the distance x, ie $Z(x) = Z_0(1 + \alpha x)^{-2}$. This corresponds to an acoustic cone of increasing diameter;

2. three sections with impedances in the ratio 1:2:4, ie areas in the ratio 4:2:1. This will demonstrate the effect of severe discontinuities between sections;

3. that due to an area profile representing a grossly simplified upper airway.

The appropriate reflectance function is derivable analytically for the first case, and for the second case is readily calculated from the Ware-Aki polynomials. For the area distribution representing the upper airway, however, the reflectance is best calculated by the method described in Section 3.4. In each case, the Ware-Aki reconstruction is to be regarded as the ideal against which the other methods are compared. The impedances are given in arbitrary units as a function of sample point i (corresponding to time or distance).

4.2.1 Impedance decreasing as the reciprocal of distance squared

It can be shown [Sondhi and Gopinath 1971] that an impedance decreasing as $Z(x) = Z_0(1 + \alpha x)^{-2}$ has a reflectance function of $-\alpha \exp(-\alpha x)$. This example was chosen to illustrate how well the approximate reconstruction methods work when applied to a continuous, monotonic impedance change. Furthermore, if α $(= \alpha' \Delta x)$ is much smaller than unity, we can simplify the reconstruction calculations to bring out the algebraic similarities and differences between the methods.

Ware-Aki method

In the region of impedance change, the reflectance terms are $R_i \simeq -\alpha$ for small α. Use of the Ware-Aki algorithm (Equation 4.1) and the recursion relations (Equations 3.9 and 3.10) for the polynomials yields–

$$r_0 = -\alpha$$

$$r_1 = \frac{-\alpha}{(1-\alpha^2)}$$
$$r_2 = \frac{-\alpha - \frac{\alpha^3}{(1-\alpha^2)}}{(1-\alpha^2)(1-\left(\frac{\alpha}{(1-\alpha^2)}\right)^2)}$$
$$r_3 = \cdots$$

for the individual reflection coefficients. These simplify further to $r_i \simeq -\alpha$ for all i. The section impedances (and hence areas) are calculated in the usual way from Equation 4.2–

$$\frac{Z_{i+1}}{Z_i} = \frac{1+r_i}{1-r_i} \simeq \frac{1-\alpha}{1+\alpha}$$

Applying this successively allows the mth impedance Z_m to be written in terms of the initial impedance Z_0 and the reflection coefficients α as–

$$Z_m \simeq Z_0 \left(\frac{1-\alpha}{1+\alpha}\right)^m \tag{4.9}$$

which can be expanded as–

$$\frac{Z_m}{Z_0} = 1 - 2m\alpha + 2m^2\alpha^2 - (4m^3/3 + 2m/3)\alpha^3 + \cdots \tag{4.10}$$

Primaries method

Applying the Primaries method (Equation 4.3) to the case of all $R_i = -\alpha$, we obtain successive reflection coefficients–

$$r_0 = -\alpha$$
$$r_1 = \frac{-\alpha}{(1-\alpha^2)}$$
$$r_2 = \frac{-\alpha}{(1-\alpha^2)(1-\left(\frac{\alpha}{(1-\alpha^2)}\right)^2)}$$
$$r_3 = \cdots$$

ie, r_0 and r_1 are the same as for the full Ware-Aki reconstruction, and thereafter the simplified numerator causes the reflection coefficients to be under-estimated. Again, in the limit of small α, all the reflection coefficients evaluate to $r_i \simeq -\alpha$, and Equations 4.9 and 4.10 apply.

Uncorrected Primaries method

Equations 4.9 and 4.10 hold for all values of α, since $|\alpha| < 1$.

Integral method

Using Equation 4.8 with all $R_i = -\alpha$ gives–

$$\frac{Z_m}{Z_0} = \frac{1 - m\alpha}{1 + m\alpha} \tag{4.11}$$

for the mth impedance, which can be expanded as–

$$\frac{Z_m}{Z_0} = 1 - 2m\alpha + 2(m\alpha)^2 - 2(m\alpha)^3 + \cdots \tag{4.12}$$

Note the difference between Equations 4.10 and 4.12, from third order upwards. With the Integral method, the calculated impedances change more rapidly than with the Primaries and Uncorrected Primaries methods. It is a more "aggressive" reconstruction algorithm.

Numerical comparison for $\alpha = 0.02$.

The numerical results for $\alpha = 0.02$, extending over 20 data points (giving an overall halving of impedance), are presented in Table 4.2. The Table gives the calculated impedances Z_i for the four different reconstruction methods, together with the percentage errors ΔZ_i in the impedances, compared with their correct values as calculated by the Ware-Aki algorithm. Errors of less than 0.1% are not indicated. Figure 4.1 shows the same data in graphical form.

The Primaries method underestimates the change (ie overestimates the final impedance) by 1.2%, and the Uncorrected Primaries by 1.4%. The Integral method overestimates the change by 1.2%. Evidently, all the reconstruction methods work well with this gentle, monotonic taper.

4.2.2 Impedance ratios 1:2:4

The reflectance function of an impedance profile with one intermediate section is readily calculated from the Ware-Aki polynomials, and has already been given

reflectance		Ware-Aki	Primaries		Uncorr. Prims.		Integral	
i	R_i	Z_i	Z_i	$\Delta Z_i(\%)$	Z_i	$\Delta Z_i(\%)$	Z_i	$\Delta Z_i(\%)$
1	-0.020	2.000	2.000	-	2.000	-	2.000	-
2	-0.019	1.923	1.923	-	1.923	-	1.923	-
3	-0.019	1.850	1.850	-	1.850	-	1.850	-
4	-0.019	1.780	1.781	-	1.781	-	1.780	-
5	-0.018	1.715	1.715	-	1.715	-	1.715	-
6	-0.018	1.653	1.654	+0.1	1.654	+0.1	1.653	-
7	-0.018	1.595	1.595	-	1.596	+0.1	1.594	-0.1
8	-0.017	1.540	1.540	-	1.541	+0.1	1.538	-0.2
9	-0.017	1.487	1.488	+0.1	1.489	+0.2	1.485	-0.2
10	-0.017	1.437	1.439	+0.2	1.439	+0.2	1.435	-0.2
11	-0.016	1.389	1.392	+0.3	1.392	+0.3	1.387	-0.2
12	-0.016	1.344	1.347	+0.3	1.348	+0.4	1.341	-0.3
13	-0.016	1.301	1.305	+0.4	1.306	+0.5	1.297	-0.4
14	-0.015	1.260	1.265	+0.5	1.266	+0.6	1.255	-0.5
15	-0.015	1.221	1.227	+0.6	1.228	+0.7	1.216	-0.5
16	-0.015	1.184	1.190	+0.6	1.192	+0.8	1.177	-0.7
17	-0.014	1.149	1.156	+0.7	1.157	+0.8	1.141	-0.8
18	-0.014	1.115	1.123	+0.8	1.124	+0.9	1.106	-0.9
19	-0.014	1.082	1.091	+0.9	1.093	+1.1	1.072	-1.0
20	-0.014	1.051	1.062	+1.1	1.063	+1.2	1.040	-1.1
21	0.000	1.021	1.033	+1.2	1.035	+1.4	1.009	-1.2

Table 4.2: *Numerical results for an impedance changing as the reciprocal of distance squared. See Figure 4.1 and text.*

(Equation 3.12). For impedances in the ratio 1:2:4, the reflection coefficients are $r_0 = r_1 = 1/3$, and we obtain–

$$R(1,z) = 0.3333z + 0.2963z^2 - 0.0329z^3 + 0.0037z^4 - 0.0004z^5 + \cdots \quad (4.13)$$

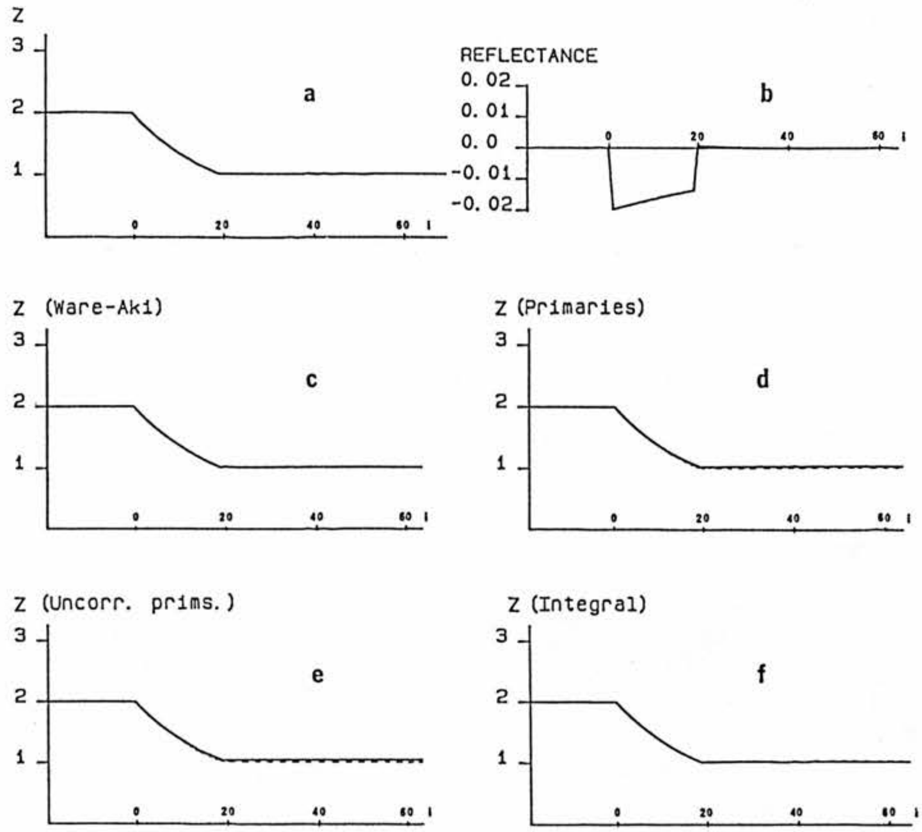

Figure 4.1: *The four reconstruction algorithms applied to the case of an impedance which decreases as the reciprocal of distance squared. (a) The impedance profile; (b) the reflectance. Impedance reconstruction by (c) the Ware-Aki method, (d) the Primaries method, (e) the Uncorrected Primaries method, and (f) the Integral method. The horizontal axis is labelled in terms of the section number i, and the true impedance profile is shown in dashed line. See Table 4.2.*

which clearly shows how successive terms die away as $-r_0r_1 = -1/9$. Table 4.3 and Figure 4.2 present the reconstructed impedances in the same format as for the previous example. Despite the highly discontinuous nature of the impedance function, the rapid fall off of the reflectance terms is due to the monotonic nature of the impedance profile.

reflectance		Ware-Aki	Primaries		Uncorr. Prims.		Integral	
i	R_i	Z_i	Z_i	$\Delta Z_i(\%)$	Z_i	$\Delta Z_i(\%)$	Z_i	$\Delta Z_i(\%)$
1	0.3333	1.000	1.000	-	1.000	-	1.000	-
2	0.2963	2.000	2.000	-	2.000	-	2.000	-
3	-0.0329	4.000	4.000	-	3.684	-7.9	4.400	+10.0
4	0.0037	4.000	3.680	-8.0	3.449	-13.8	3.959	-1.0
5	-0.0004	4.000	3.715	-7.1	3.475	-13.1	4.000	-
6	-	4.000	3.711	-7.2	3.472	-13.2	4.000	-
7	-	4.000	3.711	-7.2	3.472	-13.2	4.000	-

Table 4.3: *Numerical results for the reflectance corresponding to impedances in the ratio 1:2:4. See Figure 4.2 and text.*

Perhaps the most striking feature of the Ware-Aki algorithm is the way in which the reconstructed impedance remains constant even when the reflectance is non-zero. This "memory" effect is of course simply due to the convolution appearing in the numerator, and it parallels the way in which trapped (reverberant) energy emerges slowly.

For an overall impedance change by a factor of 4 times, taking place in just two steps, the Primaries method underestimates the change by 7.2%, whilst the Uncorrected Primaries method underestimates by 13.2%. Despite an initial overshoot of 10%, the Integral method settles to exactly the correct result.

4.2.3 Airway model

A more complex example is now presented. To illustrate the problems of using approximate reconstruction algorithms with the highly non-monotonic area profiles met with in the human airway, the method described in Section 3.4 was used to calculate numerically the reflectance corresponding to a grossly simplified model of the airway. The model's area was defined as follows; initial area 2.0 cm^2, representing the source tube; increasing to 6.1 cm^2 and then returning

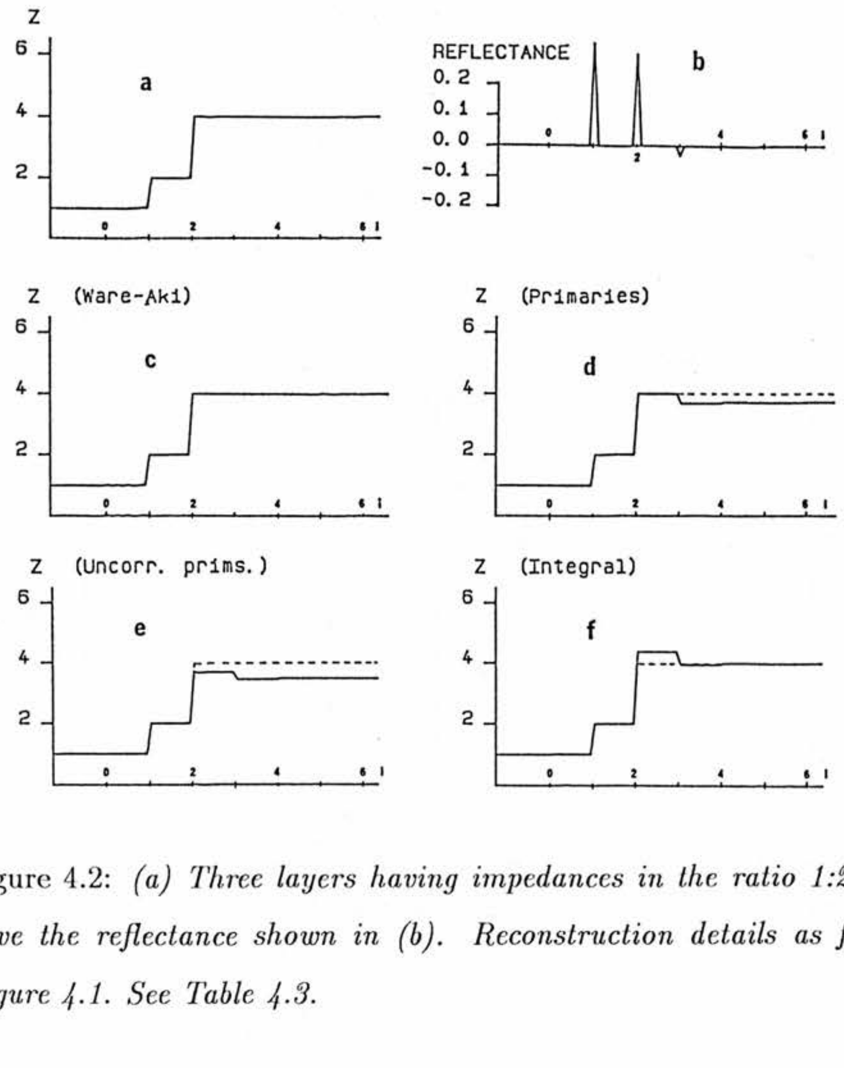

Figure 4.2: *(a) Three layers having impedances in the ratio 1:2:4 have the reflectance shown in (b). Reconstruction details as for Figure 4.1. See Table 4.3.*

to 2.0 cm^2 over 24 sections, representing the mouth; then an increase to 4.1 cm^2 over the next 12 sections, representing the pharynx; followed by a constriction of 0.95 cm^2 representing the glottis; and a final return to 2cm ^{2} at the 74th section, representing the trachea. This area profile is shown in Figure 4.3(a) and a physical model with these dimensions is described in Chapter 8.

The reflectance was calculated for 120 sample points, of which the first 100 were then used in the reconstruction algorithms. Theoretically, the reflectance continues indefinitely, but as explained earlier, we need observe it only until the primary reflection arrives back from the furthest point of interest. In this case,

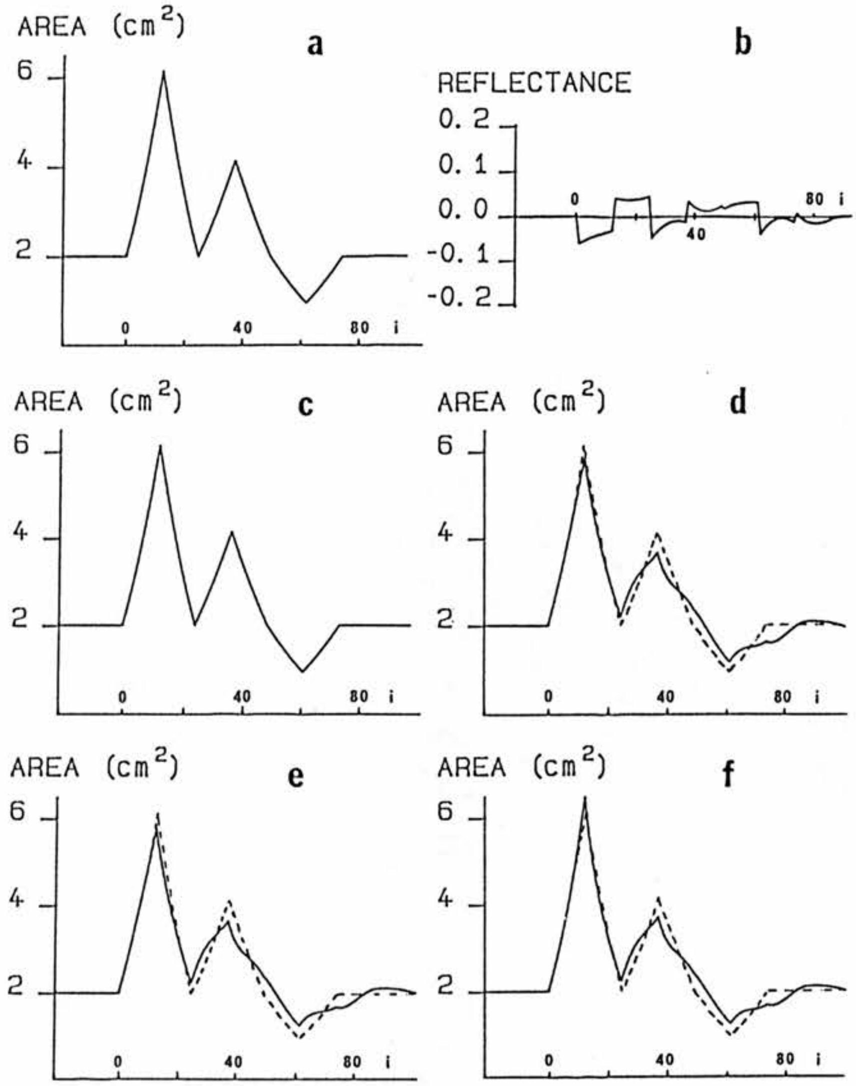

Figure 4.3: *(a) The area profile of a simplified airway model, with (b) its calculated reflectance function. Reconstruction details as for Figure 4.1. See Table 4.4.*

the area remains constant after 74 points, and so truncating the reflectance at 100 points does not throw away any information.

In this and all subsequent examples, results are given in terms of *areas* as they are more directly meaningful than impedances. Rather than tabulate all 100 points of each of the reconstructed area profiles in Figure 4.3, only the points corresponding to the maxima and minima are given in Table 4.4.

section	Ware-Aki	Primaries		Uncorr. Prims.		Integral	
i	A_i	A_i	$\Delta A_i(\%)$	A_i	$\Delta A_i(\%)$	A_i	$\Delta A_i(\%)$
1	2.000	2.000	-	2.000	-	2.000	-
14	6.124	5.825	-4.9	5.747	-6.2	6.464	+5.6
26	2.000	2.180	+9.0	2.223	+11.1	2.222	+11.1
38	4.132	3.649	-11.7	3.629	-12.2	3.696	-10.6
62	0.945	1.165	+23.2	1.236	+30.8	1.224	+29.5
74	2.000	1.621	-19.0	1.683	-15.9	1.682	-15.9

Table 4.4: *Area reconstruction from the reflectance corresponding to a simple airway model. Only the maxima and minima of the area profile are given. See Figure 4.3 and text.*

The shortcoming of the approximate algorithms in reconstructing areas beyond a maximum (or indeed a minimum) are apparent from Figure 4.3 and Table 4.4. Although the three methods give reasonably accurate values for the first maximum (to within 6%), the remainder of the area reconstructions appear distorted compared with the true area. The area minimum at point 26 is overestimated by 9% in the Primaries case, and by 11% for the other methods. The second maximum, at point 38, is underestimated by around 12%, whilst the area minimum at point 62 is overestimated by as much as 31% by the Uncorrected Primaries method. The true area function has returned to 2 cm^2 by point 74, but the approximate reconstructions return to this value only slowly with distance.

Using a practical number of sample points ($N = 100$ for this example) allows an accurate assessment of the relative speeds of the reconstruction algorithms. The author's implementation in Turbo Pascal, running on a 10MHz 80286 machine achieved the times shown in Table 4.5. We see that for $N = 100$, the Ware-Aki method takes at least 20 times longer to run than the approximate methods,

Method	Time (N sections)	Time ($N = 100$)
Ware-Aki	$100 + 0.2N^2$	2.1s
Primaries	$60 + 0.2N$	80ms
Uncorrected Primaries	$60 + 0.09N$	69ms
Integral	$80 + 0.2N$	100ms

Table 4.5: *Typical reconstruction times for the four methods.*

even when the (fixed) program overheads are taken into account. There is relatively little to choose between the three approximate methods as far as speed is concerned.

4.3 Area uncertainty in reconstruction

Although stating earlier that the accuracy obtainable with the Ware-Aki algorithm decreases as the number of sections increases, we have not yet shown explicitly how this arises. Let us begin by assuming that the terms in the reflectance are subject to some error ΔR. This may be a random variation, or it may be a systematic error such as an "offset". Then inspection of Equation 4.1 shows that the error in determining the reflection coefficients is approximately–

$$\Delta r_j = \Delta R \sum_{k=0}^{j-1} F_k \tag{4.14}$$

where we have neglected the transmission correction, which is of order unity for any "reasonable" impedance change. The F_k are the coefficients of the F polynomial, of which the first (F_0) is unity. The impedances are calculated from the reflection coefficients by successive use of Equation 4.2, and the areas are found from $\rho c/Z_i$. An error of Δr_j in a reflection coefficient leads to a fractional error of $2\Delta r_j/(1 - r_j^2)$ in the determination of Z_{j+1} with respect to Z_j, so that for i sections, the cumulative error (in the worst case of a systematic error ΔR), is–

$$\frac{\Delta A_{i+1}}{A_0} = \sum_{j=0}^{i} \frac{2\Delta r_j}{1 - r_j^2} \tag{4.15}$$

Making the usual approximation regarding r_j^2, this simplifies to–

$$\frac{\Delta A_{i+1}}{A_0} \simeq 2\Delta R \sum_{j=0}^{i} \sum_{k=0}^{j-1} F_k \tag{4.16}$$

Although the higher terms in F diminish with k, we see that the area uncertainty grows at least linearly with reconstruction distance.

For the Primaries method, we retain only the term F_0, and Equation 4.16 simplifies further to–

$$\frac{\Delta A_{i+1}}{A_0} \simeq 2i\Delta R \tag{4.17}$$

which clearly shows that the area uncertainty increases linearly with distance (ie with i). The same relationship follows automatically for the Uncorrected Primaries method.

The situation with the Integral method is very similar. In the discrete formulation, the integral is replaced by the summation $S_i = \sum_{j=0}^{i-1} R_j$, so that an error ΔR in each reflectance term leads to an error $\Delta S_i = i\Delta R$. Application of Equation 4.8 (or rather, its inverse) to find the i^{th} area leads to an uncertainty of–

$$\frac{\Delta A_i}{A_0} = \frac{2i\Delta R}{1 - S_i^2}$$

which is of the same form as for the other reconstruction methods.

4.4 Comparison of reconstruction methods

The three approximate reconstruction methods studied are much faster than the Ware-Aki method (typically 20 times for 100 sections), leading to errors of the order of 1% for smoothly changing impedances and 10% for a discontinuous change by a factor of 2. In some applications, these inaccuracies may be acceptable, and the substantial time-saving of the approximate methods over the complete Ware-Aki solution appears very attractive. Amongst the approximate algorithms, the Integral method appears to give slightly better results than the other two, and is to be preferred. The Uncorrected Primaries method is (not surprisingly) the least accurate, and its use would not normally be justified.

For the highly non-monotonic area profile of the upper airway model, the approximate algorithms fare less well. Although the "mouth" and "pharyngeal" area maxima can be estimated to within about 10%, the "glottal" minimum is badly overestimated by as much as 30%. Evidently the approximate algorithms may be acceptable for measurements of supraglottal airway dimensions, and for the rapid assessment of airway patency at lower levels. For accurate measurements, the Ware-Aki algorithm is clearly necessary.

We have seen that the uncertainties in reconstructed areas increase (at least) linearly with distance.

Chapter 5

The production of acoustic impulses

5.1 Impulsive excitation

5.1.1 Introduction

The theory of multiple reflections developed in Chapters 3 and 4 is strictly valid only for impulsive (ie broadband) excitation of the object being measured. In principle, the reflected pressure wave due to an arbitrary excitation can be deconvolved with the incident pulse shape to yield the reflectance. However, deconvolution can be quite time-consuming, and it was decided to investigate the production of approximate impulses using readily available transducers. This has two advantages–

1. The reflected pressure waveform is approximately the reflectance, without the need for deconvolution. This allows immediate viewing of the reflectance signal as the object is altered, and speeds up the measurement and display process. This will be important when the equipment is used clinically.

2. In Section 7.6.2, it will be shown that a short-duration incident pulse allows use of a compact acoustic system, whilst retaining a very simple method of separating the incident and reflected waveforms.

After a brief review of the literature pertaining to acoustic pulse production, a novel means of producing short-duration pulses from a resonant transducer will be described, before the general problem of driving an arbitrary transducer is discussed. Some of the material has appeared previously [Marshall 1990], but is now greatly expanded to include the results of a systematic survey of loudspeakers.

5.1.2 Simple means of pulse production

Various methods have been used to approximate impulsive pressure waves in air, for applications in architectural acoustics, musical instrument research, and in the measurement of human airways.

Spark discharges are inconsistent and require the use of high voltages (30kV) for their production, but can produce pressure waves with a duration of order 200μs [Jackson et al 1977].

Explosive methods [Lewis and Smith 1978] suffer from similar problems of repeatability, and are clearly not appropriate for clinical use.

Simple means of driving electroacoustic transducers to produce short-duration pressure pulses have been reported by several authors. [Watson and Bowsher 1988] used a 10μs electrical pulse to excite a "tweeter" loudspeaker; [Sondhi and Resnick 1983] used a 200V voltage step applied to a custom device made from Mylar film; and [Fredberg et al 1980] used a "double pulse" to drive a wide-range loudspeaker. In all three of these cases, the resulting pressure pulse duration was approximately 2ms, corresponding to a travel distance of 600mm. This is considerably greater than the 15mm or so of axial resolution desired in the present application, and so these techniques must be used with deconvolution of the reflected pressure waveforms.

5.2 Pulse production using resonant devices

5.2.1 Theory of the "step" method

Generally speaking, manufacturers aim to produce audio transducers with as broad a frequency response as possible. However, several electromagnetic " ear-pieces" that were to hand were found to have a very peaked response, and a simple technique was devised for producing short pressure pulses from such devices. The method is in fact applicable to any transducer having a marked resonance in its response. Despite its simplicity, the technique is not widely known, and very few related references appear in the literature (see for example [Fitch 1979]). Figure 5.1(a) shows the idealized *step* response of such a transducer, which is in the form of a damped sinusoid $P(t) = P_0 \exp^{-\alpha t} \sin \omega_0 t$, where the natural period is $\tau = 2\pi/\omega_0$ and the excitation is a step voltage proportional to P_0. Now suppose that at time $t = \tau/2$ an additional step of relative amplitude $\exp^{-\alpha\tau/2}$ is applied, as shown in Figure 5.1(b). Assuming that the transducer behaves linearly, the response to the additional step will be exactly out of phase with the response from the original step, and the amplitude will be such as to cancel the remainder of the response, leaving only the first half cycle (Figure 5.1(c)). We will refer to this technique as the "step" method. It should produce a pressure pulse equal in duration to half the natural period of an ideal resonant transducer.

5.2.2 Experimental arrangement

The experimental system used to test the "step" method is shown in Figure 5.2, and consists of the transducer under test coupled to one end of a 1m-long wave tube, at the far end of which is a pressure-sensitive microphone. Experiments were carried out with both steel and flexible polyurethane tubing, and the effect of wall material on sound propagation is discussed in Chapter 7. For now, suffice it to say that the difference between steel and polyurethane was found to be negligible in terms of the results achieved. This is partly because there

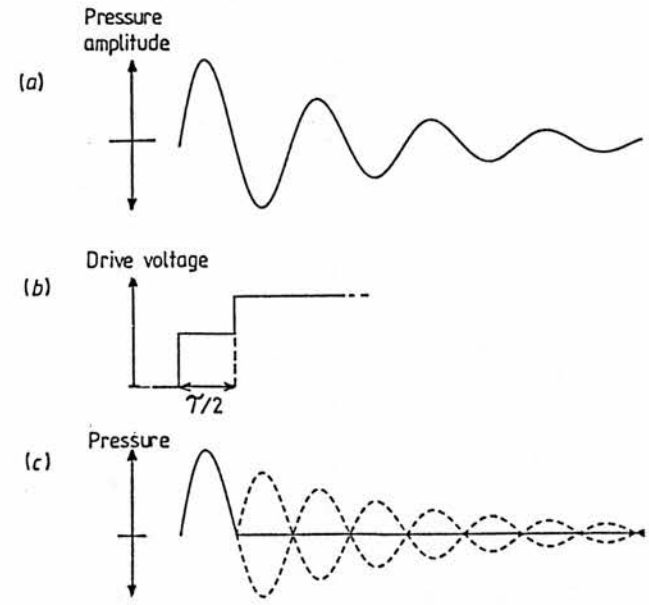

Figure 5.1: *The "step" method of driving a resonant transducer: (a) the idealized step response; (b) when driven with a suitable double-stepped waveform, only the first half-cycle of the pressure response is produced ((c), solid line), the remainder (dashed line) being exactly cancelled.*

is little intrinsic difference anyway, and partly because the microphone records the pressure waves *after* propagation down the tube, thus allowing removal of any attenuation effects. The tube length is great enough so that the transducer response can be recorded before reflections from the source arrive back at the microphone. A length of 1m enables us to investigate responses lasting 6ms, this being the round-trip delay. A standard laboratory (double) pulse generator was used to drive the transducer under test.

The microphone used is a Knowles BL1785 piezoceramic type with integral FET. Its nominal sensitivity of 3mV/Pa was confirmed by calibration against a standard microphone, and the frequency response was found to be flat within 1dB from 50Hz to at least 7kHz. It is an inexpensive alternative to the Brüel

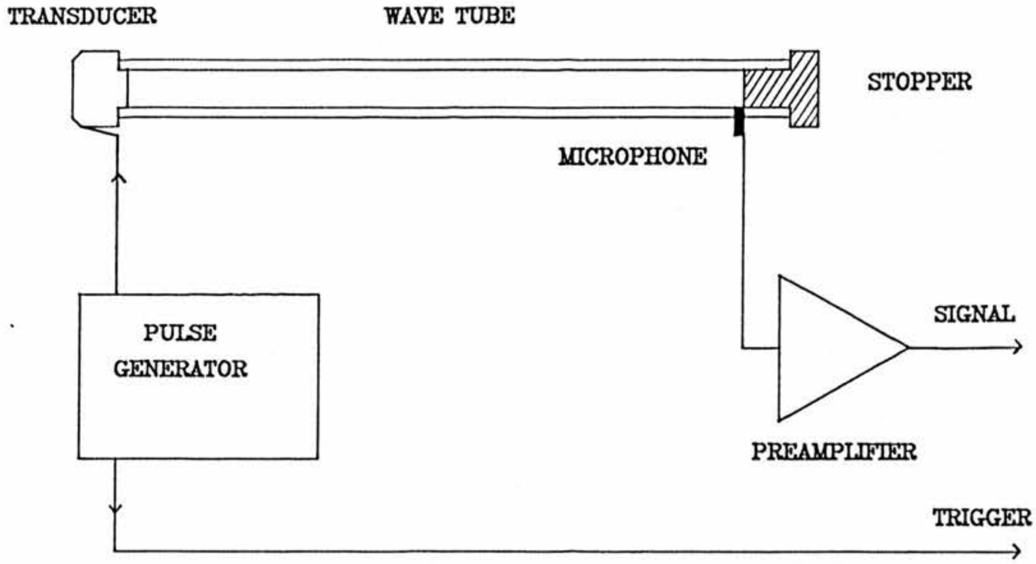

Figure 5.2: *The experimental system used for investigating resonant transducers.*

and Kjær types often used in acoustic research, and is suitable here because we do not need an extended high frequency response. The microphone is set in the wall of the tube, with its inner end flush with the interior wall, so minimizing spurious reflections. The tube is fitted with a hard plastic stopper at the position of the microphone, so that the observed pressure waveform consists of the incident pulse with the superimposed reflection off the stopper; ie the waveform has (approximately) twice the amplitude of the incident pulse.

A preamplifier (voltage gain 5.5 and 3dB bandwidth 60Hz to 12kHz) brings the microphone signal up to a level suitable for capture by a computer system fitted with an Analogue to Digital Converter (ADC). The computer system will be described in Section 5.4.1. A trigger pulse from the pulse generator instructs the computer to begin sampling the microphone signal.

5.2.3 Results with the "step" method

Electromagnetic earpiece

The first device tested with the "step" method was a low-impedance electromagnetic earpiece (Maplin Electronic Supplies, type LB24B) of the type intended for use with personal radio sets. Its step response (Figure 5.3(a)) shows a strong resonance at 2.5kHz, which decays with a time constant of approximately 1ms. Figure 5.3(b) shows the result of applying a double-stepped drive waveform to

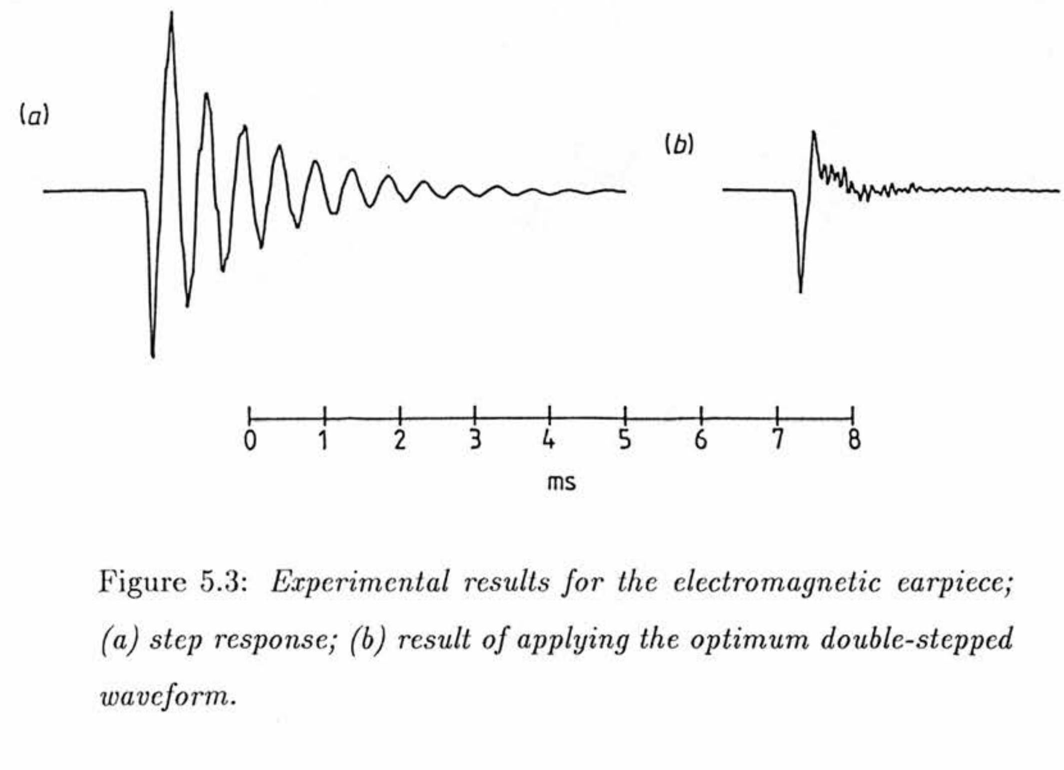

Figure 5.3: *Experimental results for the electromagnetic earpiece; (a) step response; (b) result of applying the optimum double-stepped waveform.*

the earpiece. The step sizes and delay were adjusted empirically to obtain the optimum pulse shape. Whilst the essential features of the theory are borne out, that part of the waveform immediately following the desired pulse is distorted, presumably because the step response does not have a simple exponential decay. Additionally, incomplete cancellation of the latter part of the waveform has occurred. Although the fundamental resonance has been successfully suppressed, there remains some ripple (at 12kHz) due to a higher order mode which was barely discernible in the original step response.

Piezoelectric transducer

A piezoelectric transducer disc removed from a "bleeper" (STC, type U535R12V) was found to be highly resonant when suspended freely at the end of the wave tube, and so was a suitable candidate for the "step" method. (Fixing it to the end of the tube severely damped its response.) The step response is as shown in Figure 5.4(a). Notice how lightly damped the response is; in fact the recording had to be truncated to avoid reflections off the source. The best short-duration

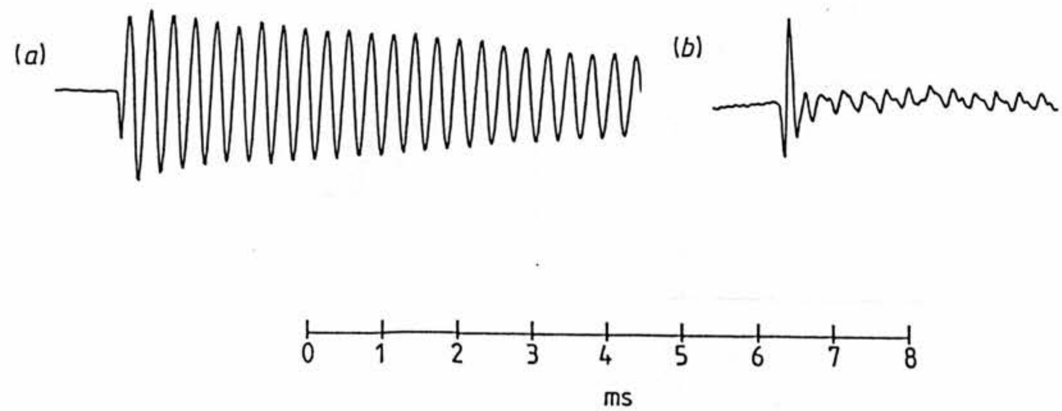

Figure 5.4: *Experimental results for the piezoelectric disc; (a) step response; (b) result of applying the optimum double-stepped waveform.*

pulse that could be achieved is shown in Figure 5.4(b), from which it can be seen that the fundamental resonance of 3kHz has not been eliminated, and the initial pulse shape is biphasic. These effects are a consequence of the non-monotonic nature of the step response decay envelope: careful observation of Figure 5.4(a) reveals that the amplitude initially *increases*. Nevertheless, an acoustic pulse with Full Width at Half Maximum (FWHM) of approximately $100\mu s$ has been achieved.

5.2.4 Comparison with published literature

The experimental results show that it is possible to produce short-duration acoustic pulses with a simple, stepped drive waveform. In some applications, the imperfect nature of the pulses would be acceptable, especially when the extreme simplicity of the technique is considered.

[Fredberg et al 1980] used a "double pulse" excitation of a loudspeaker (University type 60-ID), consisting of equal-amplitude $200\mu s$ and $150\mu s$ pulses, separated by $150\mu s$. They did not explain the rationale for choosing this particular drive waveform, and since the published pulse shape has a duration of more than 2ms, they were evidently not trying to produce impulses.

Mention should be made of [Ibisi and Benade 1982], who drove a piezoelectric disc (resonant frequency ω_0, period τ, bandwidth g) with a voltage ramp $V_0(1 - \exp^{-gt/2})(0 \leq t \leq \tau$; constant thereafter). Theoretically, this should give a single pressure pulse of the form $P_0(1 - \cos\omega_0 t)$. They claim to have achieved pulses with a FWHM of $100\mu s$, but since this reference is a meeting abstract, no results are shown. Presumably, problems of non-ideal transducer behaviour would be encountered as in the present work.

5.3 The general problem : inverse filtering

The general problem of driving a transducer to produce an arbitrary pulse waveform (and in particular, a short-duration impulse) has received surprisingly little attention in the literature, despite the potentially wide applicability of a suitable technique.

In principle, one treats the transducer, coupler and microphone assembly as a linear system having an impulse response $h(t)$, which is measured. The corresponding *inverse filter* $g(t) = h^{-1}(t)$ is then calculated, and implemented (typically as a digital filter), being placed in cascade with the transducer. Exciting the inverse filter with the desired waveform then causes the transducer to produce that pressure waveform, since the distorting effect of $h(t)$ is cancelled by the filter $g(t)$.

The situation is shown schematically in Figure 5.5, where $h(t)$ represents the impulse response of the transducer, acoustic path and microphone system, and $g(t)$ is the inverse filter which is excited by the original drive waveform $v(t)$. The observed microphone signal $p(t)$ is given by–

$$\begin{aligned} p(t) &= h(t) \otimes g(t) \otimes v(t) \\ &= v(t) \end{aligned}$$

where the symbol $\otimes$ denotes convolution. Since the microphone response is

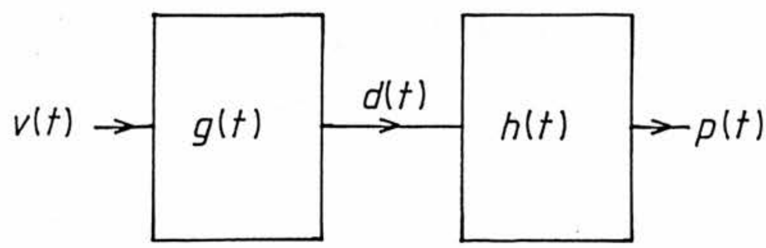

Figure 5.5: *The inverse filtering method. Inverse filter $g(t)$ compensates for the distortion $h(t)$ caused by the transducer and acoustic system. The calculated drive waveform $d(t)$ may be applied directly to the transducer to generate the desired pressure waveform $p(t)$.*

known to be uniform over the frequency range of interest, the acoustic pressure waveform is essentially the same as the microphone signal. If this were not the case, then the action of the inverse filter would be to tailor the *microphone signal* to the waveform $v(t)$, although the actual pressure waveform would depart from the ideal. We assume that the entire system behaves linearly, and that the response is time-invariant.

Useful work along these lines has been carried out by [Winter et al 1975] and by [Davies et al 1981], who measured the response of transducer-microphone systems, and hence calculated suitable inverse filters. [Winter et al 1975] dealt with a single (unspecified) loudspeaker, and gave little detail except that they determined the impulse response by applying a 1ms electrical excitation. Since this pulse contains significant energy up to only 1kHz, it is questionable whether a sufficiently accurate determination is possible. This shortcoming may be responsible for the poor pulse shapes of some of their results. [Davies et al 1981] took the work further, dealing specifically with a "wide-range" loudspeaker unit, and using a 70μs electrical excitation to measure the impulse response. Despite abruptly truncating their drive frequencies at 3kHz, reasonable results were achieved in producing single cycles of sine, square and triangular waveforms.

[Fincham 1985] and [Merhaut 1986] have used impulsive excitation of loudspeakers in order to measure frequency responses without need of large anechoic chambers. [Nicolas et al 1990] describe the use of a commercial sound analyser to produce transient signals for psychoacoustic research.

The approach in the present work is slightly different. Rather than apply the desired pulse shape to the cascaded inverse filter/transducer combination, we calculate the intermediate drive waveform $d(t)$ which is applied directly to the transducer. This is possible because we are interested in one pulse shape only, and means that there is no need to implement a digital filter.

From Figure 5.5, we see that the required drive waveform $d(t)$ is given by the convolution–

$$p(t) = h(t) \otimes d(t) \tag{5.1}$$

The calculation is most conveniently carried out in the frequency domain. Fourier transformation and rearrangement of Equation 5.1 yields the expression–

$$D(\omega) = \frac{P(\omega)}{H(\omega)} \tag{5.2}$$

where $D(\omega)$ is the (complex) Fourier transform of $d(t)$, and similarly for $P(\omega)$ and $H(\omega)$. The function $1/H(\omega)$ is notoriously ill-conditioned. Even in the absence of measurement noise, $H(\omega)$ will be zero at certain frequencies (usually the higher frequencies), causing the expression to "explode". The problem is circumvented here by two precautions–

1. We choose a pulse shape $p(t)$ such that its spectral content $P(\omega)$ is insignificant at high frequencies, enabling the division to be well-behaved. A Gaussian pulse shape is used in the present work. We accept the compromise that the pressure pulse will have a finite duration (and limited bandwidth) rather than being an ideal impulse.[1]

2. We use the *constrained* deconvolution (see Appendix B)–
$$D(\omega) = \frac{P(\omega)H^*(\omega)}{H(\omega)H^*(\omega) + k} \tag{5.3}$$
where k is a constant and $H^*(\omega)$ denotes the complex conjugate of $H(\omega)$ [Gonzalez and Wintz 1977]. The value of k is chosen to be as small as possible consistent with stability of the expression, values ranging from 0.01 to 0.03 having been found optimum in the present work.

5.4 Arbitrary pulse generation

The theory presented in the previous section was applied to a variety of loudspeakers of both the familiar electromagnetic ("dynamic") type and the piezoelectric type. The test equipment used will now be described in some detail because it forms the basis of the reflectometer systems developed in later chapters.

5.4.1 Test equipment

The acoustic system is a development of that shown in Figure 5.2. Each loudspeaker under test is coupled to the wave tube with an individual coupler,

[1]This is not a severe limitation. In Chapter 7, we will see that a limited bandwidth is actually necessary in order to prevent cross-mode propagation occurring. In any case, a real transducer could not produce an ideal impulse.

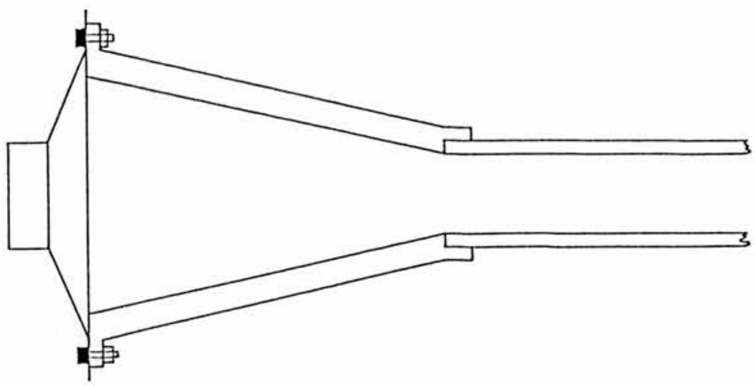

Figure 5.6: *A tapered acoustic coupler is used to connect the loudspeaker under test to the wave tube.*

custom-made from aluminium or Perspex (Figure 5.6). The gentle taper between the loudspeaker cone and the wave tube minimizes spurious reflections in the coupler itself. The loudspeaker is bolted firmly to the flange of the coupler, with silicone sealant being used to make the assembly airtight. This optimizes the low frequency performance.

Computer system and interface

The investigation initially used an IBM PS/2 80286-based computer, but a Dell 316SX 80386SX-based machine became available later. The changeover in no way affected the running of the experiments. A custom-built high-speed interface card is used to excite the loudspeaker under test, and to capture the microphone signals. Sampling is at 40kHz to ensure the best possible reproduction of waveforms, and 12-bit digitization is used. At this sampling rate, standard interrupt timing is inadequate. Although fast Direct Memory Access (DMA) techniques can be implemented for signal *acquisition* on commercial boards, DMA *output* of waveforms (to drive the loudspeaker) is not usually possible. Hence a special interface card is required. The design chosen (Figure 5.7 and Appendix D) uses

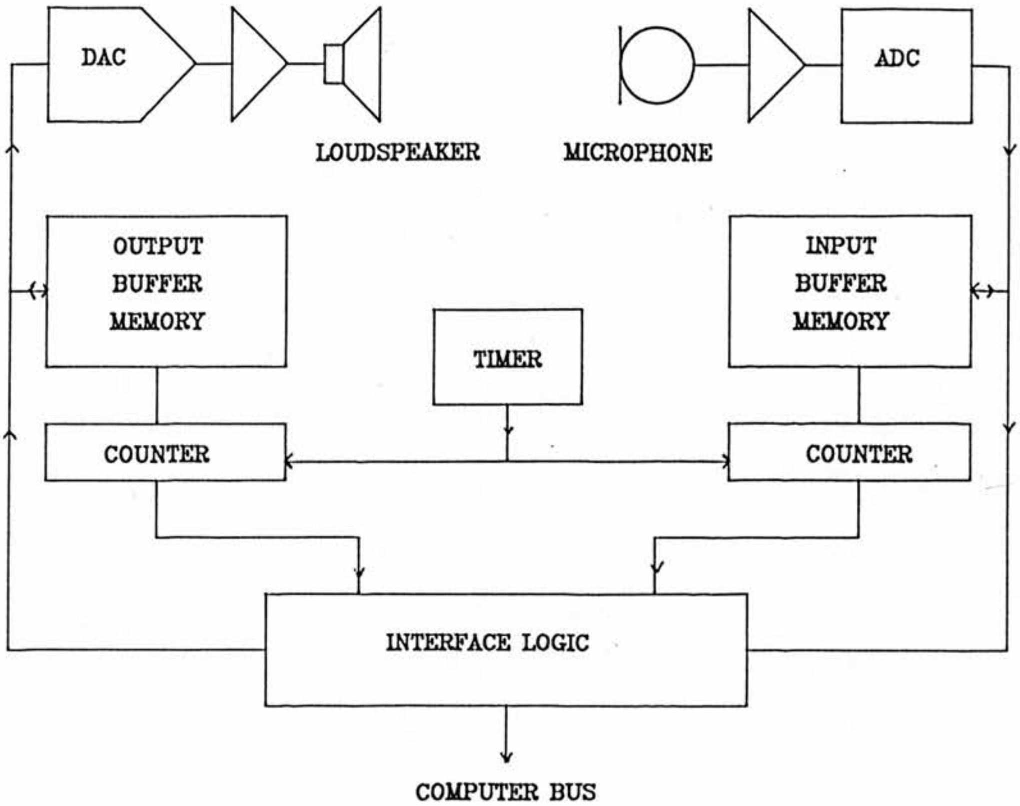

Figure 5.7: *The high-speed analogue interface card, developed for simultaneous excitation of a loudspeaker and capture of a microphone signal.*

buffer memory and hardware counters to allow high-speed, simultaneous output via a Digital to Analogue Converter (DAC) and signal acquisition from an Analogue to Digital Converter (ADC).

Operation of the interface card is as follows; (i) the on-board timer is configured to give the required sample rate, (ii) the calculated drive waveform is downloaded byte-by-byte from the computer to the output buffer memory, (iii) the numbers of input and output samples are stored in the appropriate counters, and (iv) the computer interrupt is enabled and sampling is started. The output waveform is sent to the DAC at the correct rate, and hence drives the loudspeaker via the power amplifier. At the same time, the signal from the microphone preamplifier is sampled by the ADC and stored in the input buffer memory. When both input and output processes are complete, the interface card interrupts the computer. The newly-acquired data can then be uploaded into the computer's main memory "at leisure". The output amplifier is a TDA2030 integrated circuit type, mounted on the interface card and powered from the computer's ±12V supplies. It was found necessary to construct the microphone preamplifier as an external unit with its own ±15V power supply, as a card-mounted version picked up too much interference from the computer bus and supply rails.

Experimental method

The experiment consists of the following stages–

1. A 25μs rectangular pulse is used to excite the loudspeaker[2], and the resulting microphone signal is captured. The averaged signal from ten such excitations is taken to be the impulse response of the system.

2. The drive waveform $d(t)$ necessary to produce a Gaussian pulse $p(t) = p_0 \exp^{-2(t/\tau)^2}$ is calculated using Equation 5.3 and 256-point Fast Fourier Transforms (FFTs). The parameter τ is set to three sample periods, ie 75μs, which defines a pulse of duration approximately 90μs (FWHM). The corresponding spectral content is 3dB down at 3.5kHz (10dB at 6.4kHz), which is quite adequate for the present application.

3. The drive waveform just calculated is truncated at 2ms, and smoothly tapered to its "tail level" over the period from 1ms to 2ms. Figure 5.8 illustrates the terms "tail level" and "quiescent level".

4. The tailored waveform is applied to the loudspeaker, and the resulting microphone signal captured. The loudspeaker drive voltage is reset to

[2]A rectangular pulse of duration T has spectral content $T\sin(\pi fT)/(\pi fT)$, so that for $T = 25\mu$s, the excitation is uniform (to within 1dB) to 10kHz.

its pre-pulse ("quiescent") level. The microphone signal (taken to be the same as the pressure pulse waveform) from ten excitations is averaged, and displayed.

5. The spectral content of the pressure pulse is calculated and displayed.

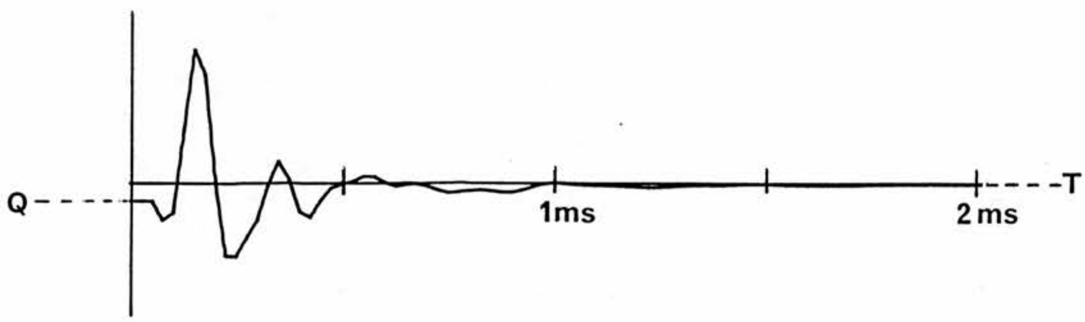

Figure 5.8: *Manipulation of the result of Equation 5.3 to produce the final drive waveform. Q: quiescent level; T: tail level (equal to zero in this example). Vertical axis: voltage, in arbitrary units.*

5.4.2 Electromagnetic loudspeakers

Fifteen electromagnetic loudspeakers, comprising seven different types, were tested as described above. The loudspeakers are listed in Table 5.1 together with the manufacturers' quoted sensitivities (given in dB of sound pressure at 1m distance, produced by 1W of electrical input) and the experimentally determined sensitivities (in terms of peak pulse pressure produced by the calculated drive waveforms). A selection of loudspeakers and couplers is shown in Figure 5.9 on Page 64.

Identification	Type	Sensitivity	
		dB/W/m	Pa/V
A, B	Philips AD0162/T8 25mm dome tweeter	94	25
C-E	RS 250-227 18mm tweeter	89	10
F, G	Maplin WF43W tweeter	-	15
I	Fane MD2050 50W compression driver	105	34
K	RS 250-211 100mm wide-range	88	-
L-O	Goodmans 110mm wide-range	94	15
P, Q	Audax HD100D25 50W dome tweeter	89	15

Table 5.1: *Details of the electromagnetic loudspeakers studied. Sensitivities in dB/W/m are taken from manufacturers' data, and refer to sine wave measurements. Experimentally-determined sensitivities are given in terms of the peak amplitude of Gaussian pressure pulses.*

Results with electromagnetic loudspeakers

Despite differing impulse responses, most of the devices produced acceptable Gaussian pulses of duration 90-100μs (FWHM), differing mainly in their sensitivities. Some representative results are now shown in detail.

Loudspeaker B Figure 5.10(a) (Page 65) shows the impulse response of loudspeaker B (a Philips AD0162/T8 dome tweeter) measured using a 10V, 25μs electrical excitation. The reflected pulse is superimposed on the response as explained above. The amplitude shown in these diagrams is that of the incident pulse itself, assuming perfect reflection at the stopper. The response consists essentially of a biphasic pulse followed by a few damped oscillations. Its frequency content[3] (Figure 5.10(b)) shows peaks around 1kHz and 3kHz, with a gradual

[3]Magnitude spectra are shown throughout this work, although all calculations are carried out on the complex (real and imaginary) representations.

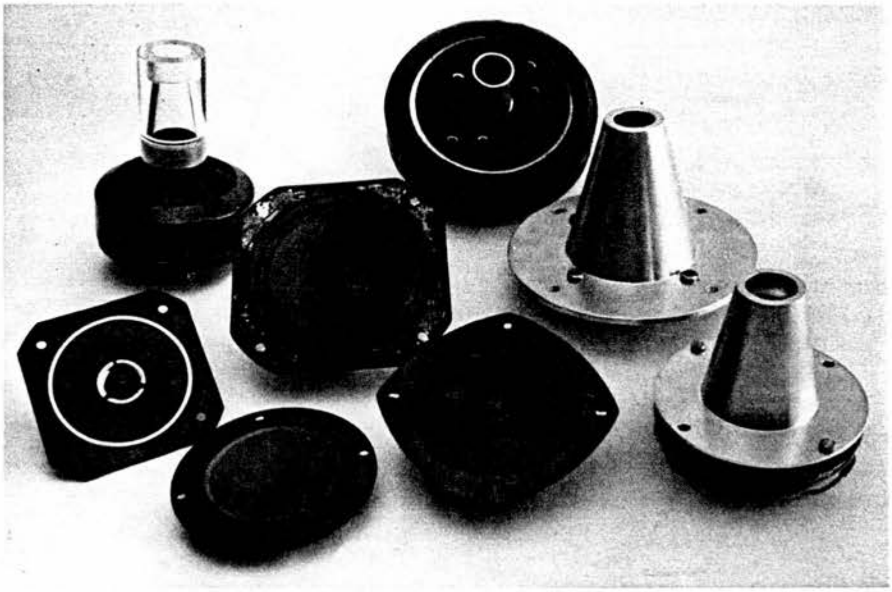

Figure 5.9: *A selection of the loudspeakers studied, together with some acoustic couplers. Back row, left to right: piezoelectric horn driver J (with coupler), speaker K, compression driver I (with coupler), and speaker Q (with coupler). Front row, left to right: Speaker C, piezoelectric tweeter H, speaker G, and speaker A (with coupler).*

fall-off at higher frequencies. Notice that there is very little response below about 300Hz, and none at all at DC. This is common to all the loudspeakers tested, and is the main limitation in producing Gaussian pulses. Figure 5.10(c) shows the drive waveform $d(t)$ as calculated by Equation 5.3, after inverse transformation to the time domain, and truncation as in Figure 5.8. When this drive is applied to the loudspeaker, the pressure pulse of Figure 5.10(d) results. The peak pressure achieved is approximately 200Pa (140dB SPL) in the incident pulse, with a FWHM of 100μs. The spectral content of the pulse (Figure 5.10(e)) shows a distribution that is much smoother than that of the original impulse response, being quite close to Gaussian above 1kHz. The inverse filtering has not been able

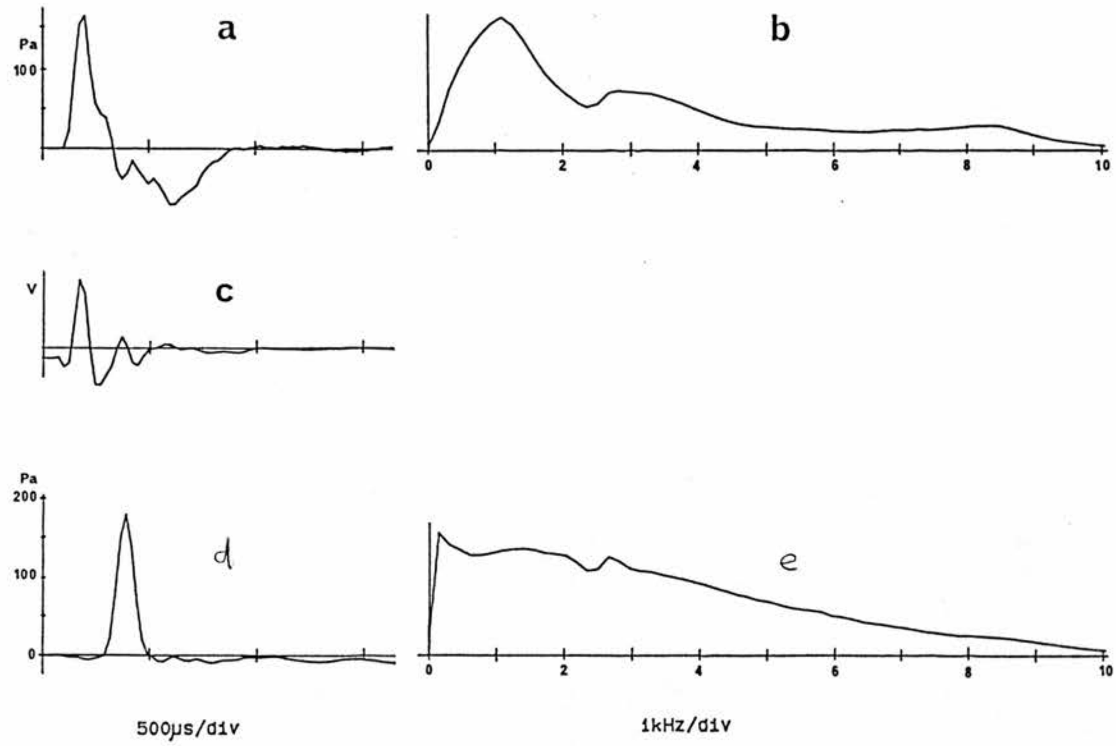

Figure 5.10: *Loudspeaker B used to produce a Gaussian pulse. (a) The impulse response with (b) the corresponding frequency response; (c) the calculated drive waveform; (d) the pressure pulse achieved and (e) the corresponding spectral content.*

to greatly improve the low frequency response, particularly below 200Hz where very little information was available. This lack of energy in the region DC-200Hz accounts for the slightly bipolar appearance of the pulse in (d).

Loudspeaker A, which is of the same type as B, behaved identically. This was found to be the case for all loudspeakers of a given type.

Loudspeaker I Loudspeaker I (Fane MD2050 50W compression driver) was the most sensitive of the devices studied, and also the most massive. The preamplifier gain was reduced to 3.3 for measurements on this loudspeaker. Pressure peaks of up to 370Pa (in the incident pulse) could be achieved, with a FWHM of $100\mu s$. The results are shown in Figure 5.11. The high pressures present in

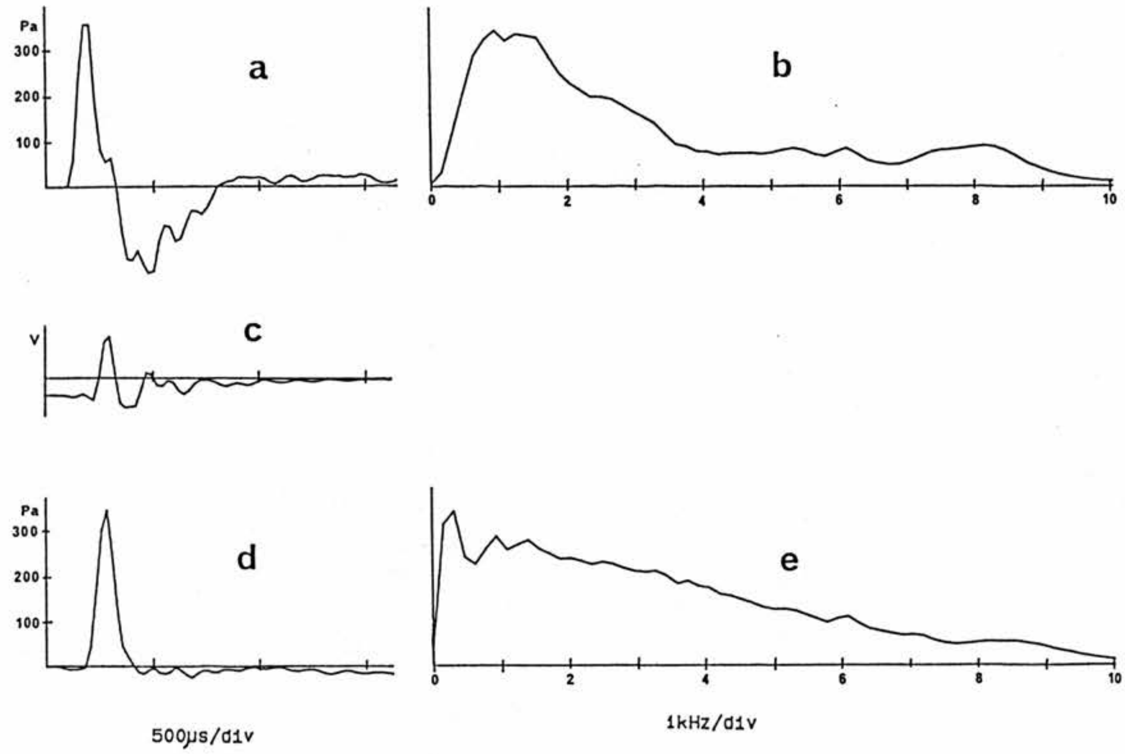

Figure 5.11: *Loudspeaker I used to produce a Gaussian pulse. Details as for Figure 5.10.*

the superimposed incident and reflected pulse (being almost 1% of atmospheric pressure) caused concern that the assumptions of linearity might no longer be strictly valid. This aspect was investigated by varying the amplitude of the drive waveform, and recording the corresponding pressure pulse. It was found that linearity is maintained (within observable limits) up to microphone pressures of around 400Pa, with the response being less than predicted at higher pressures. For example, the pulse amplitude is approximately 5% down at 740Pa. This is probably due to imperfections in the loudspeaker and microphone rather than to the breakdown of the small pressure assumptions made in acoustics.

Loudspeaker K Of all the electromagnetic loudspeakers, only device K was unsuitable for pulse production. Its impulse response (Figure 5.12(a)) shows significant ripple superimposed on a slowly-decaying, low-frequency signal. The

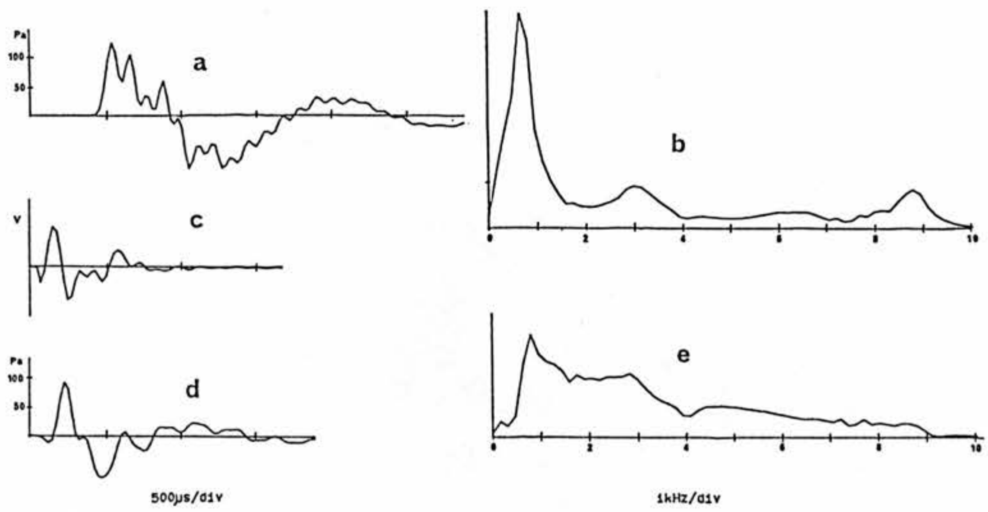

Figure 5.12: *Loudspeaker K was unsuitable for pulse production. Details as for Figure 5.10.*

corresponding spectrum of Figure 5.12(b) shows resonances at around 600Hz, 3kHz and 9kHz. The calculated drive waveform (c) has a complex appearance, and produces a poor result (d). Because the spectrum in (e) shows the *magnitude* of the frequency components, it does not look as bad as might be expected from the pulse waveform. Presumably the *phase* factors are far from ideal.

5.4.3 Piezoelectric loudspeakers

Piezoelectric loudspeakers are becoming increasingly popular as high frequency tweeters, as they consume very little power. Two types, both manufactured by Motorola, were available for evaluation.

Identification	Type	Sensitivity	
		dB/W/m	Pa/V
H	Motorola piezo tweeter	-	6
J	Motorola KSN1086A mid-range horn driver	94	17

Table 5.2: *The two piezoelectric loudspeakers studied. Details as for Table 5.1.*

Loudspeaker H Loudspeaker H is shaped like a conventional small tweeter, but is extremely light as there is no magnet. Its impulse response (Figure 5.13(a)) shows an initial resonance which is lightly damped and is followed by the emergence of a higher mode. The corresponding spectrum of Figure 5.13(b) indicates

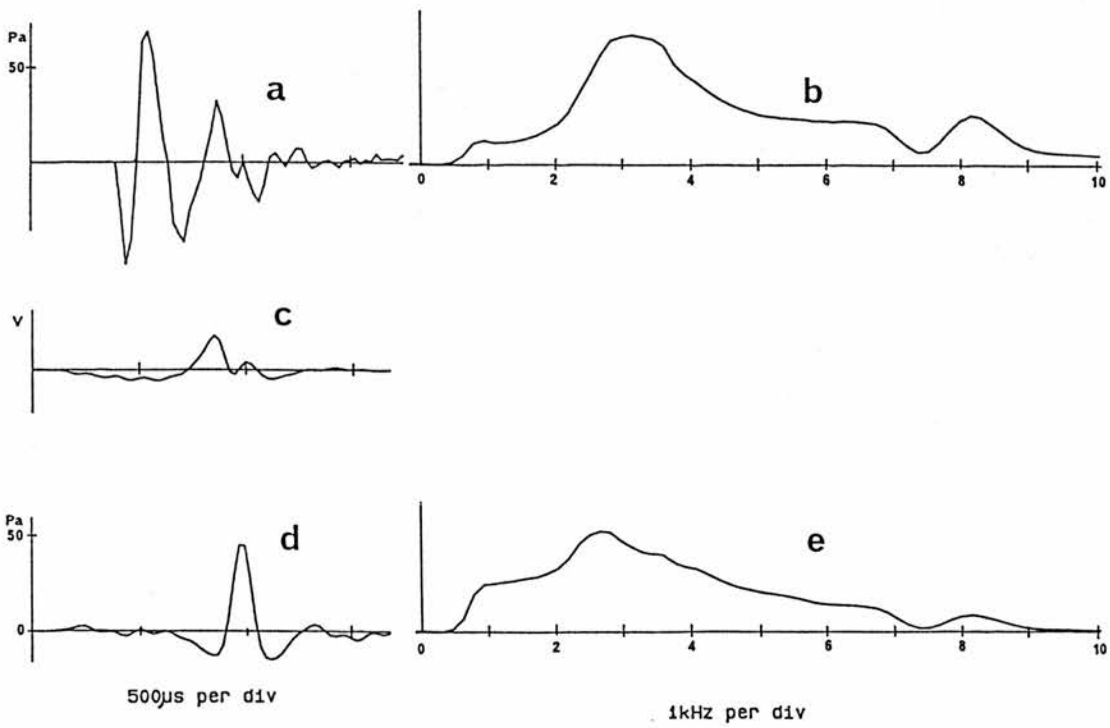

Figure 5.13: *Piezoelectric speaker H was unsuitable for pulse production. Details as for Figure 5.10.*

very little energy below 2kHz, with peaks at 3kHz and 8.5kHz. The calculated drive waveform (c) appears quite different from those used with the electromagnetic loudspeakers, and is unable to produce an acceptable pulse shape (d). The pulse's spectral content (e) is better than that of the original impulse response, the peaks having been smoothed out. However, the response falls very abruptly below 1kHz, accounting for the distinctive bipolar nature of the pressure pulse; the lack of low frequency information causes the undulating baseline.

Loudspeaker J The other piezoelectric device evaluated is Loudspeaker J, a Motorola horn driver for which a threaded coupler was made. The impulse response (Figure 5.14(a)) is bizarre, consisting of lightly damped, high frequency oscillations superimposed on a low-amplitude, low frequency baseline. The corre-

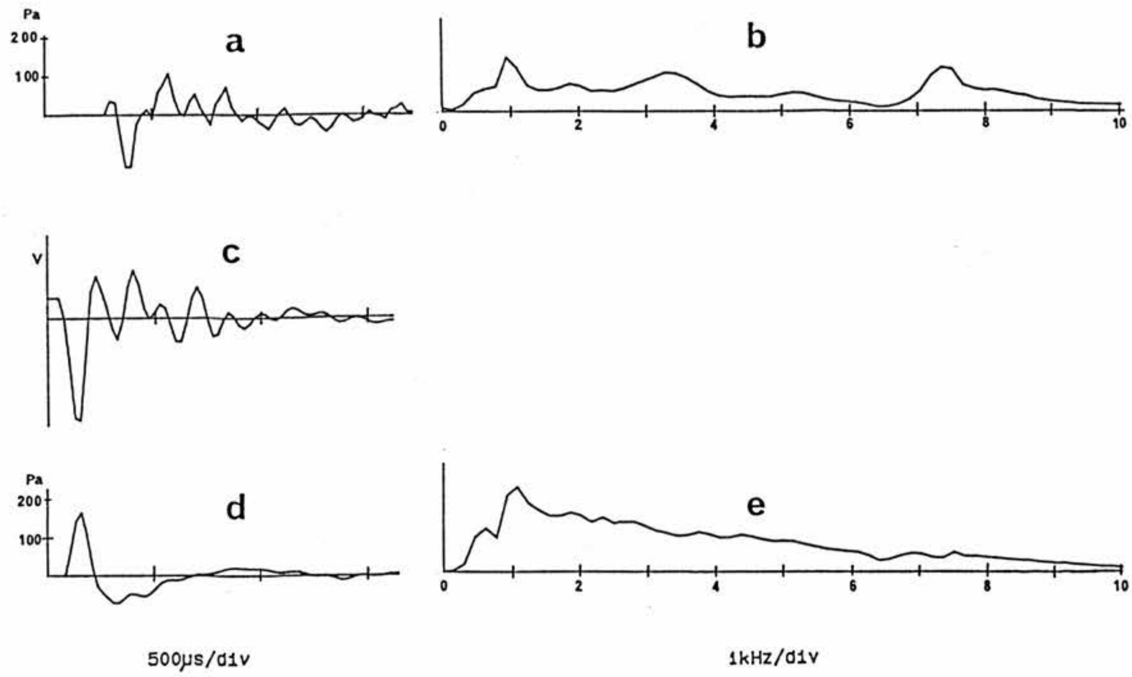

Figure 5.14: *Piezoelectric horn driver J was also unsuitable for pulse production. Details as for Figure 5.10.*

sponding spectrum of Figure 5.14(b) shows that there is very little energy below 500Hz, with peaks at 1kHz, 3.5kHz and 7.5kHz. There is also a lack of response in the region 5-7kHz. The calculated drive waveform (c) is quite complex, and the latter part has been compromised by the truncation and tapering to 2ms. It was not possible to produce an acceptable pulse shape with this loudspeaker, the best result being shown in (d). Again, the main problem is the lack of low frequency information, which is responsible for the bipolar pulse shape and the undulating baseline.

5.4.4 Choice of loudspeaker for pulse production

Many readily available electromagnetic loudspeakers are capable of producing approximately Gaussian pressure pulses when excited by an appropriate electrical drive waveform. A drive waveform of 2ms duration allows acceptable pulses of width $100\mu s$ to be achieved. Of the seven different types of electromagnetic loudspeaker tested, only one (Device K; a light, "mid-range" type) was unable to produce acceptable pulse shapes with the current technique. There was very little to choose between the others in terms of the pulse shape achieved. The highest amplitude pulses could be produced with Loudspeaker I (a massive "compression driver"), but this was considered too heavy and bulky for incorporation in a reflectometer system. All further work is carried out with tweeters A and B, which were found to be the next most sensitive loudspeakers.

Neither of the two piezoelectric loudspeakers (H and J) was capable of producing an acceptable pressure pulse. The main problem is the lack of response below 1-2kHz, which causes the pulse shapes to be bipolar with undulating baselines. Perhaps this is not really surprising when one considers that these piezoelectric devices are usually sold as add-on "super tweeters". It appears that *low* frequency response is more important than *high* frequency response if monopolar pulse shapes are required.

In the next chapter, we will use the measured pulse shape of Loudspeaker A to simulate the pressure waveforms that will be observed in a complete reflectometer system.

Chapter 6

Synthesis and analysis of simulated reflections

6.1 Introduction

Having covered the basic theory of multiple reflections, and having investigated the pulse shapes that can be produced by readily available loudspeakers, we are now in a position to simulate the actual reflection signals that will be observed in a complete reflectometer system.

If it were possible to excite the acoustic system with an ideal pressure impulse (a *delta*-function $\delta(t)$), then the resultant reflection would simply be the required reflectance $r_o(t)$. However, as we saw in the previous chapter, we are in practice restricted to using a Gaussian approximation $f(t)$ of an impulse. The reflected signal $m(t)$ then depends on the characteristics of both $f(t)$ and $r_o(t)$; in fact it is given by their convolution. With a short duration pulse $f(t)$, it will sometimes be acceptable to use the observed reflection as an estimate of the reflectance, but in general we will want to carry out a full analysis by deconvolving the reflection with the pulse shape. Appendix B covers the basic theory of convolution and deconvolution, and several important results are used in the present chapter.

Calculated reflectance functions will first be used to study the effect of bandlimited measurement, and then reflection signals will be simulated by convolving idealized reflectance functions with the incident pulse waveform. Area reconstruction is investigated without deconvolution, with frequency domain deconvolution, and with time domain deconvolution.

6.2 Effect of limited bandwidth

The result of any measurement process inevitably has a restricted bandwidth, and so it is worth considering the effect of bandwidth-limited reflectances on subsequent area reconstructions. Figure 6.1 shows the area profile and the calculated reflectance $r_o(t)$ for an object having three sections with internal areas in the ratio 4:2:1. (This example will be recognized from Section 4.2.2, where it was presented in terms of impedance.) The reflectance consists of two main peaks, followed by a succession of much smaller impulses of alternating polarity. The entire area profile is made up of 512 data points with a spacing of 20μs; ie the waveforms are of total duration 10.24ms.

6.2.1 Loss of high frequency information

When the reflectance is transformed to the frequency domain by a 512-point fast Fourier transform, and presented as the spectral modulus $|R_o(\omega)|$ (Figure 6.2(a)), it is seen to have essentially a cosine-squared form. The reflectance has been bandlimited (low pass filtered) by multiplication in the frequency domain by a rectangular function of extent $\pm f_0$ where f_0 is 25kHz. In the time domain (Figure 6.2(b)), this corresponds to convolution of the reflectance with the sinc function $\sin 2\pi f_0 t / 2\pi f_0 t$, and so "ripple" at 25kHz appears [Tenoudji and Quentin 1982]. Area reconstruction by the Ware-Aki method (see Section 4.1.1) (Figure 6.2(c)) is hardly affected by the ripple, as reconstruction algorithms are integral in nature and therefore fairly immune to high frequency

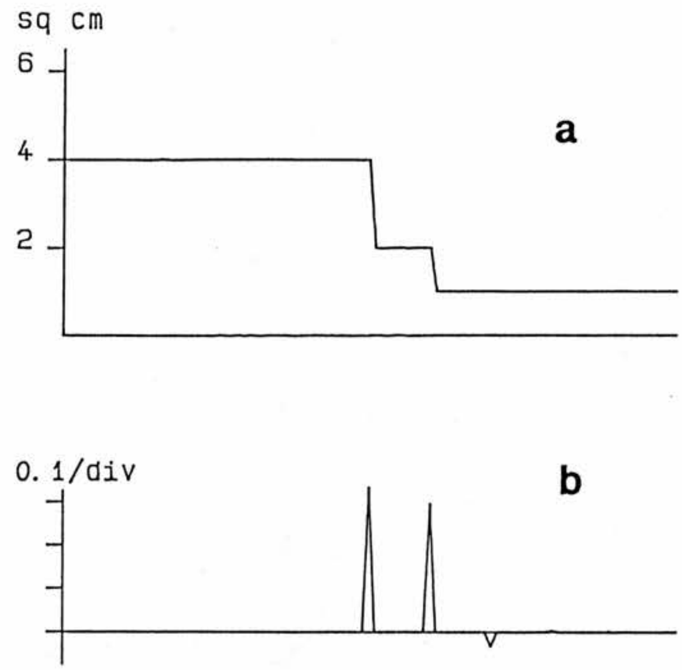

Figure 6.1: *(a) The (time domain) area profile used to illustrate the effects of limited bandwidth, and (b) the corresponding reflectance function.*

noise. When the bandwidth is reduced to 10kHz (Figure 6.3), the ringing is rather more noticeable on both the reflectance and the reconstructed area. The reflectance peaks are diminished in amplitude, but broadened in proportion, so that their integrals remain the same, and the area changes are correctly reconstructed. The steps between sections have discernible slopes, because of the broadened reflectance peaks. These effects are exactly what one expects in a low pass filtered measurement. In Figure 6.4 we see the effects of a further reduction in bandwidth, to only 5kHz. The reflectance peaks are significantly broadened, with the corresponding area transitions sloped. Ripple at 5kHz is apparent, but does not affect the overall area changes, because of the integrating action of the reconstruction algorithm.

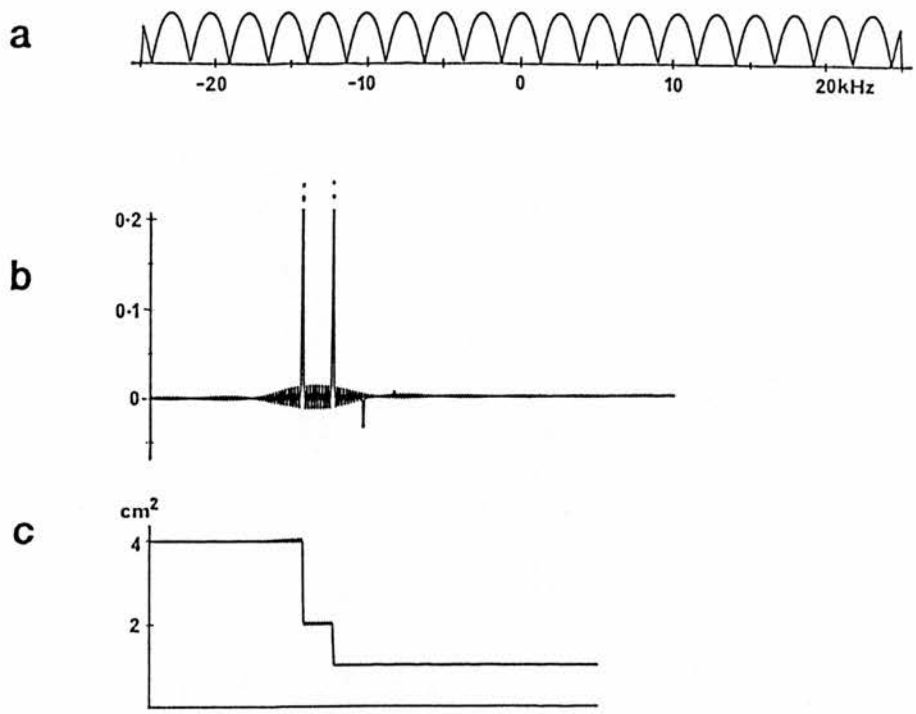

Figure 6.2: *(a) The reflectance of Figure 6.1 is truncated (in the frequency domain) at ±25kHz, and (b) transformed back to the time domain. Area reconstruction then yields the profile shown in (c).*

6.2.2 Loss of low frequency information

We now consider what happens when *low* frequency information is removed from the same reflectance function, ie the effect of high pass filtering. Figure 6.5(a) shows the reflectance function after truncation at ±25kHz and removal of the zero frequency (DC) component. The lowest frequencies remaining in the (discrete) frequency domain are ±100Hz[1]. 25kHz ripple is apparent as before, but close scrutiny reveals that the mean value of the ripple has now been shifted slightly below zero. The effect of this shortcoming on the subsequent area reconstruction (Figure 6.5(b)) is dramatic, and is another consequence of the integral nature of the reconstruction process. An offset in the reflectance, even a barely

[1]Actually 50kHz/512 or 97.5Hz

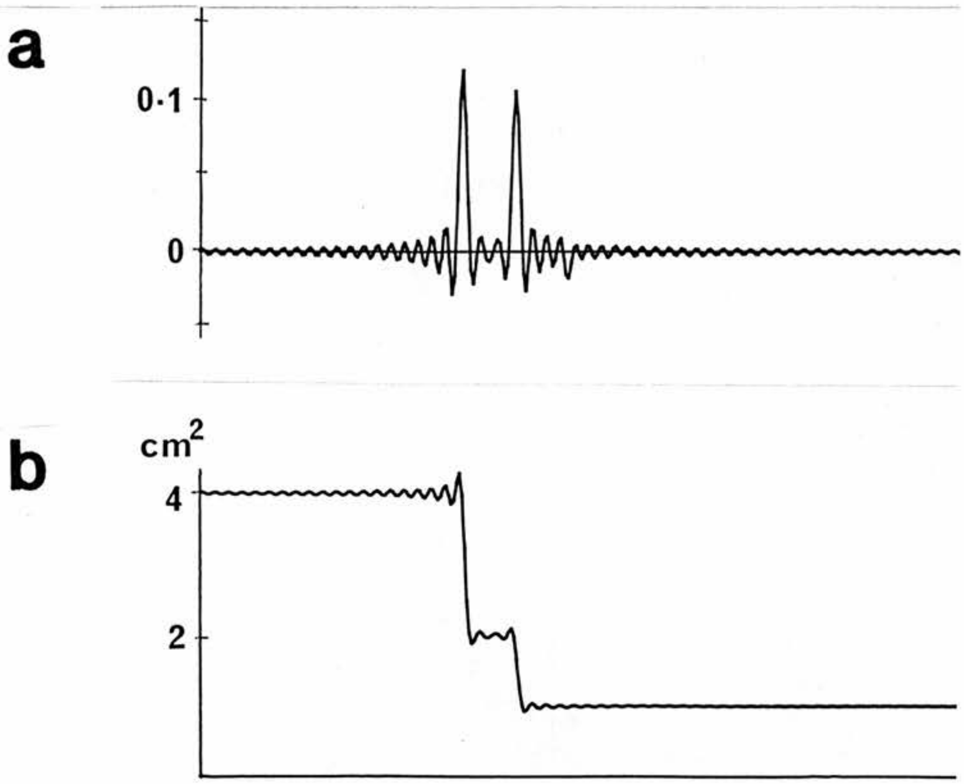

Figure 6.3: *(a) The same reflectance function, after truncation at ±10kHz, and (b) the corresponding area reconstruction.*

perceptible one as in this example, causes significant drift in the subsequent reconstruction. The steps in the reconstructed area remain sharp, because high frequency information is present. Figure 6.6 shows the effect of removing the zero and 100Hz frequency components; ie all information below 200Hz. The reflectance function now has a baseline that is clearly offset from zero, and undulating. The corresponding area reconstruction is severely distorted.

It is evident that the reconstruction process is tolerant of high frequency errors, but is extremely susceptible to offset and low frequency errors. This is unfortunate, since we saw in Section 5.4 that readily available loudspeakers produce very little energy below 200Hz. When we come to implement a reflectometer, careful consideration will need to be given to the treatment of this problem.

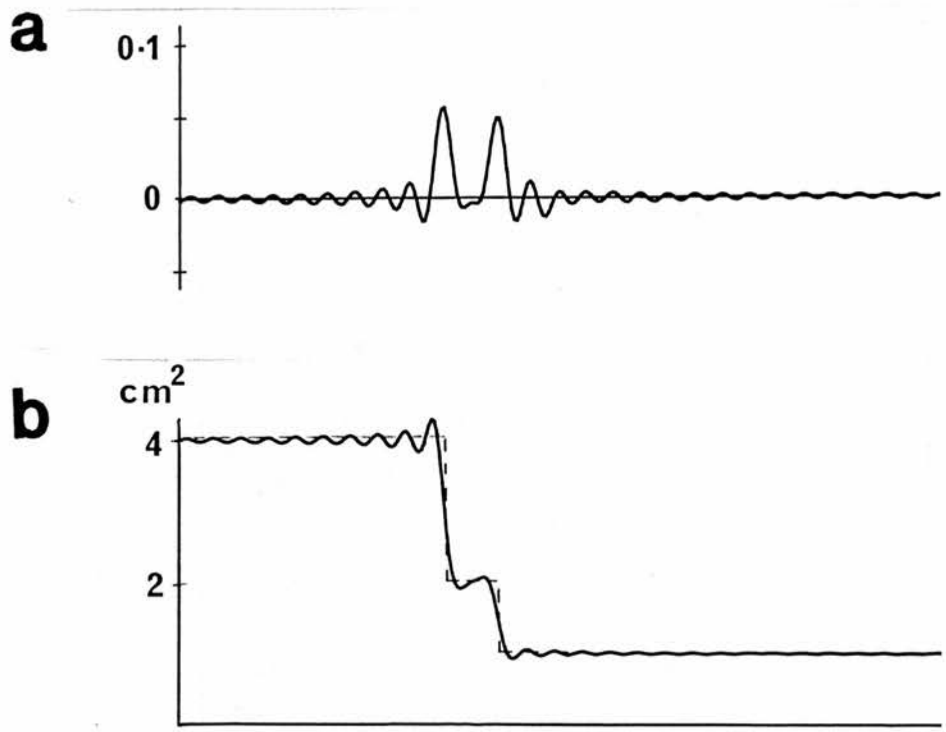

Figure 6.4: *(a) The same reflectance function again, after truncation at ±5kHz, and (b) the corresponding area reconstruction. The true area profile is shown in dashed line.*

6.3 Simulation of reflection signals

We turn now to simulating the reflection signals that can be expected in an actual reflectometer when it is excited by the pulses produced by Loudspeaker A (or B). The pulse shape $f(t)$ and corresponding spectral content were given in Figure 5.10, but for convenience are repeated here as Figure 6.7. The reflected signal $m(t)$ is given by the convolution of $f(t)$ with the object's reflectance $r_o(t)$. As an example, we will consider a cylindrical object having stepped internal diameters such that its cross sectional area has successive values of 2.0, 4.9, 3.1, 1.8 and 0.8cm^2. Unless otherwise stated, time domain functions in the remainder of this work consist of 256 data points spaced 25μs apart (ie. a sample rate of 40kHz), and 256-point Fourier transforms are used. The steps in this example are 16

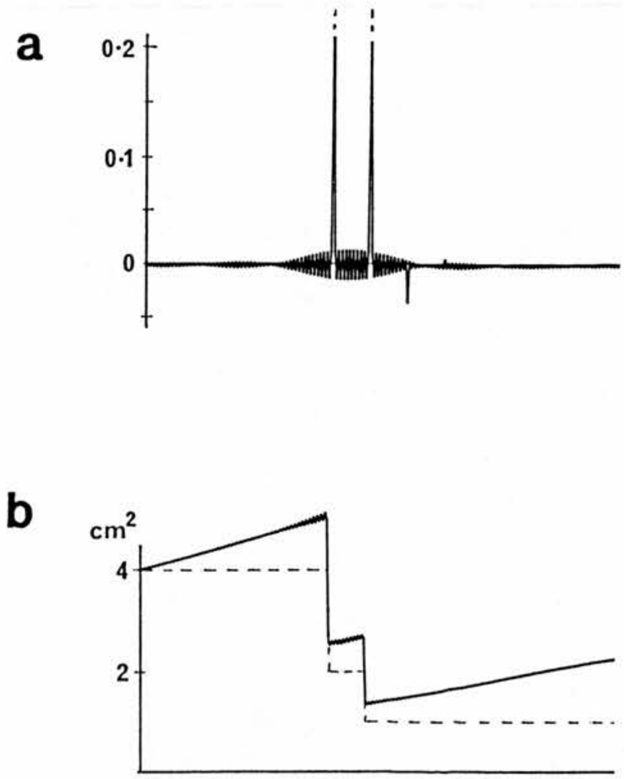

Figure 6.5: *(a) The reflectance function after removal of frequencies below 100Hz, and truncation at ±25kHz. (b) The corresponding area reconstruction. The true area profile is shown in dashed line.*

samples (400μs) long, corresponding to a (two way) distance of 70mm at a speed of sound of 340m/s. A physical model having these dimensions is detailed in Appendix E and is used in later chapters to evaluate actual reflectometers. This area profile is shown in Figure 6.8, together with the corresponding reflectance calculated by Stansfield's method [Stansfield and Bogner 1973] as described in Section 3.4. The reflectance consists of a series of impulses because of the discontinuous nature of the area changes.

The reflection signal was calculated in the frequency domain, where convolution is replaced by multiplication of the Fourier transforms $F(\omega)$ of $f(t)$ and $R_o(\omega)$ of $r_o(t)$. Figure 6.8(c) shows the result after inverse transformation to the time domain. As expected from the bandlimiting examples in Section 6.2,

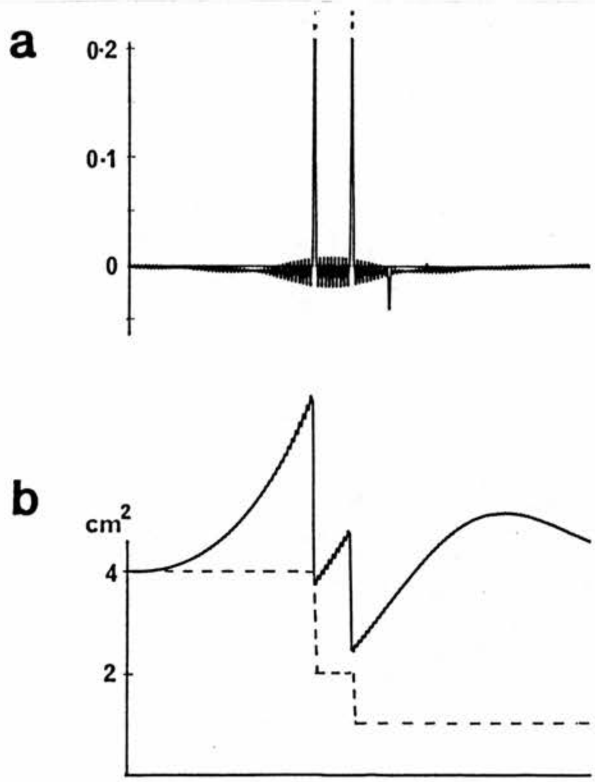

Figure 6.6: *(a) As for Figure 6.5, but all frequencies below 200Hz have been removed.*

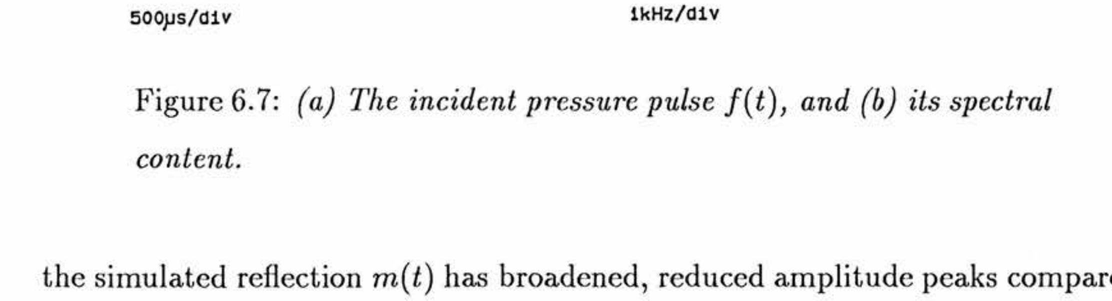

Figure 6.7: *(a) The incident pressure pulse $f(t)$, and (b) its spectral content.*

the simulated reflection $m(t)$ has broadened, reduced amplitude peaks compared with the ideal reflectance. Although the pulse waveform has little energy above 10kHz, its response falls off gradually so that the "ripple" artefact is absent from

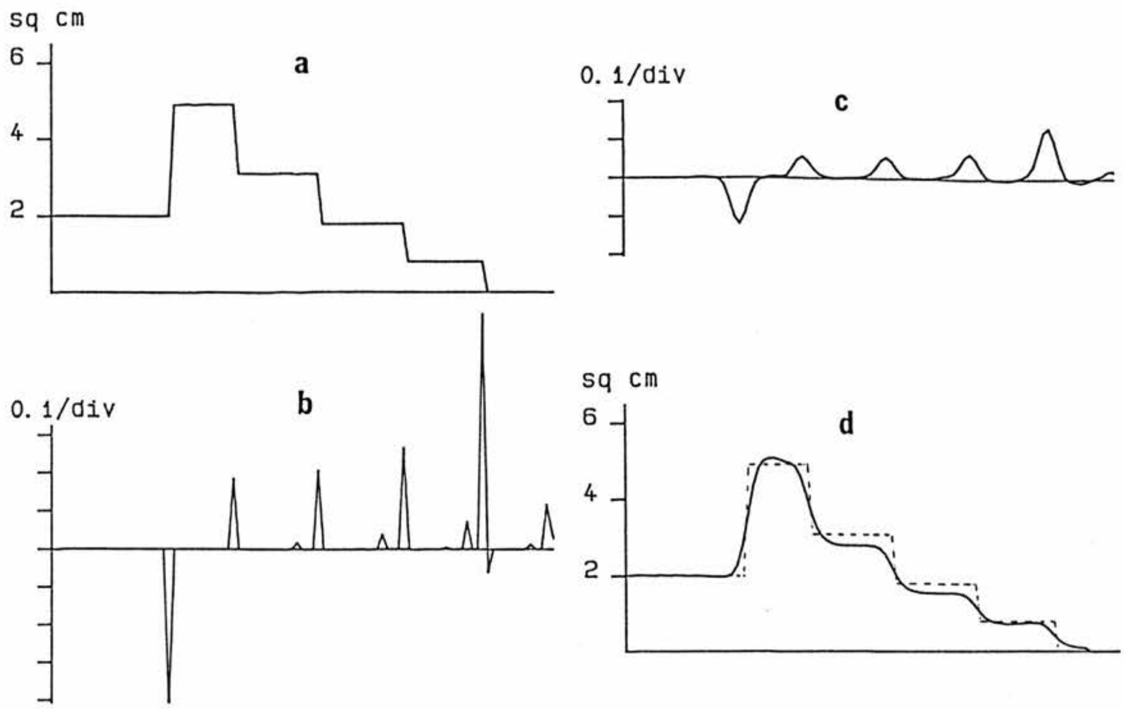

Figure 6.8: *Simulation of a reflection signal. (a) The example used is that of an object having internal areas of 2.0, 4.9, 3.1, 1.8 and 0.8cm², with a closed end. The calculated reflectance of the object (b) is convolved with the incident pulse shape to simulate the reflection (c). (d) The area profile that results from direct reconstruction of the reflection. The true area is shown in dashed line.*

$m(t)$. A slight baseline shift is just discernible in Figure 6.8(c), with a small positive offset near the beginning of the reflection, and a small negative offset near the end. This is the waveform that would result from a real acoustic experiment, and which would be used to reconstruct the object's area.

Ware-Aki reconstruction from the reflection waveform *without* deconvolution is shown in Figure 6.8(d). The slight downwards slope on the first area section, and the slight upwards slope on the final section (which prevents the reconstruction from "closing" correctly at the end) are due to the baseline shifts in the reflection, caused by lack of low frequency information. The broadened reflection peaks, due to lack of high frequency information, cause the area changes to be sloped rather than abrupt. Despite these deficiencies in detail, the result is a reasonable estimate of the original area profile (shown in dashed line), and this is because the acoustic pulse shape is a fairly good approximation to an ideal impulse.

6.4 Analysis of simulated signals

We now investigate the improvements in area reconstruction that can be achieved when the simulated reflection is deconvolved with the original pressure pulse waveform.

6.4.1 Frequency domain deconvolution

Frequency domain deconvolution is discussed in Appendix B, Section B.3, where it is shown that an estimate $\hat{R}_o$ of the reflectance can be calculated from the constrained deconvolution—

$$\hat{R}_o = \left(\frac{F^*}{FF^* + k}\right) M$$

(This is Equation B.19.) F is the Fourier-transformed acoustic pulse waveform, M the transformed reflection signal, and k is the constraining constant. This expression was applied to the simulated reflection signal. With F normalized, values of k in the range 0.01 to 0.5 gave acceptable results, and a value of 0.3 was selected. The calculated result $\hat{R}_o$ is transformed back to the time domain, as shown in Figure 6.9(a). Compared with the reflection signal, some sharpening of the peaks has occurred, but at the expense of small overshoots appearing adjacent to them. This is typical of the artefacts associated with deconvolution. Ware-Aki reconstruction leads to the area profile of Figure 6.9(b), which is more accurate than when deconvolution was omitted (Figure 6.8(d)).

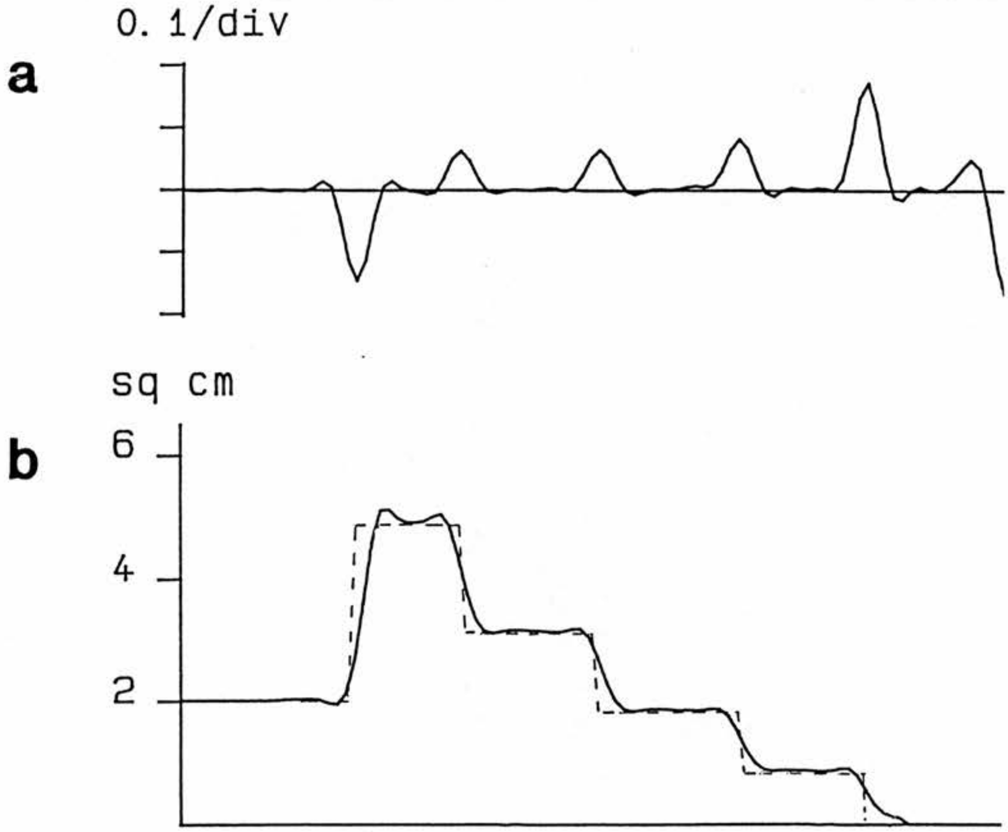

Figure 6.9: *Frequency domain deconvolution of the simulated reflection signal yields the estimated reflectance (a), which leads to the area reconstruction (b). The true area is shown in dashed line.*

6.4.2 Time domain deconvolution

Deconvolution in the time domain is possible using van Cittert's method as described in Appendix B, Section B.2.3. The simulated reflection signal $m(t)$ is taken as an initial estimate $\hat{r}_0$ of the reflectance, and improved estimates are given by—

$$\hat{r}_{k+1} = \hat{r}_k + \lambda[m - (f \otimes \hat{r}_k)]$$

This is Equation B.5, with the subscript o (for object) dropped from the reflectance. At each iteration, a proportion λ of the difference between $m(t)$ and the estimated output $f \otimes \hat{r}_k$ is added to the previous estimate. The estimated output term is itself calculated by a time domain convolution. In the present application, a value of $\lambda = 0.3$ was found to be optimum in terms of the number of iterations required for sucessful deconvolution. Figure 6.10 shows the initial estimate $\hat{r}_0$ and the first five iterates $\hat{r}_i$. Even after only three iterations, the

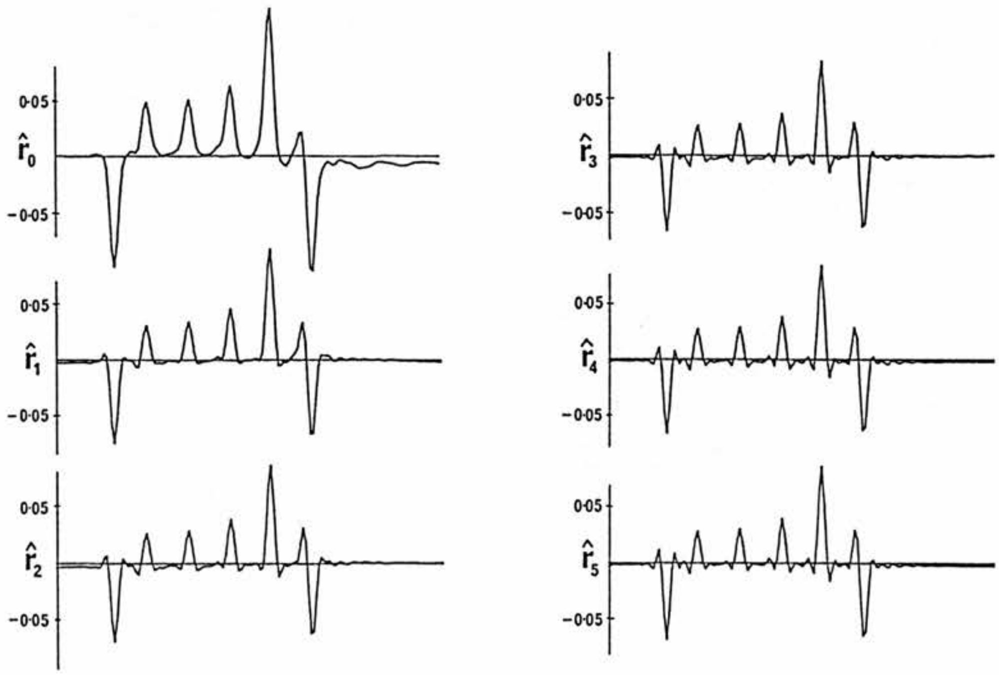

Figure 6.10: *Iterative deconvolution in the time domain. The initial estimate $\hat{r}_0$ is simply the reflection signal $m(t)$ itself. Five iterations are shown for the case $\lambda = 0.3$.*

reflectance peaks have been sharpened, and little further improvement occurs with continued iteration. However, the "ringing" adjacent to the peaks becomes progressively worse, such that the optimum number of iterations appears to be four or five. The deconvolved reflectance is seen to have a negative offset on the baseline, which is an artefact. We know *a priori* that the reflectance should be zero right at the beginning of the trace, and so we can use this portion to adjust the baseline. This is a technique which will be used later with real reflectometer data. Adjusting the baseline and performing Ware-Aki reconstruction results in the area profile of Figure 6.11. The estimated area is seen to be in good

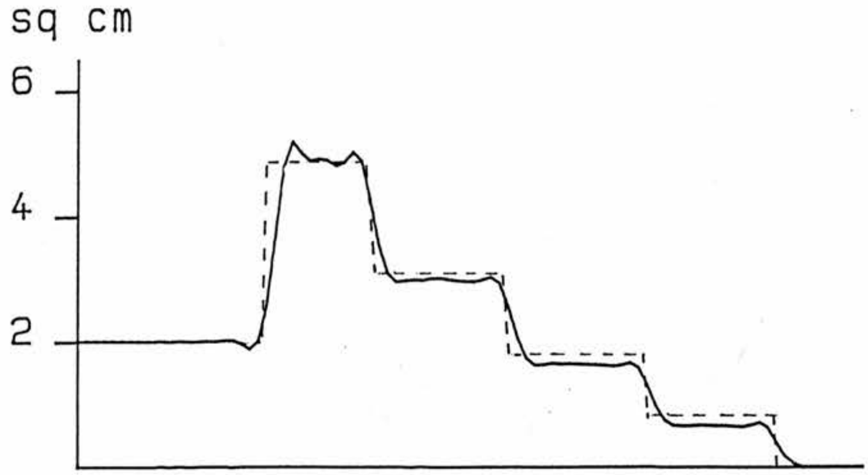

Figure 6.11: *Area reconstruction of the time domain deconvolved reflection signal, after offset correction. The actual area is shown in dashed line.*

agreement with the original area of the object, shown in dashed line.

6.5 Choice of deconvolution method

There is little to choose between the results of deconvolution in the frequency domain (Figure 6.9(b)) and in the time domain (Figure 6.11). Neither method can recover completely the sharpness of the original calculated reflectances. Frequency domain calculation may be faster if assembly language routines are available for the necessary Fast Fourier Transforms. On the other hand, with van Cittert's method it is possible to monitor the process, and stop iterating when the result is acceptable. The two methods are used interchangeably in the remainder of this work.

Figure 6.12 summarizes the theoretical framework that has been developed so far, in preparation for the implementation of an acoustic reflectometer.

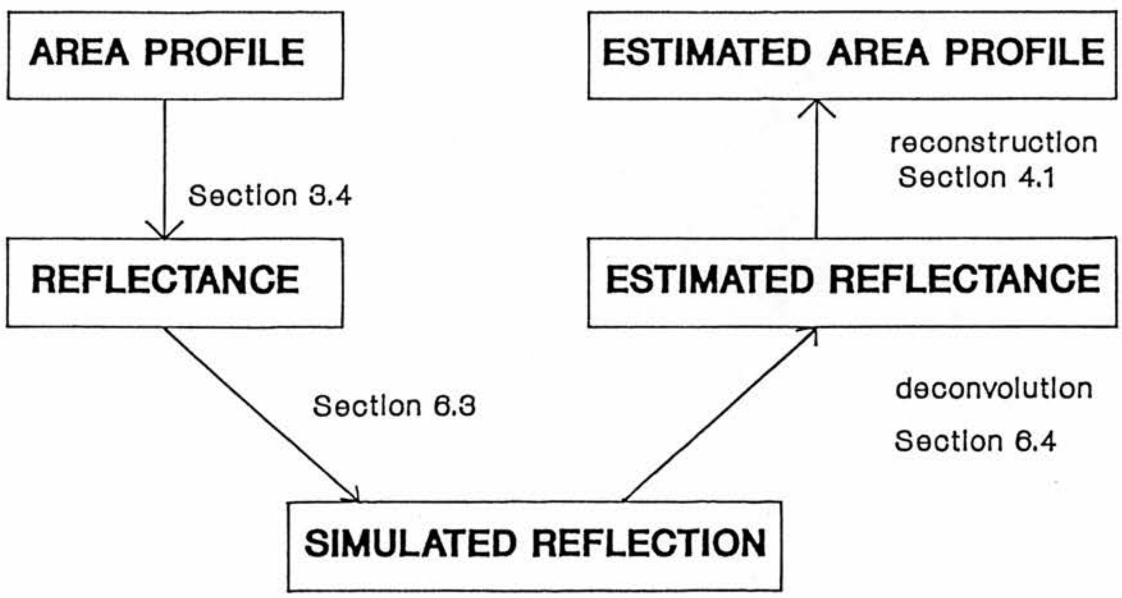

Figure 6.12: *The theoretical framework developed so far.*

Chapter 7

Implementation of a simple reflectometer

We are now in a position to implement a practical acoustic reflectometer based on the theory developed in previous chapters.

7.1 Principle of operation

The simplest possible reflectometer is constructed as shown in Figure 7.1, and is a development of the instrumentation used for pulse production in Chapter 5. A source loudspeaker is acoustically coupled to one end of a source tube, and a microphone is set flush with the inner wall at the far end of the tube. A computer with an analogue interface card controls the reflectometer. Calibration consists of closing the source tube at the microphone position, recording the impulse response of the loudspeaker, and calculating the drive waveform necessary to produce a short Gaussian pressure pulse. (This is the same experiment as carried out in Section 5.4). The actual pressure pulse achieved is recorded for later use. With the source tube open, the object (or patient) to be measured is coupled to the far end, and the pressure waveform is recorded. Separation of the reflected part of the waveform, deconvolution and area reconstruction follow.

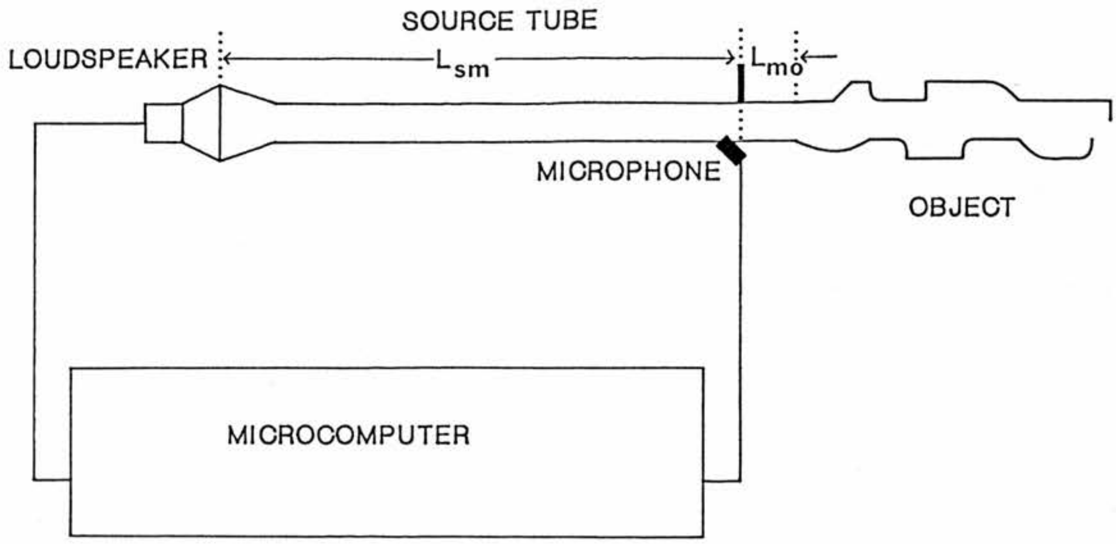

Figure 7.1: *A simple reflectometer.*

7.2 Dimensions

The diameter of the source tube is not critical, although it is sensible to achieve an approximate impedance match with the objects to be measured. Tubing with a bore of 16mm is used throughout this work. The distance between the source and the microphone L_{sm} is dictated by several factors–

1. We have to be able to measure the impulse response of the loudspeaker without multiple reflections, so that it can be used in calculating the necessary drive waveform. The tube must therefore be acoustically longer than the impulse response. For the loudspeaker used (A or B), the impulse response had a duration of approximately 3ms.

2. The tube, including the section of length L_{mo} between the microphone and the object, must be longer than the longest object to be measured, so that the primary reflection from the far end of the object can be recorded before the first reflection off the source reaches the microphone. This portion of the reflected signal is necessary and sufficient for area reconstruction of the

object.

3. Connection of test objects and patients should be convenient.

We selected a source tube of length 1130mm, which fulfills all the above criteria. In Chapter 11 we will see how the length constraints can be relaxed at the expense of further computation.

In Section 7.6, it is shown that making L_{mo} greater than the length of the incident acoustic pulse improves separation of the incident and reflected waveforms. The Gaussian pulses used (nominally 100μs FWHM) have a baseline length of approximately 70mm, so this condition is easily met by choosing $L_{mo} = 130$mm.

A slide valve is positioned immediately beyond the microphone. It is machined from Perspex, with rubber "O" rings placed either side of the sliding piece to ensure an airtight seal. The valve is used to completely close the source tube during calibration. When opened for acoustic measurements to be made, its internal diameter of 16mm matches that of the source and coupling tubes so that no spurious reflections are caused.

7.3 Choice of source tube material

Most previous reflectometers have used straight metal tubing [Jackson et al 1977, Resnick 1979, Fredberg et al 1980, Sondhi and Resnick 1983, Deane 1986], but this makes them bulky, and rules out portability. [Watson 1989] experimented with 34m of coiled plastic tubing when he wanted to record the extended reflectances of trombones (beyond the portion necessary for area reconstruction). He was able to produce acceptable results because his interest extended to only 1kHz, at which frequency attenuation down the tube was not too great. Attenuation and dispersion occur through thermo-viscous loss mechanisms in the air and at the tube walls. The latter effect dominates for small diameter tubing, and is influenced by the tube material.

Our method of calibration produces a known pulse shape at the microphone position, and hence automatically compensates for attenuation down the source tube itself. However, attenuation still occurs in the section L_{mo} and in the test object, and it is desirable to correct for these effects.

Attenuation was quantified in three different tube materials—steel, hard polyurethane plastic (Tygon "Tygothane", Norton Perfomance Plastics, Newcastle, Staffs.), and soft plastic (Tygon 3603). In each case, tubing with an internal diameter of 16mm was used. Both plastic types were heavy-walled (3mm wall thickness), but were reasonably flexible. All three tube materials were of uniform bore without visible flaws.

Pulse attenuation was measured using a reflectometer having a Tygothane source tube. Different lengths of the tubing under test were attached to the reflectometer and closed at their far ends with a hard plastic stopper, as shown in Figure 7.2. When the loudspeaker is driven in the usual way, the recorded

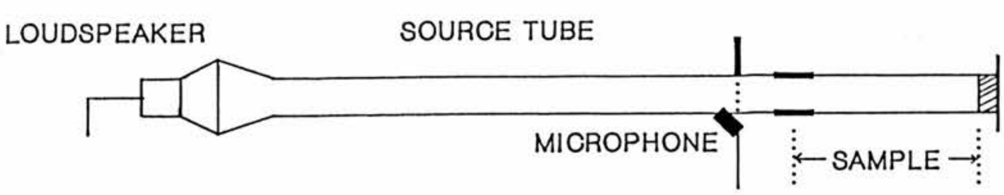

Figure 7.2: *Experimental arrangement to measure pulse attenuation.*

pressure waveform consists of the incident pulse passing the microphone, followed by the reflection of the pulse off the stopper. The latter is of reduced amplitude because of three effects—

1. Attenuation during two-way propagation along the tubing sample.

2. Non-ideal reflection at the stopper.

3. Losses at the coupling between the reflectometer and the tube sample.

By expressing the reflected pulse amplitude $p(x)$ as a proportion of that for the shortest sample studied $p(0)$, the latter two effects can be cancelled out to leave the propagation loss. We assume that attenuation can be expressed in the form $p(x) = p(0)\exp(-\beta x)$, where β is the attenuation coefficient, and plot $ln[p(x)/p(0)]$ against x to determine β. The reflected pulses were also Fourier transformed so that the dispersion of different frequency components could be studied. The results are summarized in Figure 7.3 and Table 7.1.

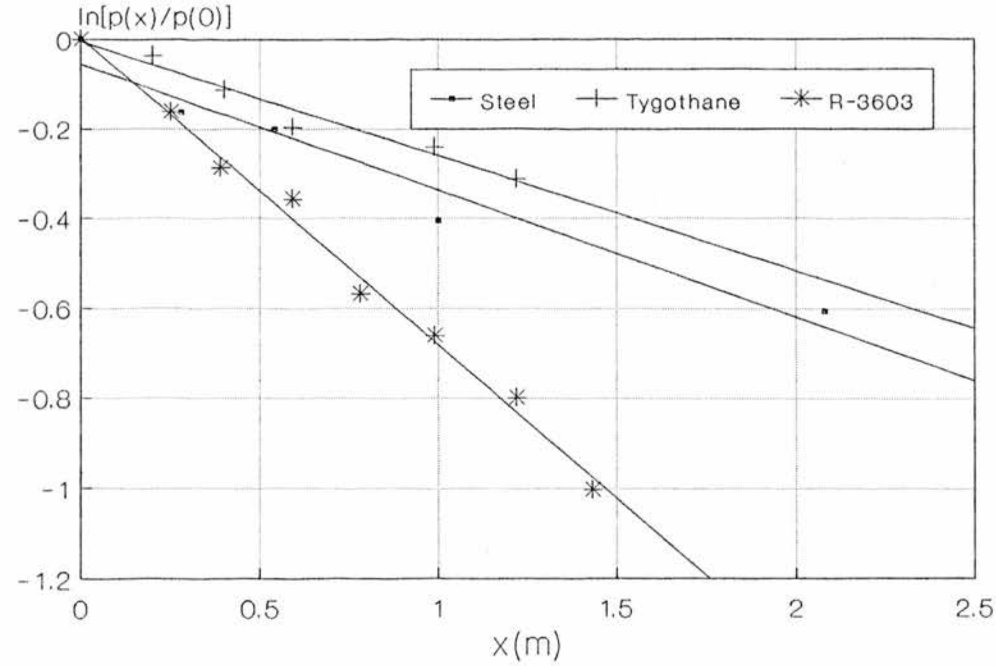

Figure 7.3: *Attenuation of Gaussian pressure pulses down 16mm bore tubing.*

Also included in Table 7.1 are the theoretical attenuation coefficients $2.93 \times 10^{-5} f^{1/2}/a$, where f is the frequency and a the tube radius [Kinsler and Frey 1982]. It will be seen that there is not a great deal of difference between steel ($\beta = 0.32$ overall) and Tygothane ($\beta = 0.26$ overall), the attenuation in both cases being about 50% greater than that predicted by theory. The R-3603 tubing attenuates

Frequency (f)	Steel	Tygothane	R-3603	Theoretical
1kHz	0.19	0.14	0.44	0.12
2kHz	0.28	0.25	0.71	0.16
3kHz	0.40	0.31	0.95	0.20
4kHz	0.45	0.33	0.86	0.23
5kHz	0.42	0.46	0.67	0.26
6kHz	0.39	0.48	0.62	0.28
Effective	0.32	0.26	0.68	(~0.18)

Table 7.1: *Summary of attenuation coefficients for 16mm tubes. The theoretical values are calculated from* $2.93 \times 10^{-5} f^{1/2}/a$*, where* a *is the radius. The "effective" frequency refers to attenuation of a 100μs Gaussian pulse.*

sound by more than twice as much. The attenuation coefficients for the Gaussian pulse amplitude are similar to the values for 2kHz, because the peak of the pulse enegy lies around this frequency. Our values of β for the steel and Tygothane are in excellent agreement with the value of 0.4 that [Deane 1986] measured for 13mm brass tubing, when corrected to take account of the different bore using the theoretical $1/a$ relationship.

Tygothane tubing thus appears quite suitable, and was used in the final construction of the reflectometer. Based on these results, a correction factor of $\exp(0.3x)$ is applied to the reflection signals recorded from test objects. This is a gross simplification, being independent of frequency, object area and wall material, but it will be shown that useful results are achieved. The correction amounts to 11% over a distance of 400mm.

With flexible tubing it is also possible to curve the reflectometer to make it more compact and to assist with patient connection. Although in principle a curved tube appears acoustically shorter and wider than an equivalent straight one, the corrections are insignificant for gentle curves. For example, the correction factors for a tube of diameter 16mm and a radius of curvature of 200mm differ from unity by less than 0.1% [Nederveen 1969].

7.4 Signal to noise ratio

Signal to noise ratio is not discussed in the acoustic reflectometry literature, except for a brief comment in [Deane 1986]. However, careful selection of transducers and drive levels was found to be crucial in achieving satisfactory results with the simple reflectometer. Signal averaging techniques can be used for *in vitro* measurements, but are not suitable for clinical applications because the airway area may vary from moment to moment. We must make "single-shot" measurements.

The incident pressure peak must therefore be great enough to allow adequate signal to noise (S:N) ratio in the reflected waveform. Figure 4.3(b) showed that the reflections of interest from a smoothly tapered area profile will be less than 0.03 (-30dB) of the incident amplitude. To record such reflections with, say, at least 40dB S:N ratio thus requires incident pressure pulses 70dB above the noise level. Extraneous acoustic disturbances were not found to be a problem, the noise level being determined by the broadband electronic noise inherent in the microphone's inbuilt FET buffer. This noise was 300μVpp in the bandwidth 60Hz to 12kHz, for several samples of the Knowles BL1785 microphone. Thus we need incident pressure pulses producing microphone signals of the order of 1V. The Knowles BL1785 has a sensitivity of 3mV/Pa, and so the incident pulse amplitude should be approximately 300Pa. In practice, 200Pa Gaussian pulses are readily achieved with Loudspeaker A/B (Section 5.4), and these gave satisfactory reflectometer results.

A disadvantage with pulse techniques is the rather limited energy present in a single short-duration pulse. In radar systems, this limitation is often overcome by using pseudo-random pulse sequences and matched filtering of the echoes.

This high degree of complexity is not necessary in the present work.

A flat frequency response is not required of either microphone or loudspeaker, as deconvolution of the recorded reflection signal makes the appropriate compensation.

7.5 Cross modes, resolution and sampling

7.5.1 Cross mode propagation

The theory of reflectometry assumes one-dimensional propagation of sound, and cannot take account of cross-mode propagation. This may occur if frequencies having wavelengths less than twice the maximum object diameter are excited. Cross modes degrade the reflections and hence the area reconstructions. Our $100\mu s$ Gaussian pulse has a spectral content that is 3dB down at 3.5kHz, and 20dB down at 9kHz. We can say that the highest frequency excited is about 10kHz, corresponding to a wavelength of 34mm. Hence cross modes cannot exist in objects of less than 17mm diameter, and are progessively more likely as the maximum diameter is increased. We might expect to see some evidence of cross modes in objects with areas greater than $3cm^2$ (diameter 20mm), and this will be investigated in the next chapter.

7.5.2 Spatial resolution

The spatial resolution of an imaging technique is generally limited to a fraction of the wavelength employed, and this applies also to acoustic reflectometry. With significant acoustic energy up to 10kHz, the axial resolution will be limited to the order of 10mm, which means that we will not be able to measure accurately details smaller than this.

Note that, because of the need to avoid cross modes, the resolution is dependent on the object's maximum diameter. We can write—

$$\lambda_{min}/2 = D_{max}$$

and

$$\Delta x \simeq \lambda_{min}/4$$

so that—

$$\Delta x \simeq D_{max}/2$$

where λ_{min} is the minimum wavelength used, D_{max} the maximum diameter of the object, and Δx the axial resolution. The factor of 4 is intended as a guide only; [Fredberg et al 1980] used a factor of 6 when discussing resolution.

7.5.3 Sampling

The discrete sampling of the reflection signal should be fast enough so as not to further limit the axial resolution. We use a 40kHz sample rate (25μs per sample), giving a spacing between data points of 4.25mm. Sound (at a velocity of 340m/s) covers the two way distance of 8.5mm in 25μs. The sample spacing is approximately half that determined by the fundamental resolution limit.

We are interested in objects no longer than 400mm, so that area reconstructions will cover a maximum of 100 data points from the end of the reflectometer. Waveforms are recorded for 256 data points (ie a duration of 256$\times$25μs or 6.4ms), and 256-point Fast Fourier Transforms (FFTs) are used. The spectral resolution is then 40kHz/256=156Hz.

The reflectometer software is written in Turbo Pascal, chosen for its ease of use and the speed of the compiled code. The main program is listed in Appendix C. This program and the supporting procedures together comprise approximately 3000 lines of source code.

7.6 Operation of the reflectometer

7.6.1 Calibration

During calibration, the slide valve is closed and the loudspeaker impulse response determined. The loudspeaker is then driven to produce a Gaussian pressure pulse, and the actual waveform p_{cal} is recorded (Figure 7.4). 10 excitations are

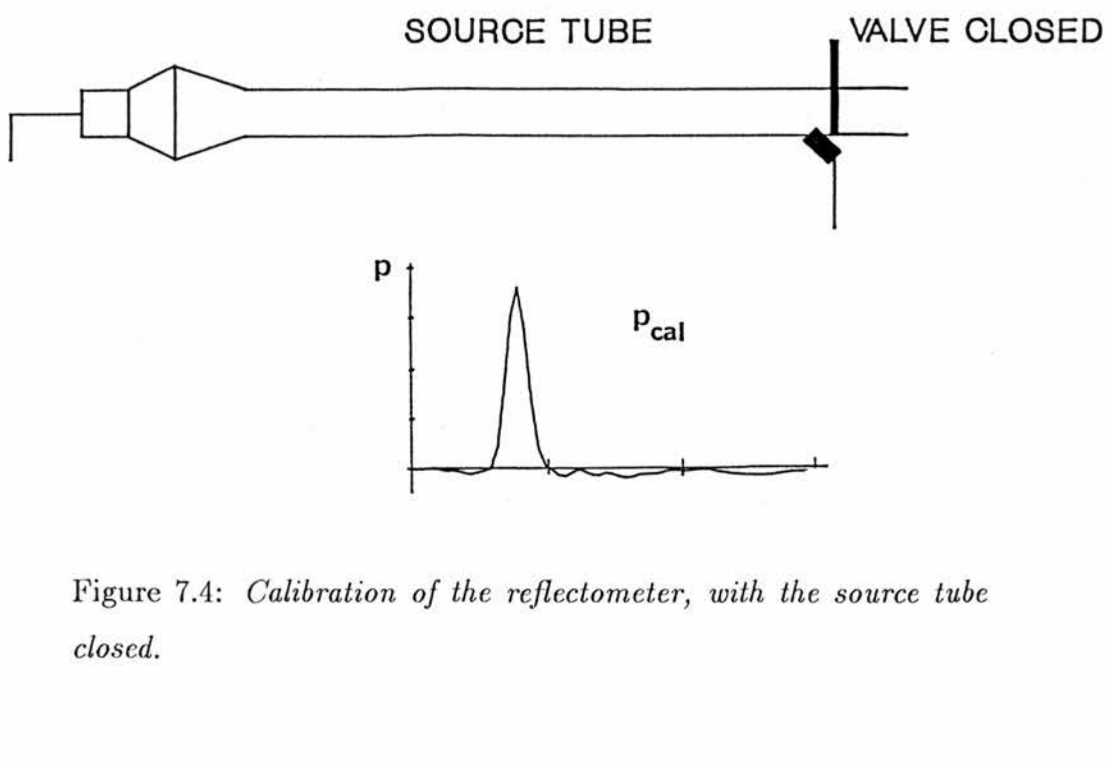

Figure 7.4: *Calibration of the reflectometer, with the source tube closed.*

averaged for each of these two steps, and the results are truncated at 4ms to ensure that reflections off the loudspeaker (which occur at time $2L_{sm}/c$) are excluded. p_{cal} consists of the incident pulse with the superimposed reflection off the slide valve. If the slide valve were an ideal reflector, p_{cal} would have exactly twice the amplitude of the incident pulse p_{inc}, but we generalize the ratio to α.

7.6.2 Separation of incident and reflected waveforms

With the slide valve open and an object attached to the reflectometer, the pressure waveform p_{sig} is recorded, as shown in Figure 7.5. By arranging for the

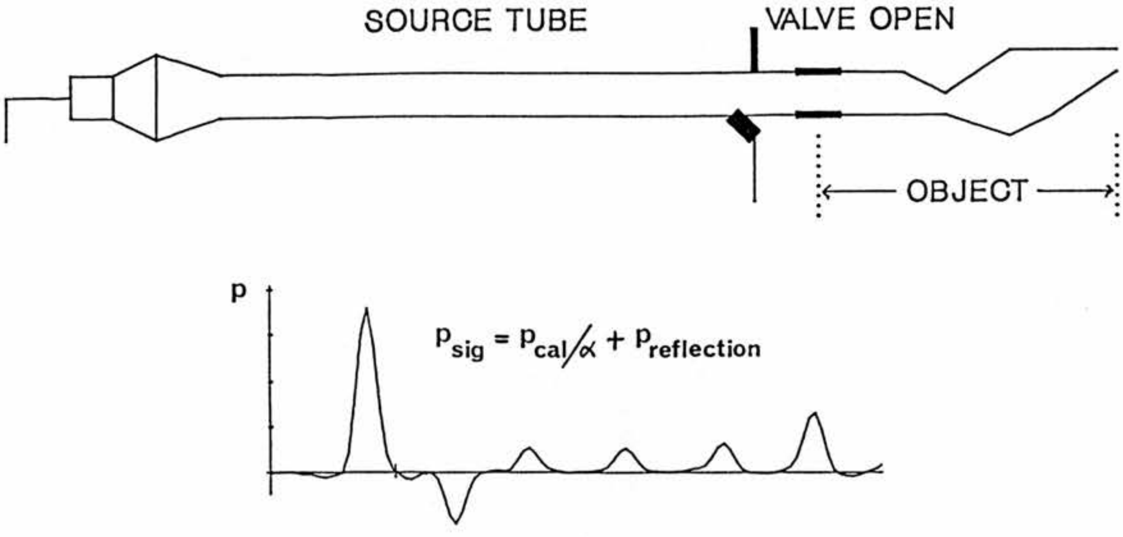

Figure 7.5: *Operation of the reflectometer, showing temporal separation of the incident and reflected waves.*

distance L_{mo} to be greater than the incident pulse duration, the incident and reflected parts of p_{sig} are temporally separated. In general, the incident pulse may have a long, low-amplitude "tail", and more accurate results are achieved by performing a subtraction. The value of α is determined by minimising the error function

$$p_{error} = \sum (p_{sig} - p_{cal}/\alpha)^2$$

where the summation is over all the data points in which p_{cal} has significant amplitude. α is initially taken to be 2, and is reduced in steps of 0.01 until a minimum in p_{error} is found. Then, we have—

$$p_{inc} = p_{cal}/\alpha$$

$$p_{reflection} = p_{sig} - p_{cal}/\alpha$$

This is essentially Fredberg's method, but is greatly facilitated by the slide valve. The determination of α is improved by reducing the amount of overlap between the incident and reflected parts of p_{sig}. Values of α are typically in the range 1.8 to 1.9.

Alignment A refinement to the separation procedure is the alignment of the p_{sig} and p_{cal} waveforms before optimisation of the error function. The position of the incident pulse is found in each waveform, and p_{sig} is shifted to bring it into alignment with p_{cal}. This technique is designed to overcome any drift in temperature or gas composition that may occur during use. The source and connecting tube are together about 150 sample points long. A worst case 6% change in absolute temperature, from 293K (20°C) to 310K (37°C), would cause a corresponding 3% change in wave speed[1], and so shift the measured object reflection by 4 or 5 data points. This would be enough to make separation unsatisfactory in the absence of prior alignment. The associated 3% scaling error in length determination is not significant in clinical practice, and consequently no attempt is made to measure and correct for temperature changes.

Interrupts Computer system timer interrupts occur at the rate of 18 per second, and may last for several hundred microseconds. If one of these happened in between exciting the loudspeaker and preparing to collect the microphone signal, the recorded pressure waveform would be shifted by many data points, making alignment difficult. To guard against this, reflectometer measurements are "synchronized" to the computer timer by waiting until an interrupt has just occurred before driving the loudspeaker and collecting the response. The interval of 55ms before the next interrupt is sufficient to ensure an uninterrupted measurement.

---

[1]The speed of sound is proportional to the square root of the absolute temperature

7.6.3 Deconvolution and area reconstruction

Deconvolution The separated object reflection $p_{reflection}$ is deconvolved with the incident pulse shape p_{inc} in either the time or frequency domain, as described in the previous chapter. The resulting waveform is the object's reflectance $r_o(t)$ (Figure 7.6). Optionally, deconvolution may be omitted, and the reflection simply scaled by the amplitude of the incident pulse.

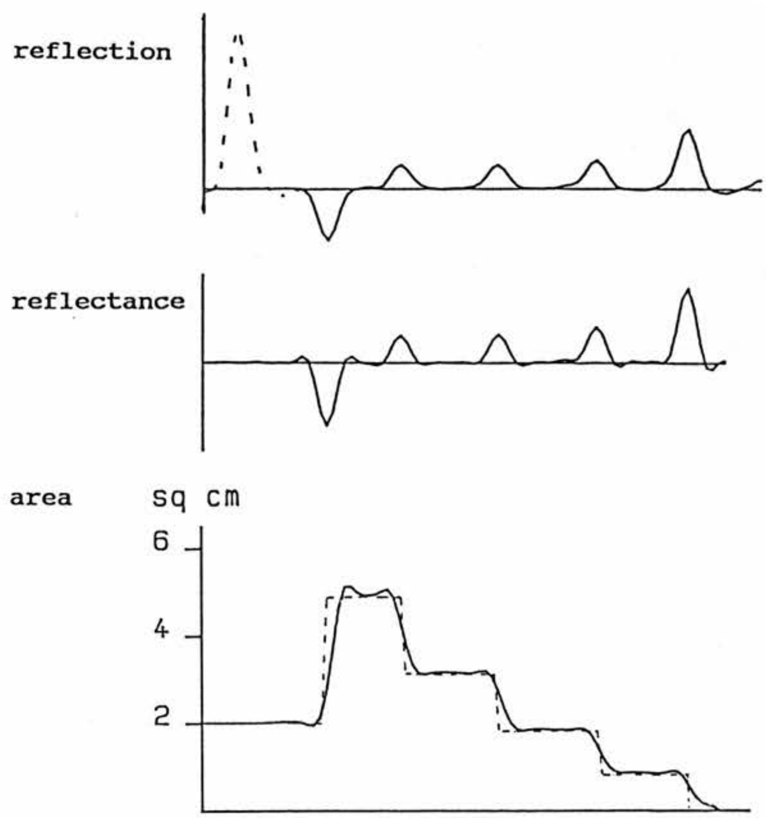

Figure 7.6: *Processing of the separated reflection consists of deconvolution, offset and attenuation correction, and area reconstruction.*

Offsets We saw in Sections 4.3 and 6.2.2 that area reconstruction algorithms are very susceptible to baseline offsets in the reflectance. Even when the ADC has no electrical offset, baseline errors arise as deconvolution artefacts, because there is very little energy at low frequencies. An offset of $\Delta R = 0.001$ in the reflectance, for example, leads to a false area change of 20% over 100 data points, and this is clearly not acceptable. It is evident from the literature that previous researchers met with similar problems. [Resnick 1979] "extrapolated" to DC in the frequency domain, by setting the mean of the DC and two lowest frequency terms to unity. [Fredberg et al 1980] determined the offset from the portion of the reflectance signal corresponding to propagation along the source tube.

One method of offset correction used in the present work considers the portion of tube in between the microphone and the object. There is no reflected energy in this region, so we can take the mean value of the reflectance over this length as the offset. The offset is then subtracted from the entire reflectance. Although only a crude "zero-order" correction, this method improves area reconstruction in some cases. However, the length of L_{mo} has been made deliberately short, so that only a few data points can be included in this method. For a given reflectometer arrangement, more consistent results are achieved by subtracting an empirically determined value from the reflectance, and this method is used in the remainder of this work. Attenuation correction is also applied at this stage.

Area reconstruction The corrected reflectance is used with one of the area reconstruction algorithms discussed in Chapter 4. Knowing the cross sectional area of the source tube (2cm^2), the object's area profile can be displayed. Optionally, the areas can be expressed in terms of relative acoustic impedances by taking their inverse.

Chapter 8

Results with the simple reflectometer

In this chapter, the performance of the simple reflectometer is investigated. It is used to measure the area profiles of a variety of test objects, using either a complete analysis (deconvolution and Ware-Aki area reconstruction) or an approximate method (no deconvolution, and Integral area reconstruction). Accuracy, reproducibility and resolution are studied.

8.1 Measurement of test objects

A variety of test objects was constructed for validation of the reflectometer. They all have cylindrical symmetry, and are of two types–

1. objects with stepped internal diameters (ie, discontinuous area changes), which are a severe test of the effectiveness of deconvolution;

2. objects with smoothly changing diameters, representing simple models of the human airway.

Mechanical drawings of the objects are contained in Appendix E.

8.1.1 Objects with stepped diameters

Two objects were made with stepped internal diameters; one with area increasing with distance, and the other with area decreasing.

Object A The first object is of aluminium, and has stepped internal diameters (ID) of 25, 30, 35 and 40mm, each section being 70mm long. The corresponding areas are 4.9, 7.1, 9.6 and 12.6cm^2. The object couples to the reflectometer (ID 16mm) with a short adaptor.

Figure 8.1 shows typical results obtained with Object A, when its far end is closed with a stopper. The separated reflection signal is shown at (a), and

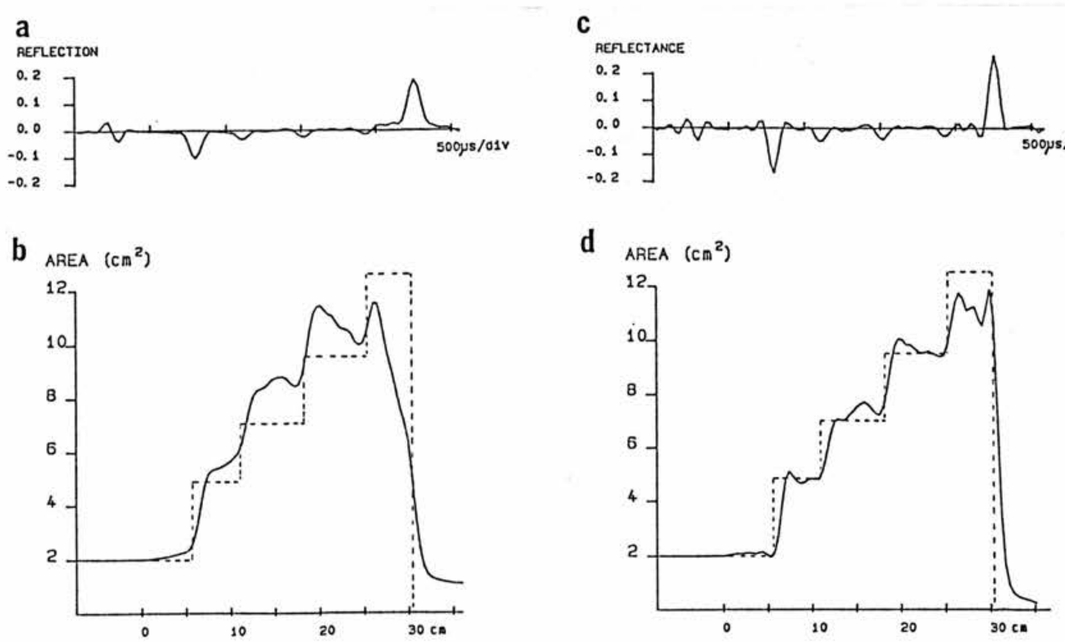

Figure 8.1: *Measurement of Object A: (a) the reflected pressure wave with (b) an approximate area reconstruction (no deconvolution, and the Integral method); (c) the deconvolved reflectance and (d) the area reconstructed from it by the Ware-Aki method. The true area is shown in dashed line.*

an approximate area reconstruction (using the Integral method) at (b). The initial part of the reflection shows the residual incident pulse, left by imperfect separation. This does not affect subsequent area reconstructions, because the reconstruction algorithms are started after this region, at the point labelled '0' on the distance axis. Without deconvolution, the result is not very convincing: a small negative offset in the early part of the reflectance causes the first two area steps to slope upwards. A positive offset in the later part of the reflectance causes a severe downward slope in the third area step, and completely obscures the final step. Over the whole object, these effects tend to cancel out, but this is purely fortuitous.

When the reflection is deconvolved to give the reflectance (c), there is a noticeable sharpening of the peaks. A Ware-Aki reconstruction then gives the area profile in (d). Deconvolution has improved matters significantly, although at the expense of causing "ringing" artefacts either side of the main reflectance peaks. There is still some trouble from offsets in the later part of the reflectance, and the widths of the reflectance peaks cause the area changes to occur over several data points rather than being abrupt. In an object with such large diameters (up to 40mm) we might expect some cross mode propagation, and perhaps this is partially responsible for the inability to measure the final area accurately.

Object B The second object is similar to Object A, but with internal diameters of 25, 20, 15 and 10mm, each section again being 70mm long. The corresponding areas are thus 4.9, 3.1, 1.8 and 0.8cm^2. This area profile was introduced in Section 6.3 (Figure 6.8) when calculating simulated reflection signals. Object B also couples to the reflectometer by a short adaptor.

Figure 8.2 shows typical results with Object B. The separated reflection signal (Figure 8.2(a)) should be compared with the simulated reflection of Figure 6.8(c); the similarity shows that the multiple reflection theory and the reflectometer measurement technique are in good agreement. However, offsets in the real reflection prevent the approximate area reconstruction of Figure 8.2(b) from

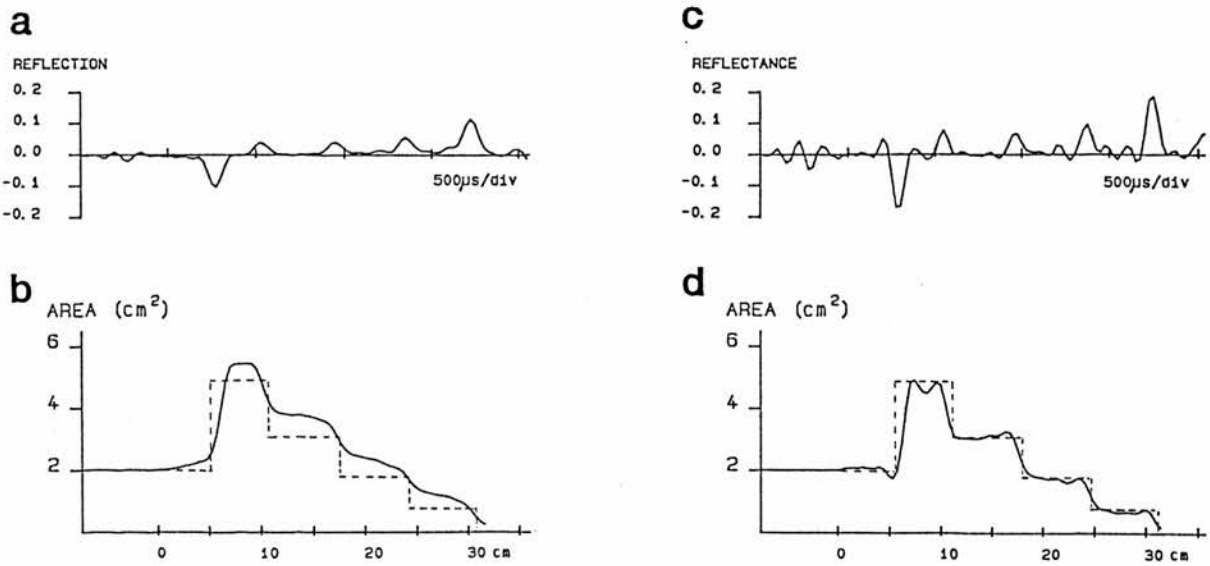

Figure 8.2: *Measurement of Object B: details as for Figure 8.1.*

being as good as that achieved with the synthetic data of Figure 6.8. The acoustically measured area steps have a good deal of slope because of the offsets.

The situation is much improved by deconvolution and a full Ware-Aki reconstruction, and the resulting area profile (Figure 8.2(d)) is then in very good agreement with the actual area. The spurious peaks either side of the (negative) first main peak in the reflectance are the usual deconvolution artefacts, and they cause the false "dips" in the area profile before and during the first expansion. Despite these, the area estimate is better than that for Object A, and is accurate to within a few percent. Cross modes are unlikely in Object B, and this may well be part of the reason for the improved accuracy.

8.1.2 Simple airway models

Although a real airway does not have cylindrical symmetry, and a straight tubular object does not correctly model the bend at the back of the mouth (the oropharyngeal junction), simple airway models are nevertheless useful in investigating the performance of the reflectometer.

Airway Model 1 An object having a smoothly varying internal diameter was made by shrinking heatshrink tubing onto a metal former, and then removing the former. The internal diameter increases from 16mm at the reflectometer to a maximum of 27mm (area 5.7cm^2) at a distance of 150mm, and then decreases to 13mm (1.3cm^2) at 325mm. There is a final increase to 20mm ID (3.1cm^2) at the far end of the object, 500mm away from the reflectometer. In a very crude way, the main area expansion represents that expected of a human mouth, although the overall length of the model is exaggerated.

The walls of this model are slightly yielding, especially in the "mouth" region, but this does not appear to adversely affect the result shown in Figure 8.3. This result was produced using frequency domain deconvolution and Ware-Aki reconstruction. Apart from errors of approximately 15% in estimating the areas of the constriction and of the end of the model, good agreement is achieved with the actual area profile over a distance of 400mm.

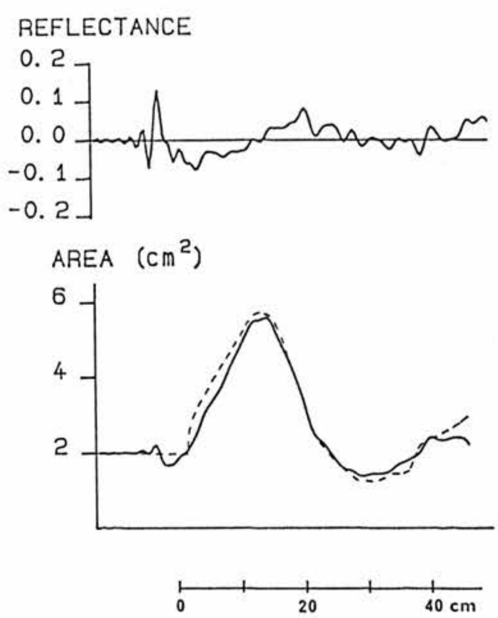

Figure 8.3: *Measurement of Airway Model 1. Deconvolved reflectance and Ware-Aki area reconstruction.*

Airway Model 2 A few preliminary airway measurements (to be described in Section 8.7) guided the construction of a more realistic airway model. It was machined from Perspex, and consists of four interlocking parts;

Part A Over a total length of 200mm, the internal diameter first increases from 16 to 39mm, then decreases to 16mm before increasing to 23mm, and finally returning to 16mm. The corresponding area expansions of 11.9cm^2 and 4.1cm^2 represent the mouth and pharynx respectively.

Part B As Part A, except that the "mouth" diameter is 28mm, giving an area of 6.1cm^2.

Part C Over a length of 100mm, the internal diameter decreases from 16mm to 11mm, and then returns to 16mm. The area constriction of 0.9cm^2 represents a glottis.

Part D As Part C, except that the minimum diameter is 8mm, with a corresponding "glottal" area of 0.5cm^2.

Parts B and C together are the physical realization of the area profile that was studied theoretically in Section 4.2.3.

Results with Airway Model 2 are shown in Figures 8.4 to 8.6. For the purposes of measurement, the model was terminated with 16mm diameter tubing to eliminate end reflections within the time for which signals were recorded.

In Figure 8.4(b) we see that approximate measurements are not really suitable for highly non-monotonic objects. Although the "mouth" is estimated with reasonable accuracy (9.6cm^2 instead of 11.9cm^2), the "pharynx" is not very well defined at all. The pharyngeal peak area is estimated as 2.8cm^2 at 160mm from the reflectometer, whereas it is actually 4.1cm^2 at 180mm. Deconvolution yields a reflectance (Figure 8.4(c)) which does not appear to be very different from the reflection, but when a complete Ware-Aki area reconstruction is carried out as well (Figure 8.4(d)), much better results are obtained for the pharyngeal region. Its peak area is now estimated as 4.5cm^2 at 170mm. The glottal constriction is clearly recognizable, but seriously underestimated as $0.4cm^2$ instead of $0.9cm^2$. It is possible that some of the shortcomings may be due to cross mode propagation in the large "mouth" of Part A.

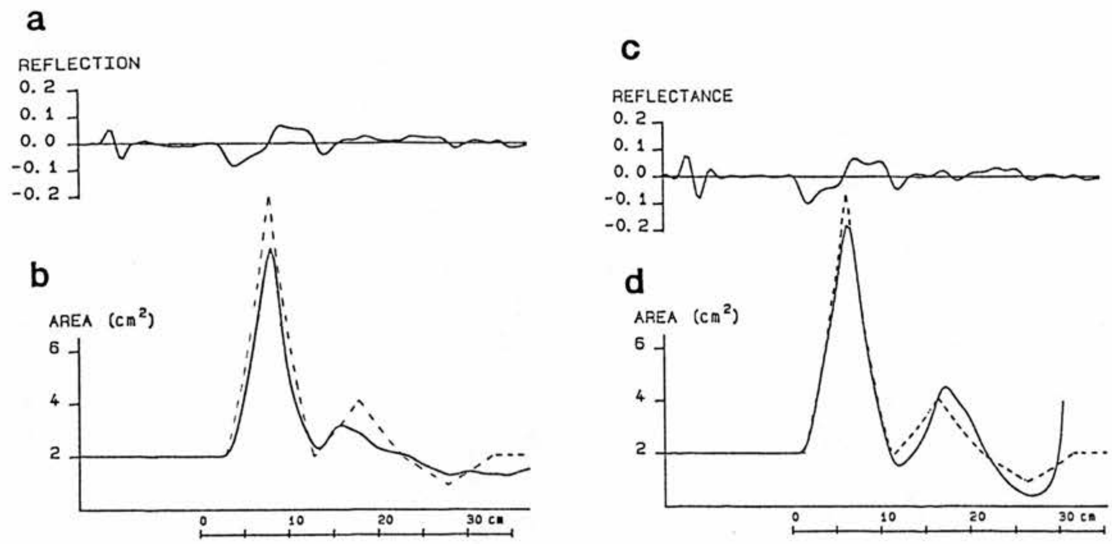

Figure 8.4: *Measurement of Airway Model 2 with a "mouth" of $11.9cm^2$, a "pharynx" of $4.1cm^2$, and a "glottis" of $0.9cm^2$. (a) reflection with (b) Integral area reconstruction; (c) deconvolved reflectance with (d) Ware-Aki area reconstruction. The true area profile is shown in dashed line.*

Figure 8.5 shows results with the smaller ($6.1cm^2$) "mouth"of Part B. With an approximate measurement, the "mouth" is underestimated by 10% and the pharyngeal peak by 25%, although the latter appears in the correct place. When a full analysis is carried out (Figure 8.5(d)), the result is very good indeed, even beyond the "glottis". This is better than could be achieved with Part A, presumably because of the less severe area expansion of the smaller "mouth".

As a final example with Airway Model 2, Part C (the $0.9cm^2$ "glottis") was replaced by the much smaller "glottis" of Part D. A complete analysis (deconvolution and Ware-Aki reconstruction) was used for Figure 8.6, which shows that the

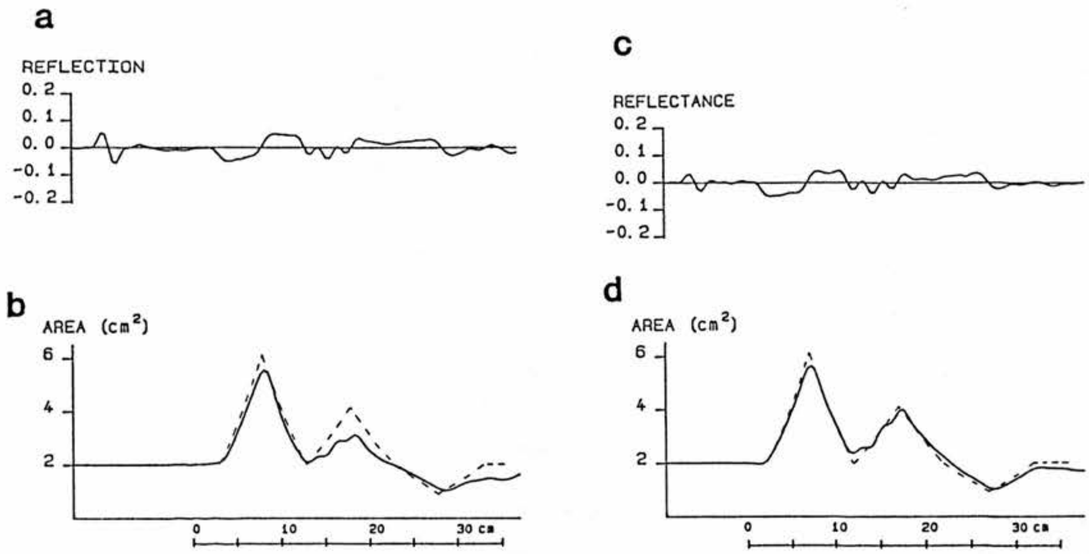

Figure 8.5: *As for Figure 8.4, except with a "mouth" of 6.1cm^2.*

glottal area of 0.5cm^2 is estimated well, although the pharyngeal peak is slightly overestimated in this particular example. Beyond the glottal constriction, the area should return to that of the terminating tube (2cm^2), but a significant overshoot is present. It is possibly caused by a small offset in the reflectance, combined with the reconstruction algorithm's sensitivity to small errors beyond an extreme of impedance.

8.1.3 Complete versus approximate area estimation

Accuracy Although reasonable approximations to Gaussian pulses can generally be produced, they may have long, low-amplitude tails which contribute to offsets in the reflected waveforms. Area reconstruction is then very dependent on the precise pulse shape, and the results can be disappointing as these studies show. Deconvolution largely corrects for non-ideal pulse shapes, and the deconvolved reflectance then benefits from a complete Ware-Aki reconstruction. This is especially true for non-monotonic objects. It may be sensible to halt the recconstructuion at areas less than, say, 0.5cm^2, or greater than, say, 20cm^2.

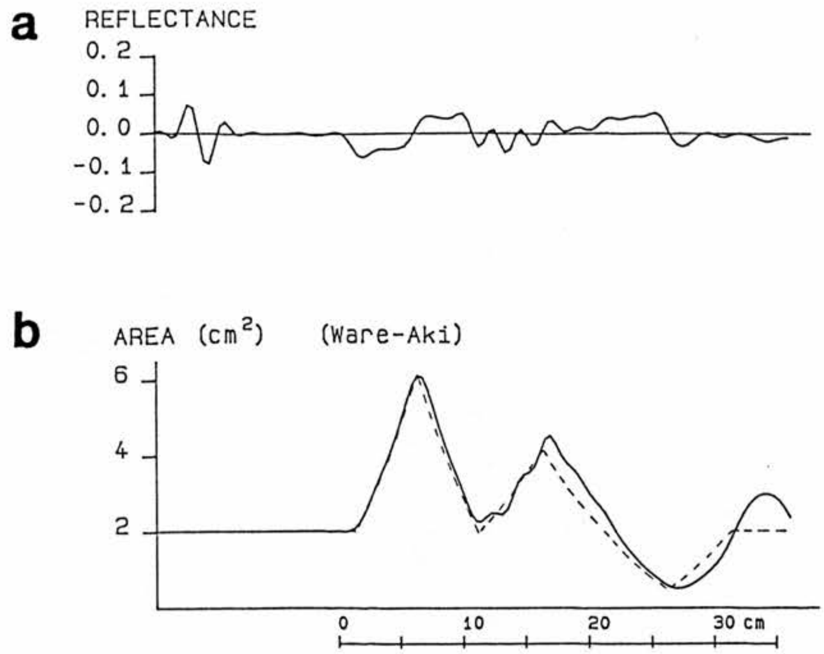

Figure 8.6: *Measurement of Airway Model 2 with a "mouth" of 6.1cm^2, a "pharynx" of 4.1cm^2, and a "glottis" of 0.5cm^2. (a) the deconvolved reflectance with (b) the area reconstructed by the Ware-Aki method.*

Speed When the algorithms are implemented in Turbo Pascal and run on a 10MHz 80286-based computer, the time for a complete measurement and display cycle (deconvolution, and Ware-Aki reconstruction) is 10 seconds. Without deconvolution, and with the Integral method of reconstruction, the corresponding time is 2 seconds. These times are approximately halved when a maths coprocessor is installed. The 5-second processing time then necessary to maintain the best possible accuracy will be just acceptable for clinical use, although it is inconveniently long. In the next chapter, ways of reducing the measurement time to enable "real-time" display of areas will be discussed.

8.2 Comparison of rigid and flexible source tubes

Since a flexible source tube has only once before been used to implement a reflectometer [Watson 1989], it was important to confirm that the results achieved are comparable with those from a rigid-tubed reflectometer. Airway Model 2 (parts B and C) was measured with the Tygothane source tube, and then with a steel source tube of identical dimensions. As can be seen from Figure 8.7, the two results are very similar, with the Tygothane measurement being slightly more accurate. From here on, a full analysis has been used for all the results presented, unlesss otherwise stated.

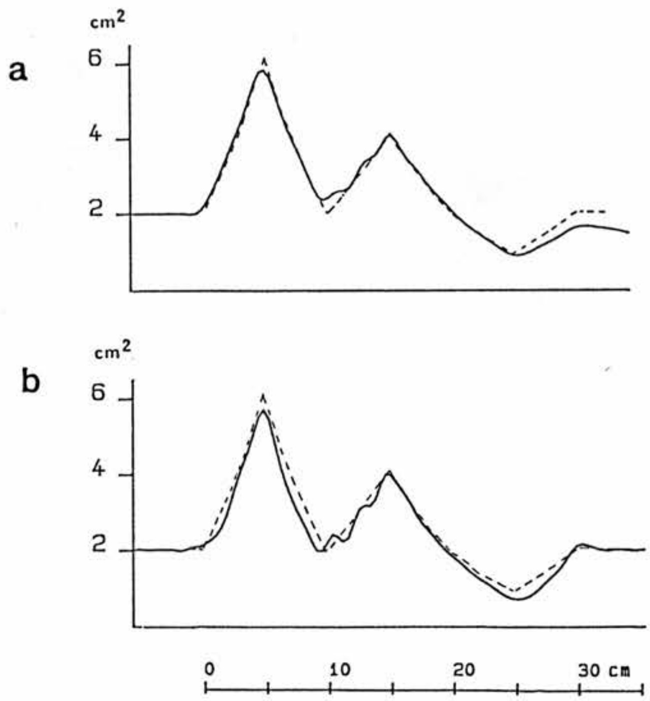

Figure 8.7: *Measurements with (a) the Tygothane source tube, and (b) a steel source tube of identical dimensions.*

Coiling the source tube with a radius of curvature of 250mm or even 120mm did not adversely affect accuracy. In another experiment, most of the source tube was coiled with a radius of curvature of 120mm, and the far end was moved laterally by 100mm in between calibration and measurement. There was no significant effect on area reconstructions.

A flexible source tube made of Tygothane thus appears robust against artefacts due to curving or flexing during measurements. Such a tube is used in all the reflectometer variations discussed in the remainder of this work.

8.3 Reproducibility and drift

The intrinsic reproducibility of area measurements is important in determining the size of area changes that can be confidently detected. Reproducibility was investigated extensively in a week-long experiment. Airway Model 2, Part A was used, with the "mouth" expansion limited to 5.7cm^2 by means of a tubular insert (Part B was not available at the time, and it was believed that a realistic mouth area would be nearer 6cm^2 than 12cm^2). Early each morning, 5 runs of 20 measurements were made of the peak "pharyngeal" area, nominally 4.1cm^2. Each run used the same calibration data, and the reflectometer was recalibrated in between runs. The equipment had been switched off overnight, so that these measurements are referred to as "cold" data. This protocol was repeated 4 hours later, during which time the equipment had been left switched on. These later measurements are referred to as "warm" data. The procedure was carried out on each of 5 days.

In all, 1000 measurements were made, and the results were subjected to statistical analysis[1]. The mean of all pharyngeal area measurements was 3.6cm^2, compared with an actual area of 4.1cm^2, an underestimation of 12%. The *within-run* standard deviation ranged from 0.04 to 0.08cm^2, with most runs giving 0.06cm^2. We can say that the worst case within-run variability of measurements is $\pm$0.08cm^2, which is a coefficient of variation[2] (CV) of 2%.

[1]All statistical analyses in this work have been carried out using the UNISTAT package (Unistat Ltd, London).

[2]Standard deviation divided by the mean, expressed as a percentage.

The *run-to-run* variation ranged from 0.03 to 0.07cm^2 for the groups of 5 runs carried out in the same session. Table 8.1 summarizes the means and standard deviations for the ten sessions ("cold" and "warm" for each of five days). A two-sample, separate variance t-test shows that there is a significant difference between the "cold" and "warm" measurements on Day 1 only.

Day	Cold	Warm	Difference	p-value
1	3.75 ± 0.04	3.67 ± 0.03	0.08	0.01
2	3.61 ± 0.06	3.56 ± 0.03	0.05	0.12
3	3.51 ± 0.07	3.52 ± 0.05	-0.02	0.68
4	3.59 ± 0.05	3.65 ± 0.06	-0.06	0.15
5	3.54 ± 0.04	3.53 ± 0.04	0.01	0.71

Table 8.1: *Reproducibility of area measurements; means ± standard deviations for groups of 100 measurements. Areas are in cm^2.*

In conclusion, the simple reflectometer is capable of area measurements of a smoothly tapered, rigid object with a CV of approximately 2%. This will be quite adequate for clinical use, being well below the expected level of physiological variation.

Accounting for the variability In Section 4.3, it was shown how errors ΔR in the measurement of the reflectance lead to errors in the reconstructed area of order $2i\Delta R$ when ΔR has the same value across the majority of the data points. This is usually the case, because DC and low frequency errors dominate. The measured variation in the pressure signals was typically 5mV, compared with an incident pulse amplitude of 10V; ie ΔR is 0.0005. Over the 40 or so data points to the pharyngeal peak of the test object, the area uncertainty should therefore reach ±4%. Our observed value of CV is ±2%, so that 95% of all measurements will indeed fall within ±4%.

Measurements beyond a severe expansion (or constriction) should show greater variability, because acoustic energy is "wasted" in the expansion and less is available to probe the region of interest. To test this hypothesis, the following experiment was carried out: the "pharynx" of Airway Model 2 (Part A) was measured, the incident pulse having first travelled through the $12.1 cm^2$ "mouth". Over 30 measurements, the coefficient of variation was 2.4%. Part B of the same model was then reversed and coupled directly to the reflectometer so that the incident pulse entered the "pharynx" without having traversed a "mouth". In this case, the CV of 30 measurements was 1.4%, or slightly over half the figure with the large "mouth". Theoretically, 49% of the incident energy is transmitted at an area change from $2 cm^2$ (the reflectometer) to $12.1 cm^2$ or *vice versa* (Section 3.5). Hence, only one quarter of the incident pulse energy returns to the microphone as a reflection, yielding a pressure signal with half the available amplitude. Assuming that the noise level is the same, the variability should therefore be twice as great. This is in reasonable agreement with our result.

Drift In another experiment, Airway Model 2 (Part B) was used to determine the intrinsic drift of the reflectometer. The peak "pharyngeal" area was measured immediately after calibration, and at intervals thereafter. Over a total period of 3 hours, all the measurements fell within $4.0(\pm 0.1) cm^2$, with no discernible trend.

8.4 Measurement of small area changes

Clinically, it will be useful to monitor *changes* in airway areas, for example during therapy, or before and after surgery. In fact, reliable measurement of changes will yield clinically useful information even if the *absolute* accuracy of the technique is not very good. Statistically, area changes as small as the intrinsic reproducibility ($\pm 0.08 cm^2$ or $\pm 2\%$) should be just detectable.

A series of experiments was designed to investigate small area changes explicitly. Airway Model 2 (Part A) was used, with the "mouth" area restricted to 5.7cm^2, and the model terminated in a 16mm tube. Acoustic measurements of the peak "pharyngeal" area were made with and without the insertion of small Plasticene "lesions" in the pharyngeal expansion. The "lesions" were either 20mm or 10mm long, with constant cross sectional areas ranging from 0.15 to 2.51cm^2. These areas were determined directly by laying transverse sections of the "lesions" on graph paper, and counting the number of 1mm squares covered. The uncertainty in these direct measurements was estimated as $\pm$0.03cm^2.

Acoustically, the cross sectional areas of the "lesions" were estimated by subtracting the area measured with the "lesion" present in the model from the corresponding area with the "lesion" removed. The uncertainty in each of these measurements is expected to be no greater than $\pm$0.08cm^2 as usual, and they combine in a root mean square sense to give an uncertainty of approximately $\pm$0.11cm^2 in the estimated lesion areas. 30 measurements were made for each "lesion". The results are summarized in Table 8.2 and shown graphically in Figure 8.8. No correlation was found between direct area estimates and the dif-

20mm lesions			10mm lesions		
Id.	Acoustic area	Direct estimate	Id.	Acoustic area	Direct estimate
1	0.34	0.45	8	0.03	0.15
2	0.81	0.75	9	0.34	0.28
3	1.18	1.04	10	0.36	0.33
4	1.43	1.24	11	0.34	0.54
5	1.80	1.83	12	0.71	0.80
6	1.87	1.93	13	0.30	0.29
7	2.44	2.51	14	0.24	0.17

Table 8.2: *Acoustic and direct estimates of the areas (in cm^2) of small Plasticene "lesions" inserted in the "pharynx" of Airway Model 2.*

ference between acoustic and direct estimates. There was no significant difference between the results for 20mm "lesions" and those for 10mm "lesions", which is perhaps slightly surprising when one considers that the axial resolution limit is expected to be approximately 10mm. In the next section, this is investigated further. The experiments with Plasticene "lesions" confirm that the reflectometer is capable of reliably distinguishing area differences down to approximately 0.2cm^2.

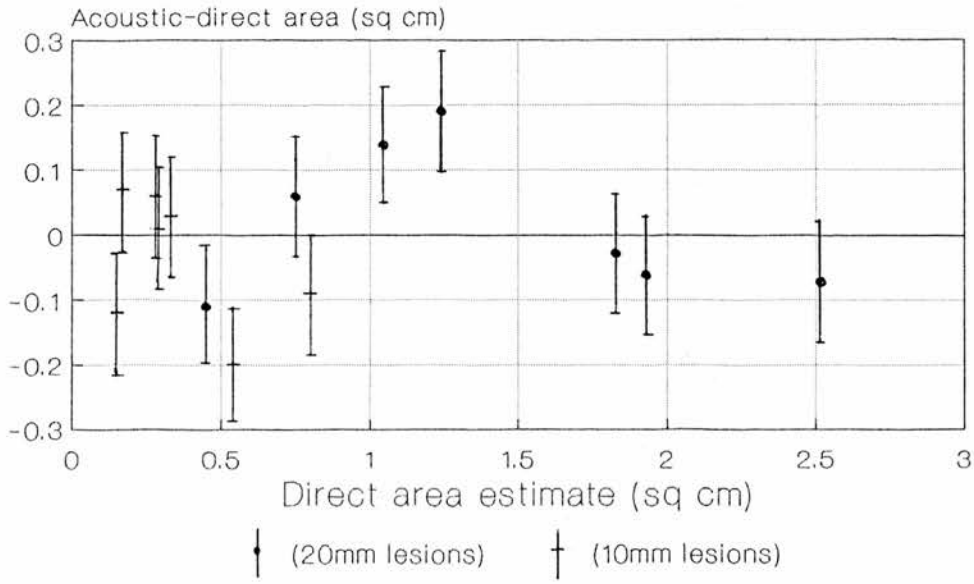

Figure 8.8: *Plot of the area data of Table 8.2.*

8.5 Axial resolution

It was stated earlier that the axial resolution is expected to be about one quarter of the shortest wavelength used. With significant pulse energy up to 10kHz, the resolution should be of the order of 10mm. To determine the actual figure, a 16mm tube was coupled to the reflectometer, and lengths of Plasticene strip were introduced into the tube to restrict its cross sectional area. All the strips were cut from the same bar of Plasticene, which had a nominal cross section of 12 × 4mm. The actual cross sectional area of the bar was measured by a water displacement method, and determined to be 0.6cm^2. Strips with lengths ranging from 70mm down to 5mm were used.

The ideal area profile taken along the tube would show an area of 2.0cm^2 (being the area of the tube), with a reduction to 1.4cm^2 for the length of the Plasticene strip. In practice, the reconstructed ends of the strip appear sloped rather than abrupt, with the area changes taking place over 15-20mm (Figure 8.9). This is because the corresponding reflectance peaks are left broadened by the imperfect deconvolution, rather than being perfectly resolved as ideal impulses. As a result, for strip lengths less than 20-25mm the true minimum

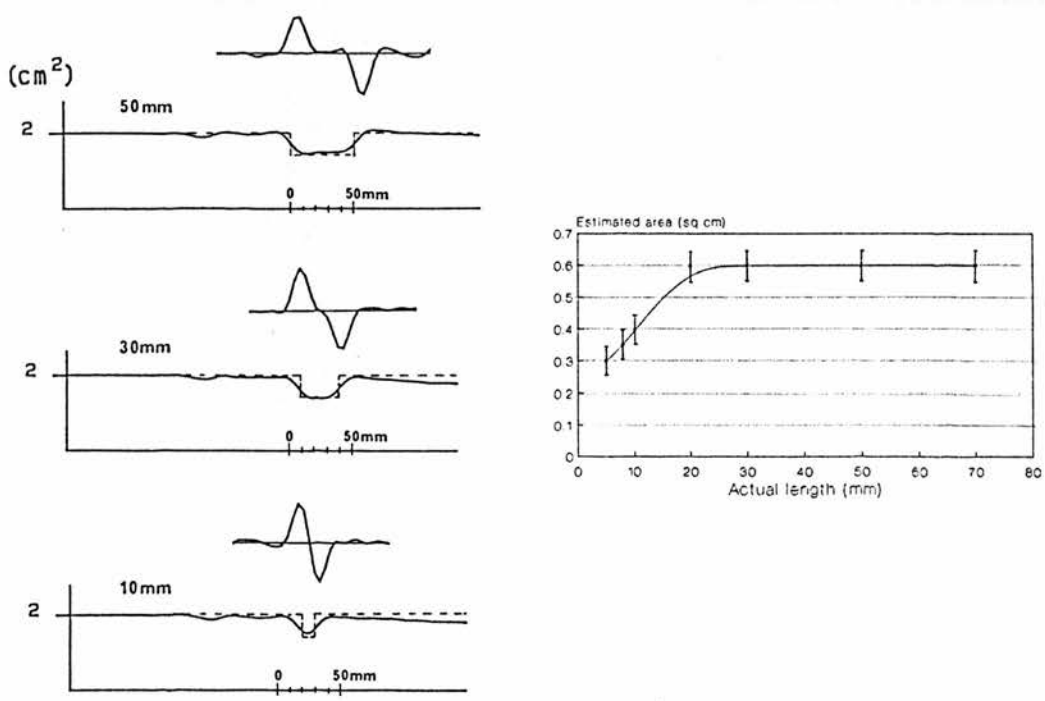

Figure 8.9: *Determination of axial resolution. Left; reflectances and area profiles for area constrictions 50, 30 and 10mm long. Right; plot of estimated areas versus actual length of the constrictions.*

cross sectional area of 1.4cm^2 is not reached. The resolution of area discontinuities is thus slightly worse than the theoretical prediction, probably because of the imperfect deconvolution rather than the intrinsic physical limitation of wavelength.

8.6 Cast of a human airway

To obtain some idea of the shape of a real airway, a plastic polymer was injected into the nose, mouth and upper airways of a human cadaver. The plastic was allowed to harden, and the surrounding tissue dissected away. It was found necessary to separate the nasal part of the resulting "positive" cast from the remainder. The oral and pharyngeal parts were joined with a common longitudinal axis, the oropharyngeal junction being thereby straightened out. The oral and pharyngeal parts of the simplified cast were then immersed in Silastic plastic resin, and the resin left to set. The Silastic was cut and peeled apart to allow removal of the cast, leaving the required model of the cadaver airway in the Silastic. Air leaks between the cut surfaces were carefully sealed with silicone rubber compound. The cadaver model was coupled to the reflectometer by a short 16mm ID tube, and acoustic measurements made (Figure 8.10).

For comparison with the acoustic measurements, transverse images of the cadaver model were taken with X-ray computed tomography (CT). The image planes were at 5mm spacing, and Region of Interest (ROI) software was used to estimate the airway area in each image. From the data, an area profile was drawn at the same scale as for the acoustic estimate.

The two profiles are seen to be in reasonable agreement in the pharygeal region (the second peak), except for a relative caudal shift of 20 to 30mm in the acoustic data. This may be due to the lack of axial resolution in the acoustic technique, tending to "low pass filter" area measurements.[3] The mouth shape was highly complex, and it was unclear from the CT images just how much cross-sectional area would actually be "seen" by the acoustic pulses. Figure 8.10 suggests that the acoustic paths do not include all the fine detail visible on the CT images. Acoustically, the mouth is underestimated by 40% compared with the CT area determination; this is too great a discrepancy to explain simply in terms

[3]An alternative explanation is that it is some effect of cross mode propagation in the mouth - see Section 8.1.2

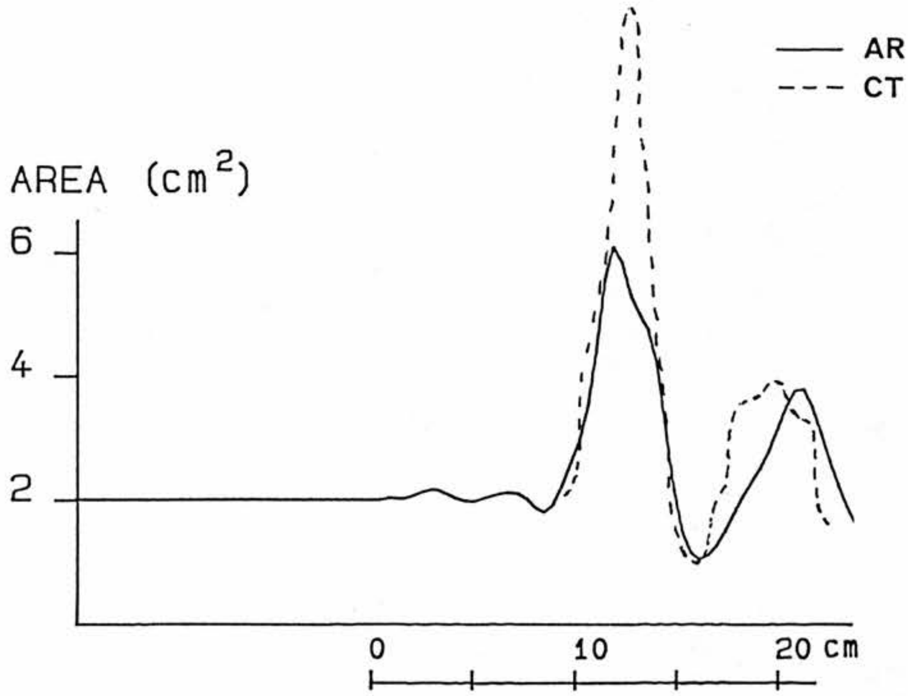

Figure 8.10: *Comparison of acoustic reflection (AR; solid line) and X-ray CT (CT; dashed line) area estimates of a human airway cast.*

of poor spatial resolution. Fortunately, our interest is primarily in pharyngeal dimensions, and accurate determination of oral sizes is not important.

8.7 Airway measurements

Although subjects cannot breathe when connected to the simple reflectometer, it is nevertheless possible to demonstrate the feasibility of the technique during breath-holding. Figure 8.11 shows a typical result. The large oral area is clearly seen, as is the area minimum in the oropharyngeal region (100mm from the incisors), and the pharyngeal peak at 130mm.

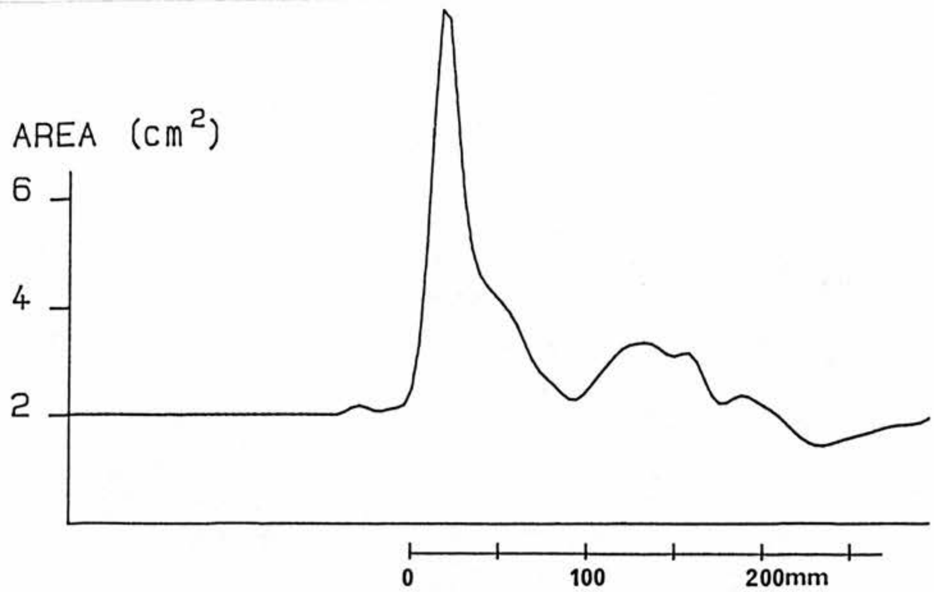

Figure 8.11: *Airway area estimation during breath holding.*

8.8 Performance

The reflectometer can measure test objects with an accuracy of typically ±10%, and a reproducibility of ±2%. These figures apply to rigid, cylindrical test objects up to 300mm long, and allow the detection of area differences as small as $0.2cm^2$.

The simple reflectometer is not really suitable for clinical use, as it requires subjects to hold their breath. In the next chapter, we describe an improved reflectometer which allows free breathing.

Chapter 9

Reflectometers for clinical use

The simple reflectometer described so far is "closed", in that there is no provision for breathing, and subjects have to hold their breath whilst airway measurements are made. Breath-holding is not only uncomfortable and impractical for anything other than short-term measurements, but it almost certainly changes the shape of the airway.

In this chapter, reflectometers that allow free breathing will be described, together with methods for making real-time airway measurements at specific points of the respiratory cycle.

9.1 Free breathing

None of the reflectometers described in the literature allows free breathing. Fredberg's equipment, for example [Fredberg et al 1980, Brooks et al 1984], requires the subject to rebreathe from a spirometer through 2m of 16mm diameter tubing. The resulting dead space of 400cm^3 is similar to the tidal volume of normal breathing, and consequently very little gaseous exchange can take place in the subject's lungs. With no mechanism for carbon dioxide (CO_2) removal, measurement sessions have to be short.

In order to extend measurements beyond a few seconds, it is necessary for the subject to breathe freely from a supply of fresh gas, and to remove the expired gas. As will be seen, the respiratory requirements of small dead space and low flow resistance conflict with the need to maintain simple acoustic geometry to avoid spurious reflections.

9.1.1 Reflectometer with side arms

Figure 9.1 shows the development of the simple reflectometer to allow free breathing from the atmosphere. Starting with the closed reflectometer at (a), we first

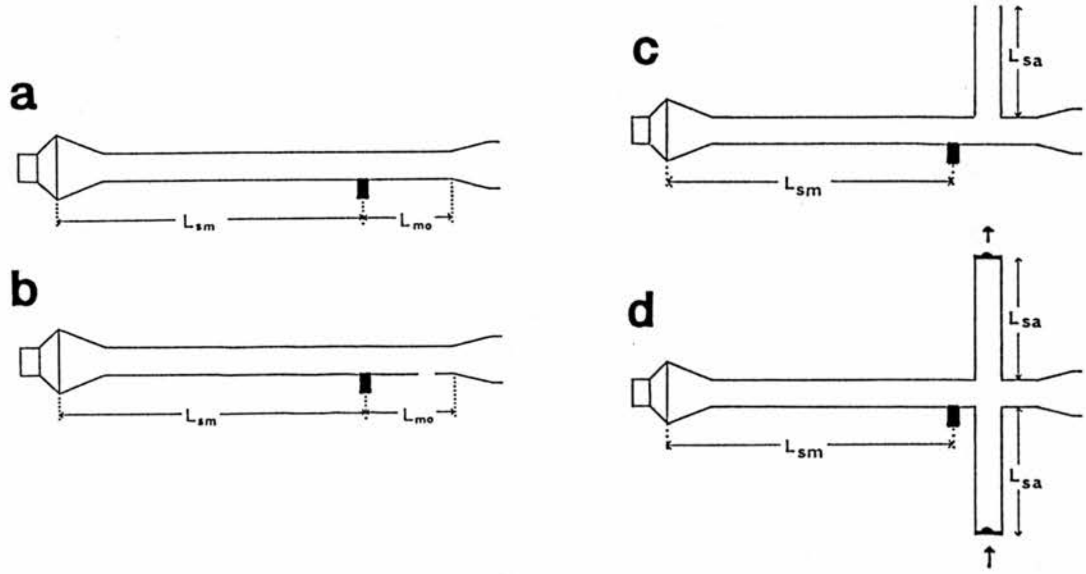

Figure 9.1: *Conceptual development of the simple reflectometer to allow simultaneous breathing and airway measurement. (a) Original reflectometer; (b) with breathing hole; (c) addition of a side arm; (d) addition of a second side arm.*

make a breathing hole in the tube wall near the mouthpiece, as shown at (b). This certainly fulfills the respiratory requirements, but makes airway measurements impossible. Acoustically, the hole appears as an open termination to the source tube, and area reconstructions beyond the hole give an indeterminately large value.

The addition of a side arm as shown in (c) limits the acoustic area increase to that of the side arm's cross sectional area for its length L_{sa}. By choosing this length to be greater than that of the airway under investigation, useful results could be achieved. The airway area is given by the difference between the reconstructed area profile and the (known) cross sectional area of the side arm. However, the respiratory dead space of the arm (for example 100cm^3 for a 50cm length of 16mm tubing) may influence breathing and airway dimensions. Attempting to minimize the dead space by reducing the bore of the side arm increases its flow resistance, and will also influence breathing.

Figure 9.1(d) shows the addition of a second side arm, and the fitting of one-way valves to the ends of both side arms. The valves ensure that air flows across the central junction, with fresh air coming in one way, and expired air being removed the other. The dead space is now reduced to the small volume between the junction and the mouthpiece. Acoustically, the airway area is found from the difference between the reconstructed area profile and the *combined* cross sectional area of the two side arms. By making both side arms longer than the airway, reflections off the valves do not reach the microphone during the critical recording period.

Implementation The simple reflectometer was modified to include side arms as described above. The 4-way junction was machined from aluminium, with care being taken to match its internal diameters to those of the source tube and side arms, to minimize spurious reflections. The side arms were made from the same 16mm tubing as the source tube, and were each 550mm long. They were terminated in standard one-way valves (Ambu type 20-1-11) as used in anaesthetic breathing circuits. The distance between the junction and the mouthpiece was 100mm, introducing a dead space of 20cm^3.

Initial validation was carried out with the mouthpiece removed, and test objects coupled instead. When the test object is simply a piece of 16mm bore tubing, the reconstructed area profile should show an increase from the 2cm^2

of the source tube to 6cm^2, this being the combined cross sectional area of the two side arms and the object. Figure 9.2 shows an actual (Ware-Aki) area reconstruction under these circumstances. Evidently, there are small mismatches

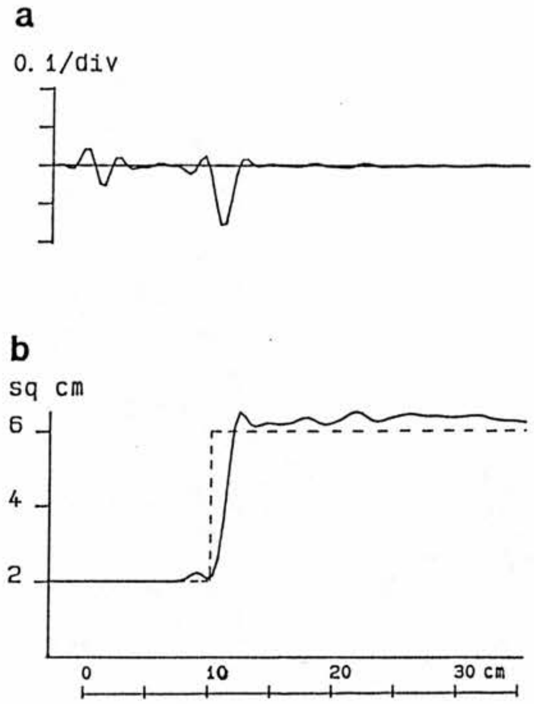

Figure 9.2: *The side arm reflectometer used to measure the cross sectional area of a length of 16mm tubing. (a) The reflectance; (b) area reconstruction. The true area profile is shown in dashed line.*

in the junction piece, which cause the area perturbations immediately after the expansion to 6cm^2, but they are not very significant. More serious was the poor reproducibility of the final area estimates, which ranged from 6cm^2 to 7cm^2.

Reproducibility was studied using Airway Model 2 (Part B) as the object. The reconstructed area beyond the junction will be 4cm^2 greater than the true area profile of the object, because of the effect of the side arms. This can be seen in Figure 9.3(a), which shows one of the better results obtained. Reproducibility, however, was disappointing. Figure 9.3(b) shows 50 consecutive measurements. Variability was quantified for the "pharyngeal" (second) peak of the model. A

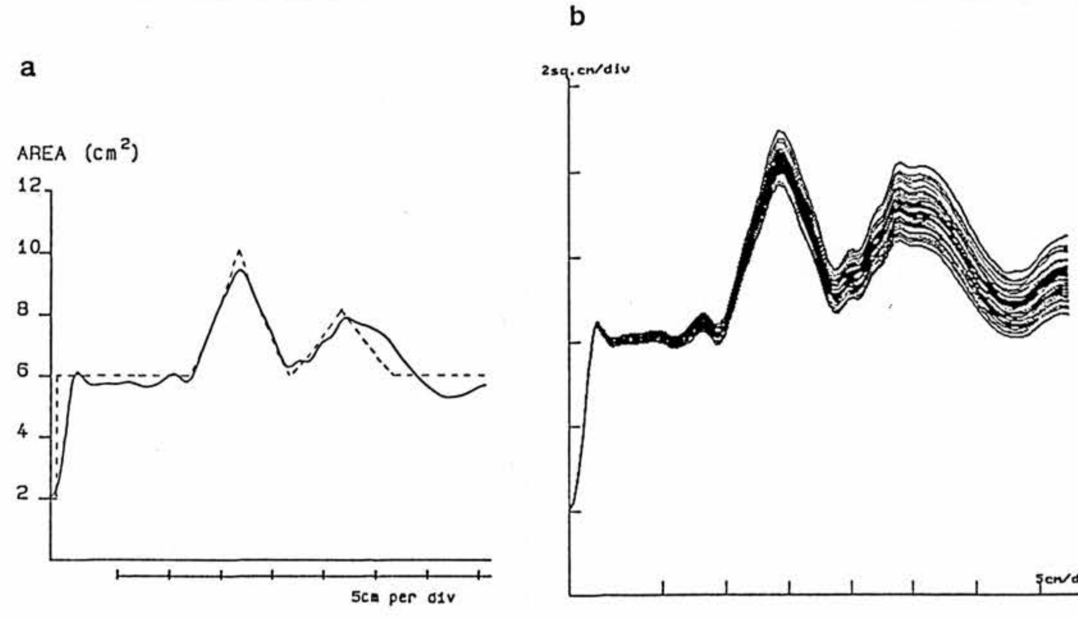

Figure 9.3: *Measurement of Airway Model 2 with the side arm reflectometer. (a) A good result; (b) variability of 50 consecutive measurements. (Note the different scales).*

comparison was made with the simple reflectometer, with and without signal averaging (of 10 measurements) and with two types of offset correction. Automatic offset correction was calculated from the deconvolved reflectance in the region between the microphone and the junction. Alternatively, fixed offset correction was used, with the value being selected empirically to give optimum reconstructed areas. The area variabilities are presented in Table 9.1. Several observations can be made from the data–

1. Averaging over 10 measurements with the other conditions being held constant reduces the variability by a factor of 1.5 to almost 4. From standard signal averaging theory, we would expect an improvement of $\sqrt{10}$ times.

2. Using a fixed offset, optimized for the particular reflectometer arrangement, yields results that have less than half the variability of measurements made with automatic offset correction.

Number averaged	Simple		Side arm	
	auto	fixed	auto	fixed
1	0.06	0.03	0.36	0.15
10	0.04	0.01	0.10	0.04

Table 9.1: *Variability of area reconstruction: standard deviations (in cm^2) of groups of 50 determinations of Airway Model 2 made using different reflectometers and offset correction methods. Each determination is either a single measurement or the average of 10 consecutive measurements.*

3. Measurements made with the side arm system are between two and six times more variable than the corresponding measurements made with the simple reflectometer.

We cannot justify the use of signal averaging when making airway measurements, so the minimum variability attainable with the side arm reflectometer is $\pm 0.15\text{cm}^2$ (single measurement, fixed offset). This is twice as large as the *worst* results with the simple reflectometer, and *four* times the typical value.

Modifying the reflectometer in this way to allow breathing has seriously compromised the reproducibility of measurements. The reason is not hard to find, and is related to the discussion of acoustic energy and branching in Sections 3.5 and 3.6. The pressure pulse from the source encounters a three-fold area increase at the side arm junction, giving an amplitude reflection coefficient of -1/2. The coefficients of energy transmission into each of the side arms and into the object itself are all equal to 1/4. That is, of the available acoustic energy, only one quarter enters the object. The reflected signal from the object splits in a similar fashion as it traverses the junction on its return journey. Only one quarter of its energy passes back into the source tube where it is recorded by the microphone. Overall, only *one sixteenth* of the original pulse energy provides information about the object. The signal to noise ratio will therefore be four times worse than with the simple reflectometer, and our results generally confirm this.

Having previously taken care to design a reflectometer system with a high signal to noise ratio, it seems a pity to accept such a drop in performance. An alternative breathing arrangement is necessary.

9.1.2 Reflectometer with a respiratory valve

To return the performance to its former level, we must dispense with the side arms. Let us reconsider the reflectometer shown in Figure 9.1(b). The problem with this arrangement is that the breathing hole appears open to the acoustic pulses, and little information is obtainable about the object. A suitable solution might be to fit a valve over the hole, closing it for a short period as each measurement is made. Admittedly, free breathing would then be momentarily interrupted, but it should be possible to limit valve closure to a small fraction of the respiratory cycle.

Two variants of respiratory valve were evaluated; the first with a simple "piston" valve, and the second with a more elaborate "shutter" valve. In both cases the valves were operated by an electromagnetic solenoid. The two systems are described below.

Piston valve A short aluminium tube was fitted in between the microphone and the mouthpiece. The tube had a breathing hole of 12mm diameter cut in the side, and the edges of the hole were coated with silicone rubber. The valve face consisted of a circular rubber pad, attached to the spindle of a solenoid (Figure 9.4(a)). Normally, a spring pulls the pad away from the hole, allowing subject breathing. When the solenoid is activated, the pad is pushed against the hole, sealing it and re-establishing the simple reflectometer geometry necessary for area measurements. The solenoid is driven by a MOSFET power transistor, which is in turn controlled by a logic level from the custom interface card. Careful adjustment was necessary to ensure that the valve face normally pulls

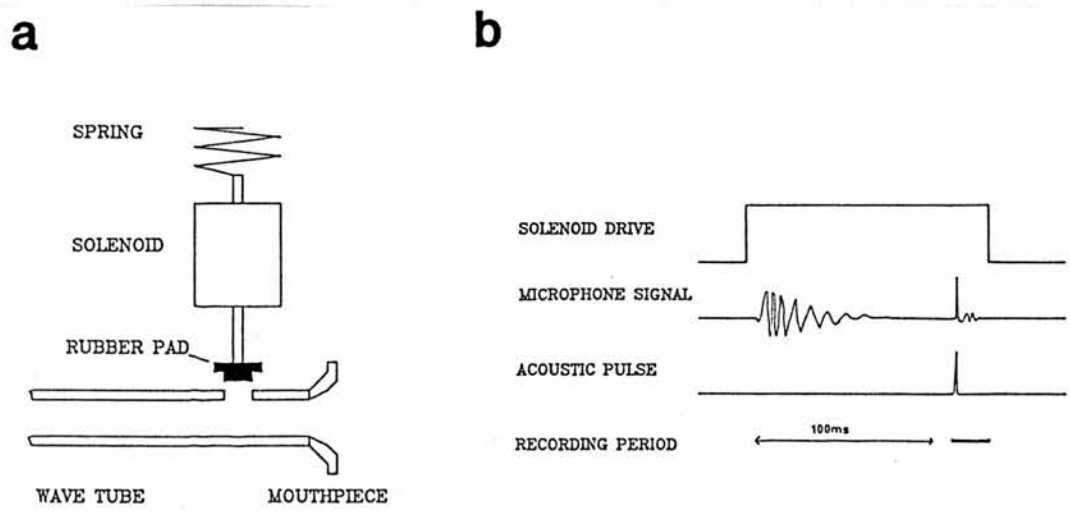

Figure 9.4: *A "piston" valve to allow breathing during measurement sessions. (a) construction of the valve; (b) timing diagram.*

sufficiently clear of the hole, and yet seals properly against the hole when acoustic measurements are made.

There is a minimum time for which the valve must remain closed, determined not by the actual acoustic measurement time (10ms), but by the need to ensure that pressure disturbances set up by the valve closure have decayed away (Figure 9.4(b)). As the piston valve closes, it pushes air ahead of it, some of which enters the reflectometer where it could degrade the acoustic measurements. Typically, the disturbance had an initial amplitude of 600mVpp, falling to the noise level of 5-10mVpp over 100ms. Added to this is the time for the valve to actually close (20ms), so that a delay of at least 120ms is necessary between activating the solenoid and making the measurement. Synchronizing measurements to the computer's timer interrupts (as described in Section 7.6.2), means that the valve is actually closed for between 100 and 150ms, a length of time which should not significantly affect breathing.

Accuracy and reproducibility of test object measurements with the piston valve reflectometer (Figure 9.5) were comparable with the simple reflectometer provided that adequate delay (greater than 150ms) was allowed between valve closure and acoustic excitation. As the delay is reduced below 100ms, variability

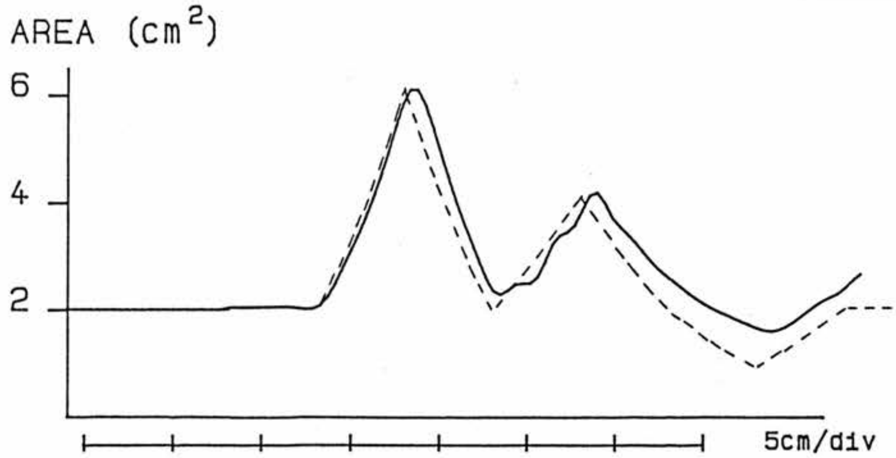

Figure 9.5: *The piston valve reflectometer used to measure Airway Model 2, parts B and C.*

begins to increase as measurements are made on the tail of the valve pressure disturbance. It was found that closure of the valve jars the reflectometer sideways. Although this is quite acceptable for the measurement of test objects, preliminary trials with a mouthpiece and human volunteers showed that the action is somewhat uncomfortable.

Shutter valve To reduce the mechanical jarring, an improved valve was designed, in which the closing action is tangential (rather than radial) to the reflectometer tube. This "shutter" valve is shown in Figure 9.6. The valve body again consists of an aluminium tube fitted between the microphone and the mouthpiece. A Teflon slide piece moves across the top of the valve body. Slots in the body and the slide piece are aligned to form a breathing route. When an area measurement is to be made, a solenoid moves the slide piece so that the slots are offset relative to one another. A return spring re-aligns the slots afterwards.

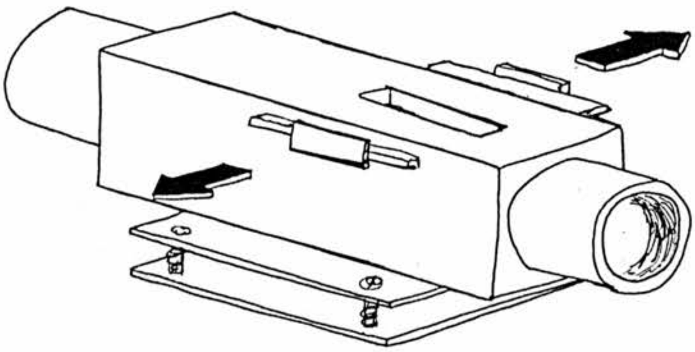

Figure 9.6: *Construction of an improved "shutter" valve. The shutter slides in the direction indicated by the arrows.*

To reduce further the mechanical jolt imparted to the reflectometer when the valve closes, a more sophisticated solenoid drive was devised. The solenoid is initially driven hard to start the slide piece moving, and then the drive is reduced to minimize the impact when the stop is reached at the end of travel. The resulting operation is gentler and quieter than the original piston valve, although for best results it was found that the delay between activation and acoustic measurement should be about the same.

This reflectometer arrangement gave satisfactory results with test objects, and the valve closure was acceptable to volunteers, and so it was rebuilt in a more permanent form. A typical airway result is shown in Figure 9.7.

9.2 Reducing the analysis time

It was stated in Section 8.1.3 that the time taken for a complete measurement and reconstruction cycle is approximately 5 seconds[1]. This time is for frequency-domain deconvolution (using 256-point FFTs) and Ware-Aki reconstruction over

[1]An approximate measurement can be made in 1 second.

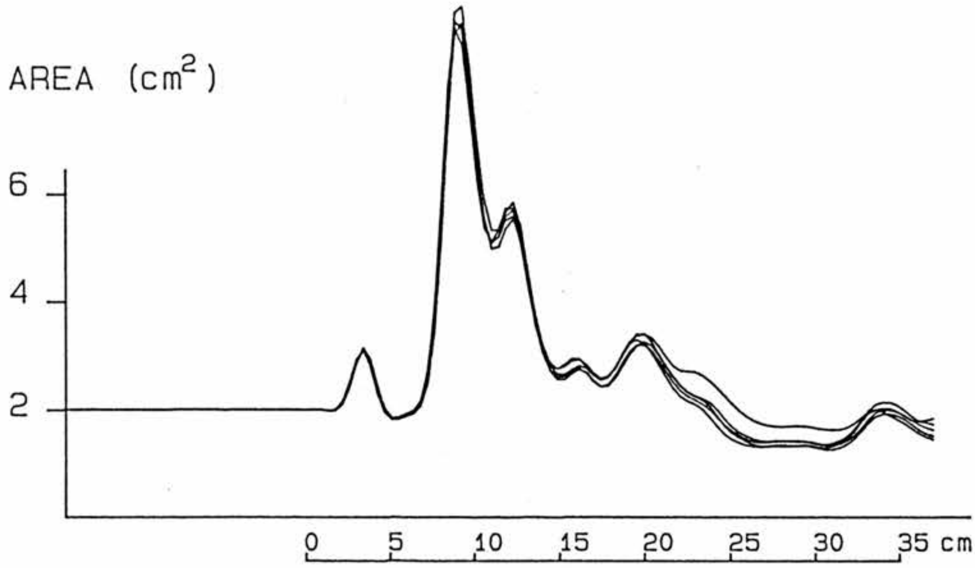

Figure 9.7: *Typical airway result with the shutter valve reflectometer. The small area expansion between 1cm and 5cm is due to the mouthpiece. The position of the subject's incisors coincides with the 5cm mark.*

80 data points, using single precision floating-point arithmetic and a maths coprocessor on a 10MHz computer system. Moving to a 16MHz computer (Dell 316SX) reduced this time to 3s, of which approximately 2s is accounted for by the deconvolution.

Using iterative time domain deconvolution instead (as described in Appendix B, Section B.2.3), the computationally demanding step is the convolution of the incident pulse shape with the latest estimate of the reflectance, for comparison with the actual reflection signal. Generally, this convolution requires N^2 multiplications, where N is the length of the data sequences, but this figure can be reduced in practice. For example, the incident pulse shape used in the present work has a significant amplitude for only 30 data points, and the reflection signal of interest lasts only about 150 data points. The remaining 30×150 convolution takes approximately 400ms, and the complete deconvolution (5 iterations) requires 2s.

Using either method of deconvolution, the complete cycle time is thus approximately 3s. This would be acceptable for clinical work, but can hardly be termed "real time". It is significantly longer than the fundamental limits set by the acoustic measurement time itself (10ms) and the valve closure time (100ms).

No further reduction in processing time seemed possible by software methods, so two hardware solutions were evaluated; the first being a commercially available general purpose Digital Signal Processing (DSP) card, and the second a custom DSP card specifically designed to carry out (de)convolution.

9.2.1 Commercial DSP card

A commercial DSP card (Vector 32C; Surrey Medical Imaging Systems) was acquired at a cost of approximately £2000, and fitted in an expansion slot in the computer. The card is based on the AT&T DSP32C floating point processor, and comes with a library of subroutines that can be called from Turbo Pascal. The subroutines are written in the processor's own code, and provide very rapid ways of carrying out *vector* operations on data arrays; that is, each element of the data array is manipulated in the same way. Data is downloaded from the main program to the card, and the results are read back after computation. Among the subroutines available are Fast Fourier Transforms which allow frequency domain deconvolution to be carried out in less than 200ms. However, the nature of the Ware-Aki algorithm does not permit such a spectacular increase in speed. The data points comprising the reflectance have to be treated separately, with the polynomials F and G (Section 3.3) being updated in between calculating each new area point.

With the board installed, the time for a complete measurement, analysis and display cycle is slightly over 1 second, which is sufficiently fast for "real time" work.

9.2.2 Custom (de)convolution card

The high cost of commercial general purpose DSP cards (£2000 for the example studied) prompted a search for suitable alternatives.

For specific applications, more restricted hardware is sometimes available at much lower cost. This is the case with time domain deconvolution, for which integrated circuit DSP filters can form the necessary convolution[2] at each iteration. The device selected for evaluation was the Inmos IMSA100. This device is structured as a 32-stage filter, with the filter weights being loaded into a set of coefficient registers, and the signal data being loaded sample by sample into an input register. The resulting multiplied and accumulated filter output is read from an output register. The device appears as a set of memory locations, and no programming is necessary. The IMSA100 was installed on a prototype card together with suitable control circuitry (Appendix D), and fitted in the computer.

The card cost approximately £200 to complete, and its performance is comparable to the far more expensive commercial DSP card. It allows a 5-iteration time domain deconvolution to be carried out in 200ms, with a complete measurement and area reconstruction cycle taking approximately 1 second. Again, no great speed improvement was possible with the Ware-Aki algorithm.

9.3 Synchronization of airway measurements

Given that airway measurements can be made in real time, and during essentially normal breathing, it will be clinically valuable to make the measurements at specific parts of the respiratory cycle. Synchronization of measurements with respiration will enable, for example, investigation of airway dimensions as lung volume changes.

To monitor respiration non-invasively, we measure the pressure p_{mpc} developed in the mouthpiece by the air flowing through the resistance R_{resp} of the

[2] Mathematically, filtering and convolution are identical.

breathing slots. We can write–

$$p_{mpc} = \dot{Q} R_{resp}$$

where $\dot{Q}$ is the airflow. This is simply a form of Ohm's law. We assume that the resistance is independent of flow, and is the same for inspiration and expiration. The pressure is then linearly related to the flow, and can be used to determine respiratory phase.

The pressure at the mouthpiece end of the valve body was sensed by a differential transducer (Sensym SCX05DN) connected via a length of 3mm bore plastic tubing. The other side of the transducer diaphragm was open to the atmosphere. The small cross sectional area (0.07cm^2) of the connecting tube did not affect acoustic measurements. The transducer was connected to a differential amplifier (gain nominally 20000, frequency response DC to 3Hz), with the gain adjusted to give an ouptut of 4V/cmH$_2$O (40mV/Pa). The sensitivity could be reduced to 1V/cmH$_2$O (10mV/Pa) for monitoring deep breathing. Figure 9.8(a) shows a typical pressure signal. When breathing normally through the mouthpiece and open valve, the negative pressure developed on inspiration is approximately 0.5cmH$_2$O (50Pa), with a similar positive pressure on expiration. There is superimposed "noise" of about one tenth of this amplitude, which is absent during breath-holding. It is probably due to turbulent airflow.

Circuitry was devised to track the maximum and minimum pressure amplitudes, with triggering occurring as the instantaneous pressure passes a threshold level set in between the extremes. The output of the trigger circuitry is connected to the computer's interface card, and initiates an acoustic measurement.

Figure 9.8(b) shows the pressure waveform when airway measurements are made at the beginning of expiration. Closure of the valve momentarily increases R_{resp} to a high value so that pressure "spikes" are produced. Similarly, Figure 9.8(c) shows the spikes associated with measurement during inspiration. The acoustic impulse itself is not discernible on these traces, because its frequency content is blocked by the low pass filtering of the transducer amplifier.

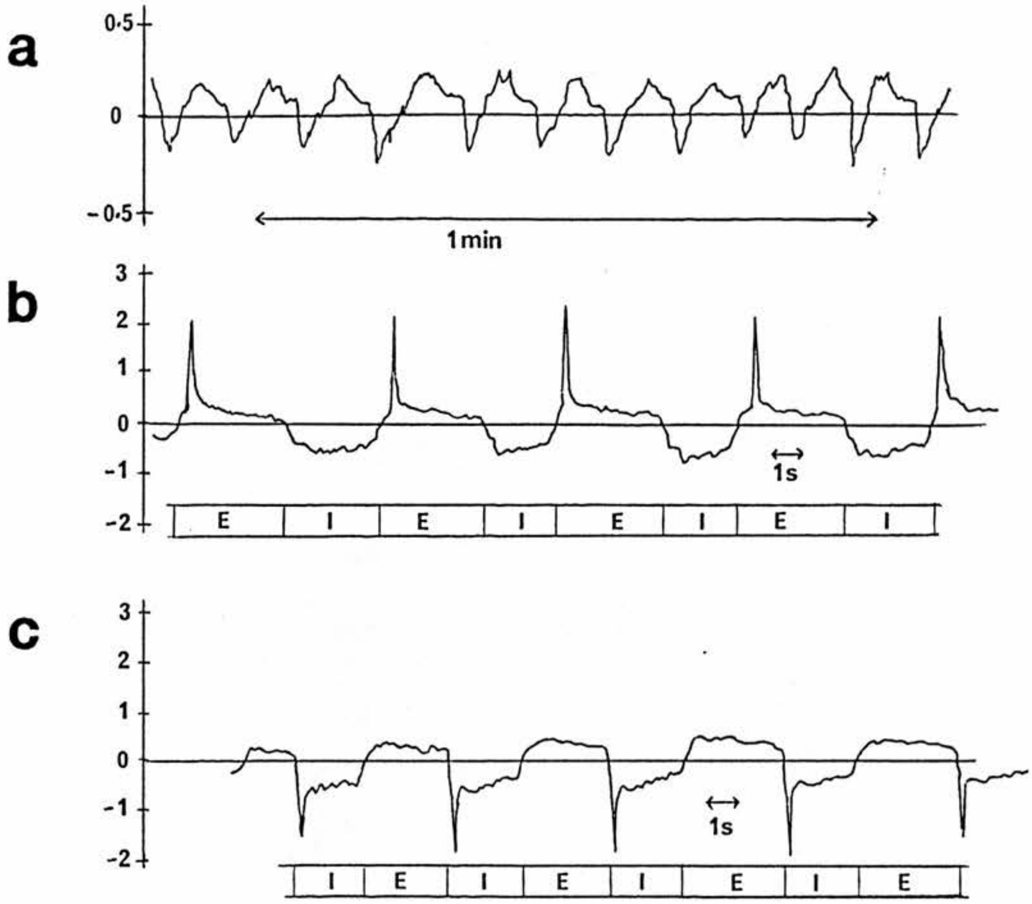

Figure 9.8: *(a) The pressure waveform developed at the mouthpiece during normal breathing, and when area measurements are made at the beginning of expiration (b) or inspiration (c). Note different scales for (a). Pressure units are* cmH_2O *(*$1cmH_2O=100Pa$*). I–inspiration: E–expiration.*

The fully developed clinical reflectometer is shown in Figure 9.9. Airway measurements made at specific parts of the respiratory cycle are discussed in the next chapter.

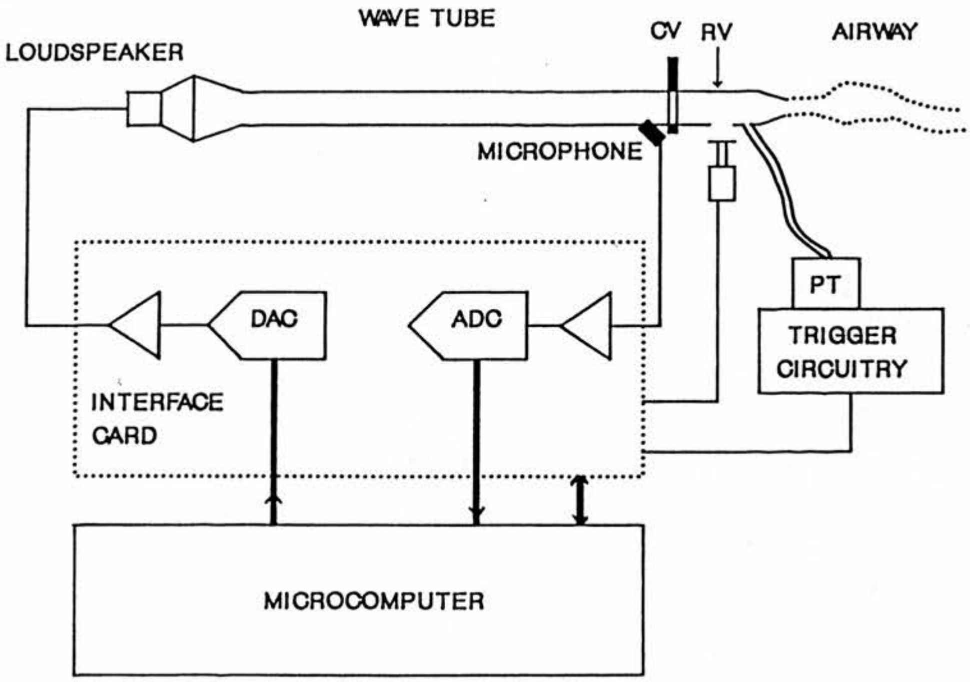

Figure 9.9: *The fully developed clinical reflectometer system. CV–calibration valve; RV–respiratory valve; PT–pressure transducer.*

Chapter 10

Preliminary trials with human volunteers

Having described the development of an acoustic reflectometer suitable for clinical use, we will now present some preliminary volunteer measurements. These pre-clinical trials are intended to assess the feasibility of the technique. Unless otherwise stated, measurements were carried out on healthy volunteers having no history of airway disease other than the common cold.

Figure 10.1 is a simplified diagram of the anatomy of the upper airways. The nasal cavities open via the nasopharynx into the oropharynx. The oropharynx is continuous forwards with the oral cavity, and downwards to the hypopharynx. The epiglottis is attached to the anterior wall of the airway, forming the margin between oropharynx and hypopharynx. The hypopharynx terminates at the vocal cords in the glottal region. The roof of the mouth is made up of the hard palate, extending posteriorly into the soft palate which acts as a moveable "flap". The combined oropharynx and hypopharynx are sometimes collectively referred to as the pharynx.

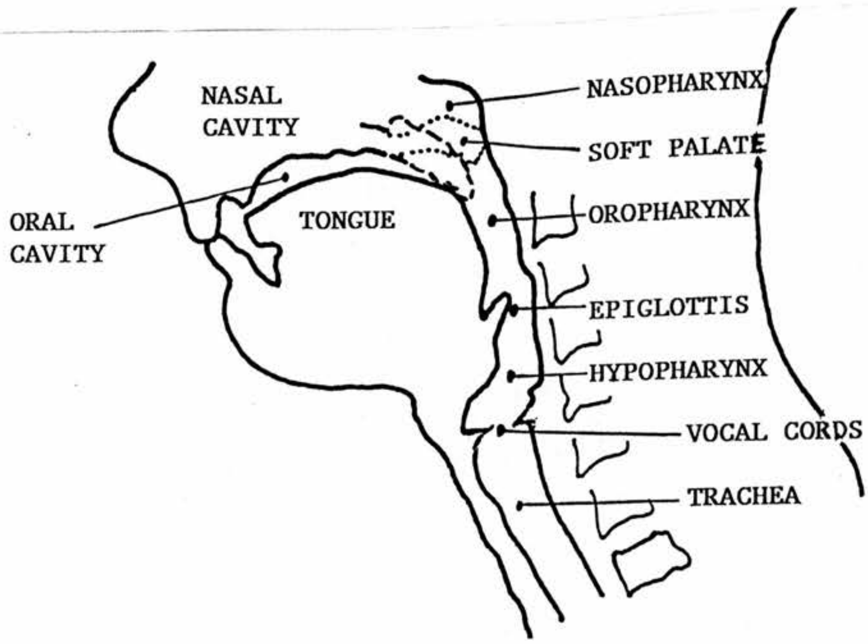

Figure 10.1: *Simplified anatomy of the upper airway, seen in a mid-line sagittal view. Soft palate raised (dotted line); lowered (dashed line).*

10.1 Effect of soft palate

Figure 10.2 shows midline sagittal sections of a subject's head and neck, imaged with Magnetic Resonance Imaging (MRI) with the subject breathing through the nose (left), and through a mouthpiece (right). During normal nasal breathing, the nasopharynx communicates with the pharynx to allow the passage of air to and from the lungs. The rear of the soft palate rests on the back of the tongue, closing off the oral cavity from the pharynx. Clearly, airway measurements cannot be made through the mouth under these circumstances, and Figure 10.3 (dotted line) shows how the reconstructed area falls to zero at the back of the mouth.

When the subject breathes through a mouthpiece (Figure 10.2 (right)), the soft palate rises and contacts the posterior wall of the nasopharynx. The oral cavity then communicates with the pharynx, and the nasopharynx is closed off.

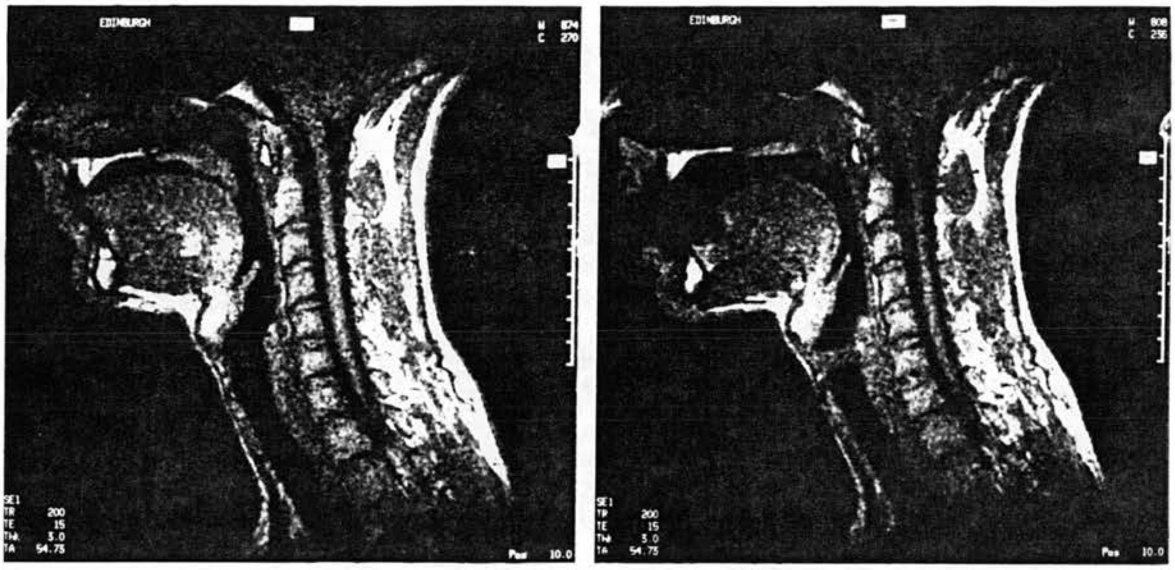

Figure 10.2: *Midline sagittal MRI images of a subject breathing through the nose (left), and through the mouth (right).*

Under these conditions, satisfactory airway measurements can be made by the oral route. Figure 10.3 (solid line) shows the corresponding area reconstruction. Unless otherwise indicated, all airway measurements have been made with the subjects breathing orally. Naïve subjects are instructed to breathe as if through a snorkel, or to imagine they are inflating a balloon. A return to nasal breathing is immediately apparent from the real-time display of the area profile.

An intermediate mode of breathing is possible, in which the soft palate lies in between the two extreme positions. This corresponds to "mixed" nasal and oral breathing, and leads to false area measurements (Figure 10.3 (dashed line)) because the acoustic pulse splits at the back of the mouth, entering both the pharynx and the nasopharynx. The cross sectional areas of the two routes appear combined, and cannot be separated. This condition is not always easy to detect, but the acoustic pulses may be heard emerging through the subject's nose.

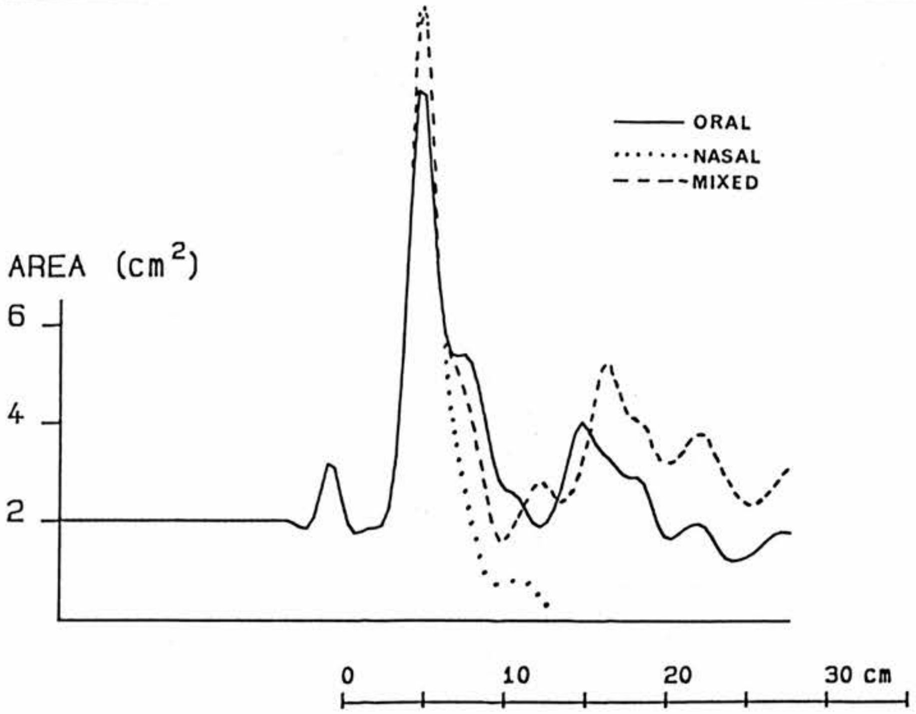

Figure 10.3: *Acoustically measured airway areas for a subject breathing through the nose (dotted line), through the mouth (solid line), and in an intermediate "mixed" mode (dashed line).*

10.2 Identification of features

Several methods are available to help identify anatomic features in the airway area profiles, a labelled example of which is given in Figure 10.4. Consciously moving the soft palate, as discussed above, shows that the large peak sometimes extending to over 10cm^2 is indeed the mouth. This is readily confirmed by pressing on the floor of the mouth, thereby reducing the size of the peak. The first (small) peak of 3cm^2 in this example is caused by not fully pushing the mouthpiece onto the reflectometer.

Knowing the position of the incisors and the distance scale allows a direct comparison with the sagittal MRI image of Figure 10.2(right), from which the approximate position of the oropharynx, hypopharynx and vocal cords can be determined. During acoustic measurements it is possible to have the subject

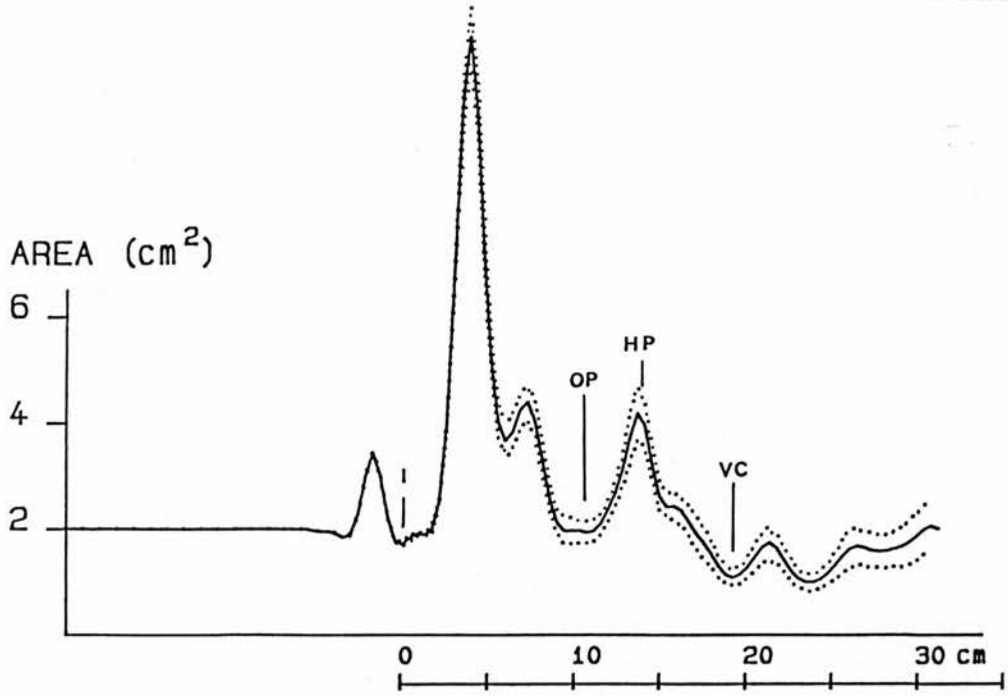

Figure 10.4: *An airway area profile with anatomic features identified. I–incisors; OP–oropharynx; HP–hypopharynx; VC–vocal cords. The dotted lines indicate the standard deviation limits of 10 measurements.*

consciously move the vocal cords as if about to speak (Figure 10.5), and their closing confirms that (acoustically) the cords appear to be 17-18cm from the incisors.

10.2.1 Interpretation of the North American literature

There are several publications relating to the acoustic reflectometer developed in Boston by Fredberg and colleagues [Fredberg et al 1980] and used in Toronto by Hoffstein and colleagues [Rivlin et al 1984, Bradley et al 1986, Brown et al 1987]. In most of this literature, subjects use custom moulded mouthpieces designed to fill the anterior part of the oral cavity. Confusingly, the authors refer to all the airway beyond the mouthpiece as "pharynx". This incorrect definition thus

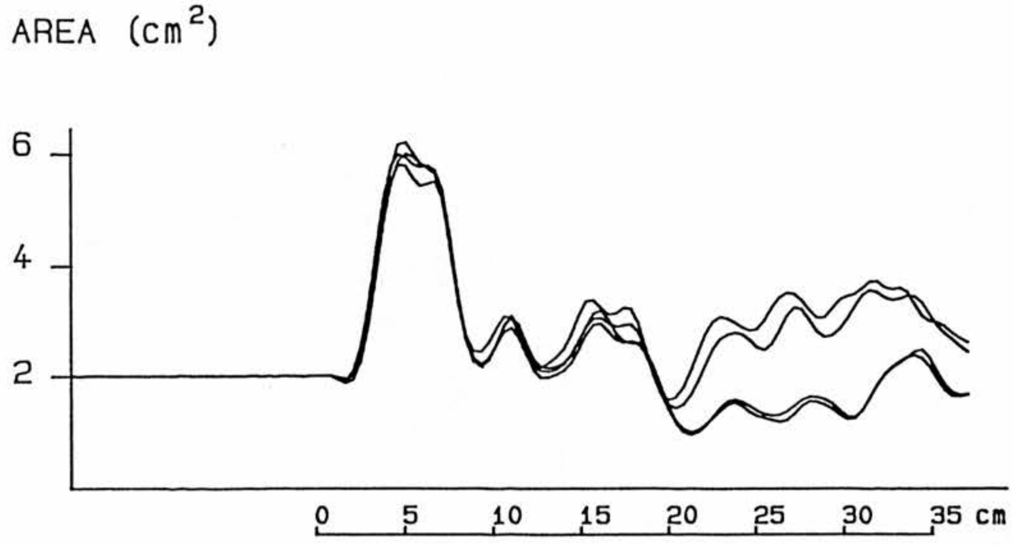

Figure 10.5: *Consecutive airway area measurements made whilst closing the vocal cords.*

includes part of the oral cavity in addition to the oropharynx and hypopharynx, and this should be borne in mind when reading the literature. In particular, two resultant peculiarities permeate the publications;–

1. No mouth is shown in their airway profiles.

2. Peak "pharyngeal" areas as great as 8cm^2 are shown.

Evidently, the "pharyngeal" areas actually refer to the posterior part of the oral cavity. Consequently, little reliance can be placed on the associated discussions of "pharyngeal" size and compliance.

10.3 Effect of mouthpiece

Readily available commercial mouthpieces of two types were used in the present work. Both types have a circular section that fits over the end of the reflectometer, but otherwise they are quite different. The first type (Ohmeda) extends about 30mm into the subject's mouth, where it has an elliptical section of 32mm by 8mm (Figure 10.6 (left)). The second mouthpiece is a "SCUBA" type (Ambu) (Figure 10.6 (right)), similar to that used by [Rubinstein et al 1987]. Its flange (85 × 40mm) fits between the teeth and lips, and the subject bites gently on the two tabs. Figure 10.7 shows airway profiles of a subject measured using the two

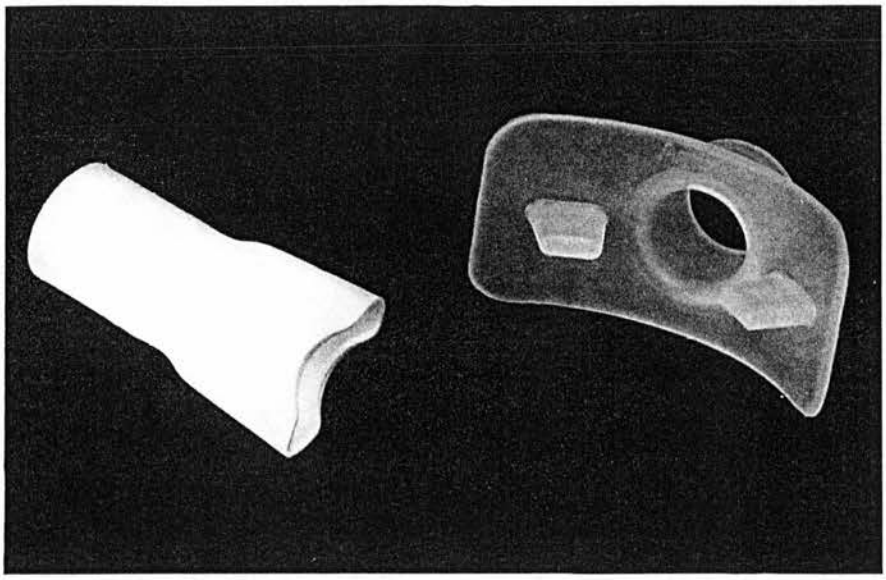

Figure 10.6: *The two mouthpieces used during trials. Left–Ohmeda type; right–Ambu SCUBA type.*

different mouthpieces. With the Ohmeda mouthpiece (a), the mouth appears larger and extends further back, without a sharp oropharyngeal minimum. This probably occurs because the mouthpiece forces the teeth apart, and extends well into the mouth. The gag reflex holds the tongue and soft palate clear of the mouthpiece. Pushing the mouthpiece a further 20mm into the mouth might be expected to reduce the oral cavity area by bypassing the cheek spaces, but in fact the gag reflex actually *increases* the observed areas beyond the mouthpiece. This probably occurs with the bulky custom mouthpieces used by previous researchers.

The mouth and oral cavity are able to assume a more natural posture with

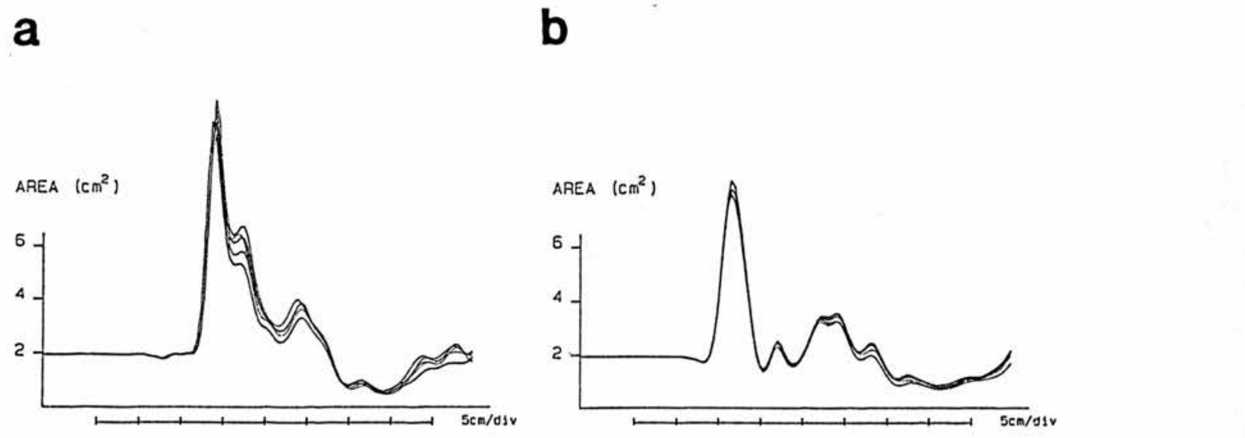

Figure 10.7: *Airway areas measured with (a) Ohmeda mouthpiece, and (b) Ambu "SCUBA" type mouthpiece.*

the Ambu SCUBA mouthpiece (Figure 10.7(b)), because it does not protrude behind the teeth. Once inserted correctly, the SCUBA mouthpiece forms a more effective seal at the mouth.

Judging from Figure 10.7, airway comparisons should be made with the same type of mouthpiece if meaningful results are to be obtained. [Rubinstein et al 1987] did not find a significant difference between using custom moulded and SCUBA mouthpieces to estimate mean pharyngeal dimensions in a group of 10 subjects. However, individual subject data are not presented, and the entire airway between the end of the mouthpiece and the glottis is averaged to produce a "pharynygeal" cross sectional area.

10.4 Reproducibility

The within-run reproducibility (mean $\pm$ standard deviation for ten measurements) for one subject is indicated in Figure 10.4. The standard deviation of pharyngeal measurements is seen to be approximately 0.2cm^2 at the oropharyngeal minimum (2cm^2) and 0.5cm^2 at the hypopharyngeal maximum of 4.1cm^2. These figures give a coefficient of variation (CV) of approximately 10%, identical to that reported by [Brooks et al 1984].

Day-to-day reproducibility was studied in four subjects on each of twenty-one days, with measurements being made at the same time (early afternoon) each day. SCUBA type mouthpieces were used for this study, and measurements were made at the beginning of inspiration. Figure 10.8 shows the results. Coefficients

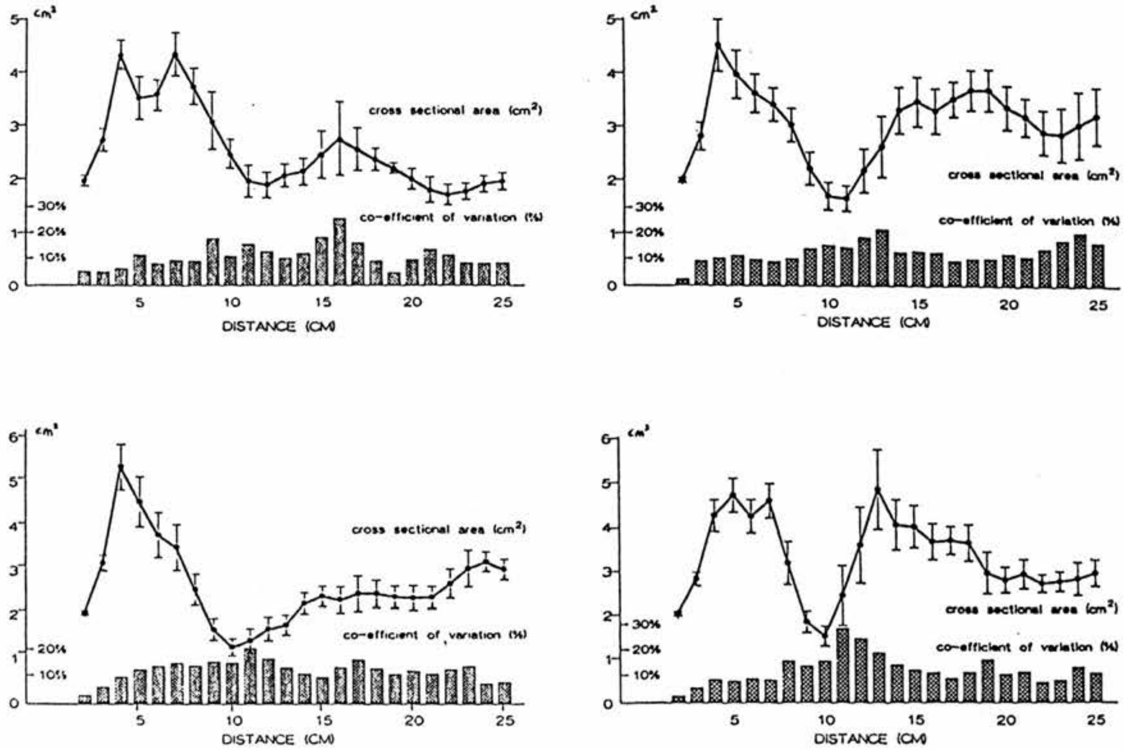

Figure 10.8: *Day-to-day reproducibility of airway measurements in four subjects over 21 days. Curves: mean ± standard deviation; histograms: coefficient of variation.*

of variation were typically 10%-20%, depending on the airway segment. The greatest variation usually occurred in the oropharyngeal region, and was probably due to movement of the soft palate and the tongue base, rather than an artefact of the measurement technique. The variation in hypopharyngeal area was typically 10%-15%.

These variabilities are acceptable in a clinical physiological technique, and are comparable to those reported by [Brooks et al 1984].

10.5 Comparison with MRI

As discussed in Chapter 1, X-ray CT and MRI are the only techniques capable of making airway measurements for comparison with acoustic area measurements. Not wishing to expose normal volunteers to ionizing radiation, CT was ruled out. Acoustic reflection estimates of airway areas have not previously been compared with MRI measurements, and acoustic estimates of *pharyngeal* areas have not previously been validated against any technique [Hoffstein and Fredberg 1991].

10.5.1 Preliminary experiment

In a preliminary experiment, a subject's airway was measured with acoustic reflectometry and then with MRI. In both cases, the subject was lying supine and breathing quietly through an Ohmeda mouthpiece. A Siemens 1 Tesla Magnetom was used with a "neck" coil to produce images which were everywhere perpendicular to the longitudinal axis of the airway, with 10mm spacing and 3mm slice thickness. 18 images covered the airway from the lips to the vocal cords. Selected images shown in Figure 10.9 are; (a) a coronal section through the mid oral cavity, showing sinuses and nasal cavities above the hard palate; (b) an oblique section through the oropharynx, just behind the tongue; (c) a transverse section through the pharynx showing the tip of the epiglottis; and (d) a transverse section at the level of the vocal cords.

Airway cross sectional areas were estimated manually from hard copies of the MRI images, with repeated determinations revealing an uncertainty of ±25%. An area profile was drawn for comparison with the acoustic profile (Figure 10.10). There is reasonable overall agreement between the acoustic and MRI data, with the limited resolution of the acoustic technique tending to broaden features. The acoustically large area at the rear of the oral cavity may be caused by the acoustic pulse finding alternative paths around the mouthpiece, which then appear "added to" the true area. The acoustic positions of the hypopharynx and vocal cords are shifted 20-30mm caudally relative to the MRI data, and are not as well defined.

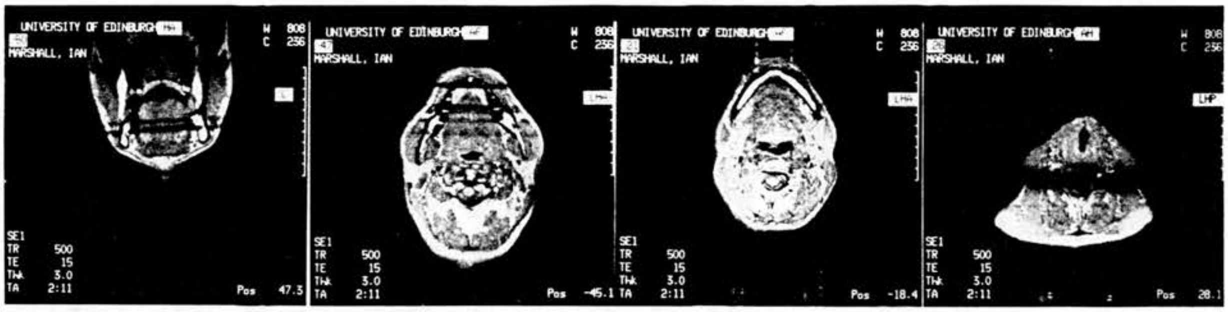

Figure 10.9: *Selected MRI images, taken perpendicular to the airway axis. (a) oral cavity; (b) oropharynx; (c) tip of epiglottis; (d) vocal cords.*

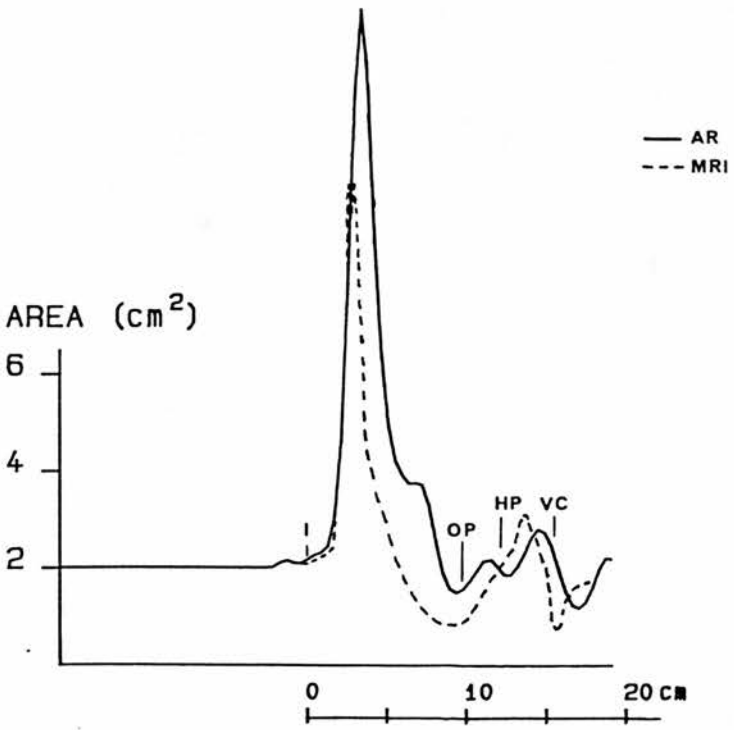

Figure 10.10: *Comparison of acoustic (solid line) and MRI (dashed line) airway measurements.*

The estimates of the hypopharyngeal area maximum agree well, with 2.9cm^2 from the acoustic measurement and 3.2cm^2 from MRI.

10.5.2 Full study

In an extended study, 11 normal volunteers were measured acoustically and then with MRI. SCUBA type mouthpieces were used, with the subjects again lying supine and breathing quietly. 26 contiguous coronal slices 5mm thick covered the airway from the lips to the posterior wall of the pharynx. A T1-weighted collection with one acquisition was used, and image analysis was carried out using the "Analyze" package (Mayo Foundation, Rochester, NY). Areas in the mouth were taken directly from the coronal images, whilst for pharyngeal measurements the data was reconstructed to give images perpendicular to a line joining the uvula and the midpoint of the vocal cords. In all images, the pixel size was 1.09mm square. Areas were determined from "regions of interest" grown automatically from seedpoints positioned by the operator. Despite the level of automation, data analysis was time consuming (taking typically 1 hour per subject) and the resulting area measurements were highly dependent on the thresholds used. Area uncertainties up to ±50% were not uncommon. [D'Urzo et al 1988] reported coefficients of variation in the range 5-33% for repeated estimates of glottal areas from CT images, so our figure is not excessive.

The mean distance from the incisors to the vocal cords for all 12 subjects studied (these 11, plus the one from the preliminary MRI experiment) was 147±15mm by MRI, and 180±11mm acoustically. The difference was best accounted for by an "offset" of 30-35mm occurring in the mouth, rather than by a scaling correction.

When acoustic and MRI area traces were aligned at the vocal cords, it was apparent that acoustic measurement tended to smooth the area changes along the airway (Figure 10.11)*. Thus the oropharyngeal and glottal areas were generally overestimated compared with MRI, and the hypopharyngeal maximum was underestimated. Multiplying the deconvolved reflection by an empirical factor of 1.3 improved the fit, presumably by compensating for airway losses. Greater

*The apparent area changes in the MRI data probably contain a high percentage of estimation noise.

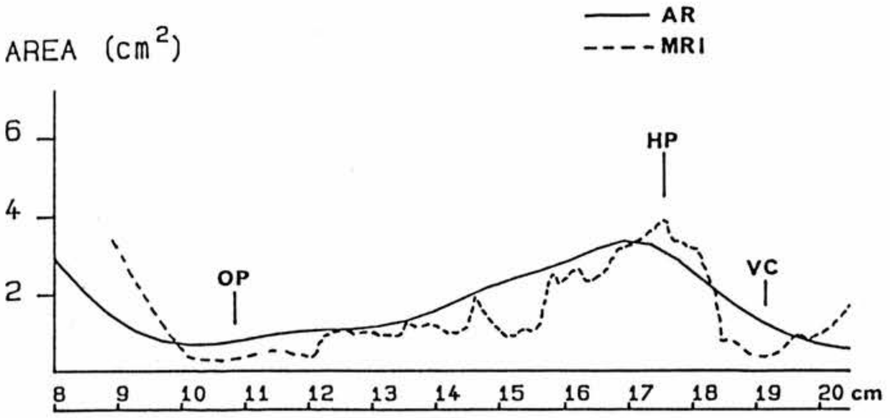

Figure 10.11: *Acoustic (solid line) and MRI (dashed line) estimates of the airway area of a subject, aligned at the vocal cords. OP–oropharynx; HP–hypopharynx; VC–vocal cords; distances measured from the incisors.*

factors caused the area reconstructions to become unstable and physically meaningless. A statistical analysis of the results was carried out by identifying the oropharynx, hypopharynx and glottis on the MRI traces. The mean cross sectional areas of 1cm segments of the airway were calculated for both the MRI and the acoustic profiles for each subject. Additionally, the total pharyngeal volume (from oropharynx to vocal cords) was calculated for both sets of measurements. Individual measurements showed discrepancies of typically 20% to 50% between the corresponding MRI and acoustic estimates. The mean results for the 10 subjects for whom a full analysis was possible[1] are given in Table 10.1, together with the significance (p) values for the differences between corresponding MRI and acoustic reflectometry (AR) estimates. The "smoothing" effect of acoustic measurement is apparent from the table, particularly in the 30% underestimation

[1] A dental pin caused extensive MRI image artefacts for one subject.

	oropharynx	hypopharynx	glottis	volume
MRI	0.9±0.5	2.6±0.9	1.1±0.4	14.9±6.0
AR	1.0±0.3	1.6±0.6	1.3±0.3	13.2±2.7
MRI-AR	-0.04±0.42	0.92±1.18	-0.22±0.36	1.6±5.8
p	0.77	0.04	0.09	0.40

Table 10.1: *Means and standard deviations of airway areas (in cm^2) and pharyngeal volumes (in cm^3), estimated by MRI and acoustic reflectometry (AR) : paired t-test, n=10.*

of hypopharyngeal areas. This is the only measure which is significantly different (in the statistical sense) between the MRI and acoustic estimates. MRI and acoustic estimates of oropharyngeal and glottal areas agree within 20% and 30% respectively, and are not significantly different. The MRI and acoustic estimates of total pharyngeal volumes agree very well (within 6%), since integrating over the whole airway removes the effect of smoothing.

Although many would regard MRI as the "Gold Standard" for airway measurement, the problems of determining Regions Of Interest areas are substantial, even when the process is partially automated. A lower bound can be set on the area uncertainties by considering the image pixels defining the airway wall (Figure 10.12). The wall passes through approximately $2\pi r/\Delta x$ perimeter pixels, each of area Δx^2, where r is the radius of the airway and Δx is the length of the pixel side. Since we cannot tell what proportion of these pixels lies inside the airway, the irreducible area uncertainty is

$$\pm\frac{1}{2} \times \frac{2\pi r}{\Delta x} \times \Delta x^2 = \pm\pi r \Delta x$$

compared with an actual area of $A = \pi r^2$, ie a proportional uncertainty of $\pm\Delta x/r$ or $\pm\Delta x/\sqrt{A/\pi}$. With a pixel side length of 1.09mm, this expression evaluates to $\pm 19\%$ for $A = 1\text{cm}^2$ and $\pm 14\%$ for $A = 2\text{cm}^2$. This uncertainty is inherent in the discrete nature of the image, and would apply even if the contrast between the airway and the surrounding tissue were infinite.

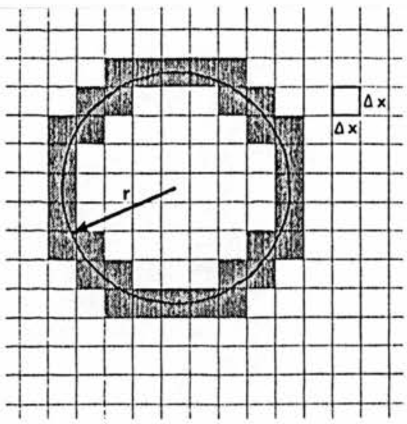

Figure 10.12: *The intrinsic uncertainty in area estimation caused by the pixel size.*

To estimate the actual repeatability of image analysis, the MRI data of 6 subjects were analysed twice by the same observer, and 3 subjects were also analysed by an independent observer. Mean intra-observer variabilities ranged from 9% to 64%, whilst mean inter-observer differences ranged from 38% to 68%. These figures are somewhat greater than the 0% to 33% reported by [Rodenstein et al 1990], and may be due in part to our use of reconstructed images.

It is interesting to note that the spatial smoothing of acoustic measurements has its counterpart in the temporal smoothing of MRI measurements. The imaging time of several minutes inevitably means that the data is averaged over many complete breaths, and therefore includes all phases of respiration. It is important that the subject remains still for this time, ideally without swallowing. With the acoustic technique, on the other hand, it is possible to make several measurements within a single breath, allowing the investigation of airway size with lung volume, and with little inconvenience to the subject.

10.6 Effect of posture

10.6.1 Head position

The effect of head position was studied in a seated subject breathing quietly through an Ohmeda mouthpiece. Measurements were made at various times throughout one day, with the subject's head and neck either in a comfortable neutral (null) position, hyperextended, or hyperflexed. Measurements were synchronized with respiration, and made either at the start of inspiration or at the start of expiration. Typical results are shown in Figure 10.13. Table 10.2 sum-

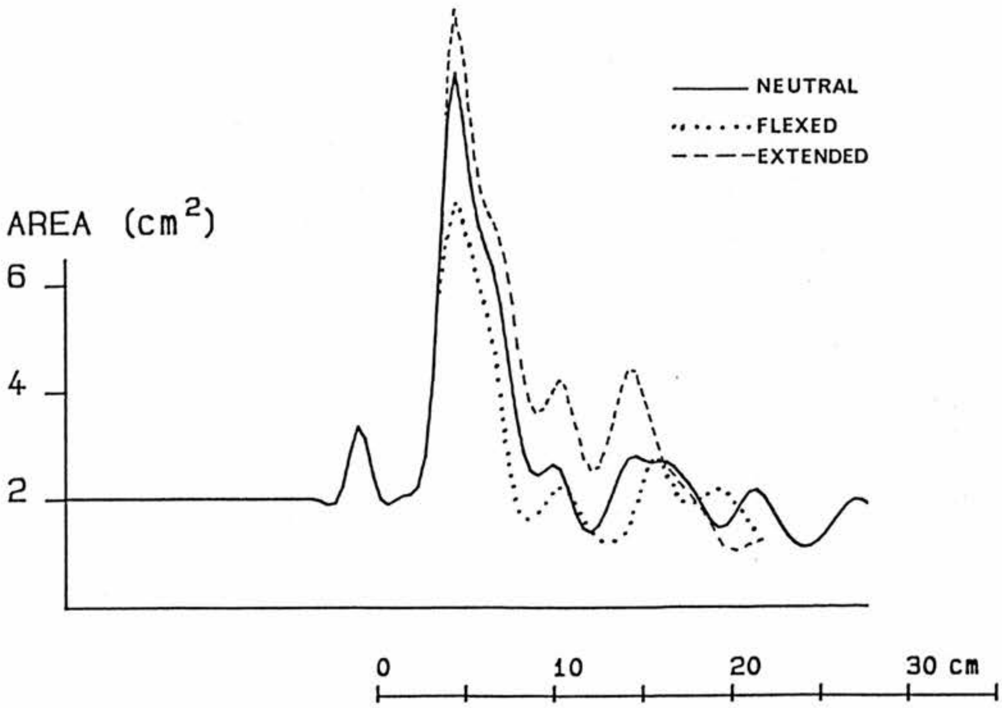

Figure 10.13: *The effect of head position on airway measurements made at the start of inspiration.*

marizes the mean values of the oropharyngeal minimum and hypopharyngeal maximum areas for all the experiments. The extended and flexed measurements are compared with the neutral measurements, and the statistical significance (p) values given. From this limited study, it can be seen that the airway areas

	OP	p	HP	p
INSP				
extended	2.9±0.9	0.01	4.9±1.2	0.01
neutral	1.4±0.2	-	2.7±0.6	-
flexed	1.2±0.2	0.23	3.0±0.2	0.31
EXP				
extended	2.9±1.0	0.04	4.6±1.3	0.23
neutral	1.8±0.6	-	3.8±1.0	-
flexed	1.1±0.2	0.01	3.6±0.2	0.58

Table 10.2: *Means and standard deviations (in cm^2) of oropharyngeal minimum (OP) and hypopharyngeal maximum (HP) areas for various head positions and two phases of respiration. The significance (p) values refer to differences from the corresponding neutral result.*

measured with the head in the hyperextended position are generally significantly greater than in the neutral position. The area differences between neutral and hyperflexed head positions are not normally significant. These findings were confirmed in a trial of 15 normal volunteers. We conclude that hyperextension of the head and neck causes a significant increase in pharyngeal area, whereas hyperflexion does not cause a significant change. This differs from the results of [Rubinstein et al 1987] (but see the discussion in Section 10.2.1 regarding the incorrect definition of "pharynx" used in the literature) in that they found no significant change with hyperextension, and a significant decrease with hyperflexion.

We found that modest angles ($\pm 20^o$) of head extension and flexion had no significant effect on pharyngeal areas, so the measurement technique does not require careful control of head position provided that the subject is in a comfortable, fairly neutral posture.

10.6.2 Seated versus supine

Clinically, it is important to investigate the behaviour of the pharynx when the subject is lying supine. 15 normal volunteers had airway measurements made when seated and when supine, at each of three different lung volumes–

Functional Residual Capacity (FRC) The lung volume after normal expiration. Measurements were made at the start of the next inspiration.

Total Lung Capacity (TLC) The lung volume after maximal inspiration. Measurements were made at the start of the next expiration.

Residual Volume (RV) The lung volume after maximal expiration. Measurements were made at the start of the next inspiration.

Ohmeda mouthpieces were used in this trial. The mean data for the 15 subjects is presented in Table 10.3, which compares seated and supine measurements of the oropharyngeal minimum and hypopharyngeal maximum areas for the three lung volumes. At TLC and RV, pharyngeal areas are seen to be significantly smaller

	Seated	Supine	p
FRC OP	1.2±1.0	0.8±1.0	0.28
HP	1.9±1.6	1.4±1.3	0.36
TLC OP	2.2±1.5	1.0±0.9	0.01
HP	3.1±1.8	1.4±1.4	0.01
RV OP	1.7±1.1	0.7±0.7	0.01
HP	2.5±1.9	1.0±1.1	0.01

Table 10.3: *Means and standard deviations (in cm^2) of oropharyngeal minimum (OP) and hypopharyngeal maximum (HP) areas for 15 subjects at three lung volumes. The significance (p) values refer to differences between seated and supine measurements.*

in a supine position than when seated. The differences are not significant at FRC.

10.7 Effect of respiratory phase

The effect of respiratory phase on airway measurements was studied explicitly in a study of 9 volunteers. Subjects were seated with the head in a neutral position, and breathed quietly through an Ohmeda mouthpiece. The respiratory pressure developed in the mouthpiece was used to trigger measurements at either the start of inspiration or the start of expiration. The results, summarized in Table 10.4, show that no significant differences were found between areas measured during

	Inspiration	Expiration	p
OP	1.9±0.5	1.8±0.4	0.64
HP	3.8±1.0	3.9±0.9	0.83

Table 10.4: *Means and standard deviations (in cm^2) of oropharyngeal minimum (OP) and hypopharyngeal maximum (HP) areas for 9 subjects. The significance (p) values refer to the differences between measurements on inspiration and expiration.*

inspiration and expiration. The pressures developed in the mouthpiece for this quiet breathing were usually about $\pm 0.2 cmH_2O$ (20Pa), with spikes of up to $\pm 2 cmH_2O$ (200Pa) during valve closure.

Very deep breathing in one subject did reveal significant area differences with respiratory phase. When breathing hard between TLC and RV, mouthpiece respiratory pressures of 2-3cmH_2O (200-300Pa) were generated, with valve closure peaks of $\pm 8 cmH_2O$ (800Pa). Averaged over 11 breaths, the oropharyngeal minimum area was $1.3 \pm 0.2 cm^2$ on deep inspiration, and $1.9 \pm 0.3 cm^2$ on deep expiration ($p < 0.001$). The corresponding figures for the hypopharyngeal maximum were $2.5 \pm 0.3 cm^2$ on deep inspiration, and $3.3 \pm 0.5 cm^2$ on deep expiration

($p<0.001$). These 30% changes in pharyngeal areas are similar to those reported by [Brown et al 1986] during slow expirations from TLC to RV in normal subjects, but the usual comments apply regarding their definition of pharynx.

In our experiments it is impossible to be sure that the apparent changes in pharyngeal area are strictly related to lung volume. It may be that the respiratory "intention" pressure (developed when the valve closes) acts on the compliant airway walls. This might cause distension during expiration, when a positive pressure of up to 8cmH_2O (800Pa) is obtained in the airway. Similarly, during inspiration, the negative intention pressure may reduce the pharyngeal area regardless of lung volume. [Brown et al 1985] attempted to measure pharyngeal compliance in snorers by having them perform isovolume manoeuvres against a distally occluded airway. Expiratory manoeuvres producing airway pressures of 10cmH_2O (1000Pa) resulted in a 36% increase in "pharyngeal" area in a group of 7 subjects. Inspiratory manoeuvres producing pressures of -10cmH_2O (1000Pa) resulted in a 20% decrease.

These aspects could be studied further by comparing forced and slow breathing between TLC and RV. It might then be possible to separate the effects of lung volume dependence and pharyngeal compliance. Lung volume could be monitored by means of a low dead-space, integrating flowmeter fitted over the respiratory valve.

10.8 Sleep apnoea patients

The reflectometer has been used successfully with a number of patients having sleep apnoea and related disorders. It is too early to draw any conclusions from the results so far, since proper age-, weight- and sex-matched trials are necessary. As an example of patient data, Figure 10.14 shows the change in hypopharyngeal size resulting from change of posture in a child with suspected sleep apnoea. The peak pharyngeal area when seated ($3.4\pm0.1cm^2$) falls to ($2.2\pm0.1cm^2$) when supine, both measurements being made at FRC. This highly significant change (p<0.0001) may indicate an unstable pharynx with a tendency to occlusion.

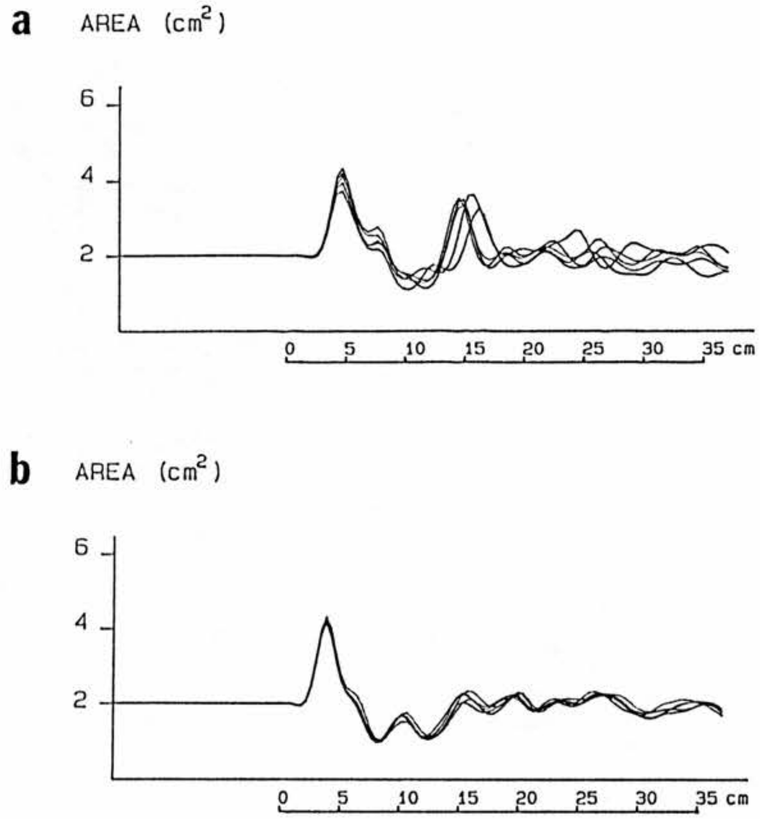

Figure 10.14: *Airway measurements made (a) in the seated position and (b) in the supine position. The subject was a child with suspected sleep apnoea. Note the highly significant reduction in hypopharyngeal area on lying down.*

10.9 Nasal measurements

In principle, acoustic reflectometry can be applied to any air-filled cavity. Hilberg and colleagues [Hilberg et al 1989, Grymer et al 1989] used the equipment developed by Jackson [Jackson et al 1977] to estimate nasal size in normal volunteers and in patients with septal deviation. They measured through one nostril at a time, with the contralateral nostril open, and were able to demonstrate reasonable correlation ($r = 0.94$) with X-ray computed tomagraphic (CT) scans. Although the nasal cavities are highly convoluted and the propagation of acoustic impulses is unlikely to be strictly one-dimensional, it thus appears possible to estimate nasal cavity dimensions acoustically. The technique is referred to as acoustic rhinometry.

10.9.1 Pharyngeal estimation through the nose

Pharyngeal measurements made through the nose, if feasible, might enable airway monitoring during sleep, which would be of great interest in the study of sleep apnoea.

A fundamental difficulty with trying to interpret the area profiles *beyond* the nasal cavities arises because of the 3-way junction where the two nasal cavities meet the nasopharynx. This is in addition to the oropharyngeal junction controlled by the soft palate. Other than by introducing packing material, there is no way of simplifying the geometry at the back of the nose, and measurements of the pharyngeal region must be regarded with some suspicion. Despite this, [Elbrønd et al 1991] were able to demonstrate some correlation ($r = 0.71$) between actual and acoustically determined volumes of adenoidal tissue removed from a group of 20 children.

In the present work, the feasibility of pharyngeal measurement by the nasal route was investigated as follows. Subjects were coupled to the reflectometer, one nostril at a time, with the contralateral nostril either open or pressed closed. They were asked to breathe either nasally or orally whilst acoustic measurements were made. Left-right differences in nasal cavity areas were clearly demonstrated. However, breathing mode and contralateral nostril termination had no significant effect on the later part of the area profiles, as would be expected if the nasopharynx were being measured properly. The most likely explanation is that severe attenuation and dispersion of the acoustic pulse occurs in the convoluted, mucus-lined nasal cavities, so that little information is received from beyond them.

When one subject was administered xylometazoline decongestant to clear the nose, breathing mode and contralateral nostril termination did affect the area profiles (Figure 10.15). During nasal breathing, the nasopharynx communicates

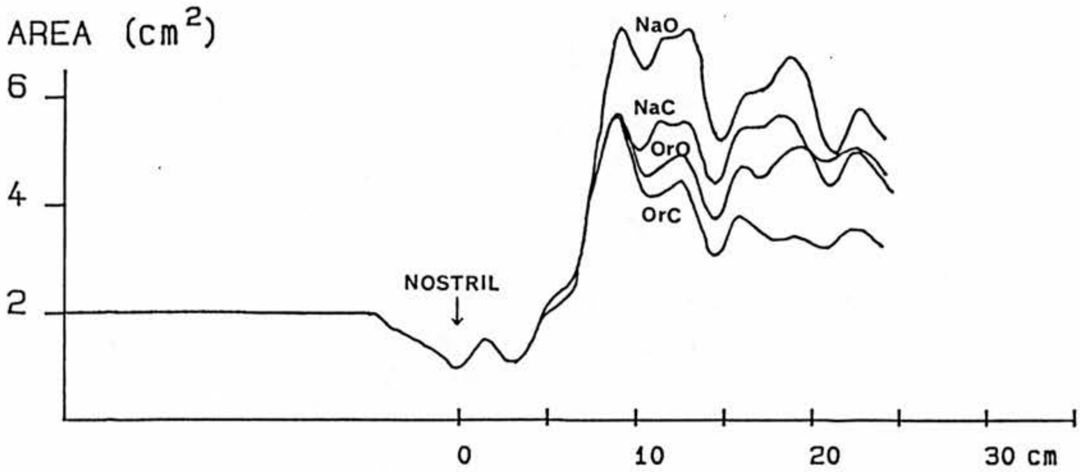

Figure 10.15: *Acoustic measurements made through the right nostril following administration of decongestant. The subject is breathing orally (Or) or nasally (Na), with the left nostril open (O) or closed (C).*

with the oropharynx, and so the airway area measured through the nose should include the oropharynx. When breathing orally, however, the soft palate closes off the nasopharynx so that the oropharynx is not "seen" through the nose. The area profiles of Figure 10.15 correctly show smaller areas for oral breathing than for nasal breathing. Some of the acoustic pulse energy inevitably enters the contralateral nasal cavity, and will escape through the nostril if open. This should appear on the profiles as a large area increase at the open nostril. Closing the contralateral nostril should remove this large increase. Figure 10.15 indeed shows smaller areas when the contralateral nostril is closed rather than open, but the differences are not as marked as might be expected.

Apart from these general trends, the precise shape of the nasal airway profiles cannot be readily explained by the anatomy of the nose and nasopharynx. It did not prove possible to associate "pharyngeal" measurements made nasally with the more reliable measurements made orally.

10.9.2 Nasal physiology

To demonstrate that *changes* in nasal areas are readily measured, a subject prone to mild hayfever was studied on a dry summer day. Normal antihistamine treatment was withdrawn 24 hours prior to the study. Acoustic measurements of the nose were made in the morning when the subject had been indoors for several hours. Without Ethics Committee approval (but having obtained informed consent), the subject was then taken outdoors and exposed to hedgerow pollens until hayfever symptoms were fully developed. Further nasal measurements were made at this time, and at 15, 35 and 50 minutes following administration of xylometazoline decongestant drops. Ten measurements (using an approximate reconstruction method) were made through the left and right nostrils at each time, and the averaged results normalized to their initial values. Figure 10.16 shows the averaged area profiles through the left nostril, whilst normalized area measurements at 50mm from the nostrils are given in Table 10.5.

In interpreting the data, it should be borne in mind that the standard deviation of the measurements amounted to 5-10% of the initial (resting) values. The 19% reduction in mean nasal area accompanying hayfever symptoms is therefore highly significant. 15 minutes after treatment with decongestant drops, the nasal area has returned to its original value. The maximum relief from symptoms was felt soon afterwards, and by 35 minutes the nasal area was slightly larger than its initial value (106%). 50 minutes after treatment, the mean nasal area is slightly less than the initial value, although the decrease is not statistically significant.

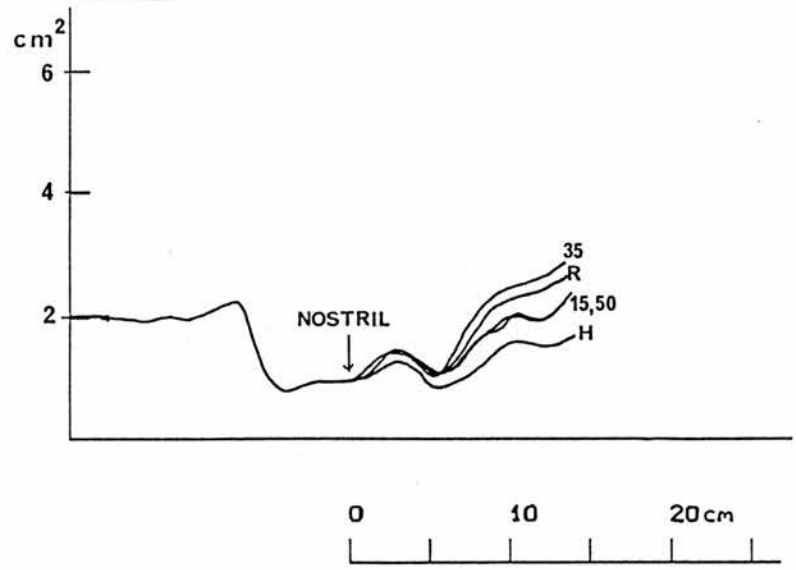

Figure 10.16: *Estimated area profiles of the left nasal cavity, measured at rest (R), with hayfever symptoms (H), and at 15, 35 and 50 minutes following treatment with decongestant.*

	Left	Right	Mean
Resting	100%	100%	100%
Hayfever	73%	88%	81%
15mins	100%	100%	100%
35mins	100%	112%	106%
50mins	91%	100%	96%

Table 10.5: *Estimated area of the nasal cavities at 50mm from the nostrils, measured at rest, with hayfever, and at 15, 35 and 50 minutes following treatment with decongestant. The areas are expressed as percentages of their resting values, and are the averages of groups of ten measurements.*

This study shows that acoustic rhinometry could be a valuable technique in the rapid, non-invasive assessment of nasal physiology.

10.10 Measurements on anaesthetized subjects

Airway narrowing leading to reduced ventilation is a serious risk during anaesthesia. The effect of head extension in anaesthetized subjects has been shown by lateral radiographs [Morikawa et al 1961], and acoustic reflectometry might be useful in investigating this common problem.

The effect of head position on airway size was studied in supine subjects before and immediately after anaesthesia was induced using intravenous propofol. Ambu SCUBA type mouthpieces were used to ensure a good acoustic seal even when subjects were unconscious. Breathing is usually by the oral route in anaesthetized subjects, as can be demonstrated by the absence of airflow at the nostrils. Dramatic increases in pharyngeal dimensions were observed in many subjects when the head and neck were extended. Figure 10.17 shows an example in which the oropharyngeal minimum area increases from 0.8cm^2 to 1.8cm^2

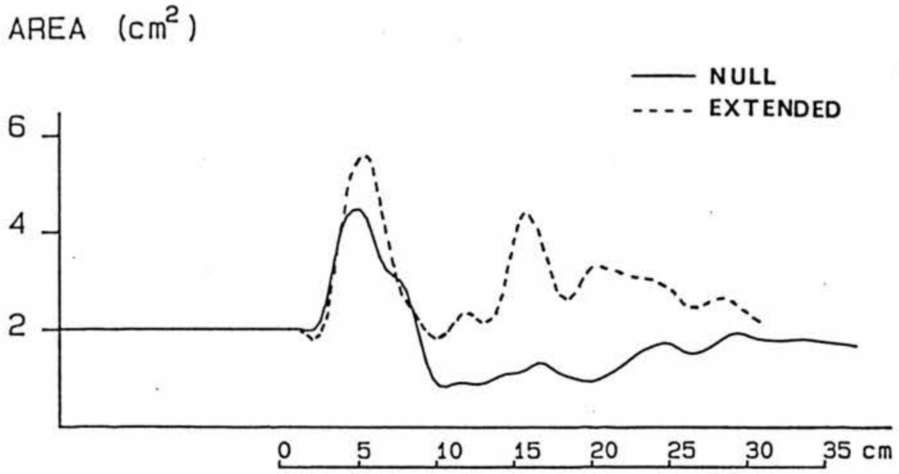

Figure 10.17: *Airway areas measured in an anaesthetized subject, with the head and neck in the null position (solid line), and extended (dashed line).*

on extension. There is a corresponding increase from 1.3cm^2 to 4.4cm^2 in the hypopharyngeal maximum area.

Acoustic reflectometry used as a monitor of airway patency during anaesthesia might be able to give advance warning of impending hypoxia, and hence reduce the risk of brain damage.

Chapter 11

Acoustic reflectometry with an arbitrarily short source tube

The research objectives stated in Chapter 1 have been met. Another innovation made during the course of development was the use of a short source tube.

We have so far used a source tube of sufficient length $L_{sm} + L_{mo}$ to enable temporal separation of the incident pulse from the reflected waveform, as discussed in Chapter 7. In this chapter, we will show how suitable signal processing allows the source tube to be made arbitrarily short. The analysis of this situation has not previously appeared in the literature [Marshall 1992b].

11.1 Non-reflecting source

As discussed in Section 7.2, the source tube is conventionally made longer than the object so that that part of the object's reflection function sufficient for area reconstruction can be recorded before any multiple reflections arrive at the microphone. This is a way of simulating a *non-reflecting* source. As we have seen, it is then relatively straightforward to deconvolve the measured reflection with the original pulse shape to obtain the object's reflectance function and hence the area profile.

Whilst the need for a source tube that is longer than the object is acceptable in the present application, it may become inconvenient in others. In a study of brass musical instruments, Watson [Watson 1989, Watson and Bowsher 1988] had to use a source tube consisting of several metres of plastic hose in order to record the complete reflection response of trombones and trumpets. Attenuation of the acoustic pulses, particularly of the high-frequency components, is inevitable under such circumstances, and measurement accuracy is degraded. It is pertinent to ask whether there is an alternative method.

In electrical transmission line reflectometers, source reflections are readily avoided. The electrical source is *matched* to the transmission line by making its internal impedance equal to that of the line; typically 50Ω [Oliver 1964, Harpham 1990]. Energy travelling back towards the source is absorbed without further reflection, and the source thus appears non-reflecting. Unfortunately, no practical acoustical matched source is available, although some form of active cancellation is a possibility.

11.2 Multiple reflections and dereverberation

If the source tube of an acoustic reflectometer is made shorter than the object length, multiple reflections obscure the required object reflection response. This is a *reverberation* problem. Methods exist for performing dereverberation (separating overlapping signals and reflections) under certain specialized conditions. We will briefly discuss the two best known examples of dereverberation, and show that they are not readily applicable to acoustic reflectometry.

11.2.1 Echo cancellation

In communication channels, multiple reflections (echoes) are frequently encountered, and it is usually required to eliminate the echoes, leaving the original signal. Often, the echoes are simply delayed and attenuated versions of the original signal, and are represented by $\alpha\delta(t-\tau)$, where τ is the delay and α is the attenuation. In the *cepstral*[1] domain $C(t)$, they appear as delta functions at multiples of the delay time, and are readily identified and removed provided that the cepstrum of the signal S is shorter than the delay time (Figure 11.1(a)). Performing the inverse cepstral transform then yields the original signal with the

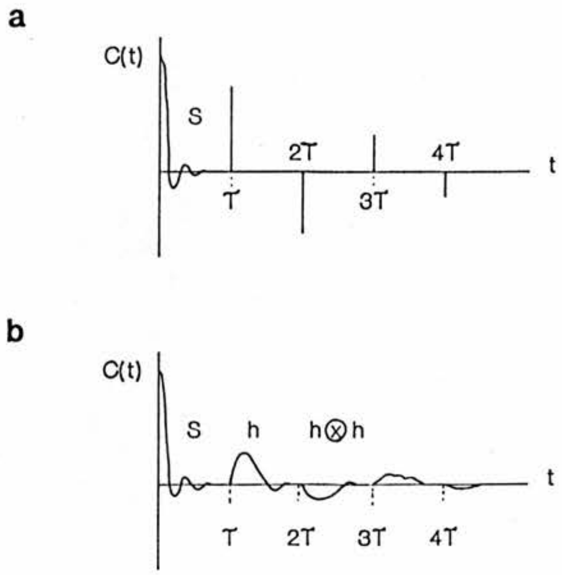

Figure 11.1: *Dereverberation in the cepstral domain C(t). (a) A signal with an echo at time τ appears with a series of delta functions at multiples of the delay time. (b) Multiple convolutions (⊗) of an echo function h(t) at successive multiples of the delay time.*

echo cancelled [Hassab 1978, Randall and Hee 1981]. This method is still applicable if the echo function is of the form $\alpha h(t-\tau)$, where $h(t)$ is some impulse response causing the echo to be a *distorted* version of the original. In the cepstral domain, the function $h(t)$ appears at time τ, the function $h(t)$ convolved with itself $(h(t)\otimes h(t))$ at time 2τ, and so on, the echo function becoming progressively

[1] The cepstrum of a signal is defined as the inverse Fourier transform of the complex logarithm of the Fourier transform of the signal.

more convolved with itself at multiples of the delay time (Figure 11.1(b)).

In reflectometry, however, we must recover the function $h(t)$ itself, since it contains the information required to reconstruct the object area. For cepstral dereverberation to work, it is then necessary that both the signal cepstrum S *and* $h(t)$ be shorter than the delay time τ, so that separation is possible [Randall and Hee 1981]. However, it is under precisely these conditions that we could simply record the acoustic reflection directly, as described above for a non-reflecting source. Cepstral dereverberation is thus seen to offer no advantages for acoustic reflectometry, and does not enable us to use a short source tube.

11.2.2 Marine seismology

Mention should be made here of another important class of dereverberation problems. In marine seismology, multiple reflections between the seabed and the surface (with round-trip delay τ) obscure the seismogram of the layers underlying the seabed. In this case, the problem is greatly simplified by the nature of the reflections. There is a large impedance mismatch between air and water, so that the surface reflection coefficient is approximately -1. Similarly, the reflection coefficient at the seabed can be characterized by a constant k, because of the large mismatch there. As a result, the multiple reflections have a particularly simple form, and it is shown in standard texts [Robinson et al 1986] how a filter such as $(1+kz^{\tau})^{-2}$ can perform dereverberation in the z-domain. In the acoustic reflectometer case, we cannot make any such assumptions, and there is no simple filter that can be applied.

11.3 General reflectometry analysis

We now analyse the acoustic reflectometer from first principles, and develop a method for making measurements when the source tube is arbitrarily short. Figure 11.2 shows the geometry of the acoustic reflection technique, together with the important dimensions. We restate below the definitions of L_{sm} and

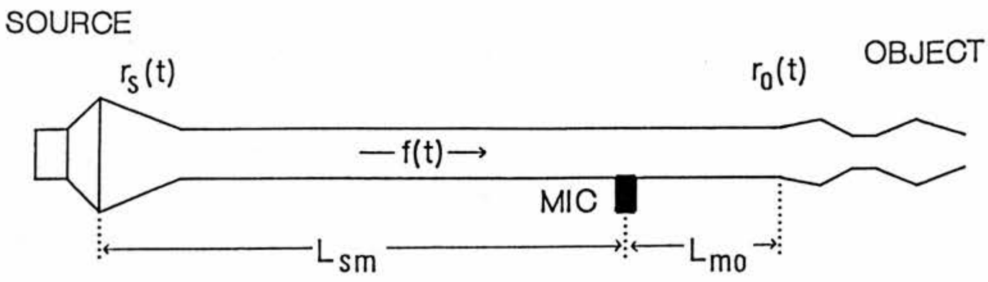

Figure 11.2: *An acoustic reflectometer showing the features relevant to the present analysis. See text for definitions.*

L_{mo}, and make some new definitions—

L_{sm} The source to microphone distance, with two-way travel time $T_2 = 2L_{sm}/c$, where c is the velocity of sound.

L_{mo} The microphone to object distance, with two-way travel time $T_1 = 2L_{mo}/c$.

$f(t)$ The pressure pulse waveform produced by the source, which has a Fourier transform of $F(\omega)$. We define $t = 0$ to be the time at which the incident pulse first reaches the microphone.

$r_s(t)$ The source reflection response, with a Fourier transform of $R_s(\omega)$. For a given geometry, this term may be taken to include the effects of attenuation over the distance L_{sm}.

$r_o(t)$ The required object reflectance function (input impulse response), with a Fourier transform of $R_o(\omega)$.

The signal $m(t)$ observed at the microphone consists of the incident pulse travelling to the right, followed (after the microphone-object round trip delay T_1) by the first reflection from the object. This latter is given by the object reflectance convolved with the incident pulse. Further components in the observed signal consist of alternate reflections off the source and the object, and the composite signal is given by the infinite series—

$$\begin{aligned} m(t) &= f(t) + f(t) \otimes r_o(t) \otimes \delta(t - T_1) + f(t) \otimes r_o(t) \otimes r_s(t) \otimes \delta(t - (T_1 + T_2)) \\ &\quad + f(t) \otimes r_o(t) \otimes r_s(t) \otimes r_o(t) \otimes \delta(t - (2T_1 + T_2)) \\ &\quad + f(t) \otimes r_o(t) \otimes r_s(t) \otimes r_o(t) \otimes r_s(t) \otimes \delta(t - (2T_1 + 2T_2)) \\ &\quad + \cdots \end{aligned} \tag{11.1}$$

where, as usual, the symbol $\otimes$ denotes convolution. We have implicitly assumed that the microphone has an ideal response. In practice, all signals will be distorted in the same way by its response, which thus cancels out. To proceed with the analysis, we transform to the frequency domain. The time delays $\delta(t-\tau)$ become phase factors $\exp(-j\omega\tau)$, the convolutions are replaced by multiplications, and Equation 11.1 reduces to—

$$\begin{aligned} M(\omega) &= F(\omega) + \exp(-j\omega T_1)F(\omega)R_o(\omega) + \exp(-j\omega(T_1 + T_2))F(\omega)R_o(\omega)R_s(\omega) \\ &\quad + \exp(-j\omega(2T_1 + T_2))F(\omega)R_o^2(\omega)R_s(\omega) \\ &\quad + \exp(-j\omega(2T_1 + 2T_2))F(\omega)R_o^2(\omega)R_s^2(\omega) \\ &\quad + \cdots \end{aligned} \tag{11.2}$$

which can be written as—

$$M(\omega) = F(\omega)\left[1 + R_o \exp(-j\omega T_1)\right] \sum_{k=0}^{\infty} \left[\exp(-j\omega(T_1 + T_2))R_o(\omega)R_s(\omega)\right]^k \tag{11.3}$$

which sums to—

$$M(\omega) = \frac{F(\omega)\left[1 + R_o(\omega)\exp(-j\omega T_1)\right]}{1 - R_o(\omega)R_s(\omega)\exp(-j\omega(T_1 + T_2))} \tag{11.4}$$

In conventional reflectometry, as described in previous chapters, the source is positioned far away from the microphone and object by using a long source tube. The source then appears non-reflecting for objects shorter than the tube and we can write $R_s(\omega) = 0$. With this condition, Equation 11.4 reduces to—

$$M(\omega) = F(\omega)\left[1 + R_o(\omega)\exp(-j\omega T_1)\right] \tag{11.5}$$

During calibration of this simple reflectometer, we measured $f(t)$ by fitting a reflector at the microphone position. During measurements, $f(t)$ was then subtracted from the observed signal $m(t)$ to leave the reflection term $f(t) \otimes r_o(t) \otimes \delta(t - T_1)$. This was then deconvolved to yield the required reflectance $r_o(t)$.

We are interested now in the case of a short source tube, when $R_s(\omega) \neq 0$, and we have to use the full form of Equation 11.4. We can define the object to begin at the microphone, so that x_1 and T_1 are both zero. Making this substitution, and rearranging, we obtain the frequency domain expression for the reflectance—

$$R_o(\omega) = \frac{M(\omega) - F(\omega)}{F(\omega) + M(\omega)R_s(\omega)\exp(-j\omega T_2)} \tag{11.6}$$

To evaluate the reflectance, we thus need to know both the spectrum of the incident pulse $F(\omega)$ and the source reflection response $R_s(\omega)$, together with the distance x_2. We will now describe a two-stage calibration procedure for estimating these functions.

The incident pressure pulse $f(t)$ is readily measured by fitting a long extension tube in place of the object under test (Figure 11.3(a)). Provided that the extension tube is acoustically longer than the pulse duration, the reflections from the far end of the tube can be discarded without loss of information. This is equivalent to Equation 11.4 with both R_s and R_o equal to zero. Measurement of the propagation delay between excitation of the loudspeaker and arrival of the pulse at the microphone determines T_2. Transformation to the frequency domain yields $F(\omega)$.

In the second stage of calibration, the extension tube is replaced by a reflecting plug or cap at the microphone position (Figure 11.3(b)). If the plug has a reflection response of $R_c(\omega)$, then analogy with Equation 11.4 shows that the (frequency domain) signal observed at the microphone will be—

$$M_{cal}(\omega) = \frac{F(\omega)\,[1 + R_c(\omega)]}{1 - R_c(\omega)R_s(\omega)\exp(-j\omega T_2)} \tag{11.7}$$

Rearranging, we obtain an estimate of the source reflection response—

$$R_s(\omega) = \frac{M_{cal}(\omega) - F(\omega)\,[1 + R_c(\omega)]}{M_{cal}(\omega)R_c(\omega)\exp(-j\omega T_2)} \tag{11.8}$$

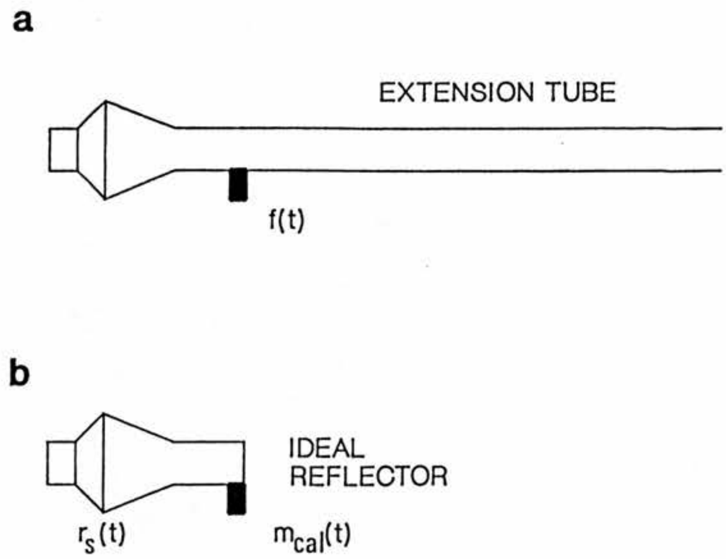

Figure 11.3: *Calibration of a reflectometer with an arbitrarily short source tube. (a) Use of an extension tube allows the source pressure waveform $f(t)$ to be determined. (b) Closing the tube with an ideal reflector at the microphone position allows determination of the source reflection function $r_s(t)$.*

For a rigid plug, we may assume that R_c is independent of frequency, and equal to unity. Calculation of the source reflection response is then simplified to—

$$R_s(\omega) = \frac{M_{cal}(\omega) - 2F(\omega)}{M_{cal}(\omega)\exp(-j\omega T_2)} \tag{11.9}$$

where all the quantities on the right are known. Finally, the object is replaced, and measurement commences, using Equation 11.6 to evaluate the object's reflectance.

To arrive at these results, it is necessary to sum *all* the multiple reflections, so that we can write Equation 11.4 as the sum of an infinite series. This poses a problem, since (theoretically) the reverberations continue indefinitely. In practice, it is sufficient to record the signals until the reverberation has decayed below the noise level. This extended recording time is the price paid for using a physically short source tube.

11.4 Experiments with a short reflectometer

The simple reflectometer of Chapter 7 was modified to have a source tube consisting of 30mm of 16mm bore "Tygothane" plastic tubing (Figure 11.4). The

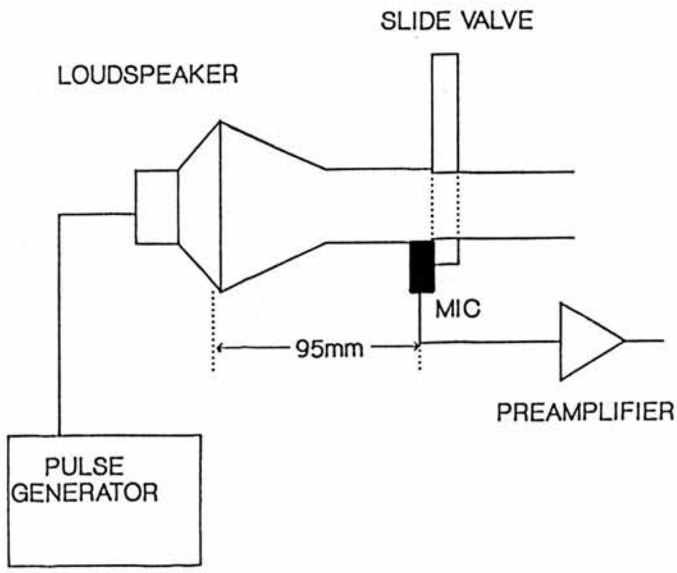

Figure 11.4: *Practical implementation of a short acoustic reflectometer. The loudspeaker coupler and source tube are together 95mm long.*

source loudspeaker (Loudspeaker B, as usual) was acoustically coupled to the source tube and driven by 10V, 25μs rectangular electrical pulses. The cone of the loudspeaker lay approximately 65mm behind the mouth of the coupler, so that the effective overall length of the reflectometer was 95mm. A slide valve, positioned immediately beyond the microphone, allowed the source tube to be closed for calibration purposes. Pressure records were 1024 samples (25.6 ms) long, and calculations were carried out using 1024-point Fast Fourier Transforms.

Calibration Calibration of the reflectometer consisted of the two stages described in Section 11.3. Firstly, a 1m long extension tube was coupled to the source tube, the loudspeaker excited by the electrical pulse, and the microphone signal recorded. It was known *a priori* that the loudspeaker impulse response (ie the source waveform) lasted less than the round-trip travel time of the extension tube (approximately 6ms), and so the source waveform could be determined unambiguously by zeroing all data points beyond 6ms, thus avoiding multiple reflections from the open end of the extension tube.

In the second stage of calibration, the extension tube was removed, and the source tube closed by the slide valve. The loudspeaker was excited as before, and the microphone signal $m_{cal}(t)$ recorded. $M_{cal}(\omega)$ and the source reflection function $R_s(\omega)$ were calculated.

Test objects Various parts of Airway Model 2 (Section 8.1.2) were used to validate the reflectometer theory presented above, and they were connected to the reflectometer by a 60mm length of tubing.

11.5 Results with the short reflectometer

Figure 11.5(a) shows the source waveform $f(t)$ measured during the first stage of the calibration process. It is simply the impulse response of Loudspeaker B when fitted with this particular coupler, and is seen to last approximately 3ms. Its frequency domain representation $|F(\omega)|$, shown in Figure 11.5(b), reveals peaks around 1kHz and 3kHz. Figure 11.6(a) shows the reverberant waveform $m_{cal}(t)$ observed when the slide valve is closed. Approximately 20 reverberations are discernible before the signal decays to the noise level, taking approximately 12ms. The signal is transformed to the frequency domain, and the spectrum $|M_{cal}(\omega)|$, shown in Figure 11.6(b), is seen to be modulated with a periodicity of 1.8kHz. This corresponds to the 560μs delay of the 95mm reflectometer length. The source reflection function $R_s(\omega)$ (Figure 11.7) is calculated using Equation 11.9. It is evident from Figure 11.7 that determination of $R_s(\omega)$ is not perfect, since unphysical values (greater than unity) occur at frequencies above 5kHz.

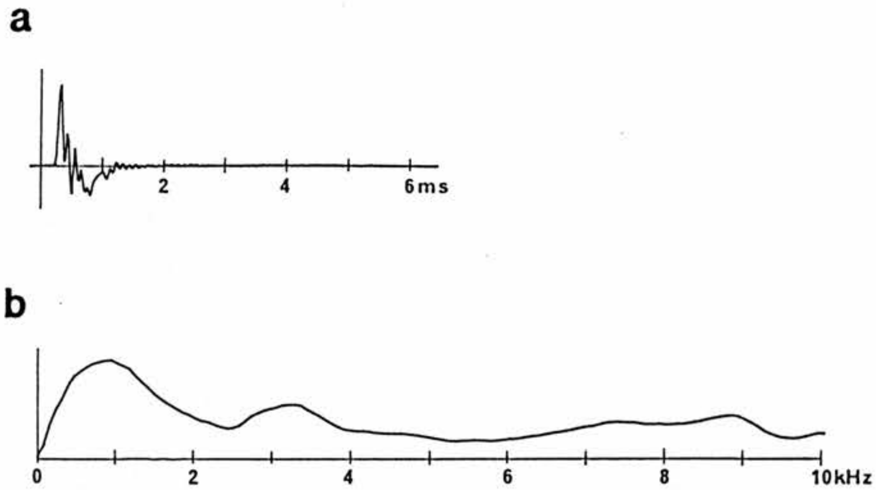

Figure 11.5: *(a) The source pressure waveform $f(t)$ observed when an extension tube is fitted to the reflectometer, and (b) its spectral content $|F(\omega)|$.*

Figures 11.8 to 11.11 show specimen results with the test objects. In Figure 11.8(a) is the microphone signal observed when Airway Model 2, Part B is measured. In this case, the reverberations have effectively died away within the measurement period. Figures 11.8(b) and (c) show the intermediate frequency domain quantities $|M(\omega)|$ and $|R_o(\omega)|$. Notice that several "spikes" of amplitude greater than unity appear in the latter. Transforming back to the time domain, we obtain the reflectance $r_o(t)$ in Figure 11.8(d). The first part of this trace is expanded in Figure 11.9(a), and the corresponding area, reconstructed by the Ware-Aki algorithm, is shown in solid line in Figure 11.9(b). The true area profile is shown superimposed in dashed line. Apart from the incorrect area expansion seen in the early part of the trace (at 5cm, in the connecting tube), the object's area profile is estimated very well (to within a few %). It should be remembered that the object (at 30cm) is three times longer than the reflectometer.

Figure 11.10 shows the corresponding reflectance and reconstructed area profiles for the "pharyngeal" ($4cm^2$) part of the same object. We see that the con-

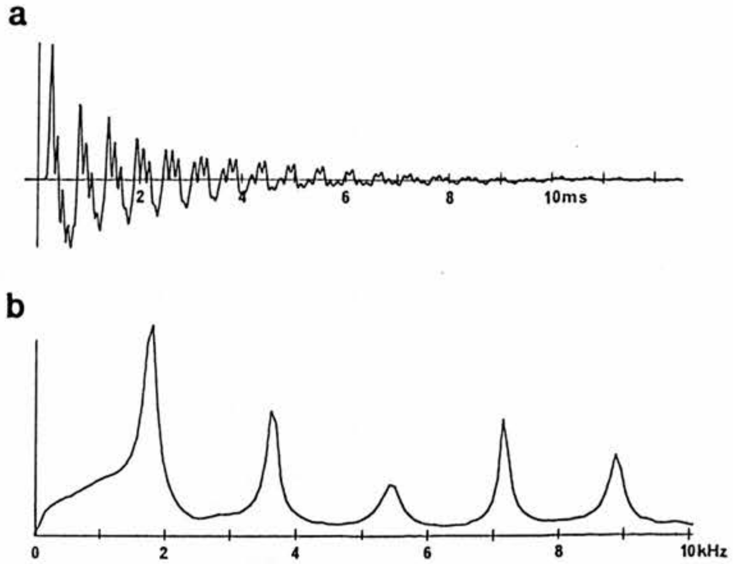

Figure 11.6: *(a) The reverberant waveform $m_{cal}(t)$ observed when the source tube is closed at the microphone position, and (b) its spectral content $|M_{cal}(\omega)|$. The periodicity of 1.8kHz corresponds to the 560μs delay of the 95mm reflectometer length.*

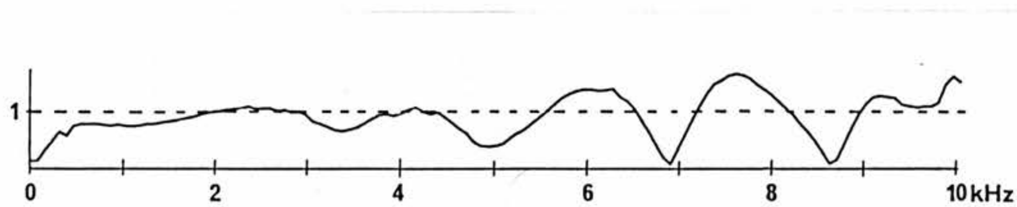

Figure 11.7: *The source reflection response $|R_s(\omega)|$ as calculated using Equation 11.9.*

necting tube is better estimated, but the area maximum is not so well defined, being 10% underestimated.

As a final example, Figure 11.11 shows measurement of Airway Model 2, Part C (having a constriction of 0.9cm^2), with its far end closed. The area of the constriction itself is well estimated, but there is an "overshoot" of nearly 50% at the beginning of the object.

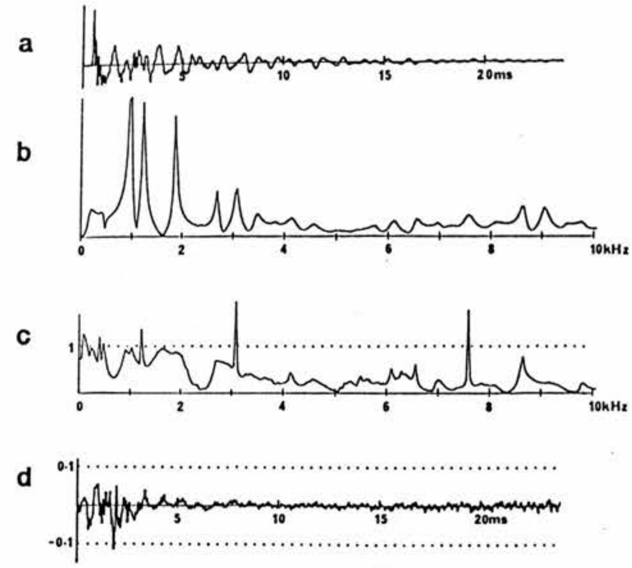

Figure 11.8: *Measurement of Airway Model 2, Part B. (a) The microphone signal $m(t)$, with (b) its spectrum $|M(\omega)|$. (c) The calculated $|R_o(\omega)|$, and (d) after transformation to the time domain reflectance $r_o(t)$.*

11.6 Discussion

The results confirm that the theory is correct, and that it can be used to implement a novel acoustic reflectometer having a source tube shorter than the object being measured. The calibration is a simple, two-step procedure, requiring only an extension tube and an end reflector.

As always, the lack of low frequency source energy leads to problems with the sensitive reconstruction algorithm. This is probably the cause of the incorrect estimation of the connecting tube area at the beginning of the trace in Figures 11.9(b), and of the overshoot in Figure 11.11(b). It was found necessary to bandlimit the calculated reflectance to reduce high frequency noise. A cosine-shaped low pass filter with a response falling to zero at 15kHz was used. Residual noise can be seen in the reflectance trace of Figure 11.8(d).

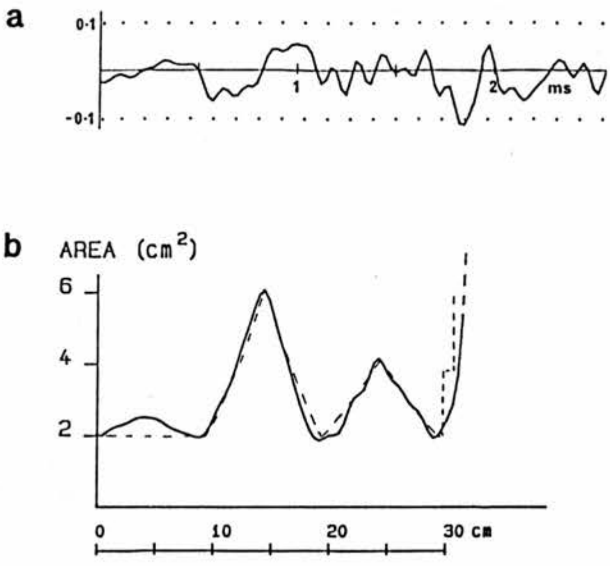

Figure 11.9: *(a) The first section of the reflectance shown in Figure 11.8, expanded, and (b) used to reconstruct the object's cross sectional area. The true area profile is shown in dashed line.*

Inspection of Figure 11.6(a) reveals that successive multiple reflections become more and more smoothed, indicating that dispersion is occurring. This non-ideal behaviour has not been taken into account in the simple theory presented here.

We have already commented on the errors in the determination of $R_s(\omega)$, which show up as unphysical values (greater than unity) in certain frequency ranges in Figure 11.7. In calculating $R_s(\omega)$, we made the assumption of perfect reflection at the slide valve, which cannot be realized in practice. However, no improvement resulted from trying (frequency-independent) values of R_c in the range 0.8 to 1.0 in Equation 11.8. Perhaps a third calibration step could be devised to measure accurately the reflection characteristics of the slide valve. It might also be worth recording the signals for more than the present 1024 samples.

Spikes with magnitudes greater than unity appear in the calculated frequency domain reflectance $|R_o(\omega)|$ (Figure 11.8), and these are also spurious.

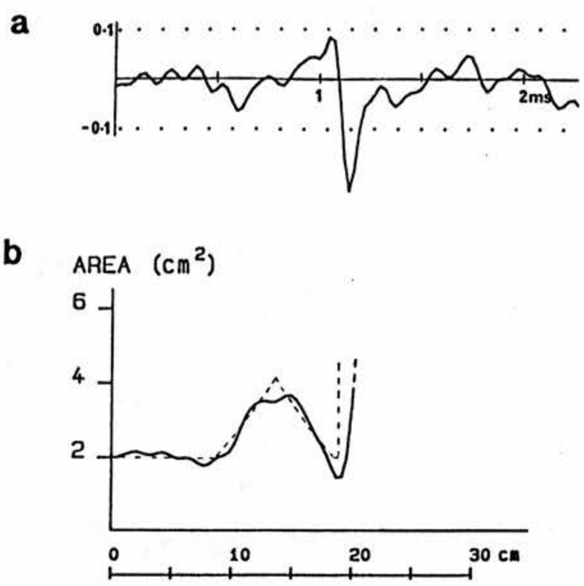

Figure 11.10: *(a) The expanded reflectance function and (b) the reconstructed area profile of a test object consisting of an expansion to 4cm^2, with the far end open. The true area profile is shown in dashed line.*

Notwithstanding the shortcomings discussed here, reasonable results can be achieved with the novel "short" reflectometer, although neither accuracy nor precision was as good as with the conventional reflectometer.

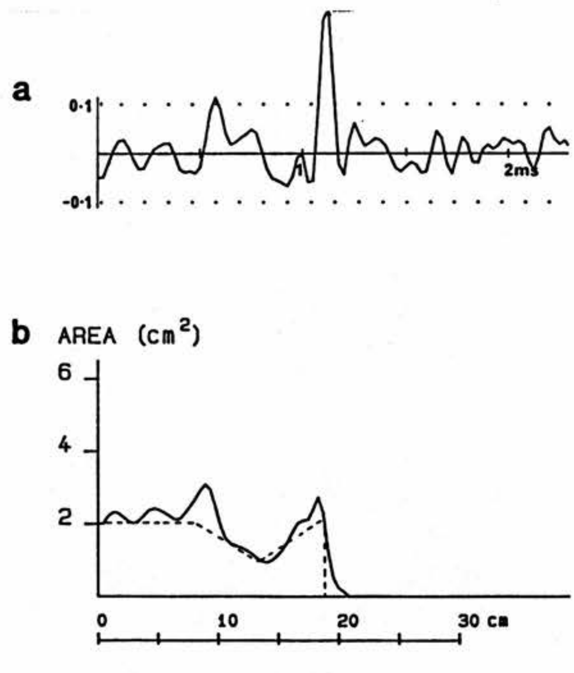

Figure 11.11: *(a) The expanded reflectance function and (b) the reconstructed area profile of Airway Model 2, Part C, with the far end closed. The true area profile is shown in dashed line.*

Chapter 12

Summary and conclusions

The objectives of the research programme have been achieved, with the development and evaluation of an acoustic reflectometer suitable for clinical use.

Although the principle of reflectometry is elegantly simple, the successful implementation of a practical reflectometer has required careful attention to many theoretical and engineering aspects. In particular, the geometry, signal to noise ratio and numerical processing methods required special consideration.

12.1 Features

In the final implementation, the reflectometer is based on a standard microcomputer fitted with a custom high speed analogue interface card. The innovations made include–

1. Portability, achieved by using short-duration pulses and a flexible source tube:

2. Subject breathing during measurement sessions, made possible by using a respiratory valve which closes momentarily when an acoustic measurement is made. Measurements can be synchronized with respiration:

3. Real-time display of airway areas, which is made possible by using either approximate algorithms or additional signal processing hardware, as described in Section 12.2.

The reflectometer is simple to use, and allows collection of scientific data in routine clinical use.

12.2 Signal processing

A comparative survey of reconstruction methods showed that "complete" methods (as exemplified by the Ware-Aki algorithm) are fundamentally slow, requiring of the order of N^2 arithmetic operations. Three approximate methods of order N were compared, and found to be adequate for smoothly tapered objects and for estimates of non-monotonic objects, but not really satisfactory for accurate reconstruction of airway area profiles.

Two methods of producing short duration acoustic impulses have been developed; one suitable for resonant transducers (the "step" method) and the other a more general method for use with arbitrary transducers. The latter method is employed in the reflectometer, with Gaussian pulses of FWHM $100\mu s$ being readily obtained by suitable driving of commercially available electromagnetic loudspeakers. Piezoelectric loudspeakers were found unsuitable due to their lack of low frequency response.

The Gaussian impulses can be used with approximate area reconstruction algorithms to produce a rapid, real-time display of airway areas with the standard microcomputer and software alone. To obtain higher accuracy, it is necessary to deconvolve the reflected waveforms with the pulse shape, a process which is computationally intensive. Deconvolution may be carried out in either the time or the frequency domain; they are mathematically equivalent and no significant differences were found between the two methods. The real-time display of areas is enhanced by the use of additional computer hardware. Two alternatives were evaluated; a standard commercial DSP card, and a custom built convolution card. The performance of the two systems was almost identical, with a complete measurement and display cycle taking approximately 1 second.

A full analysis of reflectometry led to the development of a novel reflectometer having a source tube shorter than the object to be measured. Results with test objects were reasonable, but were not considered good enough to justify building a clinical version.

12.3 Performance

Once the clinical reflectometer has been calibrated, negligible drift occurs over periods of several hours. The intrinsic *in vitro* reproducibility with test objects is ±2%, with accuracies better than ±10% for the objects studied. Area changes of the order of $\pm 0.2\text{cm}^2$ can be detected with confidence.

A wide variety of trials with human volunteers has investigated the effects of breathing mode, posture and respiration. Day to day reproducibility is ±10-20%. The apparatus has been used successfully with sleep apnoea patients and with anaesthetized subjects in preliminary clinical trials. The technique is well tolerated by volunteers and patients.

Acoustic estimates of pharyngeal dimensions made through the mouth are in reasonable agreement with those obtained from MRI images. Limited axial resolution and losses cause the acoustic measurements to be smoothed compared with MRI measurements. In a group of 9 normal volunteers, mean acoustic oropharyngeal and glottal areas were overestimated by 20-30% whilst hypopharyngeal areas were underestimated by 30%. Acoustic and MRI estimates of total pharyngeal volumes agreed within 6%. These accuracies are comparable with those found in the tracheal and glottal studies of [Hoffstein and Zamel 1984] and [D'Urzo et al 1988]. The present performance has been achieved without using He/O_2 gas.

12.4 Further work

Further work might include the development of a more compact respiratory valve and the inclusion of an integrating flowmeter to record lung volume changes. Clinical trials now in progress will seek to correlate acoustic airway measurements with other clinical indicators, for example the number and severity of apnoeic episodes during sleep.

A thorough investigation of airway wall characteristics might lead to theoretically justifiable attenuation correction factors, rather than the empirical correction presently used. However, it is questionable whether the effort involved would be worthwhile in view of the satisfactory results so far achieved.

Acoustic reflectometry may prove useful in the investigation of anterior nasal geometry, but the prospects of making pharyngeal measurements through the nose currently appear poor.

Appendix A

Units of pressure

Several systems of pressure units are encountered in a multi-disciplinary research project such as this, and it is worth explaining their inter-relationships to avoid confusion.

In general physics, the SI unit of pressure is the Pascal (Pa), the name now given to the Newton per square metre (N/m^2).

Sound pressure levels (SPL) are frequently given in decibels (dB) above a reference value p_{ref} of 2×10^{-5} Pa, where SPL=$20 \log(p/p_{ref})$ dB. p_{ref} is derived from the "threshold of hearing" for normal subjects.

Microphone sensitivities are often quoted in terms of decibels below 1V per microbar, where 1 bar is the standard atmospheric pressure of approximately 10^5Pa. The microphone used in this work (a Knowles type BL1785) has a sensitivity of 70dB below 1V/μbar, and thus generates a signal of 312μV for an incident pressure of 1μbar. This is equivalent to 3.12mV per Pascal.

To complicate matters still further, respiratory physiologists are accustomed to quoting pressures in terms of centimetres of water (cm H_2O). This dates back to the time when a simple water manometer was used to measure pressures. Taking the density of water to be 1000kg/m^3 and the acceleration due to gravity to be approximately 10m/s^2 leads to the relation 1cm H_2O=100Pa.

Table A.1 summarizes the relationships between these four systems of units.

No apologies are offered for using the various systems as seems most convenient in the particular context, but equivalents are given where appropriate.

Quantity	Pa	SPL(dB)	μBar	cm H_2O
1Pa	1	94	10	0.01
120dB SPL	20	120	200	0.20
1μBar	0.1	74	1	0.001
1cmH_2O	100	134	1000	1

Table A.1: *Pressure equivalents in different systems of units.*

Appendix B

Convolution and deconvolution

B.1 Introduction

Convolution, and the inverse process of deconvolution, are important concepts in signal processing, and are used throughout the present work. In this appendix, an overview of the essential mathematics is given, for both the time and the frequency domains. The principles apply to any convolution situation, but the notation refers specifically to the formation and subsequent analysis of the reflection signal $m(t)$ observed when an object with reflectance $r_o(t)$ is excited with an acoustic pulse $f(t)$, as shown in Figure B.1.

B.2 The time domain

B.2.1 Convolution

The reflected signal is given by the *convolution* of the incident pulse $f(t)$ and the object's reflectance $r_o(t)$, and is defined mathematically as

$$m(t) = \int_{-\infty}^{\infty} r_o(\phi) f(t-\phi) d\phi = r_o(t) \otimes f(t) \qquad \text{(B.1)}$$

where the symbol $\otimes$ denotes convolution, and ϕ is the variable of integration. Convolution can be thought of as a "distorting" or "smearing" process, as we

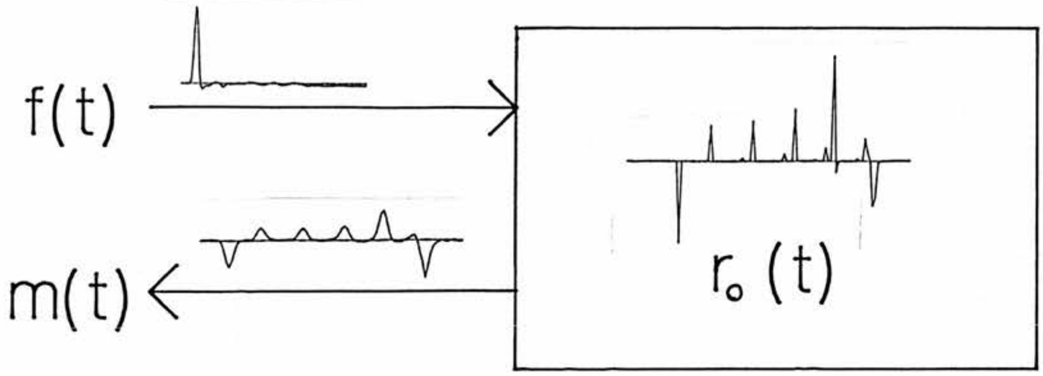

Figure B.1: *The concept of convolution: When an object of intrinsic reflectance $r_o(t)$ is excited by a pulse $f(t)$, the observed reflection $m(t)$ is a smeared version of $r_o(t)$.*

cannot observe the true reflectance, but only a version $m(t)$ which has been distorted by the probing signal $f(t)$. We have implicitly assumed that we can observe the pressure waveforms accurately. In practice, the pressure transducer will itself have some response which introduces a further distortion. However, this affects all the waveforms in the same way, and so cancels out in any analysis.

For a sampled data system, let $r_o(t)$ consist of A samples and $f(t)$ consist of B samples. The convolution $m(t)$ then consists of N samples, where $N \geq A+B-1$. $r_o(t)$ and $f(t)$ are padded with zeroes to the same length N to avoid 'wrap-around' errors, and the summation limits of $\pm\infty$ are replaced by 0 and $N-1$. This *discrete* convolution is given by—

$$m(t) = \sum_{i=0}^{N-1} r_o(i) f(t-i) \tag{B.2}$$

where $t = (0, 1, \cdots, N-1)$. In *matrix* notation, we can write $\vec{m} = \mathbf{f}\vec{r_o}$, where $\vec{m}$

and $\vec{r_o}$ are column vectors and **f** is the $N * N$ matrix—

$$\mathbf{f} = \begin{pmatrix} f_0 & f_{-1} & f_{-2} & \cdots & f_{-N+1} \\ f_1 & f_0 & f_{-1} & \cdots & f_{-N+2} \\ f_2 & f_1 & f_0 & \cdots & f_{-N+3} \\ \cdots & \cdots & \cdots & \cdots & \cdots \\ f_{N-1} & f_{N-2} & f_{N-3} & \cdots & f_0 \end{pmatrix}$$

The functions are all periodic (with period N), so that we can replace f_i with f_{i+N} wherever $i \leq 0$. Hence **f** can be written as—

$$\mathbf{f} = \begin{pmatrix} f_0 & f_{N-1} & f_{N-2} & \cdots & f_1 \\ f_1 & f_0 & f_{N-1} & \cdots & f_2 \\ f_2 & f_1 & f_0 & \cdots & f_3 \\ \cdots & \cdots & \cdots & \cdots & \cdots \\ f_{N-1} & f_{N-2} & f_{N-3} & \cdots & f_0 \end{pmatrix}$$

f is a *circulant* matrix, in which each row is a circularly shifted version of the preceding row, and the first row is a similarly shifted version of the last row. Becasue of this high level of redundancy, only N distinct values are needed to specify all N^2 elements of the array.

B.2.2 Direct (unconstrained) deconvolution

Given the observed vector $\vec{m}$ and a knowledge of the distorting function f, the objective of *deconvolution* is to determine the coefficients $r_o(i)$ which describe the underlying response $\vec{r_o}$. Using Equation B.2 directly, and expanding the matrix notation, we have—

$$m(0) = r_o(0)f(0) \quad \text{(B.3)}$$

$$m(1) = r_o(0)f(1) + r_o(1)f(0) \quad \text{(B.4)}$$

where the summations run from $i = 0$ to $i = t$ only, because f and r_o are not defined for negative time. (This is equivalent to replacing $f(-i)$ by 0.) From Equations B.3, B.4, etc., we have—

$$
\begin{aligned}
r_o(0) &= \frac{m(0)}{f(0)} \\
r_o(1) &= \frac{m(1) - r_o(0)f(1)}{f(0)} \\
etc \cdots
\end{aligned}
$$

In general, this set of equations is unstable because $f(0) \simeq 0$. Starting "later" in the function f to avoid this problem leads to a poor deconvolution because of the discarded information [Deane 1986]. In matrix terms, direct deconvolution is represented by $\vec{r_o} = \mathbf{f}^{-1}\vec{m}$, and the *inversion* of $\mathbf{f}$ to form $\mathbf{f}^{-1}$ is fraught with difficulties. There are two approaches available to overcome these problems—

(i) an iterative approximation method which is discussed in the next section.

(ii) *Wiener* filtering, for which a frequency domain method is dicussed in section B.3.3.

Direct deconvolution in the time domain would require inversion of a matrix of dimension N^2, which generally takes a time of order N^3. This is reduced to nearer N^2 because of the special properties of the circulant matrix.

B.2.3 Iterative deconvolution

[van Cittert 1931] suggested an iterative approximation method to overcome the problems of direct deconvolution in the time domain, and his work has been described and extended by others [Schafer et al 1981, Webb 1988]. The observed m is taken as an initial estimate $\hat{r_{o0}}$ of the required reflectance, and improved estimates are given by—

$$\hat{r}_{ok+1} = \hat{r}_{ok} + \lambda[m - (f \otimes \hat{r}_{ok})] \tag{B.5}$$

This "van Cittert's" algorithm improves the previous estimate by adding a proportion $\lambda\,(0 < \lambda < 1)$ to the difference between the observed function m and the estimated output $f \otimes \hat{r}_{ok}$. van Cittert used $\lambda = 1$, but this often gives unstable results, and values in the range 0.1 to 0.5 are more successful. [Jansson 1970] used $\lambda = K/f(0)$, but adapted the value of the constant K during the sequence of iterations. The squared error term

$$\epsilon^2 = \sum_{i=0}^{N-1} (m_i - (f \otimes \hat{r}_{ok})_i)^2 \tag{B.6}$$

can be used to monitor convergence. Schafer [Schafer et al 1981] generalizes van Cittert's algorithm to—

$$\hat{r}_{ok+1} = C\hat{r}_{ok} + \lambda[m - (f \otimes C\hat{r}_{ok})] \tag{B.7}$$

where C is a *constraint* to suit the physical circumstances. It is a way of using whatever *a priori* knowledge we may have regarding r_o. For example, in many image-processing applications, the *positivity* constraint can be used, because the image intensity cannot be a negative quantity. Similarly, the function may be known to exist over only a certain region, in which case the *finite support* constraint can be used. Thus, at each iteration, negative values of the estimate $\hat{r}_{ok}$ are set equal to zero (positivity), and $\hat{r}_{ok}$ is also set to zero outside the limits of measurement (finite support). [Schafer et al 1981] produce some very attractive γ-ray spectra using these constraints. One suspects that this application was carefully chosen, as fairly "aggressive" deconvolution can locate and separate adjacent spectral peaks very well.

Unfortunately, we cannot use the positivity constraint in the present application, since the reflectance r_o may equally well be negative or positive.

Each iteration of van Cittert's method requires the calculation of a convolution $f \otimes \hat{r}_{ok}$ which involves N^2 multiplications (Equation B.2). Multiplication by the parameter λ and addition to the previous estimate involves of the order of N further operations. The conservative estimate N^2 is somewhat reduced to N times the length of the *shorter* of the two data sequences f and r_o (the remaining data points being identically zero), but the convolution remains fundamentally of order N^2.

B.3 The frequency domain

B.3.1 Convolution and the convolution theorem

Certain results are more easily derived in the frequency domain, which we now consider. It is shown in standard textbooks [Brigham 1988] that convolution in one domain is equivalent to multiplication in the other domain (the *convolution theorem*), and this result is widely used to simplify the mathematics. A function is converted from the time domain to the frequency domain by using the *Fourier transform* operator $\mathcal{F}$, and back again using the *inverse* Fourier transform $\mathcal{F}^{-1}$. It is conventional to use uppercase notation in the frequency domain (and lowercase for the time domain), so that the Fourier transform of $m(t)$ is given by—

$$\mathcal{F}(m(t)) = M(\omega)$$

The transformed quantity $M(\omega)$ is *complex*, ie it has both real and imaginary parts, although frequency information is often displayed as the modulus $|M(\omega)|$.

The convolution theorem is

$$m(t) = f(t) \otimes r_o(t) \qquad \text{(B.8)}$$

$$M(\omega) = F(\omega) R_o(\omega) \qquad \text{(B.9)}$$

B.3.2 Direct (unconstrained) deconvolution

Equation B.9 leads to the direct, frequency-domain deconvolution for the reflectance $R_o(\omega)$—

$$R_o(\omega) = \frac{M(\omega)}{F(\omega)} \qquad \text{(B.10)}$$

For obvious reasons, $1/F(\omega)$ is referred to as an *inverse* filter. For the sampled data case, ω takes on discrete values $i\omega_s/N$, where ω_s is the sampling frequency, N is the number of samples, and $i = 0, 1, 2, \cdots, N-1$. The deconvolved function $R_o(\omega)$ must be converted back to the time-domain using the inverse Fourier transform. As with direct deconvolution in the time-domain, serious problems are encountered in evaluating Equation B.10. Typically, the function $F(\omega)$ has zeroes causing the calculaton to "explode", and errors in the measurement of $m(t)$ (and hence $M(\omega)$) cause instabilities, so that direct deconvolution is not possible.

B.3.3 Wiener filtering

For stable deconvolution in the frequency domain, the inverse filter must be constrained so that less weight is attached to the "noisy" parts of the data. We begin by writing the convolution relation for the acoustic reflection problem in a form that explicitly includes the effect of measurement noise $n(t)$—

$$m(t) = f(t) \otimes r_o(t) + n(t) \quad \text{(B.11)}$$

$$M(\omega) = F(\omega)R_o(\omega) + N(\omega) \quad \text{(B.12)}$$

Instead of the simple inverse filter $1/F(\omega)$, we propose a restoration filter $H(\omega)$, which produces an estimate $\hat{R}_o(\omega)$ of $R_o(\omega)$ given by

$$\hat{R}_o = HM = H(FR_o + N) \quad \text{(B.13)}$$

where we have dropped the explicit frequency dependence from the notation. We wish to minimize (in a *least mean squares* sense) the error between the true reflectance R_o and our estimate $\hat{R}_o$, ie

$$\epsilon^2 = \sum_{i=0}^{N-1} [\hat{R}_o - R_o]^2 \quad \text{(B.14)}$$

The summation is over all N coefficients of the restoration filter H. Minimizing this expression with respect to each of the coefficients, and using Equation B.12, we obtain

$$H = \frac{R_o}{FR_o + N} \quad \text{(B.15)}$$

$$= \frac{F^*}{FF^* + NN^*/R_oR_o^*} \quad \text{(B.16)}$$

where F^*, N^* and R_o^* (denoting complex conjugates) are introduced to rationalize the expression. Hence the estimated reflectance is

$$\hat{R}_o = \left(\frac{F^*}{FF^* + NN^*/R_oR_o^*} \right) M \quad \text{(B.17)}$$

We can write this last result in terms of ϕ_N and ϕ_{R_o}, the spectral powers of the noise and reflectance respectively—-

$$\hat{R}_o = \left(\frac{F^*}{FF^* + \phi_N/\phi_{R_o}} \right) M \quad \text{(B.18)}$$

Equation B.18 describes a *Wiener* filter, which represents the best estimate we can make of the reflectance in the presence of measurement noise. ϕ_N can be estimated from averaging noisy spectra in the absence of any reflections (eg by attaching a long extension tube to eliminate end reflections in the time frame studied). ϕ_{R_o} is rather more difficult to estimate: strictly speaking we need to know R_o before we can use it to estimate R_o! By averaging the spectra of many noisy reflected signals (ϕ_M) and subtracting the noise spectrum, we obtain $|FR_o|^2$, which has to serve as an estimate of ϕ_{R_o} unless we have some *a priori* knowledge or can "remove" the noise. The action of the Wiener filter is to approximate the ideal inverse filter when the signal:noise ratio is large ($\phi_{R_o} \gg \phi_N$), and to tend to zero when the converse is true. It turns out that in many practical situations, the ratio ϕ_N/ϕ_{R_o} is not critical, and it is in fact possible to use an empirical constant k in its place [Gonzalez and Wintz 1977, Webb 1988]. The filter is then more accurately known as a *constrained deconvolution* filter, taking the form—-

$$\hat{R}_o = \left(\frac{F^*}{FF^* + k} \right) M \quad \text{(B.19)}$$

Frequency domain deconvolution requires Fourier transformation of the data sequences f and m (each of length N), the division itself (Equation B.19) for each of the N values of frequency, and finally, an inverse transformation of the result. The straightforward Discrete Fourier Transform (DFT) (and its inverse) each involve of the order of N^2 multiplications, and are the time-consuming steps in this approach. [Cooley and Tukey 1965] developed a "Fast Fourier Transform"

(FFT) algorithm which reduces this to order $N \log_2 N$, thus allowing a substantial increase in processing speed for typical values $N = 256$ or 512.

B.4 Relationship between direct and indirect methods

B.4.1 van Cittert's (time domain) method

Returning to van Cittert's iterative deconvolution (Equation B.5), we have

$$\begin{aligned} \hat{r_{o0}}(t) &= m(t) \\ \hat{r_{ok+1}}(t) &= \hat{r_{ok}}(t) + \lambda[m(t) - (f(t) \otimes \hat{r_{ok}}(t))] \end{aligned}$$

In the frequency domain this is–

$$\begin{aligned} \hat{R}_{o0}(\omega) &= M(\omega) \\ \hat{R}_{ok+1}(\omega) &= \hat{R}_{ok}(\omega) + \lambda[M(\omega) - F(\omega)\hat{R}_{ok}(\omega)] \end{aligned}$$

Dropping the explicit indication of frequency-dependence, and evaluating the first few iterates, we have–

$$\begin{aligned} \hat{R}_{o0} &= M \\ \hat{R}_{o1} &= M[1 + \lambda(1-F)] \\ \hat{R}_{o2} &= M[1 + \lambda(1-F) + \lambda(1-F)(1-\lambda F)] \\ \hat{R}_{o3} &= M[1 + \lambda(1-F) + \lambda(1-F)(1-\lambda F) + \lambda(1-F)(1-\lambda F)(1-\lambda F)] \end{aligned}$$

Generally, the nth estimate $\hat{R}_{on}$ consists of the $n+1$ terms–

$$\begin{aligned} \hat{R}_{on} &= M[1 + \lambda(1-F) + \lambda(1-F)(1-\lambda F) + \cdots + \lambda(1-F)(1-\lambda F)^{n-1}] \\ &= M[1 + \lambda(1-F)\sum_{i=0}^{n-1}(1-\lambda F)^i] \\ &= \frac{M}{F}[1-(1-F)(1-\lambda F)^n] \end{aligned}$$

With $\lambda = 1$, this reduces to -

$$\hat{R}_{on} = \frac{M}{F}[1 - (1 - F)^{n+1}] \tag{B.20}$$

([Webb 1988] incorrectly gives this as $\hat{R}_{on} = \frac{M}{F}[1 - (1 - F)^n]$). F is normalized so that at all frequencies $0 \leq F \leq 1$, and as $n \to \infty$,

$$\hat{R}_{on:n\to\infty} \Rightarrow \frac{M}{F}(1 - \delta) \tag{B.21}$$

where $\delta \ll 1$. Hence, by increasing the number of iterations, we can approach arbitrarily close to the ideal direct (unconstrained) deconvolution, stopping the process when the noise begins to dominate.

B.4.2 (Frequency domain) Wiener deconvolution

The simplified Wiener filter method of deconvolution (Equation B.19) can be written as

$$\hat{R}_o = \left(\frac{M}{F + k}\right) = \frac{M}{F(1 + k')} \simeq \frac{M}{F}(1 - k') \tag{B.22}$$

which is of the same form as Equation B.21, thus showing the equivalence of the time domain and frequency domain approaches.

Appendix C

Software listings

The reflectometer control software is written in Turbo Pascal, and altogether comprises approximately 3000 lines of source code. Only the more important programs are listed here.

`acref`: This is the main high level program which calls routines from several "libraries"—Page 194.

`analogue`: A library of routines for accessing the high speed analogue interface card—Page 200.

`FFT256`: A library of Fast Fourier Transform routines, used for frequency domain deconvolution—Page 202.

`A100`: Low level routines for controlling the Inmos IMSA100 custom DSP card used for time domain deconvolution—Page 203.

```
program acref(plotter, data_file);

{ Developed from 23rd August 1990 version of'CLINIMB'.                    }
{ Intended as an all-purpose program for development work.                }
{ Uses custom high-speed analogue interface card, and  256 data points.   }
{ Choice of deconvolution and reconstruction methods.                     }
{ *** NB  Set up source tube dimensions in 'constants' section.  ***      }

{ 21st June 1991 }
{ October 1990 : program modified to run on Dell 316SX                    }
{ 'float_type' is declared in FFT256 as either 'real' or 'single'.        }
{ Incorporate INMOS A100 routines, June 1991.                             }

uses Dos, Crt, Graph, analogue, FFT256, printer, plotHPGL, A100, timeutil;

const
         n_points = 256;         {length of waveforms}
            order = 8;
              rho = 1.3;         {density of air}
                c = 340;         {speed of sound in air}
          delta_R = 0.001;       {estimated error in reflectance data}

       source_dia = 16;          {source tube diameter in mm}
              Lsm = 1175;        {source to microphone distance : MIN 975mm}
              Lmo = 55;         {microphone to object distance : MIN  50mm}
         max_area = 50;          {stop reconstruction sooner if area > 50 sq cm}
         min_area = 0.3;         {      or < 0.3 sq cm}
        drive_amp = 3000;        {sets drive waveform amplitude}
         screen_x = 909;         {screen scaling :1130 for PS/2, 909 for Dell}
         screen_y = 0.84;                      {:1    for PS/2, 0.84  for Dell}
       area_shift = 0;

var
   pressure_pulse                    : complex_array;
   spectrum                          : complex_array;
   calibration                       : complex_array;
   total_error, temp, k              : float_type;
   graph_driver, graph_mode          : integer;
   counter, inx2,rec_index,shift     : integer;
   product, beta, adj                : float_type;
   caption,comm                      : string;
   Filename                          : string;
   ans1, ans2, ans3, ans4, ans5      : string;
   command, area_string              : string;
   data_file                         : text;
   temp_int, temp2, high, low        : integer;
   v_size, v_pos, zoom               : integer;   {used for screen}
   magn                              : integer;
   sweeps                            : integer;  {instantaneous number of sweeps}
   n_sweeps                          : integer;   {target number of sweeps}
   time_1, time_2, time_3            : string;
   Z, r, WA_F, WA_G                  : ARRAY[0..180] of float_type;
   min_Z                             : float_type;
   drive_length, alignment, max_pos: integer;
   error, old_error, alpha, max      : float_type;
   quiescent, correction_factor      : float_type;
   pulse_energy, tail_amplitude      : float_type;
   offset_1, offset_2                : float_type;
   pulse_amplitude, inc_amp          : float_type;
   cal_peak_pos, inc_peak_pos        : integer;
   sync_flag                         : Boolean;
   mouse                             : registers;
   old_vec_1C                        : pointer;    { for 'synchronize' }
   ioerr, disk_err                   : Boolean;

   Key_has_been_pressed              : Boolean;
   min_distance, max_distance        : integer;
   area_meas                         : array[0..52] of float_type;
   pulse                             : integer;
   DirInfo                           : SearchRec;
   T_strings                         : array[1..30] of string;
   T_info                            : array[1..30,1..2] of word;
   T_pointer                         : integer;
   conv_length                       : integer;
   result                            : array[0..400] of integer;

   {variables associated with analogue interface card}
   ad_data, chan_data, dac_array   : integer_array;
   clock_rate, n_sample_points     : longint;

{*************************************************************************}

function caps(l_c_string : string) : string;

{converts a string into Upper Case characters}
var i : integer;
    ch1 : char;
    U_C_String : string;

begin
     U_C_String:='';
     FOR i:= 1 TO LENGTH(l_c_string) DO
     begin
          ch1:=l_c_string[i];
          U_C_String:=U_C_String + UpCase(ch1);
     end;
     caps:=U_C_String;
end;   {caps}

{*************************************************************************}

procedure Gaussian;
{set up desired Gaussian pulse shape}

const   T = 3;                       { FWHM = 25T µs at 40kHz sampling}
var     G_index  : integer;
        alpha    : float_type;


begin
     FOR G_index:= 0 TO n_points DO
     begin
          alpha := (G_index-n_points/2)/T;
          IF (alpha > 5) OR (alpha < -5) THEN
          desired_pulse[G_index,0]:=0
                                            ELSE
          desired_pulse[G_index,0]:=EXP(-2*SQR(alpha));
     end;

end;   {Gaussian}

{*************************************************************************}

procedure initialise;

var    init_index, init_index2, a    : integer;

begin
     FOR init_index:= 0 TO n_points DO
     begin
          FOR init_index2:=0 TO 1 DO
          begin
               pressure_pulse[init_index,init_index2]:= 0;
               reflectance[init_index,init_index2]:= 0;
               spectrum[init_index,init_index2]:= 0;
               desired_pulse[init_index,init_index2]:= 0;
          end;
     end;

     Gaussian;                  {set up desired pulse shape}

     F := 'RESEARCH';

     k:=0.01;          {constant in denominator of pulse deconvolution division}
     n_sweeps:=10;     {target number of sweeps for calibration}
     quiescent:=0;

{     min_distance:= 9 + TRUNC(Lmo/4.3+0.5);}
     min_distance:=18;
     max_distance:= 120;                              {MAX 180 data points}

     SetLineStyle(SolidLn,0,NormWidth);
     GetIntVec($1C,old_vec_1C);      {for use in procedure synchronize}

     {prepare analogue interface card}
     init_analogue_interface;
     n_sample_points:=500;                          {500 samples}
     clock_rate:=40000;                             {40kHz collection}
     set_sampling_clock(clock_rate);

 end;   {initialise}

{*************************************************************************}

procedure stimulate_driver;

begin
     load_DAC_buffer(n_sample_points,dac_array);
     analogue_output(n_sample_points);
     REPEAT
     UNTIL finished;

end;    {stimulate_driver}


{*************************************************************************}

procedure reset_driver;

var
   i  : integer;
begin
     n_sample_points:=2;
     FOR i:=0 TO 2 DO
     begin
          dac_array[i]:=2048+TRUNC(drive_amp*quiescent);
     end;
     load_DAC_buffer(n_sample_points,dac_array);
     analogue_output(n_sample_points);
     REPEAT
     UNTIL finished;

end;    {reset_driver}


{*************************************************************************}

procedure sketch(var        waveform : complex_array;
                           amplitude  : integer;
                             position : integer;
                         graph_label  : string);

var       i                   : integer;
          x, y                : longint;

begin
     MoveTo(0,TRUNC(position-(screen_y*amplitude*waveform[0,0])));
     i:=1;
     WHILE (i < max_distance)
                { AND (waveform[i,0] > -100)} DO
     begin
          x:= TRUNC(screen_x*(i/n_points));
          y:= TRUNC(position-(screen_y*amplitude*waveform[i,0]));
          IF (x > 639) THEN x:=639;  IF (x < 0) THEN x:=0;
          IF (y > 479) THEN y:=479;  IF (y < 0) THEN y:=0;
          LineTo(x,y);
          i:=i+1;
     end;
     OutTextXY(450,position+5,graph_label);
end;       {sketch}

{*************************************************************************}

procedure spectral_sketch(var       waveform : complex_array;
                           amplitude  : integer;
                             position : integer;
                         graph_label  : string);

var       i, j, span     : integer;

begin
     MoveTo(0,TRUNC(position-(amplitude*waveform[127,0])));
     FOR i:= 128 TO 192 DO
     begin
          LineTo(TRUNC(600*((i-127)/64)),
                 TRUNC(position-(amplitude*waveform[i,0])));
     end;
     OutTextXY(450,position+5,graph_label);
end;       {spectral_sketch}

{*************************************************************************}

procedure sketch_line(var   position : integer);

begin
     MoveTo(0,position);
     LineTo(600,position);

end;       {sketch_line}

{*************************************************************************}

procedure time_axis;

var tix          :   integer;

begin
     MoveTo(0,475);
```

```
     LineTo(600,475);
     FOR tix:= -5 TO 5 DO
     begin
          MoveTo(300+TRUNC(40*600*(tix/n_points)),475);
          LineTo(300+TRUNC(40*600*(tix/n_points)),465);
     end;
     OutTextXY(500,450,'500us/div');
end;      {time_axis}

{*******************************************************************}

procedure distance_axis(var zero_dist : integer);

var i, x0          :   integer;
    temp           : float_type;

begin
     temp:=11.9*screen_x/n_points;
     x0:=TRUNC(zero_dist*(screen_x/n_points));
     MoveTo(x0,475);
     LineTo(600,475);
     FOR i:= 0 TO 8 DO
     begin
          MoveTo(x0+TRUNC(temp*i),475);
          LineTo(x0+TRUNC(temp*i),465);
     end;
     OutTextXY(x0,450,'0');
     OutTextXY(x0+TRUNC(2*temp),450,'10');
     OutTextXY(x0+TRUNC(4*temp),450,'20');
     OutTextXY(x0+TRUNC(6*temp),450,'30');
     OutTextXY(x0+TRUNC(8*temp),450,'40');
     OutTextXY(x0+TRUNC(9*temp),450,'cm');
end;      {distance_axis}

{*******************************************************************}

procedure freq_axis;

var fix          :   integer;

begin
     MoveTo(9,10);
     LineTo(609,10);
     FOR fix:= 0 TO 10 DO
     begin
          MoveTo(9+TRUNC(60*fix),10);
          LineTo(9+TRUNC(60*fix),30);
     end;
     OutTextXY(500,40,'1kHz/div');
end;      {freq_axis}

{*******************************************************************}

procedure area_scale(var posn : integer);

begin
     MoveTo(0,posn);
     LineTo(0,posn-200);
     FOR I:=1 TO 3 DO
     begin
          MoveTo(0,posn-TRUNC(65*screen_y*I));
          LineTo(10,posn-TRUNC(65*screen_y*I));
     end;
{     OutTextXY(10,posn-TRUNC(220*screen_y),'2sq.cm/div');}
end;       {area_scale}

{*******************************************************************}

procedure ref_scale(var posn : integer);

begin
     MoveTo(0,posn+70);
     LineTo(0,posn-70);
     FOR I:=-2 TO 2 DO
     begin
          MoveTo(0,posn-TRUNC(30*I));
          LineTo(10,posn-TRUNC(30*I));
     end;
     OutTextXY(0,posn-80,'0.1/div');
end;       {ref_scale}

{*******************************************************************}

procedure error_scale(var posn : integer);

begin
     MoveTo(0,posn); LineTo(0,posn-70);
     MoveTo(0,posn-30); LineTo(10,posn-30);
     MoveTo(0,posn-60); LineTo(10,posn-60);
     OutTextXY(0,posn-80,'100% per div');
end;     {error_scale}

{*******************************************************************}

procedure record_T(s : string);

begin
     GetTime(Hour,Minute,Second,Sec100);
     T_strings[T_pointer]:=s;
     T_info[T_pointer,1]:=Second;
     T_info[T_pointer,2]:=Sec100;
     T_pointer:=T_pointer+1;
end;   {record_T}

{*******************************************************************}

procedure display_T;

var I : integer;

begin
     writeln; writeln; writeln;
     FOR I:= 1 TO T_pointer-1 DO
     begin
          writeln(T_strings[I],'    ',T_info[I,1],'.',T_info[I,2]);
     end;
     writeln;
end;    {display_T}

{*******************************************************************}

procedure impulse_response;

{record impulse response of drive transducer.}

var
  inx, I, J              : integer;

begin
     {collect pressure waveform}
     n_sample_points := 400;
     analogue_input(n_sample_points);
     REPEAT
     UNTIL finished;
     retrieve_ADC_data(n_sample_points);

     {take new sweep and add to running total}
     FOR I:=0 TO n_points-1 DO
     begin
        . pressure_pulse[I,0]:=pressure_pulse[I,0]
                              + new_data[I+((Lam - 800) DIV 5)]/2048;
     end;

end;     {impulse_response}

{*******************************************************************}

procedure average_impulse;

var  I          : integer;
{calculate and draw the averaged impulse response}

begin
     FOR I:=0 TO n_points-1 DO
     begin
          pressure_pulse[I,0]:=pressure_pulse[I,0]/sweeps;
     end;

     FOR I:= 150 TO 200 DO
     pressure_pulse[I,0]:=(200-1)/50 * pressure_pulse[I,0];

     FOR I:= 201 TO n_points-1 DO
     pressure_pulse[I,0]:=0;

     time_axis;
     OutTextXY(500,0,F);

     v_size:=100;  v_pos:=120; caption:='IMPULSE RESPONSE';
     sketch(pressure_pulse,v_size,v_pos,caption);
     sketch_line(v_pos);


end;      {average_impulse}

{*******************************************************************}

procedure pulse_deconvolution;

{calculate drive waveform}

var          shift, i, d_index, X, Y    : integer;
                      D0, D1, denom     : float_type;       {denominator}
                     N0, N1, N2, N3     : float_type;         {numerator}

begin
     transform(desired_pulse);

     transform(pressure_pulse);
     FOR X:=0 TO n_points-1 DO
     reflectance[X,0]:=SQRT(SQR(pressure_pulse[X,0])
                            +SQR(pressure_pulse[X,1]));
     v_size:=15;  v_pos:=190; caption:='SPECTRUM';

     spectral_sketch(reflectance,v_size,v_pos,caption);
     sketch_line(v_pos);

     freq_axis;

     IF (ans1='Y') OR (ans1='y') THEN
     begin
          Y_size:=400; Y_pos:=1000; plot_label:='SPECTRUM';
          spectral_plot(reflectance,Y_size,Y_pos,plot_label);
          plot_line(Y_pos);
          plot_freq_axis;
     end;

     {deconvolution division}
     FOR d_index:=0 TO n_points-1 DO
     begin
          D0:=pressure_pulse[d_index,0]*pressure_pulse[d_index,0];
          D1:=pressure_pulse[d_index,1]*pressure_pulse[d_index,1];
          denom:=D0 + D1 + k;
          N0:=desired_pulse[d_index,0]*pressure_pulse[d_index,0];
          N1:=desired_pulse[d_index,1]*pressure_pulse[d_index,1];
          N2:=desired_pulse[d_index,1]*pressure_pulse[d_index,0];
          N3:=desired_pulse[d_index,0]*pressure_pulse[d_index,1];
          reflectance[d_index,0]:=(N0+N1)/(2*denom);
          reflectance[d_index,1]:=(N2-N3)/(2*denom);
     end;

     inverse_transform(reflectance);

     {align drive waveform using 'calibration' as a temporary store}
     shift:=228;
     FOR i:=0 TO n_points-shift-1 DO
     begin
          calibration[i,0]:=reflectance[i+shift,0];
     end;
     FOR i:=n_points-shift TO n_points-1 DO
     begin
          calibration[i,0]:=reflectance[i-(n_points-shift),0];
     end;
     FOR i:=0 TO n_points-1 DO
     begin
          reflectance[i,0]:=calibration[i,0];
     end;

     {smooth truncation of drive waveform}
     drive_length:=80;
     tail_amplitude:=0;
     FOR I:=drive_length+1 TO drive_length+20 DO
     tail_amplitude:=tail_amplitude+reflectance[I,0]/20;

     FOR I:=drive_length-50 TO drive_length DO
     reflectance[I,0] := tail_amplitude
         + (drive_length-1)/50 * (reflectance[I,0]-tail_amplitude);

     FOR temp2 := drive_length+1 TO n_points-1 DO
     reflectance[temp2,0] := tail_amplitude;

     quiescent:=reflectance[2,0];
     FOR I:=0 TO 1 DO
     reflectance[I,0]:=quiescent;

     v_size:=100;  v_pos:=240;   caption:='DRIVE WAVEFORM';
     sketch(reflectance,v_size,v_pos,caption);
     sketch_line(v_pos);
```

```
end;       {pulse_deconvolution}

{*****************************************************************}

procedure collect_response;
{record actual response to drive waveform.}

var
  inx, I, J              : integer;

begin
     {collect pressure waveform}
     n_sample_points := 255;
     analogue_input(n_sample_points);
     REPEAT
     UNTIL finished;
     release_solenoid_1;
     retrieve_ADC_data(n_sample_points);
     {now take appropriate data points and align them}
     FOR I:=0 TO n_points-1 DO
     begin
          pressure_pulse[I,0]:=pressure_pulse[I,0]
                              + new_data[I+((Lam -1100) DIV 5)]/2048;
     end;

end;  {collect_response}

{*******************************************************************}

procedure average_response;

var inx, I, J    : integer;

begin
     FOR I:=0 TO n_points-1 DO
     begin
          pressure_pulse[I,0]:=pressure_pulse[I,0]/sweeps;
          pressure_pulse[I,1]:=0;
     end;

     FOR I:= 150 TO 200 DO
     pressure_pulse[I,0]:=(200-I)/50 * pressure_pulse[I,0];

     FOR I:= 201 TO n_points-1 DO
     pressure_pulse[I,0]:=0;


     {now draw the recorded waveform}
     v_size:=100;  v_pos:=330; caption:='ACTUAL OUTPUT';
     sketch(pressure_pulse,v_size,v_pos,caption);
     sketch_line(v_pos);

     {shift and save the actual output as the calibration data}
     FOR I:=0 TO n_points-1 DO
     begin
          calibration[I,0]:=pressure_pulse[I+0,0];
          calibration[I,1]:=0;
          pressure_pulse[I,1]:=0;
     end;

     pulse_energy:=0; pulse_amplitude:=0; cal_peak_pos:=0;
     FOR I:=5 TO 15 DO
     begin

          pulse_energy:=pulse_energy + calibration[I,0];
          IF (calibration[I,0] > pulse_amplitude) THEN
          begin
               pulse_amplitude:= calibration[I,0];
               cal_peak_pos:=I;
          end;
     end;

     OutTextXY(150,340,'Peak pos '+IntToStr(cal_peak_pos));
     OutTextXY(150,355,'Peak amp '+RealToStr(pulse_amplitude));
     OutTextXY(150,370,'Energy   '+RealToStr(pulse_energy));

     transform(pressure_pulse);

     FOR I:=0 TO n_points-1 DO
     begin
          spectrum[I,0]:=pressure_pulse[I,0];
          spectrum[I,1]:=pressure_pulse[I,1];
          reflectance[I,0]:=SQRT(SQR(pressure_pulse[I,0])
                                 +SQR(pressure_pulse[I,1]));
     end;

     {display modulus of frequencies; ie spectrum}
     v_size:=20;  v_pos:=420; caption:='SPECTRUM';
     spectral_sketch(reflectance,v_size,v_pos,caption);
     sketch_line(v_pos);

end;           {average_response}

{*******************************************************************}

 procedure separate_echo;

{raw echo is in 'pressure_pulse', and must be separated}
{from the incident pulse in 'calibration'}

var                          i              : integer;
                   error, old_error         : float_type;

begin

     {'average' the echo}
     FOR i:=0 TO n_points-1 DO
     begin
          pressure_pulse[i,0]:=pressure_pulse[i,0]/sweeps;
          pressure_pulse[i,1]:=0;
     end;

     inc_peak_pos:=0; inc_amp:=0;
     FOR I:=4 TO 15 DO
     begin
          IF (pressure_pulse[I,0] > inc_amp) THEN
          begin
               inc_amp:=pressure_pulse[I,0];
               inc_peak_pos:=I;
          end;
     end;

     {align with calibration waveform}
     IF (inc_peak_pos > cal_peak_pos) THEN
     begin
          FOR I:=0 TO n_points-(inc_peak_pos-cal_peak_pos) DO
          begin
               pressure_pulse[I,0]:=
                         pressure_pulse[I+inc_peak_pos-cal_peak_pos,0];
          end;
     end                              ELSE
     IF (inc_peak_pos < cal_peak_pos) THEN
     begin
          I:= n_points+(inc_peak_pos-cal_peak_pos);
          REPEAT
               pressure_pulse[I,0]:=
                         pressure_pulse[I+inc_peak_pos-cal_peak_pos,0];
               I:=I-1;
          UNTIL I = (cal_peak_pos-inc_peak_pos);
     end;


     {separate incident from reflected wave}
     old_error:=1000;  alpha:=2.1;
     {now optimise 'alpha'}
     REPEAT
          error:=0;
          FOR i:=0 TO 22 DO
          begin
               error:=error +
                    SQR(pressure_pulse[i,0] - calibration[i,0]/alpha);
          end;
          IF (error < old_error) THEN old_error:= error;
          alpha:=alpha-0.01;
     UNTIL error > old_error;
     alpha:=alpha + 0.01;

     FOR i:=0 TO n_points-1 DO
     begin
          {reflection}
          pressure_pulse[i,0]:=pressure_pulse[i,0]-calibration[i,0]/alpha;
          {incident}
          desired_pulse[i,0]:=calibration[i,0]/alpha;
     end;

     SetViewPort(370,40,639,110,ClipOn);
     ClearViewPort;
     SetViewPort(0,0,GetMaxX,GetMaxY,ClipOn);
     OutTextXY(380,95,'alpha : '+IntToStr(TRUNC(100*alpha)));
     OutTextXY(380,65,'Pos : '+IntToStr(TRUNC(inc_peak_pos)));
     OutTextXY(380,50,'Amp : '+RealToStr(inc_amp));
     OutTextXY(380,80,'error : '+RealToStr(error));

end;            {separate_echo}

{*****************************************************************}

procedure set_up_A100_coeffs;

var i,a : integer;

begin
     FOR i:=0 TO 31 DO
     begin
          port[A100_address]:=coeff[i];
          a:=TRUNC(128*calibration[i,0]);
          port[A100_write_hi]:=HI(a);
          port[A100_write_lo]:=LO(a);
      end;
end;   {set_up_A100_coeffs}

{****************************************************************}

procedure convolve(var f,h,g  : complex_array);

{Time-domain discrete convolution of 'f' with 'h' ; result is 'g'. }
{Used by procedure 'van_Cittert' for iterative deconvolution.      }
var
   i, j, m, shift : integer;

begin
     conv_length:=130;
     FOR i:=0 TO conv_length DO
     begin
          g[i,0]:=0;
          FOR m:=0 TO 50 DO
          begin
               j:=i-m;  IF (j < 0) THEN j:=j+conv_length;
               g[i,0]:=g[i,0] + f[m,0]*h[j,0];
          end;
     end;

     shift:=10;
     FOR i:=0 TO conv_length-shift DO
     g[i,0]:=g[i+shift,0];
     FOR i:=conv_length+1-shift TO n_points-1 DO
     g[i,0]:=0;

end;    {convolve}

{*******************************************************************}

procedure read_A100_data(i : integer);

type
    byterec = record
              b1,b2,b3,b4 : byte;
              end;
var
   data_out : longint;

begin

     data_out:=0;

     port[A100_address]:=D0H;
     byterec(data_out).b4:=port[A100_read_hi];
     byterec(data_out).b3:=port[A100_read_lo];

     port[A100_address]:=D0L;
     byterec(data_out).b2:=port[A100_read_hi];
     byterec(data_out).b1:=port[A100_read_lo];

     result[i]:=data_out;

end;    {read_A100_data}

{***************************************************************}

procedure A100_convolve(var f,g : complex_array);

{convolve 'f' with the pulse shape ('calibration'), and store result in 'g'}

const
     conv_length = 160;
var
```

```
   i,j, data_in, shift : integer;

begin
     FOR j:=0 TO n_points-1 DO
     g[j,0]:=0;

     {flush A100}
{     port[A100_address]:=DIR;
     port[A100_write_hi]:=$00;
     FOR j:=0 TO 31 DO
     port[A100_write_lo]:=$00;}

     FOR j:=0 TO conv_length DO
     begin
          port[A100_address]:=DIR;
          data_in:=TRUNC(1000*f[j,0]);
          port[A100_write_hi]:=HI(data_in);
          port[A100_write_lo]:=LO(data_in);
          read_A100_data(j);
      end;

      FOR j:=0 TO conv_length DO
      g[j,0]:=result[j]/1000;

     shift:=10;
     FOR i:=0 TO conv_length-shift DO
     g[i,0]:=g[i+shift,0];
     FOR i:=conv_length+1-shift TO n_points-1 DO
     g[i,0]:=0;

end;    {A100_convolve}

{**********************************************************************}

procedure van_Cittert(var a,b,c : complex_array);

{time-domain, iterative deconvolution of function 'a' with function 'b'.}
{place result in 'c'.}

const
     lambda=0.3;

var
   iteration,j,k            : integer;
   squared_error            : float_type;
   temp, error              : complex_array;

begin
     iteration:=1;
     FOR j:=0 TO 180(n_points-1) DO
     begin
          c[j,0]:=a[j,0];
     end;

     iteration:=2;
     REPEAT
           A100_convolve(c,temp);

           squared_error:=0;
           FOR j:=0 TO 160(n_points-1) DO
           begin
                error[j,0]:=a[j,0]-temp[j,0]/alpha;
                c[j,0]:=c[j,0] + lambda*error[j,0];


          end;
          iteration:=iteration+1;

     UNTIL (iteration > 5);

{     OutTextXY(0,440,'Press ENTER to continue');
     readln;
     ClearViewPort;}

end;        {van_Cittert}

{**********************************************************************}

procedure deconvolve_echo;

{The echo is in 'pressure_pulse', and must be deconvolved.         }
{The deconvolving function is in  'spectrum' (Frequency domain)    }
{  and in 'calibration' (time domain).                              }
{The (time domain) result is to be placed in 'filter_output'.      }

const
     k2   = 0.5;          {Frequency-domain deconvolution constant}

var                 i, d_index, X, Y, j  : integer;
                         D0, D1, denom  : float_type;      {denominator}
                        N0, N1, N2, N3  : float_type;        {numerator}
                  dead_zone_limit, shift  : integer;
                     correction_factor  : float_type;
                     gamma              : float_type;

begin
     IF (deconv_method = 2) THEN                          {F-domain}
     begin
          record_T('forward transform');
          transform(pressure_pulse);

          {now perform deconvolution division}
          record_T('deconvolution division');
          FOR d_index:=0 TO n_points-1 DO
          begin
               D0:=spectrum[d_index,0]*spectrum[d_index,0];
               D1:=spectrum[d_index,1]*spectrum[d_index,1];
               denom:=D0 + D1 + k2;
               N0:=pressure_pulse[d_index,0]*spectrum[d_index,0];
               N1:=pressure_pulse[d_index,1]*spectrum[d_index,1];
               N2:=pressure_pulse[d_index,1]*spectrum[d_index,0];
               N3:=pressure_pulse[d_index,0]*spectrum[d_index,1];
               reflectance[d_index,0]:=alpha*(N0+N1)/denom;
               reflectance[d_index,1]:=alpha*(N2-N3)/denom;
          end;

          {transform back to time domain}
          record_T('inverse transform');
          inverse_transform(reflectance);

     end        {F-domain}

                              ELSE  IF (deconv_method = 1) THEN

     begin
          FOR i:=0 TO n_points-1 DO                   {non-deconvolution}
          begin
               reflectance[i,0]:=pressure_pulse[i,0]*alpha/pulse_energy;
               reflectance[i,1]:=0;
          end;
     end        {no deconvolution}

                              ELSE

     begin                                     {time domain}
          read_time; start_time:=time;
          van_Cittert(pressure_pulse,calibration,reflectance);
          read_time; stop_time:=time;
     end;       {time domain}

     IF (deconv_method = 2) THEN
     {align object response with echo waveform}

     begin                         {F-domain method; shift left}
          record_T('aligning');
          shift:=120;
          FOR i:=0 TO n_points-shift-1 DO
          begin
               desired_pulse[i,0]:=reflectance[i+shift,0];
          end;
          FOR i:=n_points-shift TO n_points-1 DO
          begin
               desired_pulse[i,0]:=reflectance[i-(n_points-shift),0];
          end;
          FOR i:=0 TO n_points-1 DO
          begin
               reflectance[i,0]:=desired_pulse[i,0];
          end;
     end;            {shifting of F-deconvolved reflectance}


     {remove offset}

     FOR i:=0 TO n_points-1 DO
     begin
          reflectance[i,0]:=reflectance[i,0] - offset_1;
     end;

     {correct for attenuation}
     record_T('atten correction');
     FOR I:=0 TO max_distance DO
     begin
          correction_factor := adj*exp(c*beta*I/(clock_rate));
          reflectance[I,0]:= reflectance[I,0] * correction_factor;
     end;

     v_size:=300;  v_pos:=120; caption:='REFLECTANCE';
     sketch(reflectance,v_size,v_pos,caption);
     sketch_line(v_pos);

end;       {deconvolve_echo}

{**********************************************************************}

procedure WA;

var
   I, J                : integer;
   numerator_function : float_type;

begin
     FOR I:=0 TO max_distance DO
     begin
          WA_F[I]:=0;  WA_G[I]:=0;
     end;

     WA_F[min_distance]:=1;                    {Ware-Aki polynomials}
     WA_G[min_distance]:=r[min_distance];

     I:=min_distance+1;
     {main loop to propagate the reconstruction along the test object}
     REPEAT
          product:=product*(1-SQR(r[I-1]));
          numerator_function:=0;
          FOR J:=min_distance TO I-1 DO
          begin
               numerator_function:=numerator_function
                              + WA_F[J]*reflectance[I+min_distance-J,0];
          end;

          r[I]:=numerator_function/product;
          area[I+1,0]:=area[I,0]*(1-r[I])/(1+r[I]);     {area in sq cm}

          {now apply recursion relations to polynomials}
          J:=I;
          WHILE J > min_distance DO
          begin
               WA_G[J]:=r[I]*WA_F[J] + WA_G[J-1];
               WA_F[J]:=WA_F[J] + r[I]*WA_G[J-1];
               J:=J-1;
          end;
          WA_F[min_distance]:=1; WA_G[min_distance]:=r[I];

          I:=I+1;
     UNTIL (I > max_distance-1)
               OR (area[I-1,0] < min_area) OR (area[I-1,0] > max_area);

end;     {WA}

{**********************************************************************}

procedure Primaries;

var
   I, J                   : integer;
   running_error  : float_type;

begin
     I:=min_distance+1;
     {main loop to propagate the reconstruction}
     REPEAT
          product:=product*(1-SQR(r[I-1]));
          r[I]:=reflectance[I,0]/product;
          area[I+1,0]:=area[I,0]*(1-r[I])/(1+r[I]);
          I:=I+1;
     UNTIL (I > max_distance-1)
               OR (area[I-1,0] < min_area) OR (area[I-1,0] > max_area);

end;           {Primaries}

{**********************************************************************}

procedure Uncorr_primaries;
```

```
var
   I, J                         : integer;

begin
     I:=min_distance+1;
     {main loop to propagate the reconstruction along the test object}
     REPEAT
          r[I]:=reflectance[I,0];
          area[I+1,0]:=area[I,0]*(1-r[I])/(1+r[I]);
          I:=I+1;
     UNTIL (I > max_distance-1)
              OR (area[I-1,0] < min_area) OR (area[I-1,0] > max_area);

end;          {Uncorr_primaries}

{*****************************************************************}

procedure Integral_method;

var
   I, J               : integer;
   S                  : float_type;

begin
     I:=min_distance+1;        S:=0;
     {main loop to propagate the reconstruction}
     REPEAT
          S:= S + reflectance[I,0];
          reflectance[I,1]:=S;
          area[I+1,0]:=area[min_distance,0]*(1-S)/(1+S);
          I:=I+1;
     UNTIL (I > max_distance-1)
              OR (area[I-1,0] < min_area) OR (area[I-1,0] > max_area);

end;               {Integral_method}

{*****************************************************************}

procedure reconstruct;

{take the object's impulse response (stored in "filter_output") and use it..}
{..to perform  reconstruction of area with distance.}

var
   I, J                                    : integer;
   X, Y                                    : integer;

begin
          {initial parameters}
          r[min_distance]:=reflectance[min_distance,0];
                                         {first reflection coefficient}
          area[min_distance,0]    :=PI*SQR(source_dia)/400;
          area[min_distance+1,0] :=area[min_distance,0]
               * (1-r[min_distance])/(1+r[min_distance]);;

          FOR I:= 0 TO min_distance DO
          begin
               area[I,0]:= area[min_distance,0];
               area[I,1]:= 0;
               desired_pulse[I,0]:=0;
          end;
          FOR I:=min_distance+2 TO n_points-1 DO
          begin
               area[I,0]:=-100;
               area[I,1]:=0;
               desired_pulse[I,0]:=0;
          end;
          FOR I:=min_distance+2 TO max_distance DO
          begin
               r[I]:=0;
          end;

          product:=1;

          record_T('off to do WA');
          CASE rec_method of
          1: WA;
          2: Primaries;
          3: Uncorr_primaries;
          4: Integral_method;
          end;      {CASE}

          record_T('back from WA');

          CASE deconv_method of
          1 : OutTextXY(350,0,'Non-deconvolution');
          2 : OutTextXY(350,0,'F-domain deconvolution');
          3 : OutTextXY(350,0,'t-domain deconvolution');
          end;      {CASE}

          {optionally convert back to impedances}
{          FOR I:=0 TO 128 DO
          area[I,0]:=4/(0.995*area[I,0]);}

          v_size:=32;  v_pos:=420;
          CASE rec_method of
               1: caption:='Wara-Aki';
               2: caption:='Primaries';
               3: caption:='Uncorr. prims.';
               4: caption:='Integral';
          end;      {CASE}
          sketch_line(v_pos);

          {shift area trace to display later information}
          FOR I:=0 TO max_distance-area_shift DO
          area[I,0]:=area[I+area_shift,0];

          sketch(area,v_size,v_pos,caption);
          distance_axis(min_distance);
          area_scale(v_pos);

end;           {reconstruct}

{**************************************************************************}

procedure list_areas;

var i  : integer;

begin
     writeln; writeln;
     FOR i:=0 TO 128 DO
     begin
          IF (i MOD 8 = 0) THEN writeln;
          write(area[i,0]:7:4,'  ');
     end;
     writeln('Press ENTER to quit');
     readln;
end;      {list_areas}

{**********************************************************************}

procedure print_areas;

begin
     area_mean[pulse]:=area[62,0];
     write(lst,'  ',area_mean[pulse]:4:2,' ');
     IF ((pulse DIV 10) = (pulse/10)) THEN writeln(lst);
end;   {print_areas}

{**********************************************************************}

procedure statistics;

var
   i  : integer;
   mean, std_dev   : float_type;

begin
     writeln(lst);
     mean:=0; std_dev:=0;
     FOR i:=1 TO 50 DO
     begin
          mean:=mean + area_meas[i]/50;
     end;
     writeln(lst,'  Mean = ',mean:4:2);

     FOR i:=1 TO 50 DO
     begin
          std_dev:=std_dev + (SQR(mean-area_meas[i])/50);
     end;
     std_dev:=SQRT(std_dev);
     writeln(lst,'Std Dev = ',std_dev:4:2);
     writeln(lst);

end;    {statistics}

{************************************************************************}

procedure sync_interrupt_handler;

interrupt;

begin
     SetIntVec($1C,old_vec_1C);
     sync_flag:=TRUE;
end;           {sync_interrupt_handler}

{**********************************************************************}

procedure synchronize;

{Wait for system timer 'tick' to ensure that we are not interrupted}

begin
     sync_flag:=FALSE;
     SetIntVec($1C,@sync_interrupt_handler);
     REPEAT
     UNTIL (sync_flag);
end;     {synchronize}

{**********************************************************************}

{***** MAIN PROGRAM *****}

begin

     graph_driver:=VGA; graph_mode:=2;
     InitGraph(graph_driver,graph_mode,'C:\PASCAL');

     initialise;

     FOR temp2 := 0 TO n_points-1 DO          {set up impulse}
     begin
          dac_array[temp2]:=2048;
     end;
     dac_array[3]:=4095;                   {for tweeter driver}
                                           {with preamp at +/-12V and gain=5.5}

     {dummy stimulation to clear interface card}
     n_sample_points:=5;
     stimulate_driver;       {with a spike}
     impulse_response;       {collect impulse response}
     delay(300);

     FOR temp2:=0 TO n_points-1 DO
     begin
          pressure_pulse[temp2,0]:=0;
          pressure_pulse[temp2,1]:=0;
     end;
     sweeps:=0;

     SetFillStyle(SolidFill,12);
     Bar(0,0,300,60);      SetColor(0);
     OutTextXY(40,10,'Close calibration valve.');
     OutTextXY(40,35,'Press ENTER when ready');
     readln;   SetColor(15);
     ClearViewPort;

     REPEAT
         n_sample_points:=5;
         synchronize;
         stimulate_driver;       {with a spike}
         impulse_response;       {collect impulse response}
         sweeps:=sweeps+1;
         delay(100);
     UNTIL (sweeps >= 10) {OR Keypressed};
     average_impulse;        {calculate averaged impulse response}
     pulse_deconvolution;          {estimate drive waveform to..}
                             {..produce desired pulse}

      {set up drive waveform for DMA output}
      FOR temp2 := 0 TO (n_points-1) DO
      begin
          dac_array[temp2] := 2048+TRUNC(drive_amp*reflectance[temp2,0]);
          IF (dac_array[temp2] > 4095) THEN dac_array[temp2] := 4095;
          IF (dac_array[temp2] < 0)    THEN dac_array[temp2] := 0;
      end;

     FOR temp2:=0 TO n_points-1 DO
     begin
          pressure_pulse[temp2,0]:=0;
          pressure_pulse[temp2,1]:=0;
     end;
     sweeps:=0;
```

```
      reset_driver;
      delay(300);
      REPEAT
              n_sample_points:=drive_length;
              synchronize;
              stimulate_driver;     {with the estimated drive waveform}
              collect_response;
              sweeps:=sweeps+1;
              reset_driver;         {ready for next sweep}
              delay(150);
      UNTIL (sweeps >= 10) {OR (KeyPressed)};
{      release_solenoid_2;}
      average_response;      {display actual response and its spectrum}

      Bar(180,35,550,75); SetColor(0);
      OutTextXY(200,50,'Open valve and press ENTER to continue');
      REPEAT UNTIL KeyPressed;
      ch:=ReadKey;
      IF (ch='e') OR (ch='E') THEN exit;
      SetColor(15);
      ClearViewPort;

      init_A100;
      set_up_A100_coeffs;

REPEAT   {UNTIL 'Q' for Quit}
      deconv_method:=3;       {1=none; 2=Freq; 3=time      }
      rec_method:=1;          {1=WA; 2=Prim; 3=UP; 4=Integral method}
      offset_1:=+0.003;    adj:=0.80; beta:=0.3;
 REPEAT
      reset_driver;  delay(100);
  REPEAT
      T_pointer:=1;
      FOR temp2:=0 TO n_points-1 DO
      begin
           pressure_pulse[temp2,0]:=0;
      end;
      sweeps:=0;
      REPEAT
            wait_for_trigger;
            operate_solenoid_1;  {it is released during 'collect_response'}
            delay(120);            {wait for pressure disturbance to decay}
            n_sample_points:=drive_length;
            synchronize;
            stimulate_driver;
            collect_response;
            sweeps:=sweeps+1;
            reset_driver;
{            delay(100);   }   {delay required here when signal averaging}
      UNTIL (sweeps >= 1);

      separate_echo;
      deconvolve_echo;
      reconstruct;

      SetViewPort(140,180,220,220,ClipOn);         {clear offset from screen,}
      ClearViewPort;                               {leaving area sketch }
      SetViewPort(0,0,GetMaxX,GetMaxY,ClipOn);

      OutTextXY(140,180,'offset='+IntToStr(TRUNC(1000000*offset_1)));
      SetColor(0);  Bar(0,0,200,40);
      OutTextXY(30,20,'Press <P> to Pause');
      SetColor(15);
      UNTIL KeyPressed;
      ch:=ReadKey;

      SetViewPort(0,0,300,10,ClipOn);
      ClearViewPort;
      SetViewPort(0,0,GetMaxX,GetMaxY,ClipOn);
      SetColor(0);  Bar(0,0,330,60);
      OutTextXY(20,20,'Press <R> to Resume');
      OutTextXY(20,30,'Press <C> to Clear screen and resume');
      OutTextXY(20,40,'Press <D> to Draw (plot) latest area');
      SetColor(15);
      REPEAT
       REPEAT UNTIL KeyPressed;
       ch:=ReadKey;
      UNTIL ch IN ['e','E','c','C','r','R','d','D','+','-'];
      IF (ch = 'e') OR (ch = 'E') THEN exit;
      IF (ch = 'c') OR (ch = 'C') THEN ClearViewPort;
      IF (ch = 'r') OR (ch = 'R') THEN
      begin
           SetViewPort(0,0,340,60,ClipOn);
           ClearViewPort;
           SetViewPort(0,0,GetMaxX,GetMaxY,ClipOn);
      end;
      IF (ch='k') THEN begin adj:=adj+0.01;ClearViewPort;end;
      IF (ch='l') THEN begin adj:=adj-0.01;ClearViewPort;end;
      IF (ch='a') THEN begin beta:=beta+0.02;ClearViewPort;end;
      IF (ch='b') THEN begin beta:=beta-0.02;ClearViewPort;end;
      IF (ch='+') THEN begin offset_1:=offset_1+0.001;ClearViewPort;end;
      IF (ch='-') THEN begin offset_1:=offset_1-0.001;ClearViewPort;end;

   UNTIL (ch = 'd') OR (ch = 'D');

      ClearViewPort;
      deconv_method:=3;      {1=none; 2=Freq; 3=time      }
      rec_method:=1;         {1=WA; 2=Prim; 3=UP; 4=Integral method}
      offset_1 :=+0.003; adj:=0.80;  beta:=0.3;

      deconvolve_echo;
      reconstruct;
      v_size:=32;  v_pos:=420;
              CASE rec_method of
                    1: caption:='Ware-Aki';
                    2: caption:='Primaries';
                    3: caption:='Uncorr. prims.';
                    4: caption:='Integral';
              end;     {CASE}
              sketch_line(v_pos);
              sketch(area,v_size,v_pos,caption);
              distance_axis(min_distance);
              area_scale(v_pos);

              v_size:=300;  v_pos:=120; caption:='REFLECTANCE';
              sketch(reflectance,v_size,v_pos,caption);
              sketch_line(v_pos);
              ref_scale(v_pos);


              OutTextXY(100,300,'offset='+IntToStr(TRUNC(1000000*offset_1)));

      plot_results(min_distance);

      SetColor(0); Bar(370,250,630,310);
      OutTextXY(400,270,'R(esume) or Q(uit)?');
      REPEAT UNTIL KeyPressed; ch:=ReadKey;
      SetColor(15);
      ClearViewPort;


   UNTIL (ch = 'q') OR (ch = 'Q');

      CloseGraph;

  end.     {acref}

  {*****************************************************************}
```

```
unit analogue;

{ Software for custom high-speed analogue interface card }
{ Uses IRQ5 to signal completion of analogue input/output transfers.  }
{ Also drives two solenoids via PPI port C lines  }

{ 19th August 1991 }

interface

uses Dos, Crt;

const
      base=$300;
      counter0 = base; counter1 = base+1; counter2 = base+2;
      counter_control = base+3;
      portA = base+4; portB = base+5; portC = base+6;
      port_control = base+7;

type
     integer_array = ARRAY[0..1024] of integer;

var
   finished           : Boolean;          {controlled by interrupts}
   new_data           : integer_array;    {used to retrieve new ADC data}
   dummy              : integer_array;    {used to initialise interface}
   dummy_ch           : char;

procedure init_analogue_interface;

procedure set_sampling_clock(sample_rate : longint);

procedure load_DAC_buffer(N_samples : longint;
                          value     : integer_array);

procedure analogue_output(N_samples : longint);

procedure analogue_input(N_samples : longint);

procedure analogue_io(n_in, n_out : longint);

procedure retrieve_ADC_data(N_samples : longint);

procedure operate_solenoid_1;
procedure release_solenoid_1;
procedure operate_solenoid_2;
procedure release_solenoid_2;

procedure wait_for_trigger;

{---------------------------------------------------------------------}

implementation

var
   old_vec                    : pointer;

{*********************************************************************}

procedure enable_irq(IRQ : byte);

var
   mask   : byte;


begin
      mask := (NOT (1 shl IRQ)) AND $FF;
      port[$21]:=port[$21] AND mask;
end;          {enable_irq}

{*********************************************************************}

procedure disable_irq(IRQ : byte);

var
   mask   : byte;

begin
      mask := (1 shl IRQ);
      port[$21]:=port[$21] OR mask;
end;              {disable_irq}

{*********************************************************************}

procedure IRQ5_interrupt_handler;

interrupt;

begin
      disable_irq(5);
      SetIntVec(13,old_vec);               {restore old IRQ5 vector}
      finished:=TRUE;
      port[$020]:=$20;                     {end of interrupt}
end;       {IRQ5_interrupt_handler}

{*********************************************************************}

procedure init_analogue_interface;

var
   i : integer;
   rate, N  : longint;

begin
      disable_irq(5);
      port[port_control]:=$92;  {ports A and B are inputs, port C is output}
      GetIntVec(13,old_vec);    {save IRQ5 vector}

      release_solenoid_1;
      release_solenoid_2;

      N:=20;    rate:=10000;
      set_sampling_clock(rate);
      FOR i:=0 TO 25 DO
      dummy[i]:=2048;
      load_DAC_buffer(N,dummy);
      analogue_input(N);            {dummy operations... }
      analogue_output(N);           {... to set counter outputs high }
      REPEAT
      UNTIL finished;
end;                   {init_analogue_interface}

{*********************************************************************}

procedure operate_solenoid_1;

begin
     port[$308]:=$FF;   {dummy access sets flip-flop}
end;

{*********************************************************************}

procedure release_solenoid_1;

begin
     port[$30C]:=$FF;   {dummy access clears flip-flop}
end;

{*****************************************************************}

procedure operate_solenoid_2;

begin
     port[$310]:=$FF;   {dummy access sets flip-flop}
end;

{*********************************************************************}

procedure release_solenoid_2;

begin
     port[$314]:=$FF;   {dummy access clears flip-flop}
end;

{*****************************************************************}

procedure wait_for_trigger;

{wait for trigger from respiratory pressure circuitry}

var
   in_data : byte;

begin
      port[$31C]:=$FF;                          {clear latch}
      REPEAT
            in_data:=port[$318] AND $01;
      UNTIL (in_data = $01) OR KeyPressed;    {wait for trigger}
{      IF (KeyPressed) THEN dummy_ch:=ReadKey;}

end;    {wait_for_trigger}

{*****************************************************************}

procedure set_sampling_clock(sample_rate : longint);

{sample clock rate is derived from 10MHz:  (AT-bus B20 'clock' in PS/2) }
{ and crystal oscillator in Dell version.}
begin
      port[counter_control]:=$36;  {counter0 to produce square wave,}
                                   {load low then high byte}
      port[counter0]:=TRUNC(10000000/sample_rate) MOD 256;      {low byte}
      port[counter0]:=TRUNC(10000000/sample_rate) DIV 256;      {high byte}
end;               {set_sampling_clock}

{*********************************************************************}

procedure load_DAC_buffer(N_samples : longint;
                          value     : integer_array);

{load DAC output buffer RAM from the array passed as 'value'}

var

   i               : integer;

begin
      port[port_control]:=$90;     {make portB temporarily an output}
      port[port_control]:=$04;     {PC2 low to disable output}
      port[port_control]:=$03;     {PC1 high}
      port[port_control]:=$01;     {PC0 high to reset address counter}
      port[port_control]:=$00;     {PC0 low again}
      i:=0;
      REPEAT
            port[portB]:=value[i] DIV 256; {high byte}
            port[port_control]:=$02;    {take PC1 low.... }
            port[port_control]:=$03;    {..and back high to increment address}
            port[portB]:=value[i] MOD 256; {low byte}
            port[port_control]:=$02;    {take PC1 low.... }
            port[port_control]:=$03;    {..and back high to increment address}
            i:=i+1;
      UNTIL (i > 1000) OR (i > N_samples);
      port[port_control]:=$92;    {portB is an input again}

end;       {load_DAC_buffer}

{*******************************************************************}

procedure analogue_output(N_samples : longint);

{high-speed analogue output of samples preloaded in DAC buffer RAM}

begin
      port[port_control]:=$04;      {PC2 low to disable output}
      port[port_control]:=$03;      {PC1 high}
      port[port_control]:=$01;      {PC0 high to reset address counter}
      port[port_control]:=$00;      {PC0 low again}
      port[counter_control]:=$B0;  {counter2 to count samples}
      port[counter2]:=(N_samples-1) MOD 256;
      port[counter2]:=(N_samples-1) DIV 256;
      finished:=FALSE;
      SetIntVec(13,@IRQ5_interrupt_handler);
      enable_irq(5);
      port[port_control]:=$05;      {PC2 high to enable output}

end;        {analogue_output}

{******************************************************************}

procedure analogue_input(N_samples : longint);

{ high-speed acquisition into ADC buffer RAM, at preset sampling speed}

var
   dummy   : byte;

begin
      port[port_control]:=$0C;      {PC6 low to disable sampling}
      port[port_control]:=$0B;      {PC5 high}
      port[port_control]:=$09;      {PC4 high to reset address counter}
      port[port_control]:=$08;      {PC4 low again}
      port[counter_control]:=$70;  {counter1 to count samples}
      port[counter1]:=(N_samples-1) MOD 256;
      port[counter1]:=(N_samples-1) DIV 256;
      finished:=FALSE;
      SetIntVec(13,@IRQ5_interrupt_handler);
      enable_irq(5);
      port[port_control]:=$0D;      {PC6 high to enable sampling}
```

```
end;          {analogue_input}

{****************************************************************************}

procedure analogue_io(n_in, n_out : longint);

{ Simultaneous high-speed analogue input and output.          }
{ Output samples have been preloaded by 'load_DAC_buffer'.    }
{ Input samoples will be read by 'retrieve_ADC_data'.         }

begin
     {prepare for output}
     port[port_control]:=$04;      {PC2 low to disable output}
     port[port_control]:=$03;      {PC1 high}
     port[port_control]:=$01;      {PC0 high to reset address counter}
     port[port_control]:=$00;      {PC0 low again}
     port[counter_control]:=$80;   {counter2 to count samples}
     port[counter2]:=(n_out-1) MOD 256;
     port[counter2]:=(n_out-1) DIV 256;

     {prepare for input}
     port[port_control]:=$0C;      {PC6 low to disable sampling}
     port[port_control]:=$0B;      {PC5 high}
     port[port_control]:=$09;      {PC4 high to reset address counter}
     port[port_control]:=$08;      {PC4 low again}
     port[counter_control]:=$70;   {counter1 to count samples}
     port[counter1]:=(n_in-1) MOD 256;
     port[counter1]:=(n_in-1) DIV 256;

     finished:=FALSE;
     SetIntVec(13,@IRQ5_interrupt_handler);
     enable_irq(5);
     port[port_control]:=$05;      {PC2 high to enable output}
     port[port_control]:=$0D;      {PC6 high to enable input sampling}

end;          {analogue_io}

{*************************************************************************}

procedure retrieve_ADC_data(N_samples : longint);

{ Read newly-acquired ADC data from buffer RAM into the array 'new_data'. }
{ Array values are from -2048 (-10V) to +2047 (+10V)                      }

var
   i, w : integer;
   high, low           : byte;

begin
     port[port_control]:=$0B;    {PC5 high}
     port[port_control]:=$09;    {PC4 high to reset address counter}
     port[port_control]:=$08;    {PC4 low again}
     i:=0;
     REPEAT
           FOR w:=1 TO 10 DO       {short delay!}
           begin
           end;
           high:=port[portA];
           port[port_control]:=$0A;  {take PC5 low.....     }
           port[port_control]:=$0B;  {.. and back high to increment address}
           low:=port[portA];
           port[port_control]:=$0A;  {take PC5 low.....     }
           port[port_control]:=$0B;  {.. and back high to increment address}
           new_data[i]:=16*high + TRUNC(low/16) - 2048;
           i:=i+1;
     UNTIL (i > N_samples) OR (i > 1000);
end;           {retrieve_ADC_data}

{*************************************************************************}

{MAIN PROGRAM}

begin
end.
```

```
unit FFT256;

{provides forward and inverse Fourier transforms}
{Arrays are dimensioned from 0 to n_points, with the central}
{point being (n_points/2).}

interface

const           n_points=256;
                order   = 8;

type
      float_type = single;
      complex_array = ARRAY[0..n_points,0..1] of float_type;

    procedure transform(var func :  complex_array);
    procedure inverse_transform(var func2 : complex_array);

implementation

{Arrays are dimensioned from 0 to n_points, with the central}
{point being (n_points/2).}


var
   complex_const : complex_array;
   k, p, counter : integer;
   temp0, temp1  : float_type;
   gain          : integer;

{*******************************************************************}

procedure constants;
{generate complex constants}
var    index1 : integer;

begin
     FOR index1:=0 TO n_points-1 DO
     begin
          complex_const[index1,0]:= COS(2*PI*index1/n_points);
          complex_const[index1,1]:= SIN(2*PI*index1/n_points);
     end;
end;              {procedure constants}

{*******************************************************************}

function power(loop : integer) : integer;
{calculate 2^loop}

var    index5, temp : integer;

begin
     temp:=1;
     FOR index5:=1 TO loop DO
     begin
          temp:= temp*2;
     end;
     power:=temp;

end;      {function power}

{*******************************************************************}
procedure bit_reverse(var number : integer);

var  count : integer;

begin
     p:=0;
     FOR count:=1 TO order DO
     begin
          p:=2*p + (number MOD 2) ; number:=number DIV 2;
     end;

end;      {procedure bit_reverse}

{*******************************************************************}

procedure unscramble(var func3 : complex_array);

var     i, index4, j : integer;
            mult     : integer;

begin
     FOR index4:= 0 TO n_points-1 DO
     begin
          i:=index4;
          bit_reverse(i);
          IF index4 < p THEN            {transpose}
               begin
                    temp0:=func3[index4,0];
                    temp1:=func3[index4,1];
                    func3[index4,0]:=func3[p,0];
                    func3[index4,1]:=func3[p,1];
                    func3[p,0]:=temp0;
                    func3[p,1]:=temp1;
               end;
      end;       {index4 loop}

      {shift and re-order}
      mult:=1;
      FOR index4:=0 TO n_points-1 DO
      begin
           func3[index4,0]:=mult*func3[index4,0];
           func3[index4,1]:=mult*func3[index4,1];
           mult:=mult * -1;
      end;
      FOR index4:=0 TO TRUNC((n_points/2)-1) DO
      begin
           temp0:=func3[index4,0];
           temp1:=func3[index4,1];
           j:=TRUNC(index4+(n_points/2)) MOD n_points;
           func3[index4,0]:=func3[j,0];
           func3[index4,1]:=func3[j,1];
           func3[j,0]:=temp0;
           func3[j,1]:=temp1;
      end;


end;      {procedure unscramble}

{*******************************************************************}

procedure transform;
{calculate complex Fast Fourier Transform}

var   stage, skip, q  : integer;

begin
     FOR stage:=1 TO order DO
     begin
          k   :=0;    {top of array}
          REPEAT
           skip:=1;
           REPEAT
            q:=TRUNC(k/(power(order-stage)));
            bit_reverse(q);

            {butterfly}
            q:=TRUNC(k+(n_points/power(stage)));
            temp0:=complex_const[p,0]*func[q,0]+
                   complex_const[p,1]*func[q,1];
            temp1:=complex_const[p,0]*func[q,1]-
                   complex_const[p,1]*func[q,0];
            func[q,0]:=func[k,0]-temp0;
            func[q,1]:=func[k,1]-temp1;
            func[k,0]:=func[k,0]+temp0;
            func[k,1]:=func[k,1]+temp1;

            k:=k+1;
            skip:=skip+1;
           UNTIL skip > TRUNC(n_points/power(stage));
           k:=k+TRUNC(n_points/power(stage));
          UNTIL k > n_points-1;

     end;  {stage}

     unscramble(func);


end;     {procedure transform}

{*******************************************************************}

procedure inverse_transform;
{take complex conjugate before and after forward transform}
{and apply scaling before transform}

var     index3   : integer;

begin
     FOR index3:=0 TO n_points-1 DO
     begin
          func2[index3,0]:= func2[index3,0]/n_points;
          func2[index3,1]:=-func2[index3,1]/n_points;
     end;
     transform(func2);
     FOR index3:=0 TO n_points-1 DO
     begin
          func2[index3,1]:=-func2[index3,1];
     end;

end;       {procedure inverse_transform}

{*******************************************************************}

begin
     constants;
end.
```

```
unit A100;

{ DSP routines for INMOS A100 board }
{ 11th February 1991                }

interface

const
      {board addresses}
      A100_address  = $340;
      A100_write_hi = $344;
      A100_write_lo = $348;
      A100_read_hi  = $34C;
      A100_read_lo  = $350;

      {A100 registers}
      SCR = 64; ACR = 66; TCR = 68;
      DIR = 72; DOL = 74; DOH = 75;


var
   i : integer;
   coeff   : array[0..31] of byte;
   u_coeff : array[0..31] of byte;


   procedure init_A100;

{-------------------------------------------------------------------}

implementation

{*****************************************************************}

procedure init_A100;

begin
      {set SCR for master operation, 16bit coeffs, bank swap off,..}
      {output field [7-30], normal output, DIR input.              }
      port[A100_address]:=SCR;
      port[A100_write_hi]:=$03;
      port[A100_write_lo]:=$03;

      {zero all coefficients}
      FOR i:=0 TO 31 DO
      begin
           port[A100_address]:=coeff[i];
           port[A100_write_hi]:=$00;
           port[A100_write_lo]:=$00;
           port[A100_address]:=u_coeff[i];
           port[A100_write_hi]:=$00;
           port[A100_write_lo]:=$00;
      end;

      {flush A100 by writing 32 zeroes to the DIR}
      FOR i:=0 TO 31 DO
      begin
           port[A100_address]:=DIR;
           port[A100_write_hi]:=$00;
           port[A100_write_lo]:=$00;
      end;

      {clear and re-arm the ERROR output}
      port[A100_address]:=ACR;

      port[A100_write_hi]:=$00;
      port[A100_write_lo]:=$00;
      port[A100_write_hi]:=$00;
      port[A100_write_lo]:=$06;

      {clear test mode}
      port[A100_address]:=TCR;
      port[A100_write_hi]:=$00;
      port[A100_write_lo]:=$00;


end;     {init_A100}

{*****************************************************************}

begin
     FOR i:=0 TO 31 DO
     begin
          coeff[i]  := 32+i;
          u_coeff[i]:=    i;
     end;
end.
```

Appendix D

Circuit diagrams

A few selected circuit diagrams appear on the following pages.

High speed analogue interface card: Page 205.

Microphone preamplifier: Page 207.

Inmos IMSA100 custom DSP card: Page 208.

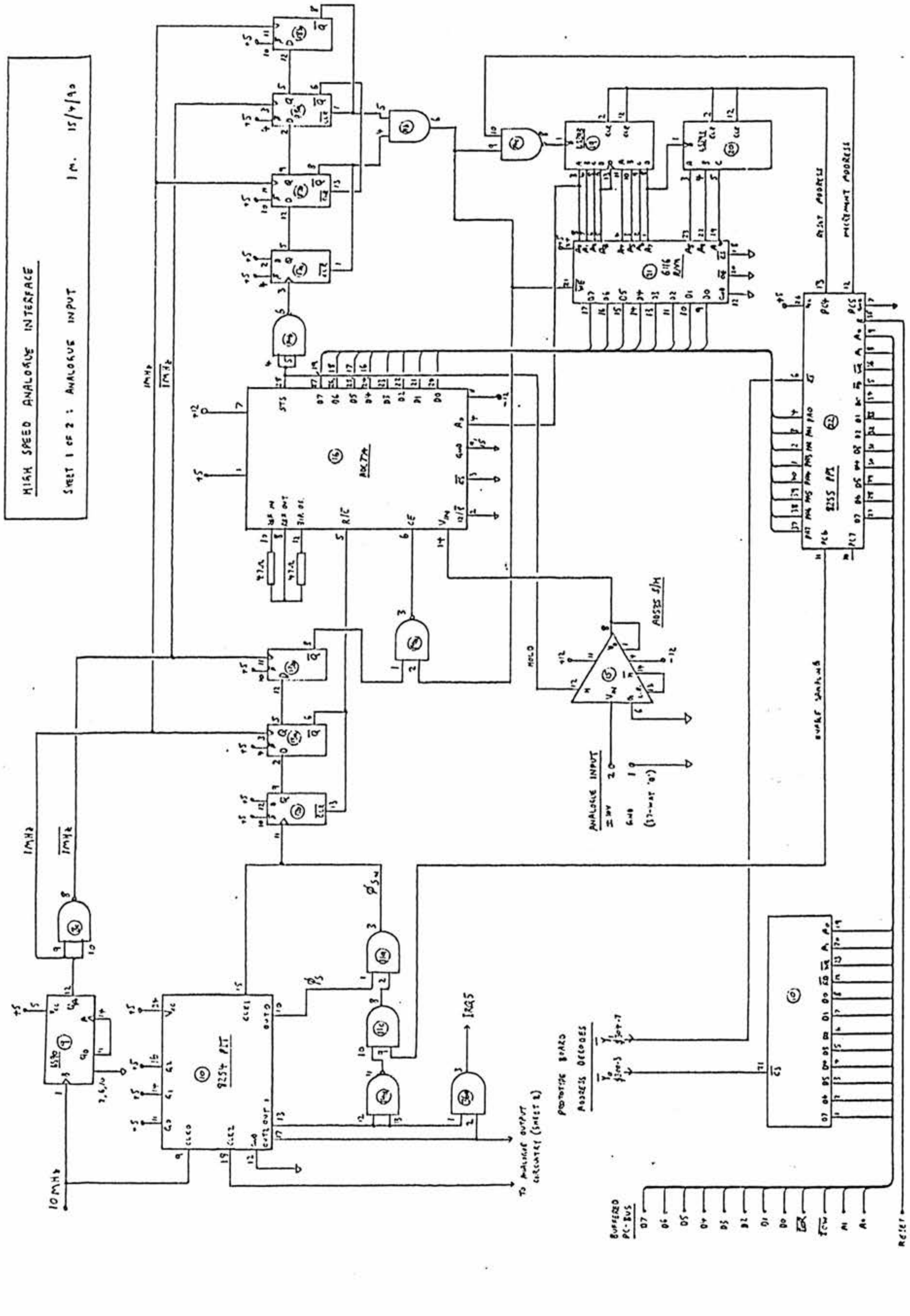
HIGH SPEED ANALOGUE INTERFACE
SHEET 1 OF 2 : ANALOGUE INPUT
I.M. 15/4/90
8254 PIT
8255 PPI
ADC574
6116 RAM
AD585 S/H
ANALOGUE INPUT
10MHz
1MHz
IRQ5
TO ANALOGUE OUTPUT CIRCUITRY (SHEET 2)
PROTOTYPE BOARD ADDRESS DECODES
ENABLE SAMPLING
RESET ADDRESS
INCREMENT ADDRESS
BUFFERED PC-BUS
RESET

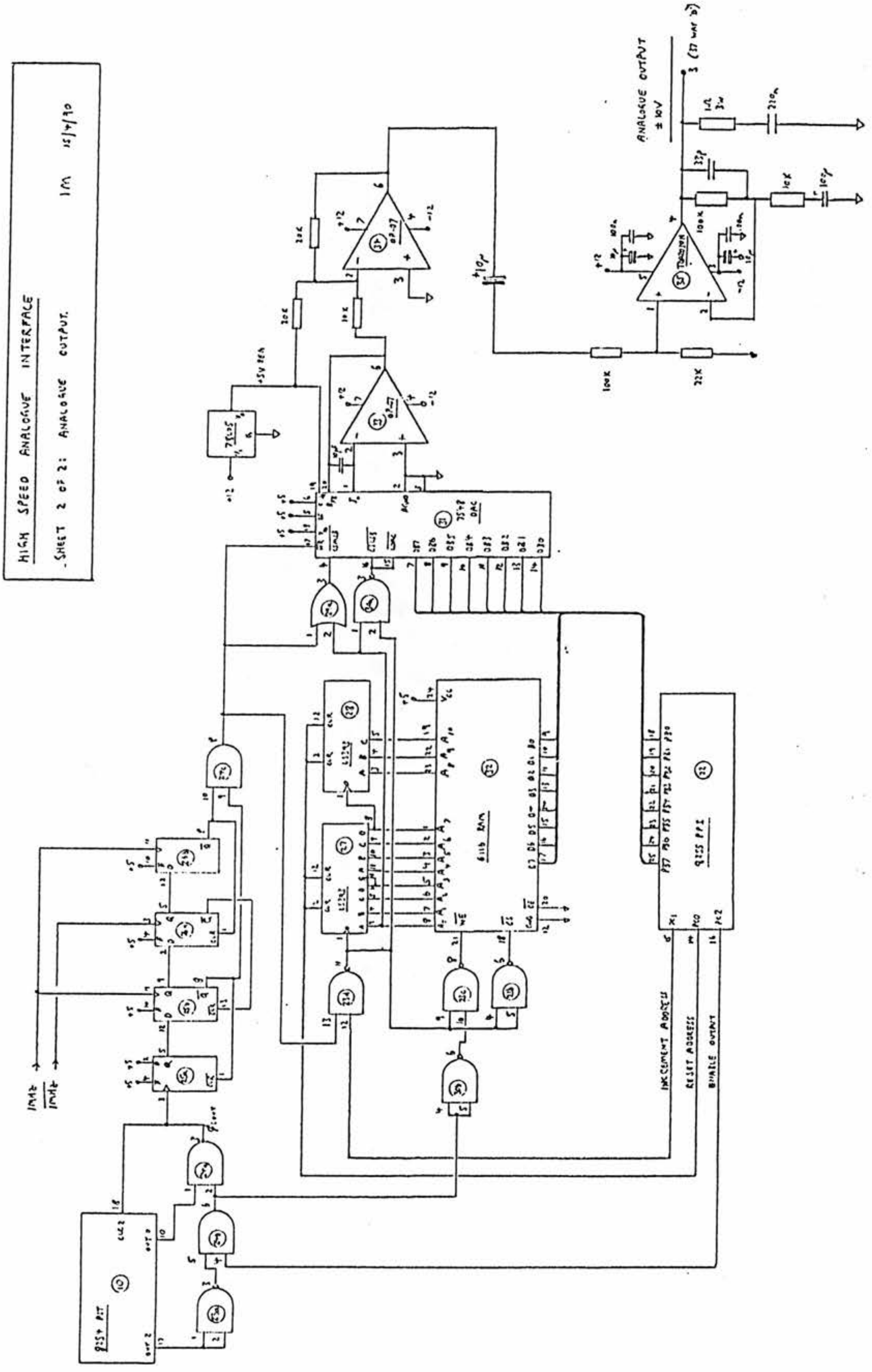
HIGH SPEED ANALOGUE INTERFACE
SHEET 2 OF 2: ANALOGUE OUTPUT.
IM 15/4/90
ANALOGUE OUTPUT
± 10V
6116 RAM
8255 PPI
8254 PIT
7548 DAC
INCREMENT ADDRESS
RESET ADDRESS
ENABLE OUTPUT

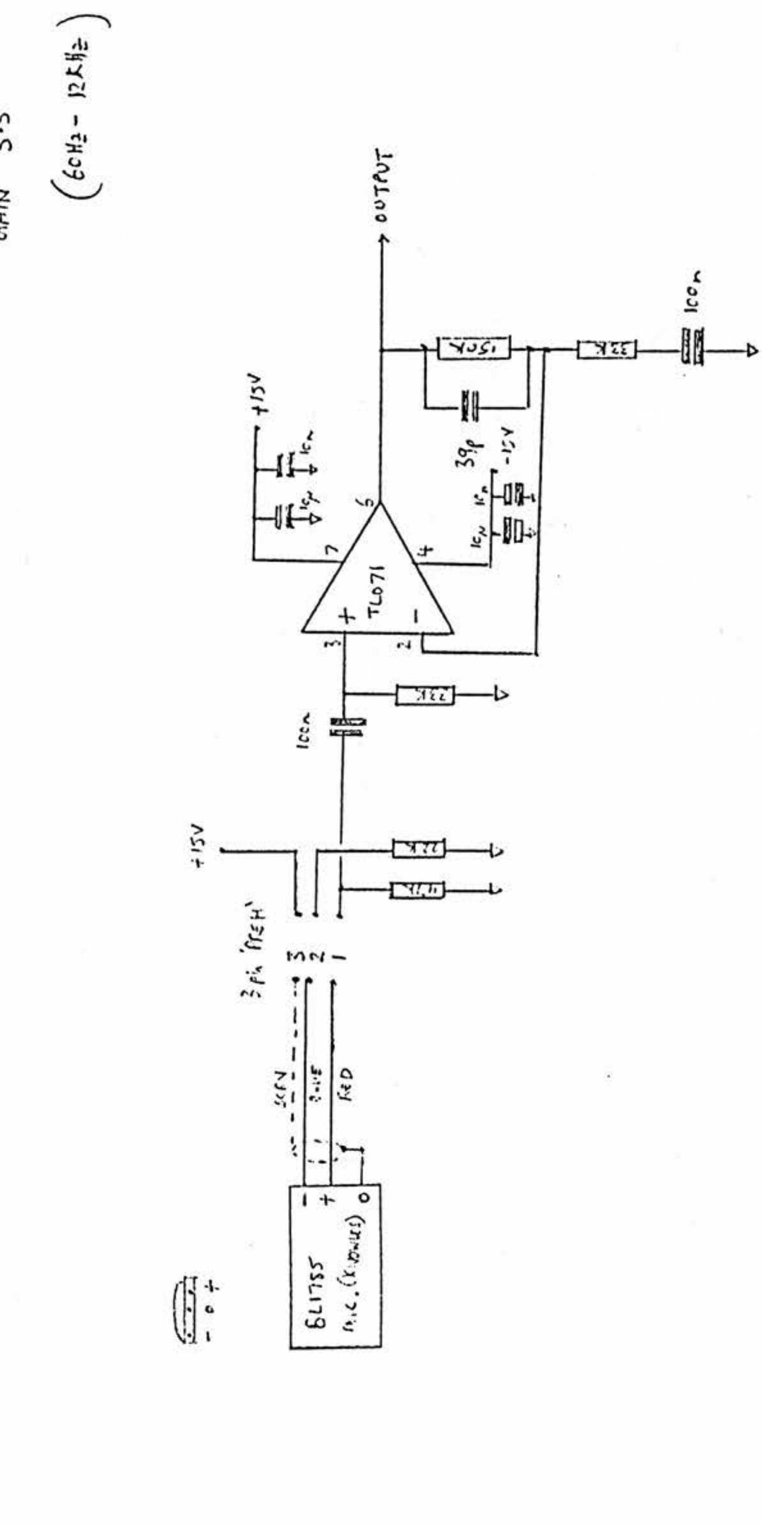
GAIN 5.5
OUTPUT
TL071
+15V
-15V
150K
39p
100n
3 pin 'PREH'
RED

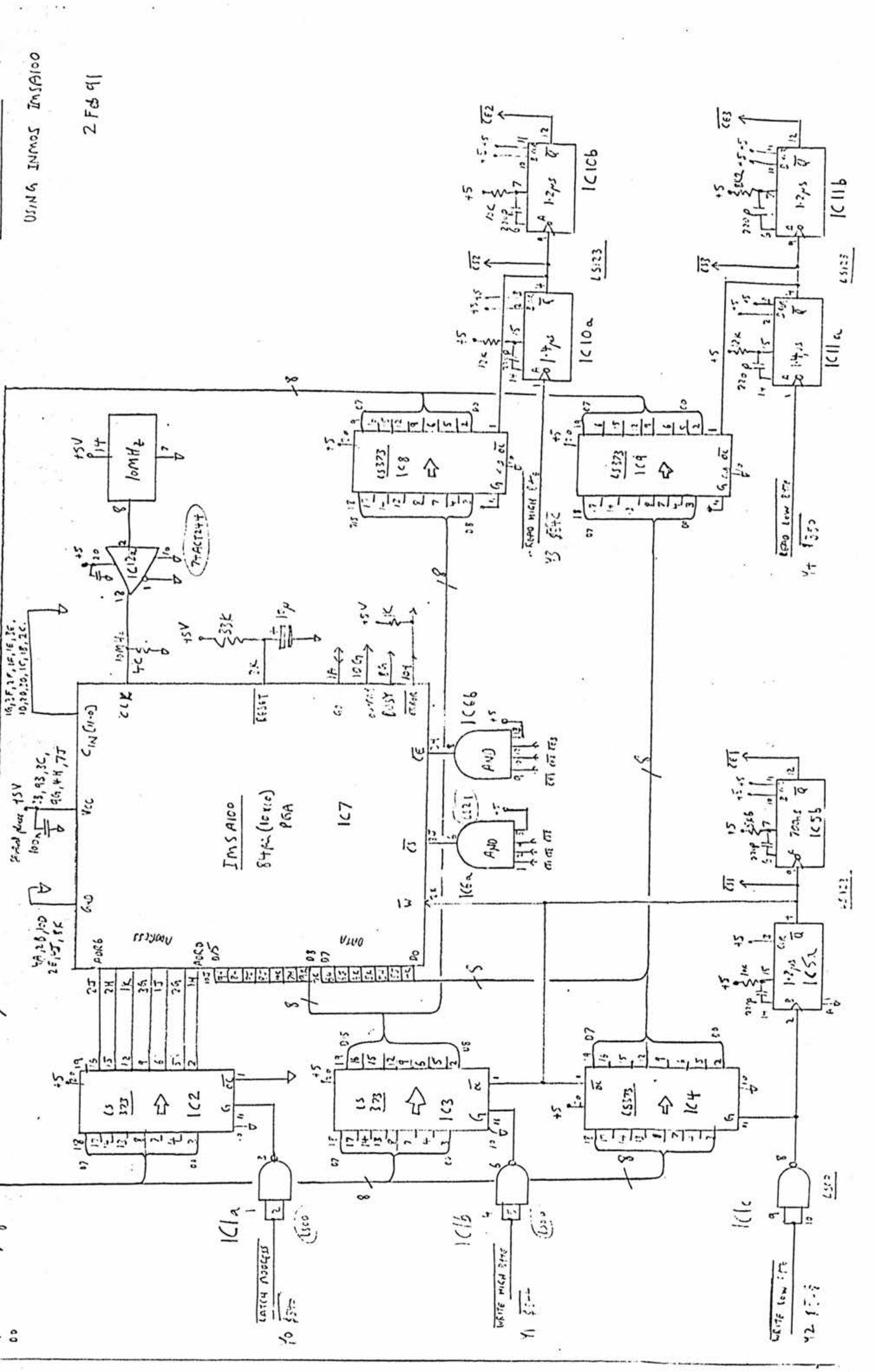
USING INMOS IMSA100
2 Feb 91
IMSA100
IC7
10MHz
IC2
IC3
IC4
IC8
IC9
IC10a
IC10b
IC11a
IC11b
IC5a
IC5b
IC6a
IC6b
IC1a
IC1b
IC1c
LS123
AND
LATCH ADDRESS
WRITE HIGH BYTE
WRITE LOW BYTE
READ HIGH BYTE
READ LOW BYTE

Appendix E

Mechanical drawings of test objects

Mechanical drawings of selected test objects used in validating the reflectometer appear on the next two pages.

Object A: Page 210.

Object B: Page 210.

Airway Model 2: Page 211.

OBJECT A

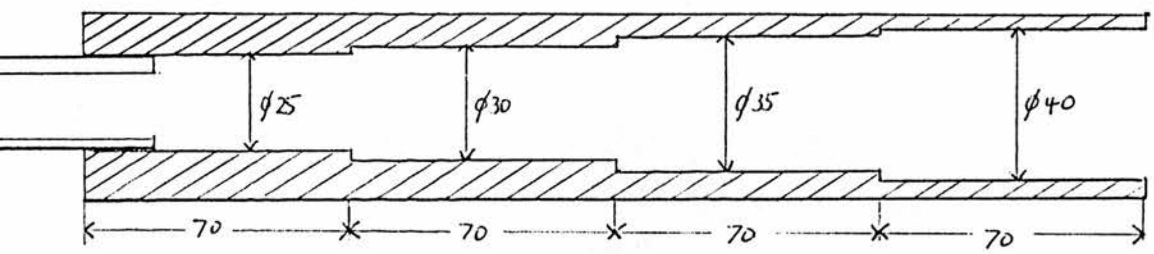

OBJECT B

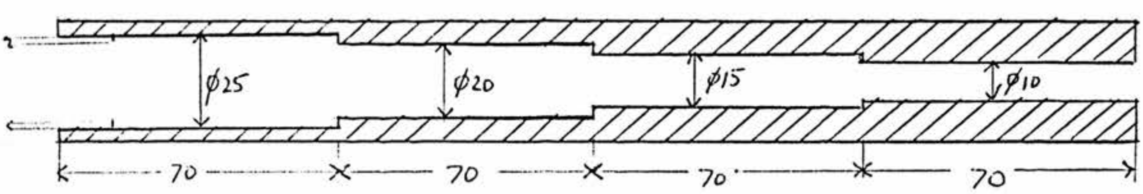

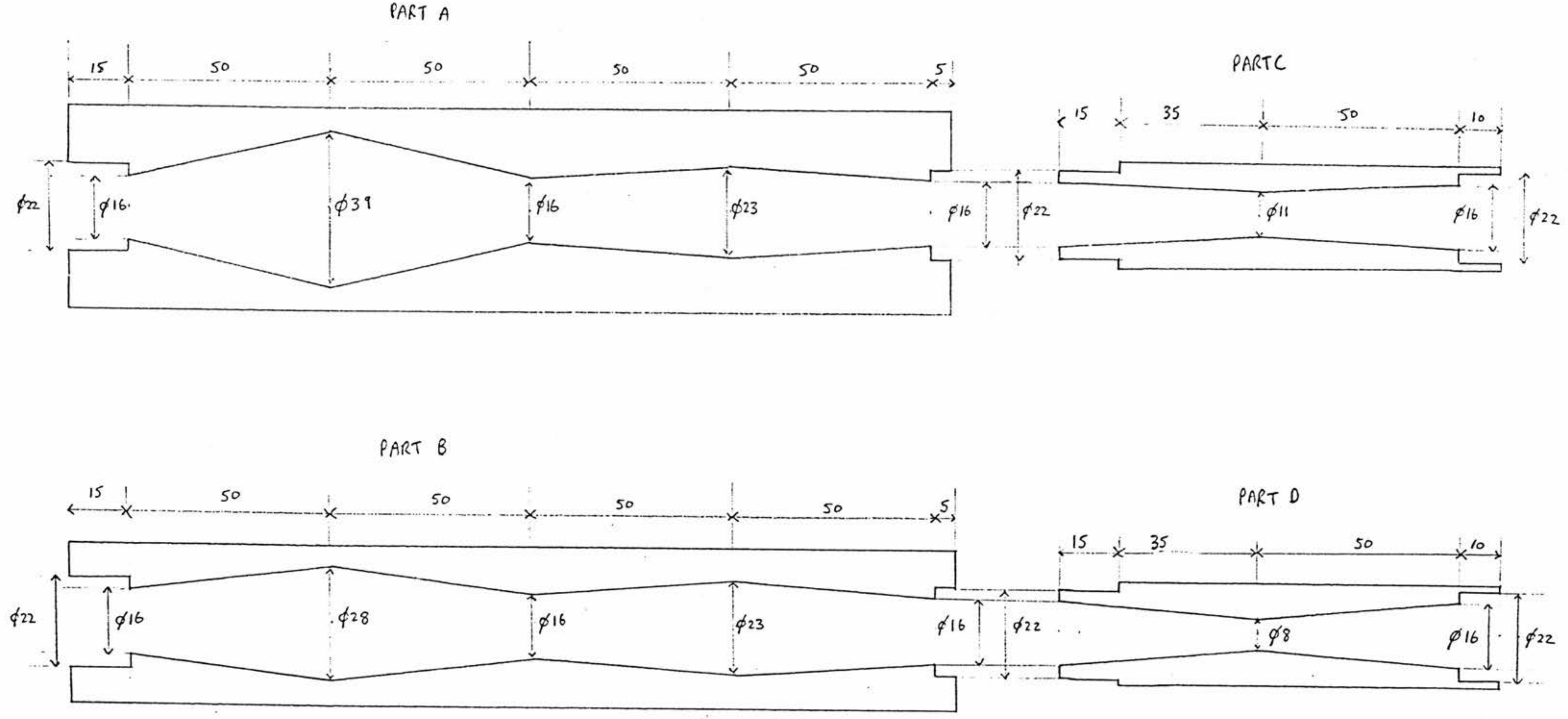

Ian Marshall
8th March 1990

AIRWAY MODEL 2.

Material : Brass, Aluminium or Plastic.

TOLERANCES: Lengths ± 1 mm
Internal Diameters : ± 0·1 mm
External Diameters : Not important except for mating end of Parts C and D.

Appendix F

Glossary

A number; cross sectional area

A_i cross sectional area

ADC Analogue to Digital Converter

B number

b_k backward (upward) travelling wave

bar standard atmospheric pressure of 10^5Pa

C constraint operator

C_1, C_2 constants

$C(t)$ cepstral domain

CT X-ray computed tomography

CV coefficient of variation (standard deviation divided by mean)

c velocity of sound

cmH_2O cm of water pressure

D_k downward (forward) travelling wave

DAC Digital to Analogue Converter

DC Direct Current; "zero frequency"

DFT discrete Fourier transform

DMA Direct Memory Access

DSP Digital Signal Processing

$d(t)$, $D(\omega)$ drive waveform

dB decibels (the ratio of p_1 to p_2 is expressed as $20\log_{10}(p_1/p_2)$ dB)

E acoustic energy

F Ware-Aki polynomial

$\mathcal{F}$ Fourier transfrom operator

$\mathcal{F}^{-1}$ inverse Fourier transform operator

F_i coefficient of z^i in Ware-Aki polynomial F

FFT Fast Fourier Transform

FRC functional residual capacity

FWHM Full Width at Half Maximum

$f(i)$ elements of matrix $\mathbf{f}$

f_k forward (downward) travelling wave

$f(x,t)$ generalized function

$f(t)$, $F(\omega)$, $\mathbf{f}$ source pressure waveform

G Ware-Aki polynomial

g bandwidth

$g(t)$ inverse filter

$g(x, t)$ generalized function

$H^*(\omega)$ complex conjugate of $H(\omega)$

$h(t)$, $H(\omega)$ impulse response; echo response; restoration filter

I incident pressure impulse

ID internal diameter

i imaginary number; index

j imaginary number

K constant

k index; constant; seabed reflection coefficient

L length

L_{mo} distance between microphone and object

L_{sa} length of reflectometer side arm

L_{sm} distance between source and microphone

MRI magnetic resonance imaging

M number

$m(i)$ elements of vector $\vec{m}$

$m(t)$, $M(\omega)$, $\vec{m}$ microphone signal

$m_{cal}(t)$, $M_{cal}(\omega)$ microphone signal during calibration

N, n number; ratio

$n(t)$, $N(\omega)$ measurement noise

OTDR Optical Time Domain Reflectometry

$P(t)$, $P(\omega)$, $p(x,t)$, $p(t)$ acoustic pressure

P_0 pressure amplitude

Pa Pascal; the SI unit of pressure (N/m^2)

p acoustic pressure; statistical significance value

p_I incident pressure amplitude

p_{mpc} mouthpiece pressure

p_R reflected pressure amplitude

p_{ref} "threshold of hearing" reference pressure level, 2×10^{-5}Pa

p_T transmitted pressure amplitude

p_0 equilibrium (atmospheric) pressure

$\dot{Q}$ flow rate

R reflection coefficient

$R_c(\omega)$ reflection response of calibration plug

$R(z)$, $R(T)$ reflectance (input impulse response)

R_i terms in the reflectance $R(z)$

$\hat{R}_o(\omega)$ estimate of $R_o(\omega)$

R_{resp} respiratory resistance

ROI Region of interest

RV residual volume

r correlation coefficient

$r_{i,i+1}$, r_i reflection coefficient between layers i and $i+1$

$r_o(i)$ elements of vector $\vec{r}_o$

$r_o(t)$, $R_o(\omega)$, $\vec{r}_o$ reflectance of an object

$\hat{r}_{ok}$ kth estimate of r_o

$r_s(t)$, $R_s(\omega)$ source reflection function

S cepstrum of signal

S_i sum of first i terms of the reflectance

$S(t)$ step response of an object

$S(t_i)$ integral of reflectance up to time t_i

SI Le Système International d'Unités

SPL Sound Pressure Level relative to $p_{ref} = 2 \times 10^{-5}$Pa

T transmission coefficient

T1 MRI relaxation time constant

T_1 source–microphone two way travel time

T_2 microphone–object two way travel time

TLC total lung capacity

t time

$t_{i,i+1}$, t_i transmission coefficient from layer i to $i+1$

U_k upward (backward) travelling wave

u particle velocity

V Volts

V_0 voltage amplitude

$V(t)$ voltage waveform

W one way travel time in the z-domain

x the x-coordinate

Z, Z_i acoustic impedance

Z_s, Z_{si} specific acoustic impedance

z discrete time variable; two way travel time

α constant; damping factor; attenuation coefficient

β attenuation coefficient

γ ratio of adiabatic to isothermal specific heats

Δ error or change in a quantity

Δt two way travel time

$\delta(t)$ delta function

ϵ error

λ constant; wavelength

$\prod$ product

ρ gas density

ρ_0 equilibrium gas density

$\sum$ sum

τ time constant; period $2\pi/\omega_0$

ϕ variable of integration; spectral power

ω angular frequency

ω_0 resonant frequency; filter cut-off frequency

ω_s sampling frequency

$\otimes$ convolution operator

Bibliography

[Barnoski and Jensen 1976] Barnoski MK and Jensen SM. Fiber waveguides: a novel technique for investigating attenuation characteristics. *Appl Opt* **15**; 2112-5.

[Beranek 1986] Beranek LL. *Acoustics* American Institute of Physics, 1986.

[Bozic 1979] Bozic SM. *Digital and Kalman filtering.* Edward Arnold, London.

[Bradley et al 1986] Bradley TD, Brown IG, Grossman RF, Zamel N, Martinez D, Phillipson EA and Hoffstein V. Pharyngeal size in snorers, nonsnorers, and patients with obstructive sleep apnea. *N Engl J Med* **315**; 1327-1331.

[Brigham 1988] Brigham EO. *The fast Fourier transform and its applications.* Prentice-Hall.

[Brooks et al 1984] Brooks LJ, Castille RG, Glass GM, Griscom NT, Wohl MEB and Fredberg JJ. Reproducibility and accuracy of airway area by acoustic reflection. *J Appl Physiol* **57**(3); 777-787.

[Brown et al 1985] Brown IG, Bradley TD, Phillipson EA, Zamel N and Hoffstein V. Pharyngeal compliance in snoring subjects with and without obstructive sleep apnea. *Am Rev Respir Dis* **132**; 211-215.

[Brown et al 1986] Brown IG, Zamel N and Hoffstein V. Pharyngeal cross-sectional area in normal men and women. *J Appl Physiol* **61**(3); 890-895.

[Brown et al 1987] Brown IB, McClean PA, Boucher R, Zamel N and Hoffstein V. Changes in pharyngeal cross-sectional area with posture and application of continuous positive airway pressure in patients with obstructive sleep apnea. *Am Rev Respir Dis* **136**; 628-632.

[Cooley and Tukey 1965] Cooley JW and Tukey JW. An algorithm for the machine calculation of complex Fourier series. *Mathematics of Computation* **19**(90); 297-301.

[Davies et al 1981] Davies JC, McIntosh J and Mulholland KA. The generation of short duration acoustic signals. *J Sound Vib* **76**; 77-82.

[Davis et al 1979] Davis DA, Harmel MH and Buckley JJ. Medical liability related to aneaesthesia: an analysis of 50 major claims. 53rd JARS Congress, Hollywood, Florida.

[Deane 1986] Deane AM. *Time domain work on brass instruments*. PhD Thesis, University of Surrey.

[Douglas 1988] Douglas NJ. The sleep apnoea/hypopnea syndrome. In *Advanced medicine 24* (edited by Sheppard MC), Royal College of Physicians, London; 62-73.

[Douglas 1990] Douglas NJ. Upper airway imaging. *Clin Phys Physiol Meas* **11**(Suppl A); 117-119.

[D'Urzo et al 1988] D'Urzo AD, Rubinstein I, Lawson VG, Vassal KP, Rebuck AS, Slutsky AS and Hoffstein V. Comparison of glottic areas measured by acoustic reflections vs. computerized tomography. *J Appl Physiol* **64**(1); 367-370.

[Elbrønd et al 1991] Elbrønd O, Hilberg O, Felding JU and Andersen OB. Acoustic rhinometry, used as a method to demonstrate changes in the volume of the nasopharynx after adenoidectomy. *Clin Otolaryngol* **16**; 84-86.

[Fincham 1985] Fincham LR. Refinements in the impulse testing of loudspeakers. *J Audio Eng Soc* **33**(3); 133-140.

[Findley et al 1988] Findley LJ, Unverzagt ME and Suratt PM. Automobile accidents involving patients with obstructive sleep apnoea. *Am Rev Respir Dis* **138**; 337-340.

[Fitch 1979] Fitch AA (ed). *Developments in geophysical exploration methods* Vol I. Applied Science Publishers; 171-2.

[Fredberg et al 1980] Fredberg JJ, Wohl MEB, Glass GM and Dorkin HL. Airway area by acoustic reflections measured at the mouth. *J Appl Physiol* **48**; 749-58.

[Gonzalez and Wintz 1977] Gonzalez RC and Wintz P. *Digital image processing.* Addison-Wesley.

[Grymer et al 1989] Grymer L, Hilberg O, Elbrønd O and Pedersen OF. Acoustic rhinometry : evaluation of the nasal cavity with septal deviations, before and after septoplastic procedures. *Laryngoscope* **99**; 1180-1187.

[Harpham 1990] Harpham S. TDR for component measurement. *Electronics and Wireless World* June 1990.

[Hassab 1978] Hassab JC. Homomorphic deconvolution in reverberant and distortional channels : an analysis. *J Sound Vib* **58**(2); 215-231.

[Hilberg et al 1989] Hilberg O, Jackson AC, Swift DL and Pedersen OF. Acoustic rhinometry: evaluation of nasal cavity geometry by acoustic reflection. *J Appl Physiol* **66**; 295-303.

[Hoffstein et al 1984] Hoffstein V, Zamel N and Phillipson EA. Lung volume dependence of pharyngeal cross-sectional area in patients with obstructive sleep apnea. *Am Rev Respir Dis* **130**; 175-178.

[Hoffstein and Zamel 1984] Hoffstein V and Zamel N. Tracheal stenosis measured by the acoustic reflection technique. *Am Rev Respir Dis* **130**; 472-475.

[Hoffstein and Fredberg 1991] Hoffstein V and Fredberg JJ. The acoustic reflection technique for non-invasive assessment of upper airway area. *Eur Respir J* **4**; 602-611.

[Ibisi and Benade 1982] Ibisi MI and Benade AH. Impedance and impulse measurements using low-cost components. *J Acoust Soc Am* **72**; S63.

[Jackson et al 1977] Jackson AC, Butler JP, Millet EJ, Hoppin FG and Dawson SV. Airway geometry by analysis of acoustic pulse response measurements. *J Appl Physiol* **43**; 523-36.

[Jansson 1970] Jansson PA. Method for determining the response function of a high-resolution infrared spectrometer. *J Opt Soc Amer* **60**(2); 184-191.

[Jones 1975] Jones JP. Impediography : a new ultrasonic technique for diagnostic medicine. In *Ultrasound in Medicine (Vol 1) : Proceedings of the 19th meeting of the American Institute of Ultrasound in Medicine* ed. White D; 489-497.

[Kinsler and Frey 1982] Kinsler LE, Frey AR, Coppens AB and Sanders JV. *Fundamentals of Acoustics.* John Wiley, 1982.

[Lavie 1983] Lavie P. Incidence of sleep apnoea in a presumably healthy, working population: a significant relationship with excessive daytime sleepiness. *Sleep* **6**; 312-318.

[Lewis and Smith 1978] Lewis PT and Smith B. A pulse technique for the measurement of the oblique incidence absorption coefficient. *Appl Acoust* **11**; 247-8.

[Marshall 1990] Marshall I. The production of acoustic impulses in air. *Meas Sci Technol* **1**; 413-418.

[Marshall et al 1991] Marshall I, Rogers M and Drummond G. Acoustic reflectometry for airway measurement. Principles, limitations and previous work. *Clin Phys Physiol Meas* **12**(2); 131-141.

[Marshall 1992a] Marshall I. Impedance reconstruction methods for pulse reflectometry. *Acustica* **76**(3); 118-128.

[Marshall 1992b] Marshall I. Acoustic reflectometry with an arbitrarily short source tube. *J Acoust Soc Am* **91**(6); 3558-3564.

[Merhaut 1986] Merhaut J. Impulse measurement of horn-type loudspeaker drivers. *J Audio Eng Soc* **34**(4); 245-254.

[Mermelstein 1967] Mermelstein P. Determination of the vocal-tract shape from measured formant frequencies. *J Acoust Soc Am* **41**; 1283-1294.

[Morikawa et al 1961] Morikawa S, Safar P and DeCarlo J. Influence of head-jaw position upon upper airway patency. *Anesthesiology* **22**; 265-270.

[Morse 1948] Morse PM. *Vibration and sound.* McGraw-Hill, New York.

[Nederveen 1969] Nederveen CJ. The curved bore. Section 37 in *Acoustical aspects of woodwind instruments* Frits Knuf, Amsterdam.

[Nicolas et al 1990] Nicolas J, Sawan M, Hétu R and Laroche C. A digitally controlled impulse-noise generation system for the study of the ear response to impulses. *Acustica* **70**; 112-126.

[Oliver 1964] Oliver BM. Time domain reflectometry. *Hewlett-Packard Journal* **15**(6); 1-8.

[Randall and Hee 1981] Randall RB and Hee J. Cepstrum analysis. *Brüel and Kjær Technical Review* **3**; 3-40.

[Resnick 1979] Resnick JR. *Acoustic inverse scattering as a means for determining the area function of a lossy vocal tract* PhD thesis, John Hopkins University.

[Rivlin et al 1984] Rivlin J, Hoffstein V, Kalbfleisch J, McNicholas W, Zamel N and Bryan AC. Upper airway morphology in patients with idiopathic obstructive sleep apnea. *Am Rev Respir Dis* **129**; 355-360.

[Robinson et al 1986] Robinson EA, Durrani TS and Peardon LG. *Geophysical signal processing* Prentice-Hall.

[Rodenstein et al 1990] Rodenstein DO, Dooms G, Thomas Y, Liistro G, Stanescu DC, Culée C and Aubert-Tulkens G. Pharyngeal shape and dimensions in healthy subjects, snorers, and patients with obstructive sleep apnoea. *Thorax* **45**; 722-727.

[Rubinstein et al 1987] Rubinstein I, McClean PA, Boucher R, Zamel N, Fredberg JJ and Hoffstein V. Effect of mouthpiece, noseclips, and head position on airway area measured by acoustic reflections. *J Appl Physiol* **63**(4); 1469-1474.

[Schafer et al 1981] Schafer RW, Mersereau RM and Richards MA. Constrained iterative restoration algorithms. *Proc IEEE* **69**(4); 432-450.

[Schroeder 1967] Schroeder MR. Determination of the geometry of the human vocal tract by acoustic measurements. *J Acoust Soc Am* **41**; 1002-1010.

[Sondhi and Gopinath 1971] Sondhi MM and Gopinath B. Determination of vocal-tract shape from impulse response at the lips. *J Acoust Soc Am* **49**; 1867-1873.

[Sondhi 1974] Sondhi MM. Model for wave propagation in a lossy vocal tract. *J Acoust Soc Am* **55**(5); 1070-1075.

[Sondhi and Resnick 1983] Sondhi MM and Resnick JR. The inverse problem for the vocal tract : numerical methods, acoustical experiments, and speech synthesis. *J Acoust Soc Am* **73**; 985-1002.

[Stansfield and Bogner 1973] Stansfield EV and Bogner RE. Determination of vocal-tract-area function from transfer impedance. *Proc IEE* **120**; 153-158.

[Tenoudji and Quentin 1982] Tenoudji FC and Quentin G. Characterization of surfaces by deconvolution of ultrasonic echoes using extended bandwidth. *J Appl Phys* **53**(6); 4057-4063.

[van Cittert 1931] van Cittert PH. Zum Einfluss der Spaltbreite auf die Intensitätswerteilung in Spektrallinien II. *Z. für Physik* **69**; 298-308.

[Ware and Aki 1969] Ware JA and Aki K. Continuous and discrete inverse-scattering problems in a stratified elastic medium. I. Plane waves at normal incidence. *J Acoust Soc Am* **45**; 911-921.

[Watson 1989] Watson AP. *Impulse measurements on tubular acoustic systems* PhD thesis, University of Surrey.

[Watson and Bowsher 1988] Watson AP and Bowsher JM. Impulse measurements on brass musical instruments. *Acustica* **66**; 170-173.

[Webb 1988] Webb S (ed) *The physics of Medical Imaging.* Adam Hilger, Bristol.

[Winter et al 1975] Winter TG, Pereira J and Bednar JB. On driving a transducer to produce pulses shorter than the natural period of the transducer. *Ultrasonics* **13**; 110-112.

[Wright 1973] Wright H. Impulse-response function corresponding to reflection from a region of continuous impedance change. *J Acoust Soc Am* **53**(5); 1356-1359.

Acknowledgements

I would like to thank Dr Gordon Drummond for first bringing acoustic reflectometry to my notice, and Dr Mike Rogers for providing the initial enthusiasm. Together with Drs Neil Douglas and Nikki Maran they have provided the clinical drive to develop the technique in Edinburgh, and have taught me all I know about respiration.

Visiting MSc student Mr Richard Newmark and clinical research fellow Dr Mohammed Jan worked together in smoothing out a final version of the reflectometer software. Mohammed then began trials with volunteers and patients.

The Scottish Home and Health Department (SHHD) generously provided the equipment for this research work, and later funded a technician to assist with patient data collection and analysis. This post has been ably filled by Karen Bradley and more recently by Sascha Martin. Between them, they have overcome the idiosyncrasies of the reflectometer and amassed vast amounts of data. SHHD also made possible a visit to the respiratory physiology laboratories in Harvard and Toronto.

Mr George Campbell hand-crafted several vital parts of the reflectometer and the test objects, and Mr Iain Bishop built up various circuit boards.

Professor Jonathan Best and Dr Ewen Rimmington kindly provided access to MRI facilities.

Dr Murray Campbell of the Department of Physics provided facilities and expertise for measuring microphone responses and acoustic impedances.

Thanks to Professor Norman McDicken and Dr Harry Brash for unobtrusive supervision and guidance.

Special thanks are due to my father and my wife Lee for proof-reeding an early version of the thesis and drawing my attention to numerous inconsistencies and spelling mistakes. Lee has provided constant moral support during my long absences in the laboratory.

Declaration

I declare that this thesis has been composed by me and that the work is my own.

........Ian Marshall................

Publications

Published

Marshall I. (1990) "The production of acoustic impulses in air". *Meas Sci Technol* **1**; 413-418.

Marshall I, Rogers M and Drummond G. (1991) "Acoustic reflectometry for airway measurement. Principles, limitations and previous work". *Clin Phys Physiol Meas* **12**(2); 131-141.

Marshall I. (1992a) "Impedance reconstruction methods for pulse reflectometry". *Acustica* **76**(3); 118-128.

Marshall I. (1992b) "Acoustic reflectometry with an arbitrarily short source tube".

J Acoust Soc Am **91**(6); 3558-3564.

Submitted

Marshall I, Maran NJ, Martin S, Jan MA, Rimmington JE,

Best JJK, Drummond GB and Douglas NJ. "Acoustic reflectometry for airway measurement. Clinical implementation and preliminary results".

Conference presentation

Marshall I. (1991) "Airway measurement by acoustic reflectometry". Biological Engineering Society meeting on respiratory measurement, Oxford, November 1991.

Clin. Phys. Physiol. Meas., 1991, Vol. 12, No. 2, 131–141. Printed in the UK

Acoustic reflectometry for airway measurement. Principles, limitations and previous work

Ian Marshall†, Michael Rogers‡ and Gordon Drummond§

† Department of Medical Physics and Medical Engineering, Western General Hospital, Edinburgh EH4 2XU, UK
‡ Department of Otolaryngology, Royal Infirmary, Edinburgh EH3 9YW, UK
§ Department of Anaesthetics, Royal Infirmary, Edinburgh EH3 9YW, UK

Received 5 July 1990, in final form 24 November 1990

Abstract. Acoustic pulse reflectometry is a relatively recent technique which allows the non-invasive measurement of human airways. The technique consists of guiding an acoustic impulse through the subject's mouth and into the airway. Suitable analysis of the resulting reflection (the 'echo') allows a reconstruction of the area-distance function. The non-invasive nature of the technique offers significant advantages over the established methods of x-ray cephalometry and CT scanning, and makes it very attractive for the investigation of ENT problems and sleep apnoea, and in the anaesthetic management of patients. This paper describes the theory and limitations of acoustic reflectometry, discusses previous work, and suggests some modifcations: it is currently being implemented clinically.

1. Introduction

There has long been an interest in estimating human airway dimensions in the field of speech research. Various workers have attempted to correlate upper vocal tract measurements with the vowel sounds being produced, with the long-term objective being the synthesis of intelligible speech by appropriate manipulation of models. With the recent explosive growth in computer technology, physical models have largely been replaced by mathematical ones, and solid state 'speech synthesisers' are now available commercially.

The early work was carried out in the frequency domain, usually by measuring the input impedance at the mouth as a function of frequency (Mermelstein 1967, Schroeder 1967, Paige and Zue 1970, Stansfield and Bogner 1973). By making an assumption about the vocal tract length, it is possible to use the poles and zeroes (the 'resonances') of the input impedance to estimate the area function.

Schroeder (1967), for example, shows clearly how the displacement of the resonant frequencies from a harmonic series can be interpreted in terms of area perturbations about a uniform tract.

In 1971, Sondhi and co-workers (Sondhi and Gopinath 1971, Sondhi and Resnick 1983) began using time-domain reflectometry at Bell Telephone Laboratories for the same purpose. The first mention of physiological application of the technique does not appear until 1977 when Jackson (Jackson *et al* 1977) set up a system at Harvard University for the investigation of excised dog tracheas and lungs.

Later, Fredberg (Fredberg *et al* 1980) developed the technique for use with human patients. His equipment is currently used experimentally at Boston Children's Hospital, and by respiratory clinicians (Hoffstein and Zamel 1984, Hoffstein *et al* 1987, Rubinstein *et al* 1987) in Toronto.

Acoustic reflectometry has also been used at the University of Surrey for the investigation of brass musical instruments (Deane 1986, Watson and Bowsher 1988, Watson 1989).

The principle of the technique is appealingly simple (figure 1). An acoustic impulse is launched from a source transducer, and passes down a wave tube into the object being measured. The impulse and the reflection from the object are recorded by a pressure-sensitive transducer and computer system. Appropriate analysis of the reflected waveform leads to a reconstruction of the impedance (and hence the area) profile of the object. The theory is similar to that of the more familiar optical time domain reflectometry (OTDR) technique employed for fault-finding on fibre-optic cables (Barnoski and Jensen 1976).

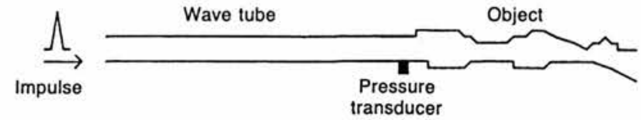

Figure 1. The principle of acoustic reflectometry.

The clinical attractions of the technique are many. It is non-invasive and intrinsically safe, with no risk to the patient. Repeated studies are thus possible, unlike the case with x-ray cephalometry or CT measurements. The equipment is simple to use. It is also cost-effective, with start-up costs of the order of £1,000 for the acoustic transducers, wavetube and computer interface card, plus £2,000 for a suitable IBM AT-compatible computer system. Acoustic reflectometry is equally suitable for use in out-patient clinics and in in-patient wards and departments.

In the next section, the derivation of the area reconstruction algorithm is summarised, and we show that approximate algorithms can be used under certain conditions. These approximate reconstruction techniques are computationally much less demanding, and permit real-time measurement of object areas.

2. The theory of acoustic reflectometry

2.1. The forward problem; the reflectance function

The theory of reflections arises naturally in many branches of physics, for example in seismography, in the study of optical films, and in electrical transmission line theory. Much of the mathematics used in the present work was originally developed by geophysicists for use in seismic surveying.

The object being measured is considered as a series of (typically 100 to 200) discrete cylinders, each having the same length L (figure 2). Since the acoustic impedance Z of a cylinder is inversely proportional to its cross-sectional area, the object is thus represented as a series of impedance sections or layers.

The object is terminated at both ends by semi-infinite sections from which there are no returning reflections. One-dimensional plane-wave propagation is assumed. An acoustic impulse I incident on the object (figure 3) will be partially reflected and partially transmitted at each interface between layers. Energy undergoing a single reflection at an interface before emerging from the object (e.g. ray R_0) constitutes a 'primary' reflection, whilst energy which has reverberated (i.e. undergone multiple reflections) before emerging (e.g. most components of ray R_3) constitutes 'secondary' and higher order reflections. The pressure waveform observed at the mouth of the object consists of a series of returning impulses spaced apart by the two-way travel time Δt through a single layer.

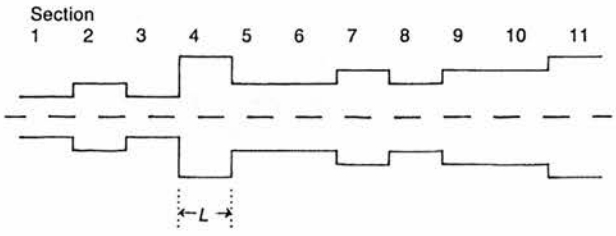

Figure 2. Discrete representation of an object.

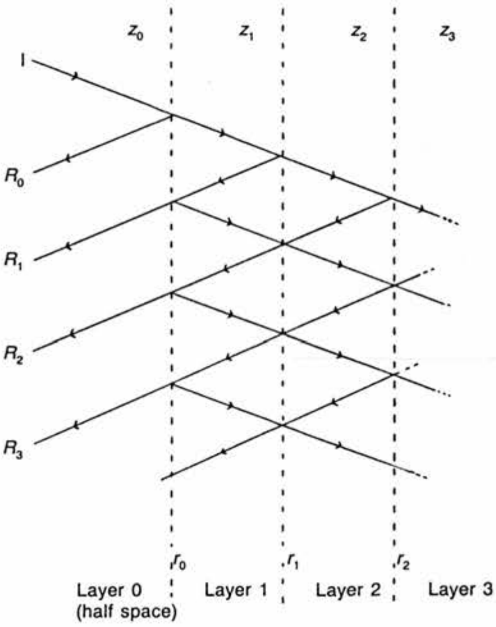

Figure 3. Multiple reflections within a series of layers. I is the incident impulse. R_0, R_1, R_2, etc., are successive terms in the observed reflectance.

An expression for the reflection pattern can be developed using recursive formulae. Stansfield and Bogner (1973) present a method which describes clearly the propagation of the incident impulse and its reflections, but at some cost to the mathematical load. The equivalent exposition by Ware and Aki (1969) is particularly suited to the reconstruction problem, and is the method summarised here. They define a 'layer matrix' which relates the forward and backward travelling waves in one section (layer k) to the forward and backward travelling waves in the adjacent layer $k + 1$ (figure 4 and equation (1)). Because their interest was in the seismological problem, the waves were labelled as 'Downgoing' (D) and 'Upcoming' (U), and the notation has become established. The layer matrix takes account of the reflection coefficient r_k at the interface, and the travel time through the

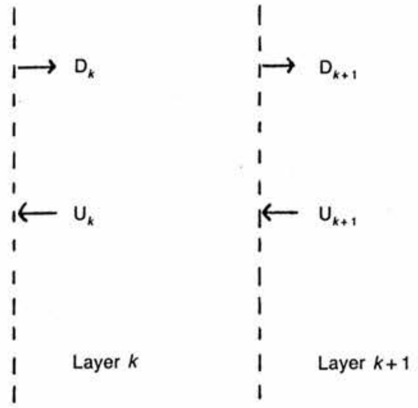

Figure 4. Forward ('Downgoing') and reverse ('Upcoming') waves in adjacent layers.

layer. The reflection coefficient is defined in the usual way as $r_k = (Z_{k+1} - Z_k)/(Z_{k+1} + Z_k)$, and the transmission coefficient t_k is given by $t_k^2 = (1 - r_k^2)$. For convenience, we work in the z-domain, with the two-way travel time being given by unit delay (z). We let W be the one-way travel time, given by $W^2 = z$.

$$\begin{bmatrix} U(k,z) \\ D(k,z) \end{bmatrix} = \frac{1}{Wt_k} \begin{bmatrix} z & r_k z \\ r_k & 1 \end{bmatrix} \begin{bmatrix} U(k+1,z) \\ D(k+1,z) \end{bmatrix} \tag{1}$$

By multiplying together successive layer matrices, it is possible to relate the first layer (0) to layer k in the general expression:

$$\begin{bmatrix} U(0,z) \\ D(0,z) \end{bmatrix} = \frac{1}{W^{k+1}\prod_{i=0}^{k} t_i} \begin{bmatrix} z^{k+1} F(k,1/z) & z^{k+1} G(k,1/z) \\ G(k,z) & F(k,z) \end{bmatrix} \begin{bmatrix} U(k+1,z) \\ D(k+1,z) \end{bmatrix} \tag{2}$$

The notation is kept to manageable proportions by introducing the recursive polynomials F and G, which are functions of the individual reflection coefficients r_i and the travel time. They are given by:

$$\begin{aligned} F(k+1,z) &= F(k,z) + r_{k+1} z G(k,z) \\ G(k+1,z) &= r_{k+1} F(k,z) + z G(k,z) \end{aligned} \tag{3}$$

with $F(0,z) = 1$ and $G(0,z) = r_0$.

The particular case of interest in pulse reflectometry is that with the following boundary conditions; (i) the Downgoing wave in the first layer is the incident impulse, with a z-transform of unity; (ii) the Upcoming wave in the first layer is the observed reflection, and under these conditions is termed the 'Reflectance' $R(z)$ (Sondhi and Resnick 1983) or the 'Input Impulse Response' (Watson and Bowsher 1988); (iii) the Downgoing wave in the bottom (nth) layer is some (unknown) transmission function, and (iv) there is no Upcoming wave returning from the terminating half-space. Inserting these boundary values in equation (2) and rearranging, we obtain an expression for the reflectance function of an arbitrary object of n layers:

$$R(z) = \frac{z^{n+1} G(n,1/z)}{F(n,z)} \tag{4}$$

2.2. The inverse problem; reconstruction

Using equation (4) to calculate the reflectance produced by a given object is the 'direct' or 'forward' problem, and we will use this later. Ware and Aki continued their exposition by developing a reconstruction algorithm for the 'inverse' problem encountered when estimating acoustic impedances from a recorded reflection; that is, given a reflectance function R, to reconstruct the spatial distribution of impedances (i.e. areas) that must have caused it. It is important to realise that we have no means of knowing how a given area is physically made up; reflectometry simply allows us to estimate an equivalent total cross-sectional area as a function of distance. In the absence of further information, we have to regard the area as having cylindrical symmetry, although this is obviously not true in the case of the human airway. Suitable rearrangement of equation (4) and expansion of the polynomials leads to equations (5), allowing the individual reflection coefficients to be evaluated in succession;

$$
\begin{aligned}
r_0 &= R_0 \\
r_1 &= R_1(1 - r_0^2)^{-1} \\
r_2 &= (R_2 + r_0 r_1 R_1)\,[(1 - r_0^2)(1 - r_1^2)]^{-1} \\
&\text{etc.}
\end{aligned} \tag{5}
$$

Generally,

$$r_{k+1} = \sum_{j=0}^{k} F_j R_{k+1-j} \left[\prod_{j=0}^{k} (1 - r_j^2)\right]^{-1}$$

where F_j is the coefficient of z^j in the polynomial $F(k,z)$.

This 'Ware-Aki' algorithm has several interesting features:

(i) To reconstruct N layers, it is necessary and sufficient to record the reflectance function up to the time that the primary reflection from the interface between layers N and $N + 1$ arrives back at the detector. It is not necessary to wait for all the reverberations to decay to an insignificant level.

(ii) It is a 'marching' algorithm, in that the estimation of more distant impedances depends on the intervening layers. Hence the accuracy obtainable deteriorates as the distance increases, particulaly if large impedance discontinuities are encountered.

(iii) Inspection of the steps involved reveals that the number of multiplications required is of the order of N^2 for reconstruction of N layers. Hence the algorithm is computationally intensive and quite slow to perform.

(iv) Implicit in the reconstrucion is an integrating action along the sampled data points. This has an important bearing on the type of noise that can be tolerated on the signals. Whilst the algorithm is fairly immune to short-term bipolar fluctuations, as might be caused by high frequency random noise on the data, it is very vulnerable to slow drifts and offsets.

2.3. Cross modes and axial resolution

The reflectance theory summarised above assumes that an ideal acoustic impulse (a δ-function) is incident on the object. In practice, this is neither realisable nor in fact desirable. The problem with using an extremely broadband pulse is that cross-modes may be excited in the object, violating the assumption of one-dimensional plane wave propagation. To avoid cross-modes, the frequency content of the pulse should be tailored to avoid frequencies whose wavelength is less than twice the maximum diameter of the object. Since the axial resolution is in turn limited to approximately the wavelength used, the smallest longitudinal details that can be measured reliably are of the same order of size as the maximum object diameter. This restricts the resolution to 2 - 3 cm in the human airway (neglecting for the moment the effect of the mouth), and obviously affects the clinical usefulness of the technique. This poor resolution may be partly responsible for the slow uptake of a technique that has so many potential advantages. In section 3, we will discuss some ways around the resolution problem.

2.4. Approximate reconstruction

With $N = 100$, the Ware-Aki reconstrucion algorithm takes approximately 2 s to run on our computer system (a 10 MHz AT-compatible machine, with the algorithm implemented in Turbo Pascal). The time taken is obviously dependent on the efficiency of the code and compiler, and is intended here as a guide figure only. Two seconds in between area reconstructions was considered unacceptably slow for investigation of 'real-time' airway geometry, and faster, approximate reconstruction methods were sought.

Expansion of the reflectance expression (equation (4)) for the simple case of two interfaces ($n = 1$) (figure 5 and equation (6)) clearly shows the primary (R_0 and R_1) and the multiple (R_2, R_3, etc) reflection terms:

$$R(1,z) = r_0 z + r_1(1 - r_0^2)z^2 - r_0 r_1^2(1 - r_0^2)z^3 + r_0^2 r_1^3(1 - r_0^2)z^4 \ldots .$$
$$(R = R_0 + R_1 + R_2 + R_3 + \ldots ..$$

(This is equation (6), the reflectance function for two interfaces.)

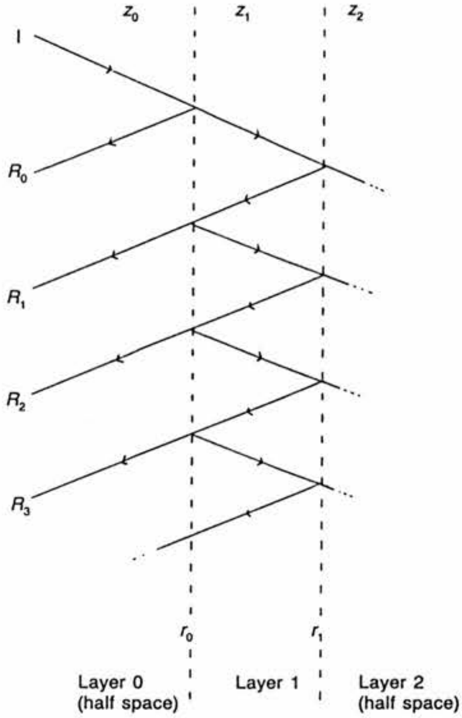

Figure 5. Reflections with two interfaces. R_0 and R_1 are primary reflections, whilst R_2, R_3, etc. are multiple reflections arising from reverberation within Layer 1.

Observing that the multiple reflection terms fall off as $r_0 r_1$ leads us to suspect that these terms may not be significant with some objects, particularly those of a smoothly tapered 'clinical' type. To test this hypothesis, reflectance functions were calculated for various objects, and the resultant data then 'reconstructed' using the Ware-Aki algorithm and several approximate methods. Figure 6 shows the results for the case of a simulated object having impedances in the ratio of 1:2:4 (i.e. area ratios 4:2:1), with discontinuities at the interfaces. When the reflectance (*a*) is processed by the full Ware-Aki algorithm, the area profile is faithfully reproduced (*b*). When the same reflectance data are processed by an approximate 'Primaries' algorithm which ignores the multiple reflection terms, the result is as shown in (*c*). The third impulse in the reflectance function causes a slight overestimation (+10%) in the final area. An alternative approximate reconstruction algorithm (based on Oliver (1964), Wright (1973) and Jones (1975)), which treats the data in a way that explicitly brings out the integral nature of the analysis, leads to the result shown in (*d*). The area reconstructed by this 'Integral' method is correct except for a slight 'undershoot' (−10%) in the transition region.

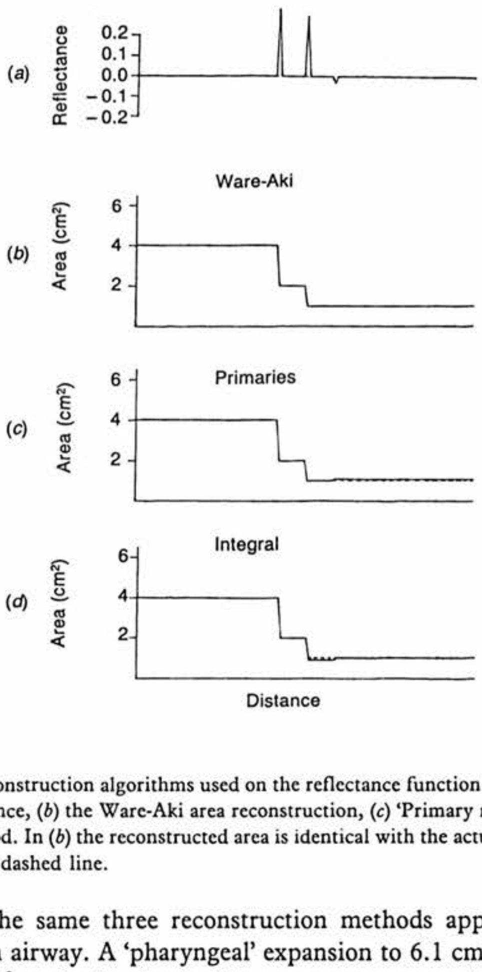

Figure 6. Alternative reconstruction algorithms used on the reflectance function of an object having areas in the ratio 4:2:1. (*a*) the reflectance, (*b*) the Ware-Aki area reconstruction, (*c*) 'Primary reflections only' reconstruction, and (*d*) the 'Integral' method. In (*b*) the reconstructed area is identical with the actual area. In (*c*) and (*d*) the actual area function is shown in dashed line.

Figure 7 shows the same three reconstruction methods applied to an area function representing a human airway. A 'pharyngeal' expansion to 6.1 cm^2 is followed by a 'glottal' constriction of 0.9 cm^2, and a 'trachea' with a constant cross-sectional area of 2.0 cm^2. The reflectance function (*a*) was calculated by a method based on Stansfield and Bogner (1973).

The Ware-Aki method (*b*) reconstructs the area function perfectly, whilst the Primaries method (*c*) underestimates the pharyngeal peak by 5% (5.8 instead of 6.1 cm^2) and overestimates the glottal area by 33% (1.2 instead of 0.9 cm^2). Beyond the glottis, the apparent tracheal area returns to 2 cm^2 only very slowly. Results with the Integral method (*d*) are very similar, except that the pharyngeal peak is this time overestimated by 7% (6.5 instead of 6.1 cm^2), and the correct tracheal area is approached more rapidly following the glottal constriction.

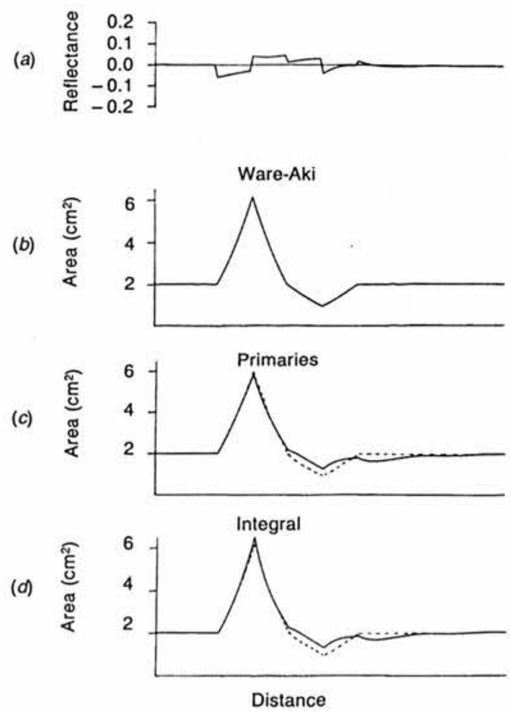

Figure 7. Reconstruction of the reflectance function of an object representing the upper airway. Details as for figure 6.

Since the number of computations for the approximate methods is of order N (rather than N^2 for the complete method), the time-saving is considerable, and results in a reconstruction time of approximately 100 ms for $N = 100$, compared with 2 s for the Ware-Aki method. Figures 6 and 7 suggest that these approximate algorithms may be acceptable for measurements of supraglottal airway dimensions, and for rapid assessment of airway patency at lower levels. For accurate measurements, especially sub-glottal ones, the Ware-Aki algorithm is clearly necessary, and we are currently investigating ways of making this feasible in true real-time.

3. Airway walls

The theory of reflectometry assumes that the object walls are acoustically rigid relative to the air, and do not yield to the internal pressure fluctuations. This is not strictly true for the human airway, whose walls are known to behave dynamically at frequencies below about 1 kHz. The effect is to degrade the reflectance and hence the reconstructed area functions.

The departure from the actual area will increase with depth because of the 'marching' nature of the signal processing, and will be most important when either great accuracy, or measurements of the lower airway are desired.

Sondhi (Sondhi and Resnick 1983) used the theory of viscous and thermal losses in trying to allow for non-ideal wall behaviour. Fredberg (Fredberg *et al* 1980, Brooks *et al* 1984) was interested in airway branching and lung morphology, and so it was important to maintain accuracy as far as possible. He favoured a direct physical approach to the wall problem, and originally used two modifications to the straightforward technique. The aim was to extend the measurement bandwidth so that a greater proportion of the data was provided by reflections in the 'rigid' wall regime, above 1 kHz. The problem with simply using higher pulse frequencies is that of exciting cross-modes as discussed in section 2.3.

(i) Recognising that cross modes would theoretically form in the mouth first (as this is the part of the airway with the greatest diameter), Fredberg initially used custom-moulded mouthpieces partially to fill the mouth of subjects. Later work by Fredberg, and in Toronto (Rubinstein *et al* 1987) replaces these special mouthpieces with simple 'scuba' types, and the results obtained are very similar. One possible explanation offered for this finding is that the distance between the cheeks is reduced when using a scuba mouthpiece. It may also be possible that the mouth area is relatively small anyway, or that cross-mode propagation is not as significant as expected in degrading measurements of areas beyond the mouth.

(ii) Fredberg's second method of extending the measurement bandwidth is to use a helium-oxygen (HeO_2) breathing mixture. Because the wave speed is twice that in air, the bandwidth can be doubled for the same object dimensions. The use of frequencies up to 12 kHz is possible for airway measurements. Unfortunately, there are several distinct disadvantages with this approach; (a) the use of HeO_2 requires considerably more complicated and bulky equipment, including valves, cylinders and reservoir bags; (b) equilibration of the subject takes several minutes, during which time uncomfortable noseclips must be worn to ensure that air does not enter through the nose and mix with the HeO_2. In view of the acoustic pulse shape used by Fredberg it is in any case questionable whether he is actually producing significant excitation at the extended frequencies. Further comparison of the use of air and HeO_2 with extended frequency is necessary.

4. Equipment considerations

4.1. Acoustic pulse production

For the production of acoustic pulses, Jackson (Jackson *et al* 1977) used a spark discharge generating frequencies up to several kHz. There were problems with stability of amplitude and frequency content. Other workers (e.g. Fredberg *et al* 1980, Deane 1986) have used the natural impulse response of a loudspeaker – that is, the pressure waveform produced when the device is excited by a short electrical pulse. Such an impulse response typically lasts 2 - 3 ms and contains significant frequency content up to only a few kHz. It is therefore necessary to deconvolve the recorded echo waveform with the impulse response in order to estimate the true reflectance, and this deconvolution can itself be quite time-consuming. In a later paper, we will describe an alternative approach which is applicable in certain cases.

4.2. Geometry

The simplest acoustic reflectometer follows the principles described, and is shown in figure 8. A pulsed sound source (e.g. a loudspeaker) is acoustically coupled to one end of a source tube, and a pressure-sensitive microphone is mounted in the tube wall near the other end. The object to be measured is coupled to this end. The overall length of the tube (L_{sm} + L_{mo}) between the source and the mouth of the object must be greater than the length L_o of the object. This is to prevent multiple reflections off the source returning to the microphone before all the primary reflections from the object have been recorded.

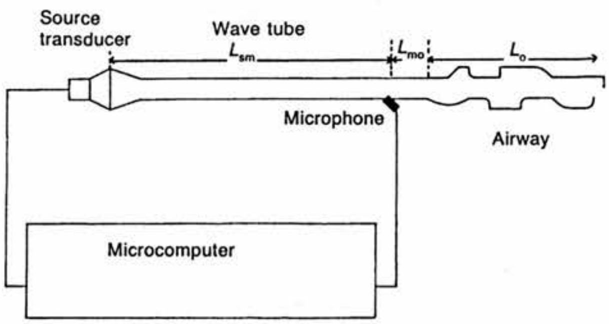

Figure 8. Block diagram of a simple 'closed' reflectometer system, showing the important dimensions (see text).

To facilitate a very simple time-domain separation of the incident pulse from the reflected signal, it is convenient for the incident impulse to have passed the microphone completely before the first reflection (from the mouth of the object) can reach the microphone. This demands that L_{mo} be greater than the spatial length of the pulse, and, for a typical loudspeaker impulse response of 3 ms, would lead to L_{mo} being approximately 1 m. This is clearly inconveniently long, and a compromise would be reached by making L_{mo} such that the initial peak of the pulse passes before reflections can return. A subtraction is then used to separate the incident and reflected pressure waveforms.

Note that the reflectometer system of figure 8 is 'closed' in that it does not allow breathing whilst measurements are in progress. The systems described in the literature (Brooks *et al* 1984, Hoffstein *et al* 1987) allow free breathing in between measurement sessions. When the subject is coupled to the wavetube to permit acoustic measurement, only rebreathing from a spirometer (via the 2 m wavetube) is possible. There is no mechanism for removal of CO_2. It would be of considerable clinical usefulness if continuous, normal breathing could be sustained without active subject cooperation, and for prolonged measurement periods.

5. Summary

The principles of acoustic reflectometry have been described, and the assumptions and limitations of the technique explained.

Acknowledgements

The evaluation of acoustic pulse reflectometry is funded in part by the Scottish Home and Health Department, who also made possible a visit to the facilities at Harvard University and Toronto General Hospital.

References

Barnoski M K and Jensen S M 1976 Fiber waveguides : a novel technique for investigating attenuation characteristics *Appl. Opt.* **15** 2112-5

Brooks L J, Castile R G, Glass G M, Griscom N T, Wohl M E B and Fredberg J J 1984 Reproducibility and accuracy of airway area by acoustic reflection *J. Appl. Physiol.* **57** 777-87

Deane A M 1986 Time domain work on brass instruments *PhD thesis* University of Surrey

Fredberg J J, Wohl M E B, Glass G M and Dorkin H L 1980 Airway area by acoustic reflections measured at the mouth *J. Appl. Physiol.* **48** 749-58

Hoffstein V, Castile R G, O'Donnell C R, Glass G M, Strieder D J, Wohl M E B and Fredberg J J 1987 *In vivo* estimation of tracheal distensibility and hysteresis in normal adults *J. Appl. Physiol.* **63** 2482-9

Hoffstein V and Zamel N 1984 Tracheal stenosis measured by the acoustic reflection technique *Am. Rev. Respir. Dis.* **130** 472-5

Jackson A C, Butler J P, Millet E J, Hoppin F G and Dawson S V 1977 Airway geometry by analysis of acoustic pulse response measurements *J. Appl. Physiol.* **43** 523-36

Jones J P 1975 Impediography: a new ultrasonic technique for diagnostic medicine *Ultrasound in Medicine* Vol 1 (Proc. 19th Meeting Am. Inst. Ultrasound Med.) ed D White pp 489-97 (New York: Plenum)

Mermelstein P 1967 Determination of the vocal-tract shape from measured formant frequencies *J. Acoust. Soc. Am.* **41** 1283-94

Oliver B M 1964 Time domain reflectometry *Hewlett-Packard Journal* February 1964 pp 1-8

Paige A and Zue V W 1970 Computation of vocal tract area functions *IEEE Trans. Audio Electroacoust.* **AE-18** 7-18

Rubinstein I, McClean P A, Boucher R, Zamel N, Fredberg J J and Hoffstein V 1987 Effect of mouthpiece, noseclips and head position on airway area measured by acoustic reflections *J. Appl. Physiol.* **63** 1469-74

Schroeder M R 1967 Determination of the geometry of the human vocal tract by acoustic measurements *J. Acoust. Soc. Am.* **41** 1002-10

Sondhi M M and Gopinath B 1971 Determination of vocal-tract shape from impulse response at the lips *J. Acoust. Soc. Am.* **49** 1867-73

Sondhi M M and Resnick J R 1983 The inverse problem for the vocal tract: Numerical methods, acoustical experiments, and speech synthesis *J. Acoust. Soc. Am.* **73** 985-1002

Stansfield E V and Bogner R E 1973 Determination of vocal-tract-area function from transfer impedance *Proc. IEE* **120** 153-8

Ware J A and Aki K 1969 Continuous and discrete inverse-scattering problems in a stratified elastic medium. I. Plane waves at normal incidence *J. Acoust. Soc. Am.* **45** 911-21

Watson A P 1989 Impulse measurements on tubular acoustic systems *PhD thesis* University of Surrey

Watson A P and Bowsher J M 1988 Impulse measurements on brass musical instruments *Acustica* **66** 170-3

Wright H 1973 Impulse-response function corresponding to reflection from a region of continuous impedance change *J. Acoust. Soc. Am.* **53** 1356-9

Sonderdruck aus / Reprint from

ACUSTICA

International Journal on Acoustics

Recognized by the
Federation of the Acoustical Societies of Europe

Recognized by the
European Physical Society

Recognized by the Institute of
Acoustics of Great Britain

Unter Mitwirkung der
Deutschen Physikalischen Gesellschaft

Avec le patronage de la
Société Française d'Acoustique

S. Hirzel Verlag · Stuttgart

ACUSTICA

International Journal on Acoustics

Recognized by the Federation of the Acoustical Societies of Europe
Recognized by the European Physical Society
Recognized by the Institute of Acoustics of Great Britain
Unter Mitwirkung der Deutschen Physikalischen Gesellschaft
Avec le patronage de la Société Française d'Acoustique

ACUSTICA is an International Journal on Acoustics. Manuscripts submitted for publication should deal with original research, not yet published elsewhere. They should together with two copies be sent to the English, French or German editor or according to the original language used or to the editor-in-chief. Manuscripts are critically refereed by two experts and reviewed by the editors and the editor-in-chief before acceptance.
For details of manuscript preparation reference is made to the hints for authors appended to the subject index of each volume. These should be carefully followed. A copy of "Hints for Authors" may also be requested from the editor-in-chief.
Acceptance is made on the understanding that the author(s) agree(s) to the exclusive transfer of the copyright to the publisher for a period of one year after publication. Thereafter the copyright automatically reverts to the author(s).
No honorarium is paid, but authors are entitled to 50 free reprints. Additional reprints may be ordered at a fixed price prior to the publication.
Books concerning acoustics may only be sent for reviewing to the editor-in-chief (see above). The editors decide upon their being reviewed or not. Copies for review will not be returned.

ACUSTICA is regularly listed in:
Applied Mechanics Reviews;
Current Contents/Physical Sciences;
Current Contents/Engineering, Technology and Applied Sciences; Science Citation Index.

ACUSTICA is published monthly in issues which are combined into volumes. The volumes do not relate to a calender year. Subscription rate: DM 288.– per volume, special price for members of the "Deutsche Physikalische Gesellschaft", the "Institute of Acoustics of Great Britain", and the "Société Française d'Acoustique" DM 230.40. The price for a single issue depends on size (see below). All prices plus postage. Subscriptions are made on a continuation basis unless ordered for a limited period. Cancellations of a subscription can be made after completion of a volume only and must reach the publisher no later than four weeks after receipt of the first issue to become effective for the subsequent volume.

Publisher: S. Hirzel Verlag GmbH & Co., Birkenwaldstraße 44, P.O. Box 10 22 37, D-7000 Stuttgart 10, F.R. Germany. Tel.: 07 11/25 82-0; Telex 23 636 daz d; Fax 07 11/25 82-2 90.

Responsible for Text Material: Dir. u. Prof. a. D. Dr. Rudolf Martin, Physikalisch-Technische Bundesanstalt, Bundesallee 100, D-3300 Braunschweig, F.R. Germany.

Responsible for Advertisements: Klaus Urbitsch, Birkenwaldstraße 44, P.O. Box 10 22 37, D-7000 Stuttgart 10, F.R. Germany. Tel. 07 11/25 82-2 45. Present effective rate card: January 1, 1992.

Typset and printed by K. Triltsch, Graphischer Betrieb, Haugerring 5, D-8700 Würzburg.

ISSN 001-7884

ACUSTICA Vol. 76, No. 1, Price of this issue: DM 50.70

Impedance Reconstruction Methods for Pulse Reflectometry

I. Marshall
Department of Medical Physics and Medical Engineering, University of Edinburgh

Impedance Reconstruction Methods for Pulse Reflectometry

Summary

A comparison is made between several algorithms used for the reconstruction of impedance layers from reflection measurements. The trade-off between accuracy and computation time is investigated for several theoretical and experimental cases. For continuous monotonic impedance changes, approximate methods producing reconstruction errors of less than 2% are some 20 times faster than the "complete" methods, when 100 sample points are used. The errors increase to 10% for discontinuous impedance changes. For highly non-monotonic impedance variations, the corresponding errors are approximately 25%. The results are applicable to geophysics, transmission line analysis, and time domain reflectometry.

Methoden der Impedanzrekonstruktion für die Impuls-Reflektometrie

Zusammenfassung

Verschiedene Algorithmen für die Rekonstruktion von Impedanzbelägen aus Reflexionsmessungen werden miteinander verglichen. Es wird für verschiedene theoretische und experimentelle Fälle der Kompromiß zwischen Genauigkeit und Rechenzeit untersucht. Für monotone Impedanzänderungen sind Näherungsmethoden, die mit einem Rekonstruktionsfehler von weniger als 2% behaftet sind, etwa 20 mal schneller als die „vollständigen" Methoden, wenn 100 Abtastpunkte benutzt werden. Für unstetige Impedanzänderungen steigen die Fehler auf 10% an, während sie für stark nichtmonotone Impedanzänderungen etwa 25% betragen. Die Ergebnisse können auf die Geophysik, die Untersuchung von Übertragungsleitungen und auf die Zeitdomänen-Reflektometrie angewandt werden.

Méthodes de reconstitution d'impédance pour la réflectométrie en impulsion

Sommaire

On compare plusieurs algorithmes utilisés pour reconstituer l'impédance de couches à partir de mesures de réflexion. On recherche un compromis entre précision et temps de calcul pour plusieurs cas théoriques et expérimentaux. Pour des variations continues monotones de l'impédance, les méthodes approchées produisant une erreur de reconstitution inférieure à 2% sont vingt fois plus rapides que les méthodes «complètes», lorsque l'on utilise un échantillonnage de cent points. Le taux d'erreur monte à 10% pour des variations discontinues de l'impédance. Pour les variations fortement non-monotones de l'impédance, les erreurs correspondantes sont d'environ 25%. Les résultats sont applicables à la géophysique, l'analyse des lignes de transmission et la reflectométrie dans le domaine temporel.

1. Introduction

The inverse problem of reconstructing a series of impedance layers from externally measured reflections arises in a number of fields in physics and engineering. Most notable are seismological surveying, electrical transmission line analysis, optical time domain reflectometry (OTDR) and acoustic pulse reflectometry.

The measurement technique known as pulse reflectometry consists of sending an impulse into the medium under investigation, and recording the resultant reflected energy (the "echo"). Various time-domain reconstruction algorithms are available for deducing the impedance layers from the reflections, but a practical, comparative survey has not been carried out. The objective of the present work is to compare, both analytically and experimentally, the performance of several reconstruction methods, bringing together the relevant literature with a common notation.

The chief impetus was the desire to investigate the importance of multiple reflections, since the algorithms which take full account of them are computationally intensive. The author's application is the measurement of human airways by acoustic pulse reflectometry. To be of clinical use, it is highly desirable to have a "real-time" display of reconstructed areas.

2. The theory of multiple reflections

2.1. The layered medium

The object under investigation is represented as a series of impedance sections or layers, terminated at

Received 12 November 1990,
accepted 3 November 1991.

I. Marshall, Department of Medical Physics and Medical Engineering, Western General Hospital, Edinburgh, EH4 2XU, United Kingdom.

both ends by semiinfinite sections ("half-spaces") from which there are no returning reflections. Losses are neglected. One-dimensional plane-wave propagation at normal incidence is assumed, although the rays are usually offset in diagrams to improve clarity. Analysis is made possible be requiring the travel times of all the layers to be equal. This "Goupillaud" model [1] is treated in standard geophysics texts [2, 3]. If the sampling interval is made small enough, the travel-time restriction has minimal effect on the interpretation of real data. Berryman and Greene [4] show how integration of the reflections over the sampling period eliminates the problem entirely.

Returning to the Goupillaud model, an impulse I incident on the object (Fig. 1) will be partially reflected and partially transmitted at each interface between layers. Energy undergoing a single reflection at an interface before emerging from the object (e.g. ray R_0) constitutes a "primary" reflection, whilst energy which has undergone multiple reflections before emerging (e.g. most components of ray R_3) constitutes "secondary" and higher order reflections. The number of multiply reflected components increases very rapidly as the number of layers is increased. The waveform observed in the near half-space (Layer 0) consists of a series of returning impulses spaced apart by the two-way travel time (Δt) through a single layer.

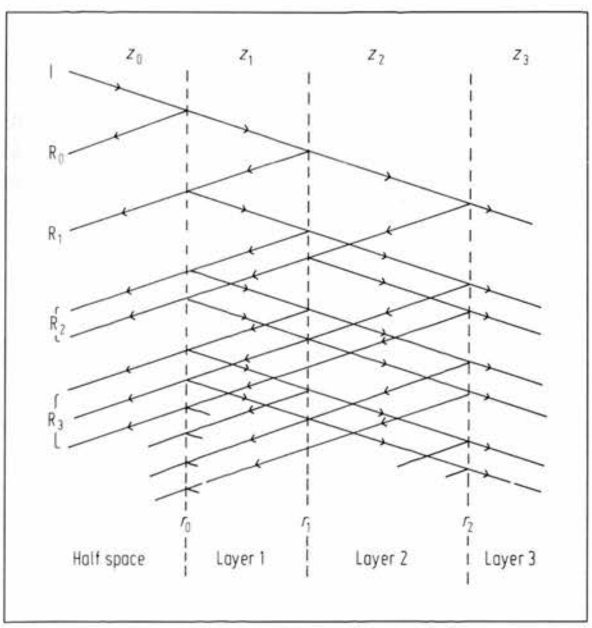

Fig. 1. Multiple reflections within a series of layers having impedances Z_1, Z_2, Z_3, etc. I is the incident impulse, whilst R_0, R_1, etc are successive terms in the observed reflectance. The thicknesses of the layers are such that the travel times are all equal, and so the various components of each reflectance term arrive simultaneously.

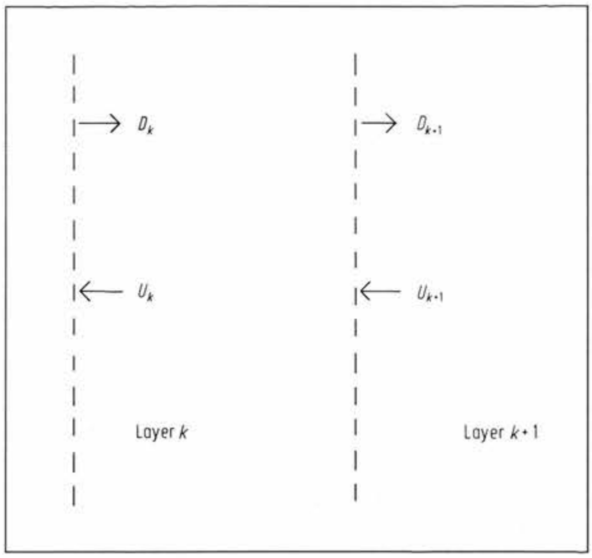

Fig. 2. Forward (D) and reverse (U) travelling waves in adjacent layers.

2.2. The forward problem: the reflectance function

An expression for the reflection pattern can be developed using recursive formulae [5, 6]. Ware and Aki [6] begin by defining a "layer matrix" which relates the forward and backward travelling waves in two adjacent layers k and $k+1$ (Fig. 2 and eq. (1)). Their interest was in the seismological problem, and they referred to the forward and backward travelling waves as downward (D) and upward (U) respectively. The layer matrix takes account of the reflection coefficient r_k at the interface, and the travel time through a layer. The reflection coefficient is defined in the usual way as $r_k = (Z_{k+1} - Z_k)/(Z_{k+1} + Z_k)$, where Z_k and Z_{k+1} are the characteristic acoustic impedances of the layers. The corresponding transmission coefficient t_k is given by $t_k^2 = (1 - r_k^2)$. It is convenient to work in the z-domain, in which the two-way travel time Δt is transformed to $z = \mathrm{e}^{\mathrm{i}\omega\Delta t}$. Letting W represent the one-way travel time (i.e. $W^2 = z$), we obtain ...

$$\begin{pmatrix} U(k,z) \\ D(k,z) \end{pmatrix} = \frac{1}{W t_k} \begin{pmatrix} z & r_k z \\ r_k & 1 \end{pmatrix} \begin{pmatrix} U(k+1), z \\ D(k+1, z) \end{pmatrix}. \quad (1)$$

By multiplying together successive layer matrices, it is possible to relate layer 0 to layer k in the general expression;

$$\begin{pmatrix} U(0,z) \\ D(0,z) \end{pmatrix} = \frac{1}{W^{k+1} \prod\limits_{i=0,k} t_i} \quad (2)$$

$$\cdot \begin{pmatrix} z^{k+1} F(k, 1/z) & z^{k+1} G(k, 1/z) \\ G(k,z) & F(k,z) \end{pmatrix} \begin{pmatrix} U(k+1, z) \\ D(k+1, z) \end{pmatrix}.$$

The notation is kept to manageable proportions by introducing the recursive polynomials F and G, which are functions of the individual reflection coefficients r_i and the travel time. They are given by;

$$F(k+1,z) = F(k,z) + r_{k+1}\, z\, G(k,z),$$
$$G(k+1,z) = r_{k+1}\, F(k,z) + z\, G(k,z), \qquad (3)$$

with

$$F(0,z) = 1 \quad \text{and} \quad G(0,z) = r_0 .$$

The particular case of interest in pulse reflectometry is that with the wave travelling forwards in the first layer being an incident impulse, with a z-transform of unity; the wave travelling backwards in the first layer is the observed reflection, and under these conditions is termed the "reflectance" $R(z)$ [7] or the "input impulse response" [8, 9]; the wave travelling forwards in the last (nth) layer is some (unknown) transmission function, and there is no backward-travelling wave returning from the terminating half-space. Inserting these conditions in eq. (2) and rearranging, we obtain an expression for the reflectance function of an object of n layers;

$$R(z) = \frac{z^{n+1}\, G(n, 1/z)}{F(n,z)}. \qquad (4)$$

Using this relation to calculate the reflectance produced by a given object is the "direct" or "forward" problem. Eq. (4) expresses the reflectance as the ratio of two polynomials, for which the calculation is feasible only in very simple cases. For arbitrary objects, Stansfield and Bogner's [5] method is more convenient for calculating the reflectance, but it is not well suited to the reconstruction problem which we now consider.

3. The inverse problem: reconstruction algorithms

3.1. The Ware-Aki method

Ware and Aki [6] developed a reconstruction algorithm for the "inverse" problem encountered when estimating layer impedances from the recorded reflectance. Suitable rearrangement of eq. (4) and expansion of the polynomials leads to eq. (5), allowing the individual reflection coefficients to be evaluated in succession;

$$r_0 = R_0,$$
$$r_1 = \frac{R_1}{1 - r_0^2},$$
$$r_2 = \frac{R_2 + r_0 r_1 R_1}{(1 - r_0^2)(1 - r_1^2)}$$

etc . . . .

Generally,

$$r_{k+1} = \frac{\sum_{j=0}^{k} F_j R_{k+1-j}}{\prod_{j=0}^{k} (1 - r_j^2)}, \qquad (5)$$

where F_j is the coefficient of z^j in the polynomial $F(k,z)$.

Having evaluated a reflection coefficient r_i from eq. (5), the Ware-Aki polynomials F and G are updated using eq. (3), and the impedance of layer $(i+1)$ can be found from;

$$\frac{Z_{i+1}}{Z_i} = \frac{1 + r_i}{1 - r_i}. \qquad (6)$$

As well as its original seismological application, the "Ware-Aki" algorithm eq. (5) has been used for the acoustic reflectometry of human airways [10, 11]. The algorithm has several interesting features:

(i) To reconstruct N layers, it is necessary and sufficient to record the reflectance function up to the time that the primary reflection from the interface between layers N and $N+1$ arrives back at the detector. It is not necessary to wait for all the reverberations to decay to an insignificant level.

(ii) Inspection of the steps involved reveals that the number of multiplications required is of the order of $3N^2$ to determine N reflection coefficients. Hence the algorithm is computationally intensive and quite slow to perform.

(iii) The numerator is the convolution of the reflectance with the Ware-Aki polynomial F. The new term R_i, appearing for the first time, is multiplied by $F_0 = 1$, and is readily identified as the primary reflection from the latest interface reached. All the other terms relate to the diminishing effect of multiple reflections.

(iv) The denominator is the correction for the combined transmission losses through all the preceding layers.

(v) The algorithm completely and correctly deals with multiple reflections, and will be regarded as the "Gold Standard" against which alternative methods will be judged.

3.2. The "Primaries" method

Suppose we ignore completely the multiple reflection terms, and consider only the primary reflection returning from each interface. Then the theory of Section 3.1 is greatly simplified, and eq. (5) is replaced by the approximation

$$r_i \approx \frac{R_i}{\prod_{j=0}^{i-1} (1 - r_j^2)}. \qquad (7)$$

Table I. Summary of reconstruction algorithms. Notes: 1. "Complexity" refers to the computational steps only, for determination of N reflection coefficients (N impedance values for the Integral method), muls are multiplication or division operations, and adds are addition or subtraction operations. 2. The times given refer to the author's implementation written in Turbo Pascal, and running on a 10 MHz AT-compatible computer. They are intended more for comparative purposes than for absolute timings.

Method	Algorithm		Complexity	Time (ms)
Ware-Aki	$r_{k+1} = \dfrac{\sum^{k} F_j R_{k+1-j}}{\prod_{j=0} (1 - r_j^2)}$	(eq. (5))	$3\,N^2$ muls $+ 3\,N^2$ adds	$100 + 0.2\,N^2$
Primaries	$r_i = \dfrac{R_i}{\prod_{j=0}^{i-1} (1 - r_j^2)}$	(eq. (7))	$3\,N$ muls $+ N$ adds	$60 + 0.2\,N$
Uncorrected Primaries	$r_i = R_i$	(eq. (8))	(no computation)	$60 + 0.09\,N$
Integral	$\dfrac{Z_i}{Z_0} = \dfrac{1 + S(t_i)}{1 - S(t_i)}$	(eq. (11))	N muls $+ 3\,N$ adds	$80 + 0.2\,N$

Each term R_i in the reflectance corresponds directly to one reflection coefficient r_i, with the appropriate transmission correction $(1 - r_j^2)$. No convolution is necessary, and we do not have the Ware-Aki polynomials to update for each iteration. The remaining computation is of order N, and consequently this algorithm runs much more quickly. We will refer to it as the "Primaries" method.

3.3. The "Uncorrected Primaries" method

We can simplify the Primaries method of Section 3.2 even further, by not correcting for transmission losses. Then we would quite simply equate the reflectance terms R_i with the reflection coefficients r_i; i.e.

$$r_i \approx R_i. \tag{8}$$

We will call this the "Uncorrected Primaries" method.

3.4. The "Integral" method

Wright [12] and Jones [13] considered the impulse response of a region of continuous impedance change. Jones showed how the time integral of the reflectance function is equal to an effective cumulative reflection coefficient $r_{m,0}$ relating the impedance of the final layer m with the impedance of the zeroth layer;

$$\int_0^\infty R(T)\,\mathrm{d}T = \frac{Z_m - Z_0}{Z_m + Z_0} = r_{m,0}. \tag{9}$$

Although this holds strictly only for small reflection coefficients ($r_i \ll 1$), we can always break down a medium into sufficiently small steps so that this condition holds. The integral up to time t_i (being the time at which the primary reflection from the $i/i+1$ interface arrives back) is in general less than the complete integral (because of the multiple reflections which continue after time t_i), but we can make the approximation

$$\int_0^{t_i} R(T)\,\mathrm{d}T = S(t_i) \approx \frac{Z_i - Z_0}{Z_i + Z_0}, \tag{10}$$

and hence estimate the impedances Z_i of successive layers.

We will refer to this as the Integral method, and the appropriate reconstruction algorithm is

$$\frac{Z_i}{Z_0} = \frac{1 + S(t_i)}{1 - S(t_i)}, \tag{11}$$

where $S(t_i)$ is the integral appearing in eq. (10). The computation involved is again of order N for N layers. Jones [13] has used the integral method for determining the impedance of human tissue by an ultrasound technique.

The notation of eqs. (10) and (11) explicitly brings out the fact that in a linear system, the time integral of the impule response (i.e. the reflectance) is equal to the step response $S(t)$. This relation suggests an alternative way of measuring impedance layers; namely by recording their response to a step function. Such an excitation is not practical in the acoustic case, but has been used for the time domain investigation of electrical transmission lines [14], and for electrical component measurement [15].

Table I summarises the reconstruction algorithms, giving also their computational complexities and typical calculation times.

4. Numerical and graphical comparisons

Computer programs were written to implement the different reconstruction algorithms, and they were applied to the reflectance functions calculated from known impedance profiles. Numerical and graphical results are presented in Tables II, III and IV and Figs. 3–5.

The following impedance distributions were investigated:

(i) an impedance that decreases as the reciprocal of the square of distance x, i.e. $Z(x) = Z_0(1+\alpha x)^{-2}$. This corresponds to an acoustic cone of increasing diameter;

(ii) three layers with impedances in the ratio 1:2:4, i.e. with large discontinuities between them; and

(iii) an object having an impedance minimum followed by an impedance maximum, i.e. a non-monotonic change.

In each case, the Ware-Aki reconstruction is to be regarded as the ideal, against which the other methods are compared. The impedances are given in arbitrary units as a function of sample point (time or distance).

4.1. Impedance decreasing as the reciprocal of distance squared (Fig. 3 and Table II)

It can be shown that an impedance decreasing as $Z(x) = Z_0(1+\alpha x)^{-2}$ has a reflectance function of $-\alpha \exp(-\alpha x)$ [16]. This example was chosen to illustrate how well the approximate methods work when applied to a continuous, monotonic impedance change.

Furthermore, if α is much smaller than unity, we can simplify the reconstruction calculations to bring out the algebraic similarities and differences between the various methods.

4.1.1. Ware-Aki method (Fig. 3c)

In the region of impedance change, the reflectance terms are $R_i \approx \alpha$ for small α. Successive use of eq. (5) together with the recursion relations of eqs. (3) yields;

$r_1 = \alpha$,

$r_2 = \alpha(1-\alpha^2)^{-1}$

$r_3 = [\alpha + \alpha^3/(1-\alpha^2)](1-\alpha^2)^{-1}[1-(\alpha/(1-\alpha^2))^2]^{-1}$,

etc.;

which simplifies further to $r_i \approx \alpha$ for all i.

Applying eq. (6) successively allows us to write the mth impedance Z_m in terms of the initial impedance Z_0 and the intervening reflection coefficients r_i:

$$Z_m = Z_0 \prod_{i=0}^{m} \left(\frac{1+r_i}{1-r_i}\right), \quad (12)$$

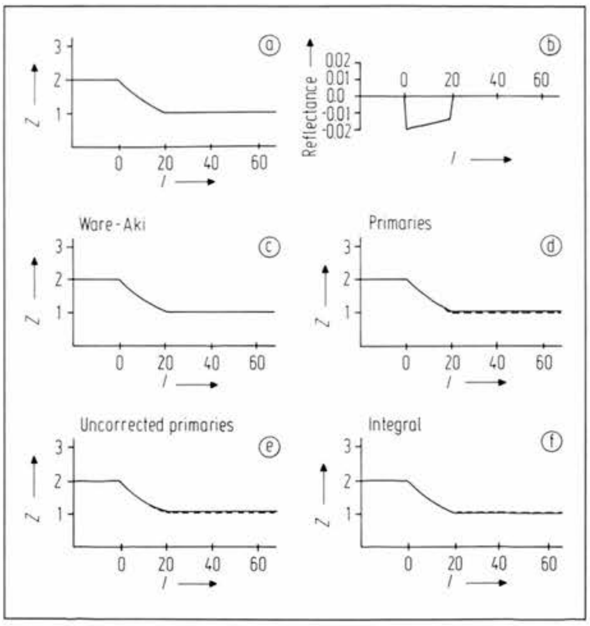

Fig. 3. The four reconstruction algorithms applied to the case of an impedance which decreases as the reciprocal of distance squared (corresponding to an acoustic cone). a) The impedance profile, and b) the reflectance function which has the form $-\alpha\exp(-\alpha x)$ in the region of change. The impedance as reconstructed by c) the Ware-Aki method, d) the Primaries method, e) the Uncorrected Primaries method, and f) the Integral method. The true impedance profile is shown in dashed line, and the axes are in arbitrary units. See Table II. The horizontal axis is labelled in terms of the layer number, I.

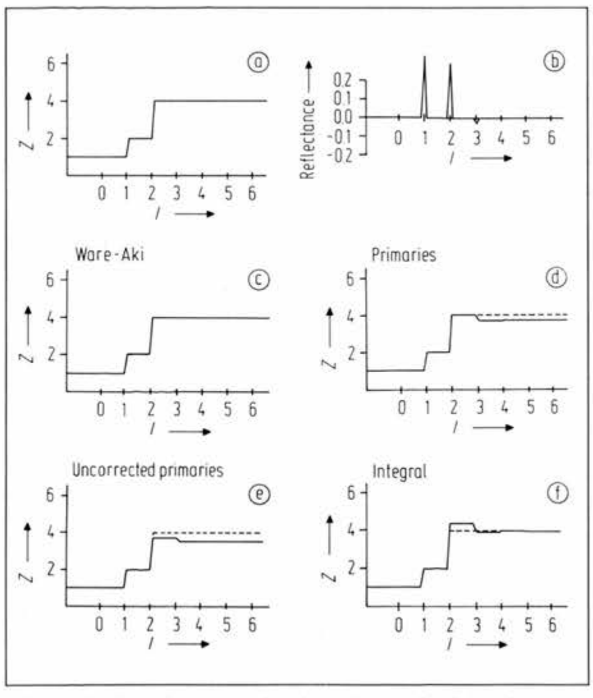

Fig. 4. a) Three layers having impedances in the ratio 1:2:4 have the reflectance shown in b). Reconstruction details as for Fig. 3. See Table III.

Table II. Numerical results for an impedance changing as the reciprocal of distance squared; $Z = Z_0(1 + \alpha x)^2$, with $\alpha = 0.02$. I is the sampling interval or Layer number. The reflectance function $R(I)$ was calculated using a method based on [5], and is in fact equal to $-\alpha \exp(-\alpha x)$ [16]. The Table gives the Layer impedances (relative to Z_0) for the four different reconstruction methods, together with the percentage errors (relative to the Ware-Aki (W-A) method) for the approximate methods. Errors of less than 0.1% are not indicated. The calculated reflection coefficients r_I are omitted for clarity. The Ware-Aki reconstruction matches the original impedance profile exactly (see Fig. 3 and text).

Reflectance		Reconstructed impedances and errors						
I	$R(I)$	$Z(I)_{\text{W-A}}$	$Z(I)_{\text{P}}$	$\Delta Z_{\text{P}}(\%)$	$Z(I)_{\text{UP}}$	$\Delta Z_{\text{UP}}(\%)$	$Z(I)_{\text{Int}}$	$\Delta Z_{\text{Int}}(\%)$
1	−0.020	2.000	2.000	–	2.000	–	2.000	–
2	−0.019	1.923	1.923	–	1.923	–	1.923	–
3	−0.019	1.850	1.850	–	1.850	–	1.850	–
4	−0.019	1.780	1.781	–	1.781	+0.1	1.780	–
5	−0.018	1.715	1.715	–	1.715	–	1.715	–
6	−0.018	1.654	1.654	+0.1	1.654	+0.1	1.653	–
7	−0.018	1.595	1.595	–	1.596	+0.1	1.594	−0.1
8	−0.017	1.540	1.540	–	1.541	+0.1	1.538	−0.2
9	−0.017	1.487	1.488	+0.1	1.489	+0.2	1.485	−0.2
10	−0.017	1.437	1.439	+0.2	1.439	+0.2	1.435	−0.2
11	−0.016	1.389	1.392	+0.3	1.392	+0.3	1.387	−0.2
12	−0.016	1.344	1.347	+0.3	1.348	+0.4	1.341	−0.3
13	−0.016	1.301	1.305	+0.4	1.306	+0.5	1.297	−0.4
14	−0.015	1.260	1.265	+0.5	1.266	+0.6	1.255	−0.5
15	−0.015	1.221	1.227	+0.6	1.228	+0.7	1.216	−0.5
16	−0.015	1.184	1.190	+0.6	1.192	+0.8	1.177	−0.7
17	−0.014	1.149	1.156	+0.7	1.157	+0.8	1.141	−0.8
18	−0.014	1.115	1.123	+0.8	1.124	+0.9	1.106	−0.9
19	−0.014	1.082	1.091	+0.9	1.093	+1.1	1.072	−1.0
20	−0.014	1.051	1.062	+1.1	1.063	+1.2	1.040	−1.1
21	0.000	1.021	1.033	+1.2	1.035	+1.4	1.009	−1.2

Table III. Numerical results for reconstruction of impedances in the ratio 1:2:4. The reflectance $R(I)$ corresponds to the first five terms in the expansion of eq. (4) with $n = 1$ and $r_0 = r_1 = 1/3$. Other details as for Table II (see Fig. 4 and text).

Reflectance		Reconstructed impedances and errors						
I	$R(I)$	$Z(I)_{\text{W-A}}$	$Z(I)_{\text{P}}$	$\Delta Z_{\text{P}}(\%)$	$Z(I)_{\text{UP}}$	$\Delta Z_{\text{UP}}(\%)$	$Z(I)_{\text{Int}}$	$\Delta Z_{\text{Int}}(\%)$
1	0.3333	1.000	1.000	–	1.000	–	1.000	–
2	0.2963	2.000	2.000	–	2.000	–	2.000	–
3	−0.0329	4.000	4.000	–	3.684	− 7.9	4.400	+10.0
4	0.0037	4.000	3.680	−8.0	3.449	−13.8	3.959	− 1.0
5	−0.0004	4.000	3.715	−7.1	3.475	−13.1	4.000	–
6	–	4.000	3.711	−7.2	3.472	−13.2	4.000	–
7	–	3.711	4.000	−7.2	3.472	−13.2	4.000	–

which reduces to

$$Z_m \approx Z_0 \left(\frac{1+\alpha}{1-\alpha}\right)^m, \tag{13}$$

which can in turn be expanded as;

$$Z_m/Z_0 = 1 + 2m\alpha + 2m^2\alpha^2 + (4m^3/3 + 2m/3)\alpha^3 + \dots. \tag{14}$$

4.1.2. Primaries method (Fig. 3d)

Applying eq. (7) to the case of all $R_i \approx \alpha$ gives successive reflection coefficients of;

$$r_1 = \alpha,$$

$$r_2 = \alpha(1-\alpha^2)^{-1},$$

$$r_2 = \alpha(1-\alpha^2)^{-1}[1 - (\alpha/(1-\alpha^2))^2]^{-1},$$

etc.,

i.e., r_1 and r_2 are the same as for the Ware-Aki method, and thereafter the simplified numerator causes the reflection coefficients to be under-estimated. Again, in the limit of small α, all the reflection coefficients evaluate to $r_i = \alpha$, and eqs. (13) and (14) apply.

Table IV. Numerical results for a highly non-monotonic impedance variation (see Fig. 5 and text).

Layer	Reconstructed impedances and errors						
I	$Z(I)_{W-A}$	$Z(I)_P$	$\Delta Z_P(\%)$	$Z(I)_{UP}$	$\Delta Z_{UP}(\%)$	$Z(I)_{Int}$	$\Delta Z_{Int}(\%)$
1	2.000	2.000	–	2.000	–	2.000	–
2	1.280	1.282	+ 0.1	1.285	+ 0.4	1.276	− 0.3
3	0.889	0.903	+ 1.6	0.910	+ 2.4	0.871	− 2.0
4	0.653	0.687	+ 5.1	0.696	+ 6.6	0.619	− 5.3
5	0.889	0.946	+ 6.5	0.951	+ 7.0	0.917	+ 3.1
6	1.280	1.292	+ 0.9	1.285	+ 0.4	1.276	− 0.3
7	2.000	1.834	− 8.3	1.800	−10.0	1.800	−10.0
8	2.492	2.089	−16.3	2.037	−18.3	2.037	−18.3
9	3.191	2.553	−20.0	2.467	−22.7	2.469	−22.6
10	4.232	3.244	−23.3	3.098	−26.8	3.121	−26.3
11	3.191	2.519	−21.0	2.438	−23.6	2.440	−23.5
12	2.492	2.320	− 6.8	2.256	− 9.5	2.257	− 9.4
13	2.000	2.243	+12.2	2.185	+ 9.3	2.186	+ 9.3
14	2.000	2.466	+23.3	2.389	+19.5	2.391	+19.6
15	2.000	2.444	+22.2	2.370	+18.5	2.371	+18.6
16	2.000	2.327	+16.3	2.262	+13.1	2.263	+13.1
17	2.000	2.212	+10.6	2.157	+ 7.9	2.158	+ 7.9
18	2.000	2.131	+ 6.6	2.082	+ 4.1	2.083	+ 4.1
19	2.000	2.097	+ 4.8	2.050	+ 2.5	2.051	+ 2.5
20	2.000	2.105	+ 5.3	2.058	+ 2.9	2.059	+ 2.9
21	2.000	2.105	+ 5.3	2.058	+ 2.9	2.059	+ 2.9
22	2.000	2.082	+ 4.1	2.037	+ 1.8	2.038	+ 1.9
23	2.000	2.047	+ 2.4	2.004	+ 0.2	2.005	+ 0.2

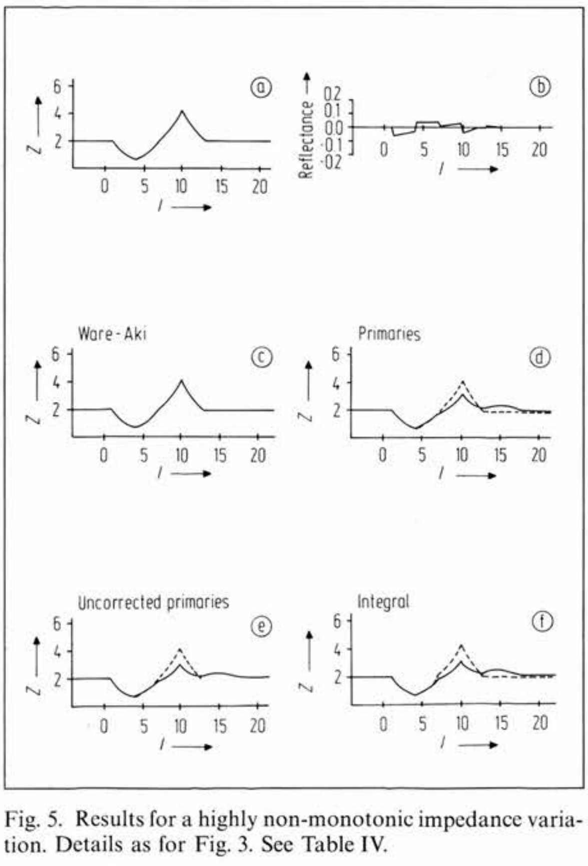

Fig. 5. Results for a highly non-monotonic impedance variation. Details as for Fig. 3. See Table IV.

4.1.3. Uncorrected primaries method (Fig. 3e)

Eqs. (13) and (14) hold for all values of α, since $|\alpha| < 1$.

4.1.4. Integral method (Fig. 3f)

Using eq. (11), with $R_i = \alpha$, gives us;

$$\frac{Z_m}{Z_0} = \frac{1 + m\alpha}{1 - m\alpha}, \tag{15}$$

which can be expanded as;

$$Z_m/Z_0 = 1 + 2m\alpha + 2(m\alpha)^2 + 2(m\alpha)^3 + \ldots . \tag{16}$$

Note the difference between eqs. (14) and (16), from the third order in α upwards. With the Integral method, the calculated impedances change more rapidly than with the Primaries and Uncorrected Primaries methods. It is a more "aggressive" reconstruction algorithm.

Care is required in the use of eqs. (11) and (15). For the case of perfect reflection, $S(t_i)$ and $(m\alpha)$ will equal unity, and the equations have a singularity. In practical work, this situation does not arise because of the non-zero transmission losses in the media.

The numerical results for $\alpha = 0.02$, extending over $x = 20$ data points (giving an overall halving of impedance), are presented in Table II. The table gives the calculated impedances Z_i for the four different reconstruction methods, together with the percentage errors in the impedances, compared with the "correct" Ware-Aki values. Fig. 3 shows the same data in graphical form.

4.2. Impedance ratios 1:2:4 (Fig. 4 and Table III)

This function was chosen because of the severe discontinuities at the interfaces. Evaluating eq. (4) for the case of two interfaces ($n = 1$) with $r_0 = r_1 = 1/3$, we obtain ...

$$R(1,z) = r_0 z + r_1 (1 - r_0^2) z^2 - r_0 r_1^2 (1 - r_0^2) z^3 + r_0^2 r_1^3 (1 - r_0^2) z^4 - r_0^3 r_1^4 (1 - r_0^2) z^5,$$

$$R(1,z) = 0.3333\, z + 0.2963\, z^2 - 0.0329\, z^3 + 0.0037\, z^4 - 0.0004\, z^5.$$

Table III and Fig. 4 display the impedance results in the same format as for the previous example.

4.3. Non-monotonic example (Fig. 5 and Table IV)

A more complex example is shown in Fig. 5. In this case, the impedance passes through a minimum of less than a third of the initial value, before attaining a maximum of twice the initial value, and finally returning to the initial value. This function was selected to illustrate the problems of using the approximate algorithms on highly non-monotonic changes, particularly when trying to reconstruct impedances beyond a severe minimum (or maximum) in impedance. The reflectance function (Fig. 5 b) has been calculated from the layer impedances using a method based on Stansfield and Bogner [5]. Table IV gives the reconstructed layer impedances as calculated by the four different methods. The Ware-Aki results $Z(l)_{\mathrm{WA}}$ correspond exactly to the original impedance profile.

5. Experimental comparisons

The four reconstruction algorithms were applied to the reflectance functions derived from acoustic measurements on rigid, cylindrical test objects [17]. It is not intended to discuss here the practical considerations involved, as these aspects have been dealt with elsewhere [7–11, 16–18].

With air as the transmission medium, the acoustic impedance is inversely proportional to the cross-sectional area of the pathway, provided that cross-modes are not allowed to propagate [19]. Furthermore, the velocity of sound is known, so that the time-series data can be interpreted directly in terms of distance. Since area has more immediate physical meaning than impedance, these experimental results are presented in terms of area profiles.

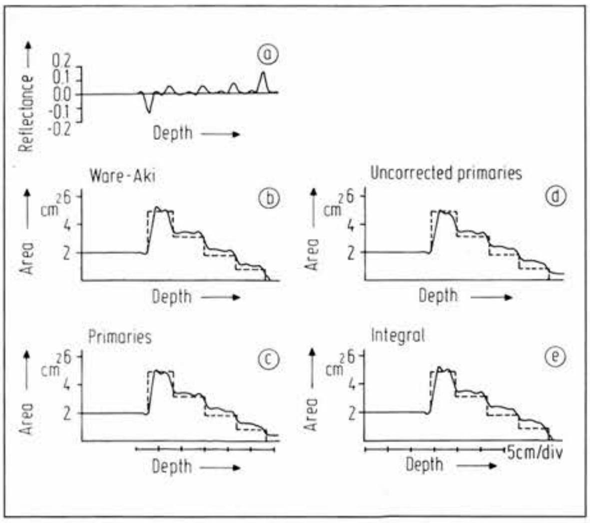

Fig. 6. Experimental results for acoustic measurement of an object having stepped internal diameters. a) The measured reflectance, and the internal cross-sectional area reconstructed by b) the Ware-Aki method, c) the Primaries method, d) the Uncorrected Primaries method, and e) the Integral method. In each case, the reconstructed area is shown in solid line, with the actual area in dashed line.

5.1. Object with stepped internal diameters

Fig. 6a shows the measured reflectance of an object with stepped internal diameters. The area had an initial expansion from 2.0 cm^2 to 4.9 cm^2, followed by successive steps down to 3.1, 1.8 and 0.8 cm^2. Fig. 6

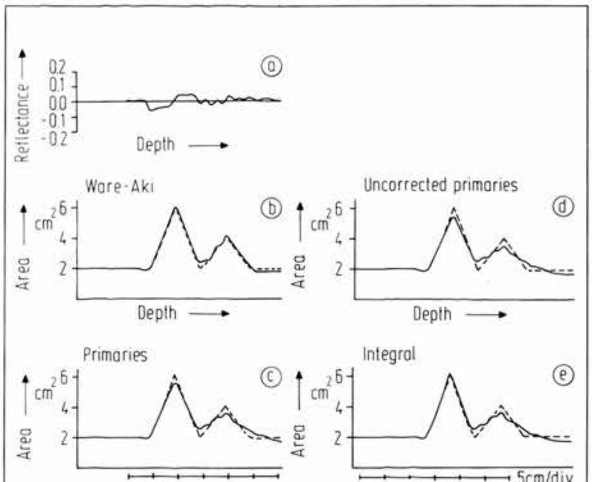

Fig. 7. Experimental results for acoustic measurement of an object with a tapering internal diameter. Details as for Fig. 6.

also shows the area function reconstructed by (b) the Ware-Aki, (c) the Primaries, (d) the Uncorrected Primaries, and (e) the Integral methods. In each case, the actual area of the object is shown in dashed line.

5.2. Internally tapered object

Fig. 7 shows the results obtained for an object with tapered internal diameters, using the same format as Fig. 6. The actual cross-sectional area of the object increases smoothly from 2.0 cm^2 to 6.2 cm^2, then falls smoothly to 2.0 cm^2 before rising to a second peak of 4.0 cm^2, and finally falling to 2.0 cm^2.

6. Discussion

6.1. Speed of algorithms

For a practical number of samples, the Ware-Aki method is considerably slower than the approximate methods because of the convolution in the numerator and the need to update the polynomials. For example, a reconstruction problem with 100 sample points (i.e. $N = 100$) takes the following calculation times in the author's implementation;

Ware-Aki method	2.1 s
Primaries method	80 ms
Uncorrected Primaries method	69 ms
Integral method	100 ms.

Thus the Ware-Aki method takes more than 20 times as long to run, even when the (fixed) program overheads are taken into account. There is relatively little to choose between the three approximate methods as far as speed is concerned.

6.2. Accuracy with synthetic data

See Tables II to IV and the corresponding Figs. 3.5.

Perhaps the most striking feature of the Ware-Aki algorithm is the way in which the reconstructed impedance may continue to change even after the reflectance terms have gone to zero, or, conversely, the impedance may remain constant although the reflectance is non-zero (Figs. 4 and 5). This "memory" effect is of course simply due to the convolution, and it parallels the way in which trapped (reverberant) energy dies away.

6.2.1. Results with impedance changing as the reciprocal of the distance squared (Table II and Fig. 3)

All the reconstruction methods work well with the gentle, monotonic taper shown in Fig. 3a, even though the impedance halves over the region of change. The Ware-Aki method (Fig. 3c) recovers the original impedance profile exactly, whilst the Primaries and Uncorrected Primaries methods underestimate the change (i.e. overestimate the final impedance value) by 1.2% and 1.4% respectively. The Integral method (Fig. 3f) overestimates the change by 1.2%.

6.2.2. Results with stepped impedances in the ratio 1:2:4 (Table III and Fig. 4)

Despite the highly discontinuous nature of the impedance function, the corresponding reflectance has terms which fall off as $-(r_0 r_1)$, i.e. as $-1/9$. For an overall impedance change of 4 times, taking place in just two discrete steps, the Primaries method underestimates the change by 7.2%, whilst the Uncorrected Primaries method underestimates it by 13.2%. Despite an initial overshoot by 10%, the Integral method settles to exactly the correct result.

6.2.3. Results for the non-monotonic object (Table IV and Fig. 5)

The shortcomings of the approximate algorithms in reconstructing impedances beyond a minimum are immediately apparent from Fig. 5. Although the three methods give accurate reconstructions of the minimum (to within 6%), the subsequent impedance maximum is underestimated by between 23% and 27%. The impedance profile beyond the maximum is also considerably distorted. There is little to choose between the approximate methods. The Integral method gives marginally better results around the minimum. The Primaries method returns only slowly to the correct final value, being slightly worse than the other two approximate methods in this respect.

6.2.4. Summary of synthetic data results

Reconstruction of the modest, monotonic impedance change of Fig. 3 (impedance decreasing as the reciprocal of distance squared) is possible to a high degree of accuracy with all four algorithms. Of the approximate methods, the Uncorrected Primaries method is marginally worse than the other two, yielding an error of 1.4% in the final impedance estimate. Evidently, the time-saving approximate methods are well suited to this type of impedance variation. Indeed, Watson [8, 9] found that the Primaries method was perfectly adequate for reconstructing the modest flares of musical instrument bores, as measured by acoustic pulse reflectometry.

When the approximate algorithms are used on a discontinuous impedance function such as that of Fig. 4, the Primaries method gives better results during the region of impedance change, whilst the Integral method gives much more accurate results for the overall change, at the expense of initial overestimation. For an impedance change of a factor of 4, the maximum errors for these two approximate algorithms are of the order of 10%, whilst the time taken is of the order of 20 times less than the (accurate) Ware-Aki method. The Uncorrected Primaries method is less accurate than either of the other two approximate algorithms, and its marginally shorter execution time does not adequately compensate for this.

For a highly non-monotonic impedance variation as shown in Fig. 5, there is little to choose between the three approximate methods, and they all produce errors of around 25% in estimating an impedance maximum beyond a severe minimum. The Ware-Aki method is evidently required for the accurate measurement of impedance variations such as this.

6.3. Experimental results

6.3.1. Stepped internal diameters

The width of the reflectance peaks in Fig. 6a is due to the imperfect pulse deconvolution that accompanies real experimental data. This limits the spatial resolution so that the areas/impedances (which actually have discontinuities) are reconstructed with sloping transitions. In addition, the small positive "ears" seen either side of the large negative peak in the Reflectance function (corresponding to the area expansion from 2.0 to 4.9 cm^2) are artefacts resulting from the deconvolution.

The object was closed at the end, so that the area reconstruction should go to zero. In Fig. 6b, it is seen that the area levels are estimated reasonably well compared with the true area function (dashed line). The maximum percentage error occurs in the last section, when an actual area of 0.8 cm^2 is estimated as 1.1 cm^2. The object is seen to be acoustically "closed". In the Primaries reconstruction of Fig. 6c, the measurement errors are larger (up to 50% overestimation of the last section of the object), and "closure" is not achieved. The Uncorrected Primaries method gives, as expected, even less accurate results. The Integral method (Fig. 6e) gives a good estimate of the first expanded area (4.9 cm^2), whilst the later results are similar to the Uncorrected Primaries reconstruction. Closure is, however, achieved because of the more "aggressive" nature of the Integral algorithm.

6.3.2. Tapered internal diameter

The measured reflectance of Fig. 7a is reconstructed by the Ware-Aki method to give an accurate estimate of the true area function (dashed line) in Fig. 7b. The limited acoustic resolution available causes an overestimation of the central constriction, but both maxima (6.2 and 4.2 cm^2) are estimated to within a few percent. The Primaries and Uncorrected Primaries methods behave very similarly to one another, underestimating the first maximum by approximately 10%, and the second by rather more. The final area estimate does not settle to a steady value within the time scale of these examples, because of the multiple reflection information which is misinterpreted by these approximate algorithms. The Integral method is more successful in estimating the magnitude of the first peak, and is similar to the Primaries method for the second peak.

7. Conclusions

Strictly, the Ware-Aki algorithm is necessary for the accurate reconstruction of impedance layers (or areas) as estimated by pulse reflectometry. The three approximate methods studied are much faster in execution (typically 20 times for 100 data points), and lead to errors of the order of 1% with modest, continuous monotonic impedance changes, and 10% for discontinuous changes. These figures apply when the impedance changes by an overall ratio of 2–4 times. In some applications (for example, the real-time measurement and display of human airway dimensions), these inaccuracies may be acceptable when the substantial time-saving of the approximate methods over the complete Ware-Aki solution is taken into account. Despite the large number of multiple reflection terms, it is evident that their combined effect is not always as significant as might be thought.

Among the approximate algorithms, the Integral method appears to give slightly better results than the other two methods, and is to be preferred. The Uncorrected Primaries method is least accurate, and its use would not normally be justified.

For non-monotonic impedance variations, particularly where reconstruction beyond a severe maximum or minimum is required, the approximate methods do not perform so well. Errors of the order of 25% are encountered in estimating impedance maxima beyond a minimum of one third of the initial value. These errors may still be acceptable for some real-time applications, provided the results are treated with caution.

References

[1] Goupillaud, P. L., An approach to inverse filtering of near-surface layer effects from seismic records. Geophysics **26**(6) [1961], 754–760.

[2] Robinson, E. A., Treitel, S., Geophysical signal analysis. Prentice-Hall, New York 1980.
[3] Robinson, E. A., Durrani, T. S., Peardon, L. G., Geophysical signal processing. Prentice-Hall, New York 1986.
[4] Berryman, J. G., Greene, R. R., Discrete inverse methods for elastic waves in layered media. Geophysics **45**(2) [1980], 213–233.
[5] Stansfield, E. V., Bogner, R. E., Determination of vocal-tract-area function from transfer impedance. Proc. IEEE **120**(2) [1973], 153–158.
[6] Ware, J. A., Aki, K., Continuous and discrete inverse-scattering problems in a stratified elastic medium. I: Plane waves at normal incidence. J. Acoust. Soc. Amer. **45**(4) [1969], 911–921.
[7] Sondhi, M. M., Resnick, J. R., The inverse problem for the vocal tract: Numerical methods, acoustical experiments, and speech synthesis. J. Acoust. Soc. Amer. **73**(3) [1983], 985–1002.
[8] Watson, A. P., Bowsher, J. M., Impulse measurements on brass musical instruments. Acustica **66** [1988], 170–174.
[9] Watson, A. P., Impulse measurements on tubular acoustic systems. Ph.D. Thesis, University of Surrey, UK, 1989.
[10] Jackson, A. C., Butler, J. P., Millet, E. J., Hoppin, E. G., Dawson, S. V., Airway geometry by analysis of acoustic pulse response measurements. J. Appl. Physiology **43**(3) [1977], 523–536.
[11] Fredberg, J. J., Wohl, M. E. B., Glass, G. M., Dorkin, H. L., Airway area by acoustic reflections measured at the mouth. J. Appl. Physiology **48**(5) [1980], 749–758.
[12] Wright, H., Impulse-response function corresponding to reflection from a region of continuous impedance change. J. Acoust. Soc. Amer. **53**(5) [1973], 1356–1359.
[13] Jones, J. P., Impediography: a new ultrasonic technique for diagnostic medicine. In: Ultrasound in Medicine (Vol. 1): Proceedings of the 19th meeting of the American Institute of Ultrasound in Medicine (White, D., ed). Plenum, New York 1975, pp. 489–497.
[14] Oliver, B. M., Time Domain Reflectometry. Hewlett-Packard Journal **15**(6) [1964], 1–8.
[15] Harpham, S., TDR for component measurement. Electronics World and Wireless World, June 1990.
[16] Sondhi, M. M., Gopinath, B., Determination of vocal-tract shape from impulse response at the lips. J. Acoust. Soc. Amer. **49**(6) [1971], 1867–1873.
[17] Marshall, I., Rogers, M., Drummond, G., Acoustic reflectometry for airway measurement. Principles, limitations and previous work. Clin. Phys. Physiol. Meas. **12**(2) [1991], 131–141.
[18] Marshall, I., The production of acoustic impulses in air. Meas. Sci. Technol. **1** [1990], 413–418.
[19] Morse, P. M., Vibration and Sound. McGraw-Hill, New York 1948.

Acoustic reflectometry with an arbitrarily short source tube

Ian Marshall
Department of Medical Physics and Medical Engineering, Western General Hospital, Edinburgh EH4 2XU, United Kingdom

(Received 2 January 1992; accepted for publication 28 February 1992)

In acoustic reflectometry, the input impulse response (*reflectance*) of an object is measured, from which its internal area profile can be deduced. Unwanted multiple reflections are normally avoided by using a source tube that is longer than the object, thus making the source appear nonreflecting. If the source tube is shorter than the object, the required reflectance is obscured by multiple reflections, which cannot be removed by conventional dereverberation. A new analysis of the acoustic reflectometry technique reveals a method by which the source tube may be made arbitrarily short. Such a novel reflectometer is implemented and used to measure objects up to three times the source tube length. Reconstructed areas have accuracies of typically 10%.

PACS numbers: 43.85.Gn, 43.60.Gk, 43.60.Qv, 43.20.Mv

I. THE PRINCIPLE OF ACOUSTIC REFLECTOMETRY

Acoustic reflectometry is used to measure the internal cross-sectional area of objects such as human airways[1,2] and musical instruments.[3] The technique consists of sending a pulse of sound down a source tube and into the object under investigation. The resulting reflections are recorded, and suitable analysis allows determination of the cross-sectional area of the object. In Fig. 1, the acoustic pulse is produced by a source, say, a loudspeaker, at the left-hand end of the tube. The pressure transducer, typically a microphone, is used to record the pressure waveforms.

The signal sensed by the transducer consists of the incident pulse traveling to the right, followed by the left-traveling reflection from the object. After the appropriate delay, the latter is itself reflected by the source and subsequently arrives back at the transducer. Multiple reflections off the object and the source continue indefinitely.

II. NONREFLECTING SOURCE

By making the source tube longer than the object, that part of the object's reflection function sufficient for area reconstruction can be recorded before any multiple reflections arrive at the microphone. This is a way of simulating a *nonreflecting* source. It is then a relatively straightforward matter to deconvolve the measured reflection with the original pulse shape to obtain the object's input impulse response (the *reflectance*). Reconstruction of the area profile from the reflectance follows, using a suitable reconstruction algorithm such as the one used in Ref. 4. While the need for a source tube longer than the object being measured is acceptable in some applications, it can become inconvenient in others. For the investigation of human airways, several research groups have used tubes of the order of 1 m in length.[1,2] In a study of brass musical instruments, Watson[3,5] had to use a source tube consisting of several meters of plastic hose in order to record the complete reflection response of trombones and trumpets. Attenuation of the acoustic pulses, particularly of the high-frequency components, is inevitable under such circumstances, and measurement accuracy is degraded.

In electrical transmission line reflectometers, source reflections are readily avoided. The electrical source is *matched* to the transmission line by making its internal impedance equal to that of the line; typically 50 Ω.[6,7] Energy traveling back towards the source is absorbed without further reflection, and the source thus appears nonreflecting. Unfortunately, no simple practical acoustical matched source is available, although some form of active cancellation is a possibility.

III. MULTIPLE REFLECTIONS AND DEREVERBERATION

If the source tube of an acoustic reflectometer is made shorter than the object length, multiple reflections obscure the required object reflection response. This is a *reverberation* problem. Methods exist for performing dereverberation (separating overlapping signals and reflections) under certain specialized conditions. We will briefly discuss the two best known examples of dereverberation, and show that they are not readily applicable to acoustic reflectometry.

A. Echo cancellation

In communication channels, multiple reflections (echoes) are frequently encountered, and it is usually required

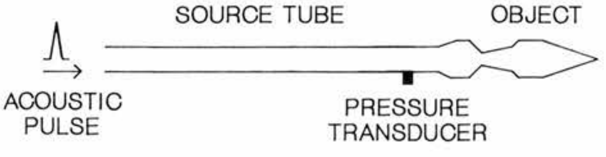

FIG. 1. The principle of acoustic reflectometry. A pulse of sound travels down the source tube into the object being measured. The resulting reflections are recorded by the pressure transducer and analyzed to yield the cross-sectional area profile of the object.

 0001-4966/92/063558-07$00.80

that we eliminate the echoes, leaving the original signal. Often, the echoes are simply delayed and attenuated versions of the original signal, and are represented by $\alpha\delta(t-\tau)$, where τ is the delay and α is the attenuation. In the *cepstral* domain $C(t)$ (defined by taking the inverse Fourier transform of the complex logarithm of the Fourier transform of the original signal), the echoes appear as delta functions at multiples of the delay time, and are readily identified and removed provided that the cepstrum of the signal S is shorter than the delay time [Fig. 2(a)]. Performing the inverse cepstral transform then yields the original signal with the echo canceled.[8,9] This method is still applicable if the echo function is of the form $\alpha h(t-\tau)$, where $h(t)$ is some impulse response causing the echo to be a *distorted* version of the original. In the cepstral domain, the function $h(t)$ appears at time τ, the function $h(t)$ convolved with itself $(h(t)\otimes h(t))$ at time 2τ, and so on, the echo function becoming progressively more convolved with itself at multiples of the delay time [Fig. 2(b)].

In reflectometry, however, we must recover the function $h(t)$ itself, since it contains the information required to reconstruct the object area. For cepstral dereverberation to work, it is then necessary that both the signal cepstrum S and $h(t)$ be shorter than the delay time τ, so that separation is possible.[9] However, it is under precisely these conditions that we could simply record the acoustic reflection directly, as described above for a nonreflecting source. Cepstral dereverberation is thus seen to offer no advantages for acoustic reflectometry, and does not enable us to use a short source tube.

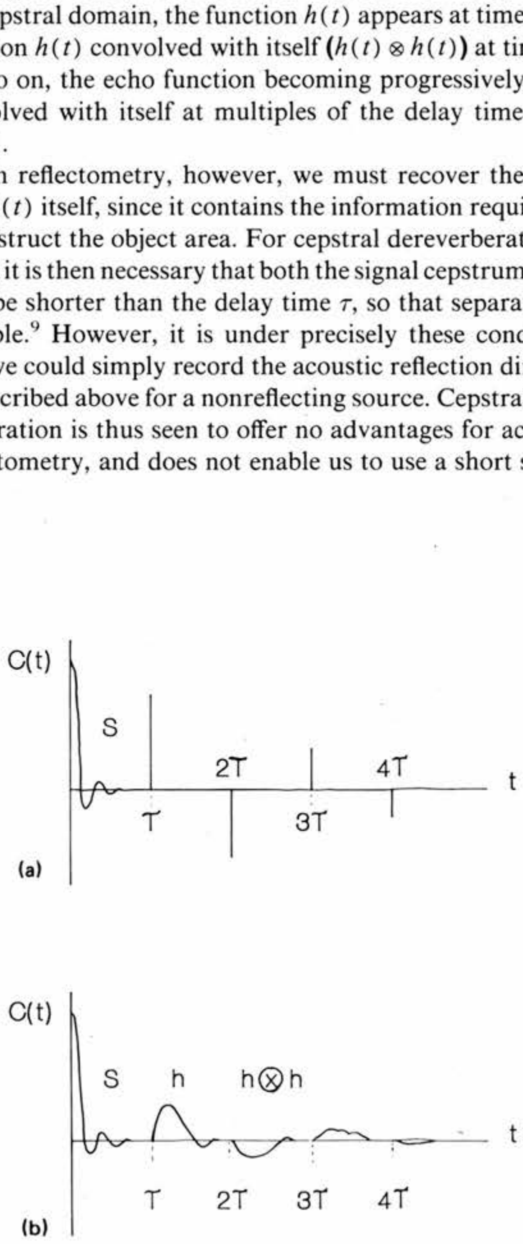

FIG. 2. Dereverberation in the cepstral domain $C(t)$. (a) A signal with an echo occurring after a delay τ appears in the cepstral domain as the signal cepstrum S, followed by a series of delta functions at multiples of the delay time. (b) An echo function $h(t)$ appears at time τ, with multiple convolutions ($\otimes$) of itself appearing at successive multiples of the delay time. Separation of the basic fucntion $h(t)$ is possible only if (as shown here) the delay time τ is greater than the duration of $h(t)$.

B. Marine seismology

Mention should be made here of another important class of dereverberation problems. In marine seismology, multiple reflections between the seabed and the surface (with round-trip delay τ) obscure the seismogram of the layers underlying the seabed. In this case, the problem is greatly simplified by the nature of the reflections. There is a large impedance mismatch between air and water, so that the surface reflection coefficient is approximately -1. Similarly, the reflection coefficient at the seabed can be characterized by a constant k, because of the large mismatch there. As a result, the multiple reflections have a particularly simple form, and it is shown in standard texts[10] how a filter such as $(1+kz^{\tau})^{-2}$ can perform derverberation in the z domain. In the acoustic reflectometer case, we cannot make any such assumptions, and there is no simple filter that can be applied.

IV. ANALYSIS

We now analyze the acoustic reflectometer from first principles, and develop a method for making measurements when the source tube is arbitrarily short. Figure 3 shows the geometry of the acoustic reflection technique, together with the important dimensions. A loudspeaker is used as the source and a microphone (MIC) is used as the pressure transducer. We make the following definitions.

- L_{sm} The source to microphone distance, with two-way travel time $T_2 = 2L_{sm}/c$, where c is the velocity of sound.
- L_{mo} The microphone to object distance, with two-way travel time $T_1 = 2L_{mo}/c$.
- $f(t)$ The pressure pulse waveform produced by the source, which has a Fourier transform of $F(\omega)$. We define $t=0$ to be the time at which the incident pulse first reaches the microphone.
- $r_s(t)$ The source reflection response, with a Fourier transform of $R_s(\omega)$. For a given geometry, this term may be taken to include the effects of attenuation over the distance L_{sm}.
- $r_o(t)$ The required input impulse response (reflectance) of the object, with a Fourier transform of $R_o(\omega)$.

The signal $m(t)$ observed at the microphone consists of the incident pulse traveling to the right, followed (after the microphone-object round trip delay T_1) by the first reflection from the object. This latter is given by the object reflectance convolved with the incident pulse. Further components in the observed signal consist of alternate reflections off the source and the object, and the composite signal is given by the infinite series

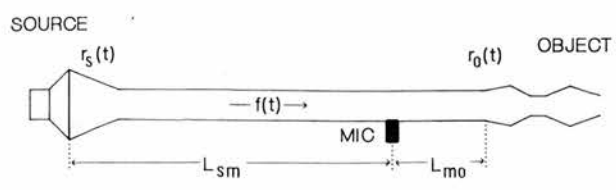

FIG. 3. An acoustic reflectometer with the important dimensions shown. MIC: microphone. See text for other definitions.

$$m(t) = f(t) + f(t) \otimes r_o(t) \otimes \delta(t - T_1) + f(t) \otimes r_o(t) \otimes r_s(t) \otimes \delta[t - (T_1 + T_2)]$$
$$+ f(t) \otimes r_o(t) \otimes r_s(t) \otimes r_o(t) \otimes \delta[t - (2T_1 + T_2)]$$
$$+ f(t) \otimes r_o(t) \otimes r_s(t) \otimes r_o(t) \otimes r_s(t) \otimes \delta[t - (2T_1 + 2T_2)] + \cdots, \quad (1)$$

where the symbol $\otimes$ denotes convolution. We have implicitly assumed that the microphone has an ideal response. In practice, all signals will be distorted in the same way by its response, which thus cancels out. To proceed with the analysis, we transform to the frequency domain. The time delays $\delta(t - \tau)$ become phase factors $\exp(-j\omega\tau)$, the convolutions are replaced by multiplications, and Eq. (1) reduces to

$$M(\omega) = F(\omega) + \exp(-j\omega T_1) F(\omega) R_o(\omega) + \exp[-j\omega(T_1 + T_2)] F(\omega) R_o(\omega) R_s(\omega)$$
$$+ \exp[-j\omega(2T_1 + T_2)] F(\omega) R_o^2(\omega) R_s(\omega) + \exp[-j\omega(2T_1 + 2T_2)] F(\omega) R_o^2(\omega) R_s^2(\omega) + \cdots, \quad (2)$$

which can be written as

$$M(\omega) = F(\omega)[1 + R_o \exp(-j\omega T_1)] \times \sum_{k=0}^{\infty} \{\exp[-j\omega(T_1 + T_2)] R_o(\omega) R_s(\omega)\}^k, \quad (3)$$

which sums to

$$M(\omega) = \frac{F(\omega)[1 + R_o(\omega)\exp(-j\omega T_1)]}{1 - R_o(\omega) R_s(\omega) \exp[-j\omega(T_1 + T_2)]}. \quad (4)$$

In conventional reflectometry, the source is positioned far away from the microphone and object by use of a long source tube. The source then appears nonreflecting for objects shorter than the tube, and we can write $R_s(\omega) = 0$, so that Eq. (4) reduces to

$$M(\omega) = F(\omega)[1 + R_o(\omega)\exp(-j\omega T_1)]. \quad (5)$$

During calibration of such a reflectometer, it is usual to measure $f(t)$, either by fitting a perfect reflector or a long extension tube at the microphone position. During measurements, $f(t)$ is subtracted from the observed signal $m(t)$ to leave the reflection term $f(t) \otimes r_o(t) \otimes \delta(t - T_1)$. This is then deconvolved, possibly in the frequency domain, to yield the required reflectance $r_o(t)$.

We are interested in the case of a short source tube, when $R_s(\omega) \neq 0$, and we have to use the full form of Eq. (4). We can define the object to begin at the microphone, so that x_1 and T_1 are both zero. Making this substitution, and rearranging, we obtain the frequency domain expression for the reflectance,

$$R_o(\omega) = \frac{M(\omega) - F(\omega)}{F(\omega) + M(\omega) R_s(\omega) \exp(-j\omega T_2)}. \quad (6)$$

To evaluate the reflectance, we thus need to know both the spectrum of the incident pulse $F(\omega)$ and the source reflection response $R_s(\omega)$, together with the distance x_2. We will now describe a two-stage calibration procedure for estimating these functions.

The incident pressure pulse $f(t)$ is readily measured by fitting a long extension tube in place of the object under test [Fig. 4(a)]. Provided that the extension tube is acoustically longer than the pulse duration, the reflections from the far end of the tube can be discarded without loss of information. This is equivalent to Eq. (4) with both R_s and R_o equal to zero, and is the calibration carried out for a conventional (i.e., "long") reflectometer. Measurement of the propagation delay between excitation of the loudspeaker and arrival of the pulse at the microphone determines T_2. Transformation to the frequency domain yields $F(\omega)$.

In the second stage of calibration, the extension tube is replaced by a reflecting plug or cap at the microphone position [Fig. 4(b)]. If the plug has a reflection response of $R_c(\omega)$, then analogy with Eq. (4) shows that the (frequency domain) signal observed at the microphone will be

$$M_{\mathrm{cal}}(\omega) = \frac{F(\omega)[1 + R_c(\omega)]}{1 - R_c(\omega) R_s(\omega) \exp(-j\omega T_2)}. \quad (7)$$

Rearranging, we obtain an estimate of the source reflection response

$$R_s(\omega) = \frac{M_{\mathrm{cal}}(\omega) - F(\omega)[1 + R_c(\omega)]}{M_{\mathrm{cal}}(\omega) R_c(\omega) \exp(-j\omega T_2)}. \quad (8)$$

For a rigid plug, we may assume that R_c is independent of frequency and equal to unity. Calculation of the source reflection response is then simplified to

$$R_s(\omega) = \frac{M_{\mathrm{cal}}(\omega) - 2F(\omega)}{M_{\mathrm{cal}}(\omega) \exp(-j\omega T_2)}, \quad (9)$$

where all quantities on the right are known. Finally, the object is replaced, and measurement commences, using Eq. (6) to evaluate the object's reflectance.

To arrive at these results, it is necessary to sum *all* the multiple reflections, so that we can write Eq. (4) as the sum

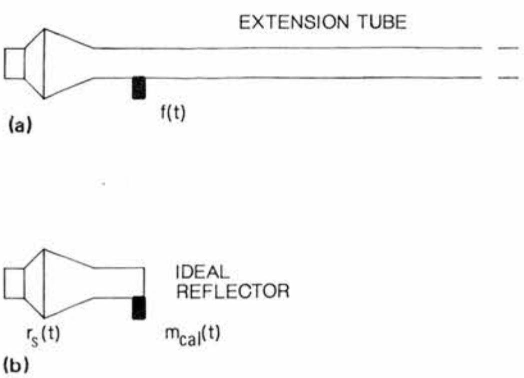

FIG. 4. Calibration of a reflectometer with an arbitrarily short source tube. (a) Use of an extension tube allows the source pressure waveform $f(t)$ to be determined. (b) Closing the tube with an ideal reflector at the microphone position allows determination of the source reflection function $r_s(t)$.

of an infinite series. This poses a problem, since (theoretically) the reverberations continue indefinitely. In practice, it is sufficient to record the signals until the reverberation has decayed below the noise level. This extended recording time is the price paid for using an arbitrarily short source tube.

V. EXPERIMENTS

A. Reflectometer

A reflectometer was implemented with a source tube consisting of 30 mm of 16-mm bore plastic tubing (Fig. 5). The source was a "tweeter" loudspeaker (RS Components type 249-435), acoustically coupled to the source tube and driven by 10-V, 25-μs electrical pulses. The cone of the loudspeaker lay approximately 65 mm behind the mouth of the coupler, so that the effective overall length of the reflectometer was 95 mm. The microphone (Knowles Electronics type BL1785) was set in the source tube wall, and connected to a preamplifier (gain 5.5, bandwidth 50 Hz to 12 kHz). The preamplifier output fed a 12-bit ADC card in an IBM-compatible computer system, sampling at 40 kHz. A slide valve, positioned immediately beyond the microphone, allowed the source tube to be closed for calibration purposes. Pressure records were 1024 samples (25.6 ms) long, and calculations were carried out using 1024-point fast Fourier transforms.

B. Calibration

Calibration of the reflectometer consisted of the two stages described in Sec. IV. Firstly, a 1-m-long extension tube was coupled to the source tube, the loudspeaker excited by the electrical pulse, and the microphone signal recorded. It was known *a priori* that the loudspeaker impulse response (i.e., the source waveform) lasted less than the round-trip travel time of the extension tube (approximately 6 ms), and so the source waveform could be determined unambiguously by zeroing all data points beyond 6 ms, thus avoiding multiple reflections from the open end of the extension tube.

In the second stage of calibration, the extension tube was removed, and the source tube closed by the slide valve. The loudspeaker was excited as before, and the microphone signal $m_{cal}(t)$ recorded. $M_{cal}(\omega)$ and the source reflection function $R_s(\omega)$ were calculated.

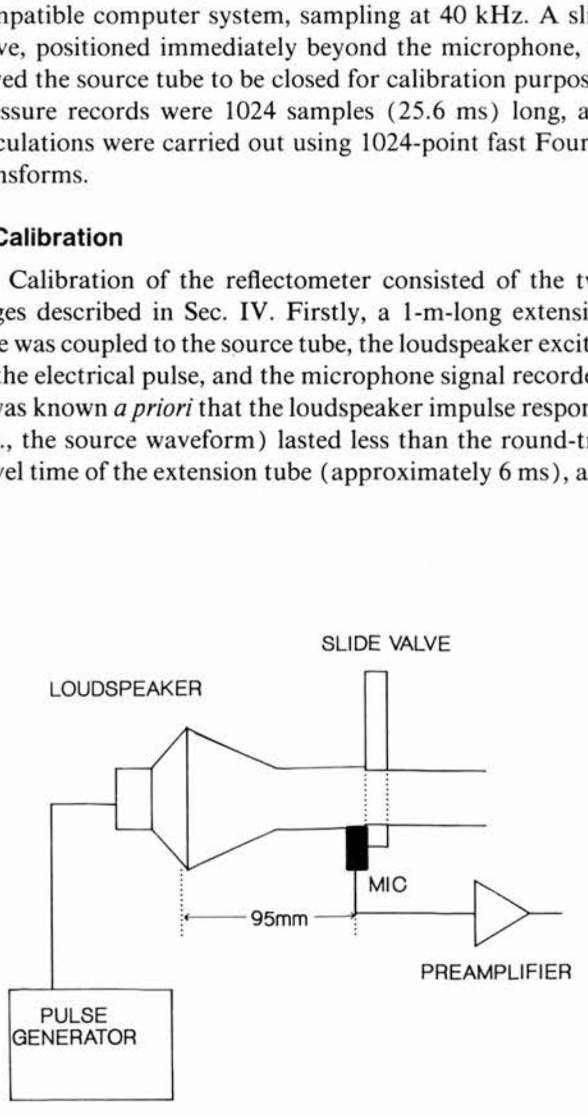

FIG. 5. Practical implementation of an acoustic reflectometer. The loudspeaker coupler and source tube are together 95 mm long. The loudspeaker is excited by 10-V, 25-μs pulses. The slide valve closes the source tube for calibration purposes. The microphone signal is recorded and analyzed by a microcomputer system.

C. Test objects

Four test objects with known internal dimensions were used to validate the reflectometer theory presented above. The objects were each 100 mm long, cylindrically symmetrical, and made of rigid plastic ("Perspex"). They had end diameters of 16 mm (cross sectional area 2.0 cm^2) to match the source tube, and could be coupled together. Two had smoothly tapered internal expansions, to 4.0 and 6.0 cm^2, respectively, whilst the other two had tapered constrictions, to 0.5 and 0.9 cm^2, respectively. The objects were connected to the reflectometer by a 60-mm length of tubing.

VI. RESULTS

Figure 6(a) shows the source waveform $f(t)$ measured during the first stage of the calibration process. It is seen to last approximately 3 ms. Its frequency domain representation $|F(\omega)|$, shown in Fig. 6(b), reveals peaks around 1 and 3 kHz. Figure 7(a) shows the reverberant waveform $m_{cal}(t)$ observed when the slide valve is closed. Approximately 20 reverberations are discernible before the signal decays to the noise level, taking approximately 12 ms. The signal is transformed to the frequency domain, and the spectrum $|M_{cal}(\omega)|$, shown in Fig. 7(b), is seen to be modulated with a periodicity of 1.8 kHz. This corresponds to the 560-μs delay of the 95-mm reflectometer length. The source reflection function $R_s(\omega)$ (Fig. 8) is calculated using Eq. (9). It is evident from Fig. 8 that determination of $R_s(\omega)$ is not perfect, since unphysical values (greater than unity) occur at frequencies above 5 kHz.

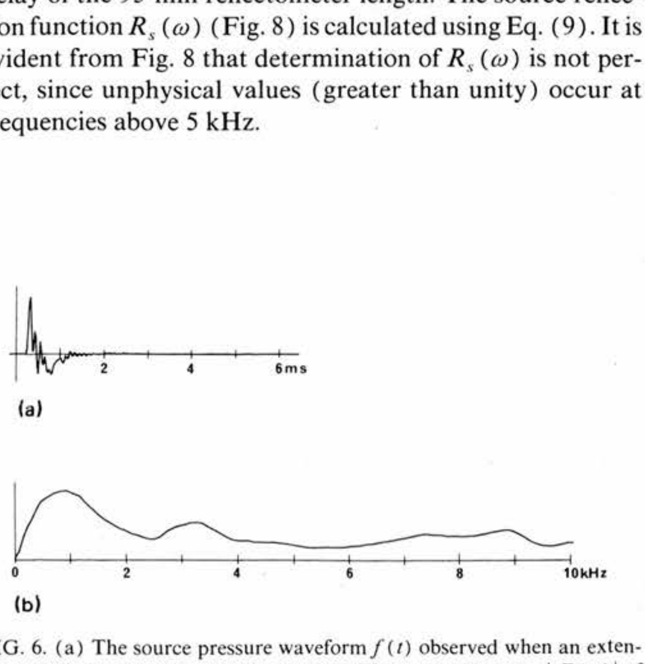

FIG. 6. (a) The source pressure waveform $f(t)$ observed when an extension tube is fitted to the reflectometer. (b) The spectral content $|F(\omega)|$ of the waveform.

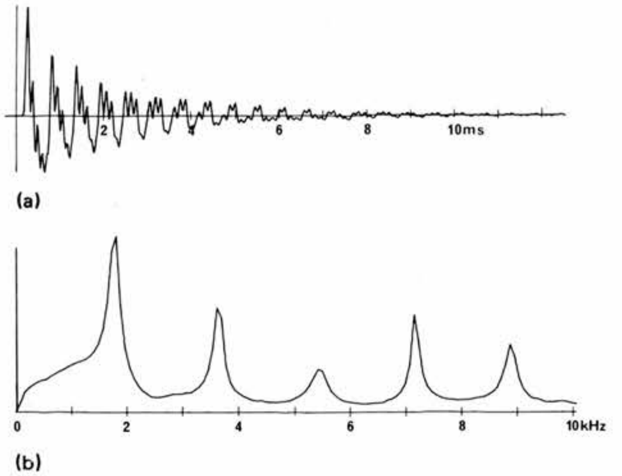

FIG. 7. (a) The reverberant waveform $m_{cal}(t)$ observed when the source tube is closed at the microphone position, and (b) its spectral content $|M_{cal}(\omega)|$. The periodicity of 1.8 kHz corresponds to the 560-μs delay of the 95-mm reflectometer length.

Figures 9–12 show specimen results with the test objects. In Fig. 9(a) is the microphone signal observed when the 6- and 4-cm^2 sections are cascaded, and the far end left open to the air. In this case, the reverberations have effectively died away within the measurement period. Figure 9(b) and (c) show the intermediate frequency domain quantities $|M(\omega)|$ and $|R_o(\omega)|$. Notice that several "spikes" of amplitude greater than unity appear in the latter. Transforming back to the time domain, we obtain the reflectance $r_o(t)$ in Fig. 9(d). The first part of this trace is expanded in Fig. 10(a), and the corresponding area, reconstructed by the Ware–Aki algorithm,[4,11] is shown in solid line in Fig. 10(b). The true area profile is shown superimposed in dashed line. Apart from the incorrect area expansion seen in the early part of the trace (at 5 cm, in the connecting tube) and some loss of definition in between the two peak areas, the object's area profile is estimated very well (to within a few %). It should be remembered that the object (at 30 cm) is three times longer than the reflectometer.

Figure 11 shows the corresponding reflectance and reconstructed area profiles for the 4-cm^2 object on its own. We see that the connecting tube is better estimated, but the area maximum is not so well defined, being 10% underestimated.

As a final example, Fig. 12 shows measurement of the test object having a constriction of 0.9 cm^2, with its far end closed. The area reconstruction estimates the constriction itself very well, but there is an "overshoot" of nearly 50% at the beginning of the object.

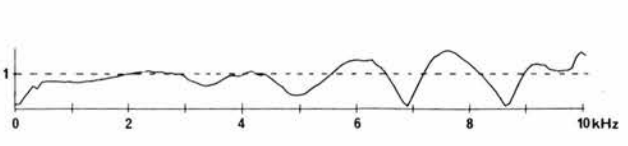

FIG. 8. The source reflection response $|R_s(\omega)|$ as calculated using Eq. (9). The values greater than unity (above 5 kHz) are physically impossible, and are due to imperfect data.

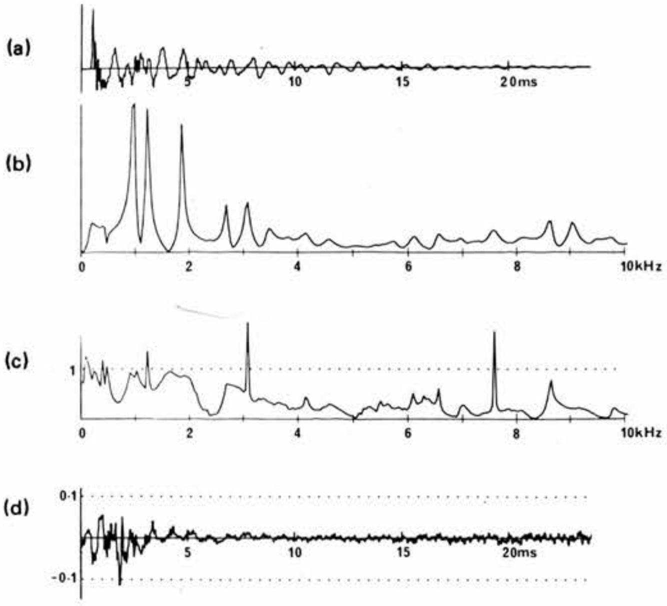

FIG. 9. Measurement of a test object consisting of expansions to 6 and 4 cm^2, with the far end open to the air. (a) The microphone signal $m(t)$, with (b) its spectrum $|M(\omega)|$. (c) The object's frequency domain reflectance $|R_o(\omega)|$ as calculated by Eq. (6). (d) The reflectance $r_o(t)$ after transformation back to the time domain.

VII. DISCUSSION

The results confirm that the theory is correct, and that it can be used to implement a novel acoustic reflectometer having a source tube shorter than the object being measured. The calibration is a simple, two-step procedure, requiring only an extension tube and an end reflector.

In assessing the area reconstructions, several limitations

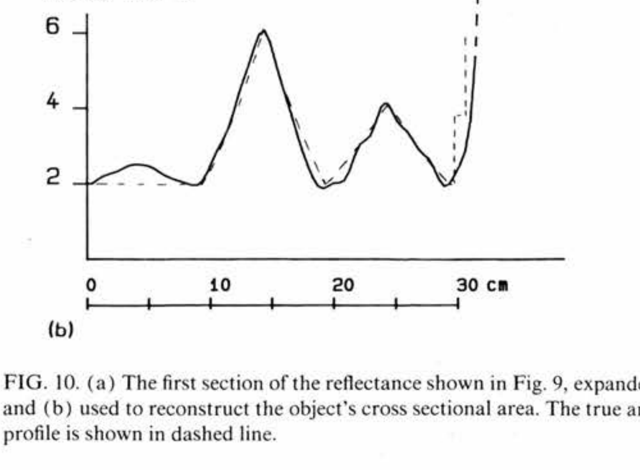

FIG. 10. (a) The first section of the reflectance shown in Fig. 9, expanded, and (b) used to reconstruct the object's cross sectional area. The true area profile is shown in dashed line.

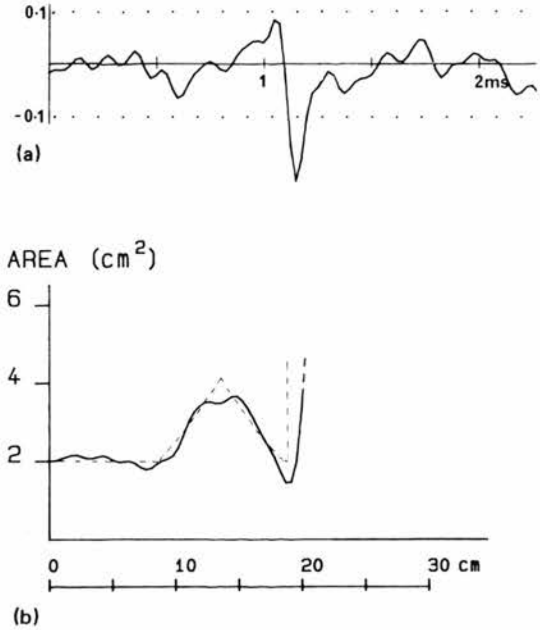

FIG. 11. (a) The expanded reflectance function and (b) the reconstructed area profile of a test object consisting of an expansion to 4 cm^2, with the far end open. The true area profile is shown in dashed line.

inherent in any type of acoustic reflectometry should be borne in mind.[11]

The spatial resolution is limited by the shortest wavelengths used, and these are in turn restricted by the need to avoid cross mode propagation in the object. The reconstructed areas show a shift away from the source compared with

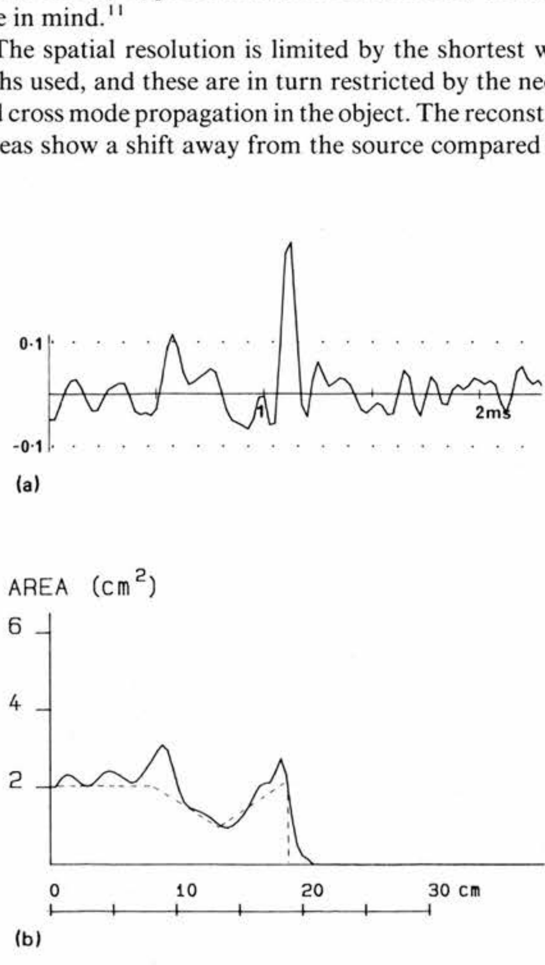

FIG. 12. (a) The expanded reflectance function and (b) the reconstructed area profile of a test object consisting of a constriction of 0.9 cm^2, with the far end closed. The true area profile is shown in dashed line.

the true areas. This is particularly evident in Fig. 12(b), and is caused by the "low-pass filtering" effect of the limited resolution.

It can be seen from Fig. 6(b) that the source produces very little energy below a few hundred hertz. Reconstruction algorithms are particularly sensitive to low-frequency errors, which show up as "drift" on the reconstructed areas. This is probably the cause of the incorrect estimation of the connecting tube area at the beginning of the trace in Fig. 10(b), and of the overshoot in Fig. 12(b). Because the source emits no energy at dc, the dc component in the (frequency domain) reflectance was set equal to the lowest frequency component. It was found necessary to bandlimit the calculated reflectance to reduce high-frequency noise. A cosine-shaped low-pass filter with a response falling to zero at 15 kHz was used. Residual noise can be seen in the reflectance trace of Fig. 9(d).

Inspection of Fig. 6(a) reveals that successive multiple reflections become more and more smoothed, indicating that dispersion is occurring. This nonideal behavior has not been taken into account in the simple theory presented here.

We have already commented on the errors in the determination of $R_s(\omega)$, which show up as unphysical values (greater than unity) in certain frequency ranges in Fig. 8. In calculating $R_s(\omega)$, we made the assumption of perfect reflection at the slide valve, which cannot be realized in practice. No improvement resulted from trying (frequency-independent) values of R_c in the range 0.8 to 1.0 in Eq. (8). Perhaps a third calibration step should be devised to accurately measure the reflection characteristics of the slide valve. It might also be worth recording the signals for more than the present 1024 samples.

Spikes with magnitude greater than unity appear in the calculated frequency domain reflectance $|R_o(\omega)|$ (Fig. 9), and these are also spurious.

Notwithstanding the shortcomings discussed here, reasonable results can be achieved with the novel "short" reflectometer, and it may well find application in acoustic research.

ACKNOWLEDGMENTS

The evaluation of acoustic reflectometry for human airway measurement is funded in part by the Scottish Home and Health Department.

[1]J. J. Fredberg, M. E. B. Wohl, G. M. Glass, and H. L. Dorkin, "Airway area by acoustic reflections measured at the month," J. Appl. Physiol. **48**, 749–758 (1980).

[2]M. M. Sondhi and J. R. Resnick, "The inverse problem for the vocal tract: numerical methods, acoustical experiments, and speech synthesis," J. Acoust. Soc. Am. **73**, 985–1002 (1983).

[3]A. P. Watson and J. M. Bowsher, "Impulse measurements on brass musical instruments," Acustica **66**, 170–173 (1988).

[4]J. A. Ware and K. Aki, "Continuous and discrete inverse-scattering problems in a stratified elastic medium. I. Plane waves at normal incidence," J. Acoust. Soc. Am. **45**, 911–921 (1969).

[5]A. P. Watson, "Impulse measurements on tubular acoustic systems," Ph.D. thesis, University of Surrey (1989).

[6]B. M. Oliver, "Time domain reflectometry," Hewlett-Packard J. **15**(6), 1–8 (1964).

[7]S. Harpham, "TDR for component measurement," Electron. Wireless World, 497–501 (1990).
[8]J. C. Hassab, "Homomorphic deconvolution in reverberant and distortional channels: An analysis," J. Sound Vib. **58**(2), 215–231 (1978).
[9]R. B. Randall and J. Hee, "Cepstrum analysis," Brüel & Kjaer Tech. Rev. **3**, 3–40 (1981).
[10]E. A. Robinson, T. S. Durrani, and L. G. Peardon, *Goephysical Signal Processing* (Prentice-Hall, Englewood Cliffs, NJ, 1986).
[11]I. Marshall, M. Rogers, and G. Drummond, "Acoustic reflectometry for airway measurement. Principles, limitations and previous work," Clin. Phys. Physiol. Meas. **12**(2), 131–141 (1991).